# Composition and Morphology Effects on the Thermal Transport Mechanisms of Low Thermal Conductivity Crystalline Nanomaterials and Frameworks

---

A

Dissertation

Presented to

the faculty of the School of Engineering and Applied Science

University of Virginia

---

in partial fulfillment

of the requirements for the degree

Doctor of Philosophy

by

Mallory E. DeCoster

May 2021

# APPROVAL SHEET

This

Dissertation

is submitted in partial fulfillment of the requirements
for the degree of

Doctor of Philosophy

Author: Mallory E. DeCoster

This Dissertation has been read and approved by the examing committee:

Advisor: Patrick E. Hopkins

Advisor:

Committee Member: Pamela M. Norris

Committee Member: Keivan Esfarjani

Committee Member: Mona Zebarjadi

Committee Member: Gaurav Giri

Committee Member:

Committee Member:

Accepted for the School of Engineering and Applied Science:

Craig H. Benson, School of Engineering and Applied Science

May 2021

# Abstract

The research detailed in this dissertation investigates the roles of composition and morphology on thermal transport mechanisms in low thermal conductivity functional materials for applications towards energy conversion (thermoelectric systems) and gas storage technologies. Specifically, I experimentally investigated the thermal transport processes of chalcogenide nanocomposite thermoelectric (TE) thin films, and pristine and infiltrated porous crystalline metal-organic frameworks (MOFs), with time-domain thermoreflectance (TDTR). I find that the roles of compositional and structural disorder in the form of defects, grain boundaries, and compositional boundaries in PbTe-PbSe nanostructured ALD composites are effective in reducing the phonon thermal conductivity, and represent a pathway for further improvement of the figure of merit (ZT) for achieving higher efficiency TE devices. While it is well known that disorder in non-porous, crystalline nanomaterials generally acts to reduce thermal transport, the role of compositional disorder, in the form of an adsorbate, within porous crystalline material remains an open question; and it is unclear whether the introduction of guest molecules into the pores helps or hinders heat transfer. To study this, I investigated the effect of adsorbates spanning a range of energy landscapes by varying both the phase (gas, liquid, solid) and guest-host bonding environment, on the thermal processes of two compositionally different, but morphologically similar MOFs (HKUST-1 and ZIF-8). The results show that the pore morphology is critical in defining the thermal transport mechanisms in MOFs. When the pores are small and rigid (HKUST-1), adsorbates drastically reduce the thermal conductivity through both extrinsic adsorbate/MOF collisions that reduce vibrational mode lifetimes, and intrinsic changes to the vibrational structure which change the mode character. The degree of each mechanisms effect is dictated by the adsorbate bonding environment. Further, larger, mechanically flexible pores (ZIF-8) serve to dampen the thermally inhibiting effects of the adsorbates, so that the overall thermal conductivity is neither enhanced nor reduced. These results are critically important for designing future MOF functional materials towards both gas storage and TE applications, where efficiency is closely tied to how thermal properties behave in the presence of adsorbates and effective medium theory is not an adequate approximation for predicting the thermal conductivity of the infiltrated system.

# Acknowledgments

I am profoundly grateful to the family, friends, collaborators, colleagues, mentors and institutions that provided me the support, encouragement and foundation to pursue and obtain this degree.

First and foremost, thank you to my husband, Bradley J. Rykal, for the unwavering consistency, love, and support that you have provided me through this process. You have been a critical sounding board, and it is from you that I gain my confidence in all things, personally, academically, and professionally. I could have never accomplished this pursuit without you. To my kids, I hope that this work serves to inspire and motivate you some day.

It is with the highest reverence that I thank my advisor, Prof. Patrick Hopkins, for taking me on as a student and offering endless guidance and encouragement throughout the PhD process. I so much admire and appreciate the energy, intellect, and positivity brought in every interaction that I had with Patrick as a student in his lab.

Next, I thank my committee members – Prof. Pamela Norris, Prof. Keivan Esfarjani, Prof. Mona Zebarjadi, and Prof. Gaurav Giri – for the support and guidance in establishing my research plan. Thank you for holding me to a high standard!

I am also so grateful to my colleagues at the ExSiTE lab for all of their support and guidance. Thank you to former members – Dr. Ramez Cheaito, Prof. Brian Foley, and Prof. Brian Donovan for helping me establish a solid foundation as an experimentalist in the lab. Thank you to the ExSiTE Lab's senior scientist, Dr. John Gaskins, for mentorship and proof-reading support. Thank you to Dr. Tomko, Dr. Olson, Ethan Scott, and Dr. Rost for their friendships throughout my time at UVA! Also thank you to my many collaborators, especially Sangeun Jung (UVA), Dr. Zeinab Hassan (KIT), Prof. Engelbert Redel (KIT), Dr. Xin Chen (ODU), Sarah Smith (NCSU), Prof. Gregory Parsons (NCSU), and Dr. Hasan Babaei (UC-Berkley) for providing critical contributions to this research.

I have been fortunate to have the support of my friends and family throughout this experience. Thank you to my mom and dad (Ginny and Tom DeCoster), my in-laws (Roxi and Tom Rykal) and my brother and sister-in-law (Evan and Jentry DeCoster) for their constant encouragement. Also, thank you to my good friends (Gary and Amanda Amoroso, Cornelia Cardillo, Gia Lenzi, Sierra Ryan, and Trish Faba) for providing me an outlet and a place to laugh.

Lastly, I would like to thank the Johns Hopkins University-Applied Physics Lab (APL) for providing me with the financial and professional support to pursue this degree. Specifically, thank you to my management, mentors, and friends at APL who encouraged me along the way including: Dr. Emma Rainey, Dr. Benjamin Rodriguez, Dr. Mike Kelly, Dr. Angela Stickle, and Dr. Tom Rosch.

# Table of Contents

## List of Figures

# List of Tables

# Chapter 1

## 1. Introduction

"Heat, like gravity, penetrates every substance of the universe, its rays occupy all parts of space. The object of our work is to set forth the mathematical laws which this element obeys. The theory of heat will hereafter form one of the most important branches of general physics."

- Jean Baptiste Joseph Fourier

## 1.1 Background and Applications

Great advancements in material fabrication and characterization techniques have been achieved over the last seventy years, starting with the invention of Molecular Beam Epitaxy (MBE) at Bell Labs in the 1960's[1] and progressing with now familiar techniques such as: Atomic Layer Deposition (ALD), optical thermometry, and various spectroscopy and microscopy methods. This has resulted in the creation and characterization of well controlled nano-materials that demonstrate unique properties, opening the door for new types of functional materials that were not otherwise achievable. The precise control with which these nano-functional materials can be fabricated allows for the ability to research heat transport properties in increasingly complex and well-defined material systems.

Nanostructured semiconductors have benefited immensely from advanced fabrication techniques and continue to be pursued for thermoelectric applications, owing to their potential for increased thermoelectric figure of merit (ZT), through enhancements to the power factor ($S^2\sigma$) with simultaneous reductions to the contribution of the lattice thermal conductivity.[2,3] Specifically, an efficient thermoelectric material can be achieved when the material exhibits a low thermal conductivity and enhanced electrical properties. Since the electronic component of the thermal conductivity is closely tied to the electrical conductivity,[4] it can be difficult to reduce the former

while simultaneously enhancing the latter property. The effects on thermal diffusivity and transmission tunability of phonons through the nanostructuring of semiconductors have been observed to contribute to a significant reduction in thermal conductivity compared to their bulk counterparts.[5–8] Phonon thermal size effects have been reported for micron length scales,[9] while electron thermal size effects have been observed at nanometer length scales.[10] Generally, in systems where the average mean free path of phonons is longer than the limiting size dimension of the sample, the thermal transport fails to follow Fourier's law and the continuum heat equation can instead be described by semi-ballistic phonon transport, where boundary scattering influences temperature profiles and the wave nature of phonons can appear if coherence is preserved.[11] Thus, well controlled nanostructured systems offer an avenue to study the origin of incoherent and coherent size effects originating from the particle/wave duality of phonons on thermal conductivity.[12–14] Therefore, advances to the field warrant investigations into the roles of structural and compositional disorder and morphology on the thermal transport mechanisms in nanostructured material towards enhanced thermoelectric properties, as detailed in this dissertation.

The inclusion of porosity in a material is an effective technique to morphologically promote thermal insulation. Further, adsorbates can be introduced into the pores to promote emergent desirable properties. While classical heat transport occurs by three mechanisms (conduction, convection, and radiation), the study of heat transport in thin solid films often focuses on the effects of a material's size and structure on thermal conduction alone; since electronic charge carriers and lattice vibration contributions dominate heat transport in most solid material systems. However, in thin solid porous films, it is important to consider not only the solid heat conduction through the framework, but also contributions from the various thermal transport mechanisms that can exist in

pores. Despite the fact that heat conduction in porous media has been heavily studied, the full thermal transport picture at the microscale, of multi-phase flow through porous media is rather incomplete and inconclusive.[15]

Porous solids are particularly interesting from an application point of view due to the ability to infiltrate the pores with adsorbate guest molecules to create a device (gas adsorption for storage or detection) or tune a material property (enhance electrical conductivity). The dominating heat transport mechanisms after infiltration with a guest molecule are unclear and heavily debated for two main reasons. First, the physical limitations of standard experimental techniques are not fully known when applied to thin porous solid materials. Specifically, it is unclear if the use of optical thermometry techniques centered on femtosecond (fs) pulsed lasers, where measurements occur on the order of picoseconds (ps) to nanoseconds (ns), have the temporal resolution to be sensitive to the heat transport in both the solid portion of the porous media and the pores.[16] Second, the thermal picture in various porous materials is not consistent. For example, highly disordered aerogels and crystalline clathrates and skutterudites are solid porous materials that exhibit contradictory thermal trends in the presence of adsorbates. It has been shown that the thermal conductivity of aerogels increases with air pressure, indicating that increasing concentrations of guest molecules inside the pores cause an increase in the thermal conductivity of the system, where adsorbates may act as a thermal bridge, enhancing the number of channels for conduction to occur.[17,18] In clathrates and skutterudites however, infiltration with a guest molecule causes a reduction in the thermal conductivity of the system, where the guest material introduces disorder in the form of a rattling mode that increases phonon scattering, or changes the vibrational structure of the material through phonon hybridization.[19,20] Further understanding is needed to illuminate

the dominating mechanisms for the guest-host interaction in porous materials capable of variable guest molecule accommodation.

## 1.2 Statement of Objectives and Scope of Dissertation

My previous works on ALD grown metal oxides[21] and solution processed modified polymers[22–24] resulted in the realization of how to devise a unique set of highly controlled materials to study the impacts of composition and morphology on thermal processes, and a robust experimental procedure for measuring the thermal and mechanical properties of solution processed thin films. These studies investigated and highlighted the gaps in understanding the role of structure on the vibrational thermal properties of nano-scale functional materials with well controlled compositional and morphological structures. A particular revelation was a realization that our understanding of the fundamental thermal processes in infiltrated porous media is rather incomplete. To fill in these gaps further, I have designed my dissertation research to systematically study the effects of structure for the purpose of modulating thermal properties.

- Research Question 1: How do compositional structure and morphology (e.g., grain boundaries and point defects) impact the thermal conductivity and phonon scattering processes in ALD grown thermoelectric materials?
    - Hypothesis: Compositional structures, grain boundaries and defects that have sizes that are roughly equivalent to the length scales of the mean free path of carriers in the intrinsic thermoelectric material will be effective in reducing the overall thermal conductivity of a two-phase nanocomposite.
- Research Question 2: What is the effect of infiltrated guest molecules on the thermal and mechanical properties of porous crystalline material?

- Hypothesis: In the presence of infiltrated molecules, metal organic frameworks (MOFs) with small pores will experience the most reduced thermal conductivity due to phonon scattering introduced by guest molecule–crystal interactions. In contrast, MOFs with larger pores will not experience as drastic of a reduction due to the decreased probability of guest–crystal collisions.

- Research Question 3: What is the effect of pore structure on the thermal and mechanical properties of crystalline porous material?

  - Hypothesis: The pore size and shape will play an important role in the thermal conductivity of MOFs. I expect the thermal conductivity to decrease with increasing pore size, due to effective medium predictions.

## 1.3 Success Criteria

The main objective of this work is to investigate the roles of composition and morphology in the form of disorder and porosity on the thermal transport mechanisms in low thermal conductivity crystalline material. To accomplish this, the materials selected for this study include chalcogenide nanocomposites and large unit cell, highly porous metal organic frameworks (MOFs). Specifically, PbTe-PbSe nanocomposites are intentionally fabricated with high degrees of both structural and compositional disorder in the form of point defects, grain boundaries and compositional phase boundaries. Additionally, two compositionally different but morphologically similar, large unit cell MOF crystals (HKUST-1 and ZIF-8) are investigated to understand the effect of compositional disorder, in the form of infiltrated guest adsorbates, on the thermal conductivity of porous crystals.

Since this dissertation is centered on experimental research, a portion of this dissertation outlines the theory and fundamental frameworks for interpreting thermal transport from a macro to a microscale perspective, and provides details about experimental analysis procedures for obtaining high fidelity measurements of the thermo-mechanical properties of novel material. The remainder of this dissertation is organized as follows:

- *Chapter 2 – Theory of Thermal Transport:* The theory of thermal transport is discussed starting from macroscopic concepts that introduce more contemporary theories pertaining to microscale heat transport. Within the microscale context, I will point out differences in various thermal transport frameworks in describing ordered (perfectly crystalline) and disordered (amorphous) material, which will be applied to describe the thermal transport in the chalcogenide and MOF material systems. I also provide a review and analysis of previous and related work pertaining to the thermal processes of ordered and disordered porous material to showcase the need for a deeper investigation into these material systems due to lacking experimental data and conflicting theoretical conclusions on the role of adsorbates on the thermal processes.

- *Chapter 3 – Experimental Techniques:* In this chapter I will provide an overview of the core concepts of time domain thermoreflectance (TDTR) which is the non-contact optical pump-probe technique used to measure the thermal properties of the thin film and thick samples investigated in this work. In addition, I will discuss the assumptions and relevance of the application of TDTR to porous medium and also provide an overview of the sensitivity and uncertainty analysis for understanding the fidelity of each reported measurement. I will also detail adapting TDTR to perform pump-probe Brillouin scattering measurements of transparent film for measuring group velocity and mechanical properties.

- *Chapter 4 – Composition and Morphology Effects on Thermal Conductivity of Nanostructured Chalcogenide Material:* This chapter will detail the thermal conductivity and phonon scattering process in a series of lead telluride-lead selenide (PbTe-PbSe) nanostructured thin films grown by atomic layer deposition (ALD). Temperature dependent thermal conductivity measurements show that the phonon scattering in these ALD-grown PbTe–PbSe nanostructured materials, along with ALD-grown PbTe and PbSe thin films, are driven by extrinsic defect scattering processes as opposed to phonon–phonon scattering processes intrinsic to the PbTe or PbSe phonon spectra. The implication of this work is that polycrystalline, nanostructured ALD composites of thermoelectric PbTe–PbSe films are effective in reducing the phonon thermal conductivity, and represent a pathway for further improvement of the figure of merit (ZT), enhancing their thermoelectric application potential.

- *Chapter 5 – Composition and Morphology Effects on Thermal and Mechanical Properties of Porous Crystalline Solids with Guest Molecules:* The thermal properties of porous media in the presence of adsorbates is an open question, where theoretical predictions offer conflicting conclusions that serve to make the knowledge about the subject quite inconclusive. This chapter investigates the roles of adsorbate phase and bonding morphology on the thermal properties of polycrystalline HKUST-1 and ZIF-8 metal organic frameworks (MOFs), which are crystalline porous material. HKUST-1 and ZIF-8 are compositionally different yet morphologically similar MOFs that interact with adsorbates in different ways due to the presence (or lack) of open metal sites, and differences in their mechanical properties and pore geometry. I explore the effect of adsorbates on the thermal properties of these two MOFs to show that adsorbates act as a

form of compositional disorder which decreases thermal transport via enhanced vibrational scattering and promoting a change in the vibrational mode character. The degree to which these effects hinder thermal transport is dictated by the pore morphology of the MOF.

- *Chapter 6 – Summary, Future Projects, and Impact:* In this chapter I summarize the main conclusions of this dissertation as they pertain to the statement of objectives outlined previously. Lastly, I provide a substantial foundation for future proposed projects related to this work that could be significantly impactful to understanding the thermal transport processes in porous materials.

# Chapter 2

## 2. Theory and Concepts

"In the elementary equations of the world, the arrow of time only appears where there is heat. The link between time and heat is therefore fundamental: every time a difference is manifested between the past and the future, heat is involved."

- Carlo Rovelli

## 2.1 Theory of Thermal Transport

### 2.1.1 Macroscopic Theory of Heat Transfer

The history of the physical understanding of energy began as early as 384 BC, when Aristotle coined the word 'energeia', which is Greek for "being at work". Energy, as a concept morphed from terms like "living force", "tensional force" and "fall force", as great minds like Julius Robert von Mayer, James Prescott Joule, and Hermann Ludwig Ferdinand von Helmholtz discovered that energy cannot be created or destroyed, but transferred from one form to another.[25] However, it wasn't until 1905, when Albert Einstein established the relationship between energy and mass though his theory of relativity, that energy was generalized into a quantitative property. Heat, on the other hand, was a much more nuanced concept, that took more time to develop. In 1824, Sadi Carnot developed an intellectual curiosity for the workings of steam engines that were emerging as a new major technology to make 'things' turn using fire. He described the working substance of the steam engines, heat, as a fluid that produces energy by "falling" from hot things to cold things. Though fundamentally flawed, because heat is not a fluid (it's a gradient of the microscopic agitation of atoms in the conduction process), he captured the essence that heat can only flow from hot to cold. This idea was further refined by a Prussian Professor, Rudolf Clausius,

into a complex and genius concept at the time, where he described the differences between potential, kinetic, and heat energy with a simple analogy: a ball can fall off a table and bounce back up, converting potential to kinetic energy and back to potential, but heat cannot! Clausius termed the irreversible progress of heat flow entropy ($\Delta S \geq 0$), and in doing so established the only fundamental law of physics that differentiates the past from the future, showing that every time a difference occurs between past and future, heat is involved.[26] It is from here that we jump off and continue to explore and expand on the fundamental heat transport processes in materials, new and old.

To begin, heat transfer relies on a temperature difference. An object that has internal energy, resulting from a distribution of microscopic particles in a system, can exchange that energy with another body through thermal contact. Here, large quantities of atoms in motion transfer energy in the form of heat. Therefore, heat is the net transfer of internal energy from one region to another, and is measured in Watts ($W=J/s$). If the net exchange of internal energy is zero, then the system has achieved thermal equilibrium. In classical thermodynamics, temperature is theoretically defined from this concept of thermal equilibrium. Two systems in thermal contact and in thermal equilibrium will have the same temperature. Further, from a statistical thermodynamics interpretation, temperature is proportional to the average kinetic energy in the system. Ultimately, temperature is nothing but a variable in an equation that describes a distribution of particles.

Heat transfer describes the movement of energy across boundaries of a system subject to a temperature gradient. At the macro-scale, heat is defined in a continuum where heat transfer occurs through three basic modes: convection (fluid motion), conduction (molecular interactions) and radiation (electromagnetic waves). At the macroscale, convection is a sum of diffusive and

advective transfer within fluids. Convection between a solid surface and a fluid interface is governed by Newtons law of cooling

$$\vec{q} = h(T_\infty - T_s), \tag{2.1}$$

where the rate of heat transfer, $\vec{q}$ ($Wm^{-2}$), is equal to the heat transfer coefficient (convection coefficient, which we will see later is an aerial conductance perpendicular to a surface, or a thermal boundary conductance), $h$ ($Wm^{-2}K^{-1}$), and the difference in the temperatures between the solid surface, $T_\infty$ and the surrounding fluid, $T_s$. This can take the form of natural convection, where the bulk flow in a fluid is due to temperature induced differences in buoyancy, or forced convection, where forces other than buoyancy (such as fluid velocity from a fan) move the fluid. I note that the heat transfer coefficient ($h$), is an equivalent to the Kapitza conductance between two solids,[27,28] and is not an intrinsic material property, but is dependent on external factors such as the flow field, fluid properties, and geometry of the solid in contact with the fluid. Convection involves the transfer of heat between a surface and a fluid through the macroscopic mixing motion of the fluid.

Conduction describes the transfer of internal energy within and through matter, by the collision of particles in the form of carriers (electrons), vibrating atoms (phonons in crystals or more generally vibrons in disordered solids), and molecules. Fourier's law provides a fundamental relationship between the heat flux ($\vec{q}$, $Wm^{-2}$) through a material to the temperature gradient and area through which the heat flows ($\vec{\nabla}T$) by

$$\vec{q} = -\kappa\nabla T, \tag{2.2}$$

where $\kappa$ ($Wm^{-1}K^{-1}$) is the thermal conductivity, which is a temperature dependent material property. At the macro level, $\kappa$ is an intrinsic property and is independent of size; however as

materials approach the microscale, the dimension of the material can drastically reduce the thermal conductivity, which will be discussed in the following section.[12,29,30] Further, transient heat flow within a material is governed by how much energy a material can hold per unit volume (volumetric heat capacity, $C_v$), and how quickly the heat can move through the material (thermal conductivity, $\kappa$). Therefore, the second governing equation is the transient heat diffusion equation written as

$$C_v \frac{\partial T}{\partial t} = \nabla \cdot (\kappa \nabla T) + Q, \tag{2.3}$$

where $Q$ is a term that describes the volumetric energy generation. The transient heat diffusion equation simplifies to Fourier's law in the case when heat transfer has no time dependence (i.e., steady-state), and the heat capacity does not play a role in heat conduction.

In brief, thermal radiation is the transfer of heat between spatially separated bodies through electromagnetic (EM) waves. Thermal radiation is typically characterized as incoherent (far-field radiation), where the wave nature of the EM waves is ignored. The rate equation for thermal radiation is described by the Stefan-Boltzmann law

$$\vec{q} = \varepsilon\sigma(T_\infty^4 - T_s^4), \tag{2.4}$$

where the rate of heat transfer ($\vec{q}$) requires information about the surface radiative properties (i.e., emissivity ($\varepsilon$)), Stefan-Boltzmann constant ($\sigma$) and the temperature of the sample surface ($T_s$) and the surrounding temperature ($T_\infty$).

This sums up a brief overview of the theory of thermal transport from a macroscale level. This dissertation is particularly interested in understanding the role of heat transport in solid nanostructured and nanoporous materials. Heat transfer at the micro scale can vary significantly from bulk processes, where new regimes defined by the limiting length scales of the system can impact heat transport characteristics. Due to these limiting length scales, the wavelengths and mean

free paths of the heat carriers (e.g., phonons) becomes comparable to or longer than the characteristic device dimension. Here, the wave properties, such as interference, diffraction, tunneling, and scattering can become quite important, in addition to increased incoherent scattering that redistributes the energies and momenta of the heat carriers, as we will investigate in the following section.

### 2.1.2 Microscopic Heat Transport (Vibrational Mode Thermal Conductivity)

At the micro and nano-scale, classical laws may no longer be valid when the wavelengths and mean free paths of the thermal carriers becomes comparable to the physical size of the material. In this situation both the particle (incoherent) and wave (coherent) properties of the energy carriers can affect heat transport; in the presence of coherence, the phase information can play a significant role. The wave properties of the energy carriers (i.e., free electrons, photons, and phonons) can result in coherent effects such as interference, diffraction, and tunneling. For example, coherence phenomena in electrons, photons, and phonons are related to their respective correlation functions, which describe how the microscopic variables at different positions are related.[31] The spatial coherence of electrons and photons involve spatial correlations of the electromagnetic field,[32–34] and the spatial coherence of phonons arises from the spatial correlation of the atomic displacement fluctuations at equilibrium.[31] Spatial coherence of phonons has been shown to play an important role in the heat transport processes in nanomaterials and nanostructures such as superlattices, nanowires, and nanomeshes.[12,13,31,35] The impact of a material's size on its thermal properties is then understood by examining some characteristic length and time scales, where rules of thumb can be established. Important length ($l$) and time scales include the mean

free path ($\lambda$), thermal wavelength ($\lambda_t$), the phase coherence length ($l_c$), and the carrier relaxation time ($\tau$). Kinetic theory relates the thermal conductivity to other material properties as

$$\kappa = \frac{1}{3} C \upsilon \lambda \,, \tag{2.5}$$

where $C$, is the material's specific heat capacity, $\upsilon$ is the phonon group velocity, and $\lambda$ is the mean free path of phonons. The mean free path (MFP) is the average distance that energy carriers travel before collisions, while the average time that a population of carriers scatter and relax into a new thermal distribution is known as the relaxation time. The MFP is spectrally varying based on the wavelength/energy of the carrier. The average thermal wavelength is representative of the average spread of energy of thermal carriers and is approximated using Planck's relation

$$\lambda_t = {}^{h\nu}/_{E}, \tag{2.6}$$

where the energy ($E$) of one quantum state is taken to be ${}^{k_b T}/_{2}$, where $k_b$ is Boltzmann constant, $h$ is Planck's constant, and $\nu$ is the speed of carriers. Lastly, the phase coherence length is a measure of the phase destroying scattering event occurring after incoherent scattering. It has been shown that if the coherence length or wavelength of the material is on the order of the characteristic length of the device, then the wave effects of heat transport matter.[14,30,31,36–39]

Diffusive dominated transport occurs by conduction in bulk materials. Here, the net movement of atoms and molecules is determined by a temperature gradient. Energy carriers can be treated as particle like in this regime and can accurately be described by the average of their microscopic motion. In order for a material to be described as 'bulk', the characteristic length (length, width, height, superlattice period thickness, etc.) of the material must be much greater than the characteristic length of energy carriers (thermal wavelength, phase coherence length, mean free path, etc.). As the characteristic length of the structure decreases to equal to or less than the

characteristic length of the energy carriers, size effects become apparent until a coherent transport regime can dominate. Generally speaking, the mean free path determines the regime where ballistic heat transport occurs, since it is greater than the coherence length, which is greater than the thermal wavelength. Ballistic transport can be incoherent or coherent and is present without a temperature gradient over a short distance. In this limiting case, the energy carriers do not scatter and a temperature cannot be defined;[11] further, the heat flux across the film can be analyzed as a radiative transfer problem similar to that of black body radiation (Eqn. 2.4), also known as the Casimir limit.[40] Figure 2.1 illustrates how the coherent and incoherent nature of energy carriers determines the thermal transport within a material based on comparing the limiting length scales of the intrinsic energy carriers to the structural length scales, like thickness.

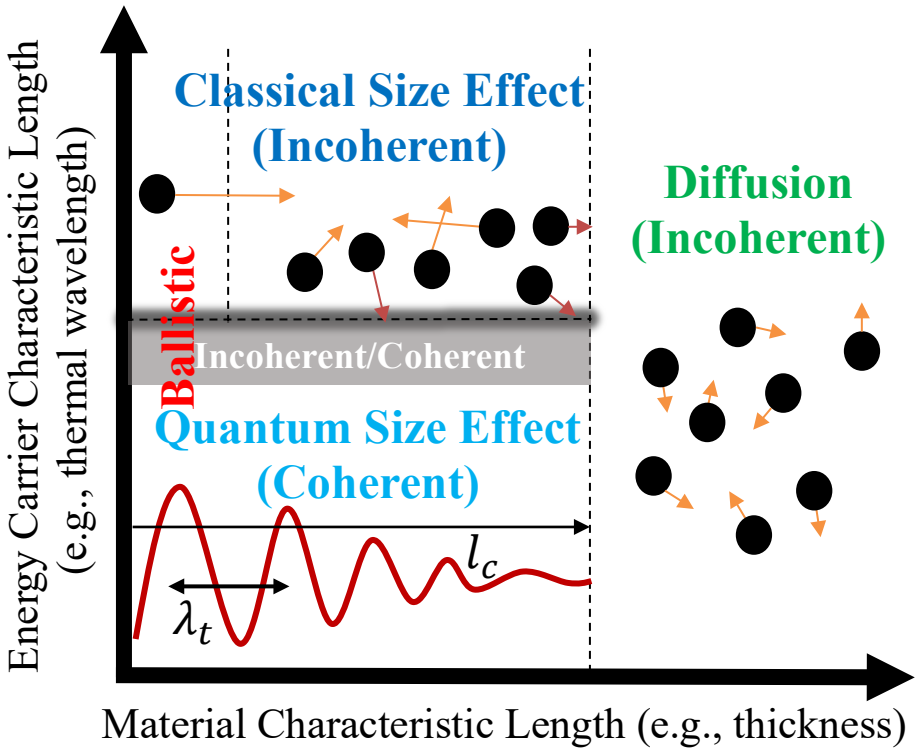


Figure 2.1: Heat transfer regimes defined by limiting length scales.

Along with length scales, it is important to consider the diffusive and specular scattering of interfaces to further determine what type of heat transport regime properly describes the system. Diffusive scattering from a rough interface typically destroys the phase information, so the wave aspect can be ignored, however specular scattering preserves the phase so that coherent transport can be considered.[41] In summary, heat transport regimes and the crossover from macro to micro/nano are determined by limiting length scales. Experimental evidence points out that determining the dominating length scales can be difficult, and characterizing the heat transport regime can be a non-trivial task.

#### *2.1.2.1 Phonons*

Perhaps the most important length scales when describing heat transport through non-metallic solids are dictated from the phonons. Heat conduction through crystalline non-metals occurs through the coupled vibrations of atoms, with finite masses, in a periodic array. This motion is not random, but a superposition of vibrations of atoms around their equilibrium sites due to the interaction with their neighboring counterparts, defined by an interatomic potential. An elastic wave, of allowed frequency/energy and amplitude, generated by these cooperative oscillations of atoms around their equilibrium position is defined as a phonon. Phonons display both particle and wave behaviors. Classically, phonons are the normal modes (longitudinal/transverse acoustic/optical) of the cooperative oscillation, existing as a superposition of different vibrational frequencies. Generally, for '*N*' atoms per unit cell in a three-dimensional crystal, there will be three acoustic branches (one longitudinal, two transverse), and *3N-3* optical branches (*N-1* longitudinal and *2N-2* transverse). The quantum mechanical view of a phonon requires the energy of the lattice vibration to be discrete, and a multiple of $\hbar\omega$, where $\hbar$ is Planck's constant (1.054 x

$10^{-34}$ Js) and $\omega$ is the angular frequency. Lastly, the phonon wave vector ($k$) points in the direction of the wave propagation, and is defined in reciprocal space.

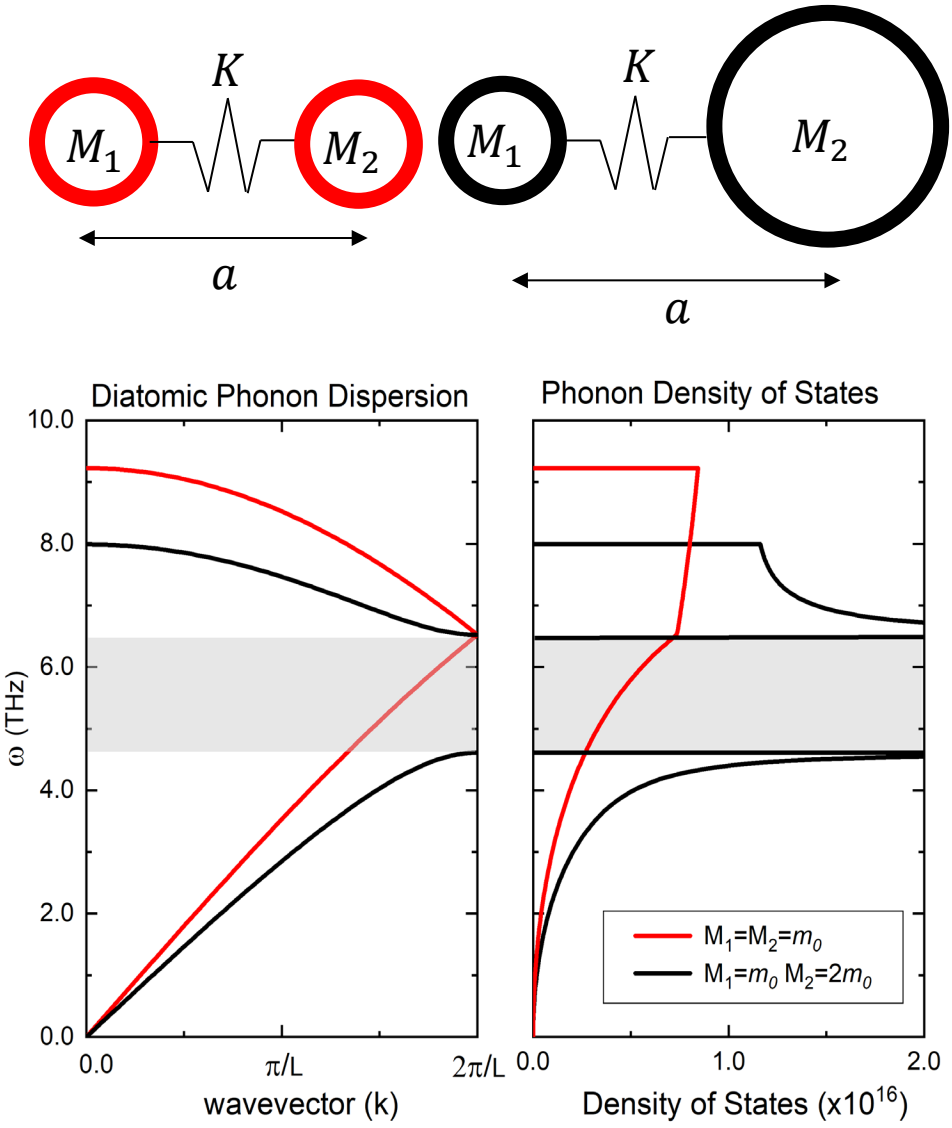


Figure 2.2: The phonon dispersion relations for a diatomic chain showing the positive k values, where the first Brillouin zone has mirror symmetry through the origin (left) and phonon density of states (DOS) (right) are modeled as a diatomic ball on spring. K is the spring constant between the masses, k is a wavevector, $a$ is the atomic spacing (lattice spacing (L) is 2a), and $m_o$ is the mass of the ball/atom. Two cases are modeled: case 1 where $M_1$=$M_2$=$m_o$ (red) and case 2 where $M_1$=$m_o$, $M_2$=2$m_o$ (black). These calculations were obtained using K = 1 $Nm^{-1}$, $a$ = 0.5 $nm$, $m_o$=4.7e-26 Kg. The grey zone demonstrates the phonon band gap that arises in case 2, due to the mismatch of atom masses.

The phonon dispersion curve relates the phonon frequency to the wave vector, where the dispersion relation is not a continuous curve, but rather a series of closely spaced points representing possible modes of vibrations. Phonon dispersion relations can be obtained directly by finding the solution of Newton's equations of motion in a periodic lattice. An example of a phonon dispersion plotted in the reduced zone scheme from $0 < k < {}^{2\pi}/_{L}$ (in this case, the lattice spacing ($L$) is related to the atomic spacing ($a$) by $L=2a$) is shown in Figure 2.2 for two cases of a diatomic linear lattice modeled as a ball and spring. The interaction of the neighboring atoms is modeled using an assumption that the force affecting the atom is linearly proportional to the displacement of the atom from its equilibrium position (Hooke's Law). The displacement of the atom from its equilibrium position is then obtained by solving the classical equations of motion (EOM) that captures the kinetic and potential energy of the system; in the case of a diatomic system, two masses require two EOM's where the solution is wavelike ($Aexp[(i(2nka \pm \omega t)]$), where $A$ is the amplitude. When the masses are equal ($m_1 = m_2 = m$), this leads to a dispersion relation that relates the wave vector and phonon frequency of the form:

$$\omega = 2\sqrt{\frac{K}{m}}\sin\frac{ka}{2}, \tag{2.7}$$

where K, is the spring constant. In the case where the masses are not equal ($m_1 \neq m_2$),

$$\omega^2 = \frac{K}{m_1 m_2}(m_1 + m_2 \pm \sqrt{m_1^2 + m_2^2 + 2m_1 m_2 \cos(ka)}\,). \tag{2.8}$$

The group velocity of the phonon modes is defined by the slope of the dispersion curve. Note the differences in the dispersions between case 1 ($M_1=M_2=m_o$) and case 2 ($M_1=m_o$, $M_2=2m_o$). A phonon band gap (forbidden zone) appears in case 2 that spans the entire first Brillouin zone (FBZ), where frequencies cannot propagate. This band gap is due to Bragg scattering, and depends on the

difference in the masses of the atoms.[38] When the two masses are equal (as in case 1), the bands join and become degenerate throughout the FBZ.

The density of states (DOS) defines the energy degeneracy within the system and is also plotted in Figure 2.2. Since each crystallographic direction has its own dispersion relation, there exists many possible combinations of wave vectors that could have the same energy. The phonon DOS has units of (states/energy/atom) and is an expression of the number or energy states per unit energy per unit space. The equation for phonon DOS of a particular phonon polarization in a three dimensional isotropic solid is

$$\mathrm{D_j}(\omega) = \frac{\omega^2}{2\pi^2 \mathrm{v_{p,j}^2 v_{g,j}}}, \tag{2.9}$$

where $j$ is the phonon branch, $v_p$ is the phase velocity, and $v_g$ is the group velocity. [42]

### *2.1.2.2 Anharmonicity and Scattering Processes*

Let us return to a discussion of thermal conductivity. Thermal conductivity is an intrinsic material property that quantifies the ability of a substance to transfer heat. The "gray" approximation to kinetic theory is a simplified view of thermal conductivity that can often be applied to systems at sufficiently low temperatures. Here, again, the thermal conductivity is a function of the material's specific heat ($C$), the Debye velocity ($v_D$), and the phonon lifetime ($\tau$)[43]

$$\kappa = \frac{1}{3} C v_D^2 \tau. \tag{2.10}$$

The Debye velocity approximates all the phonons in the system as dispersionless until a cut off frequency. This cut off frequency is determined by the Debye frequency, which is the crystal's highest normal mode of vibration (i.e., the highest temperature that can be achieved due to a single

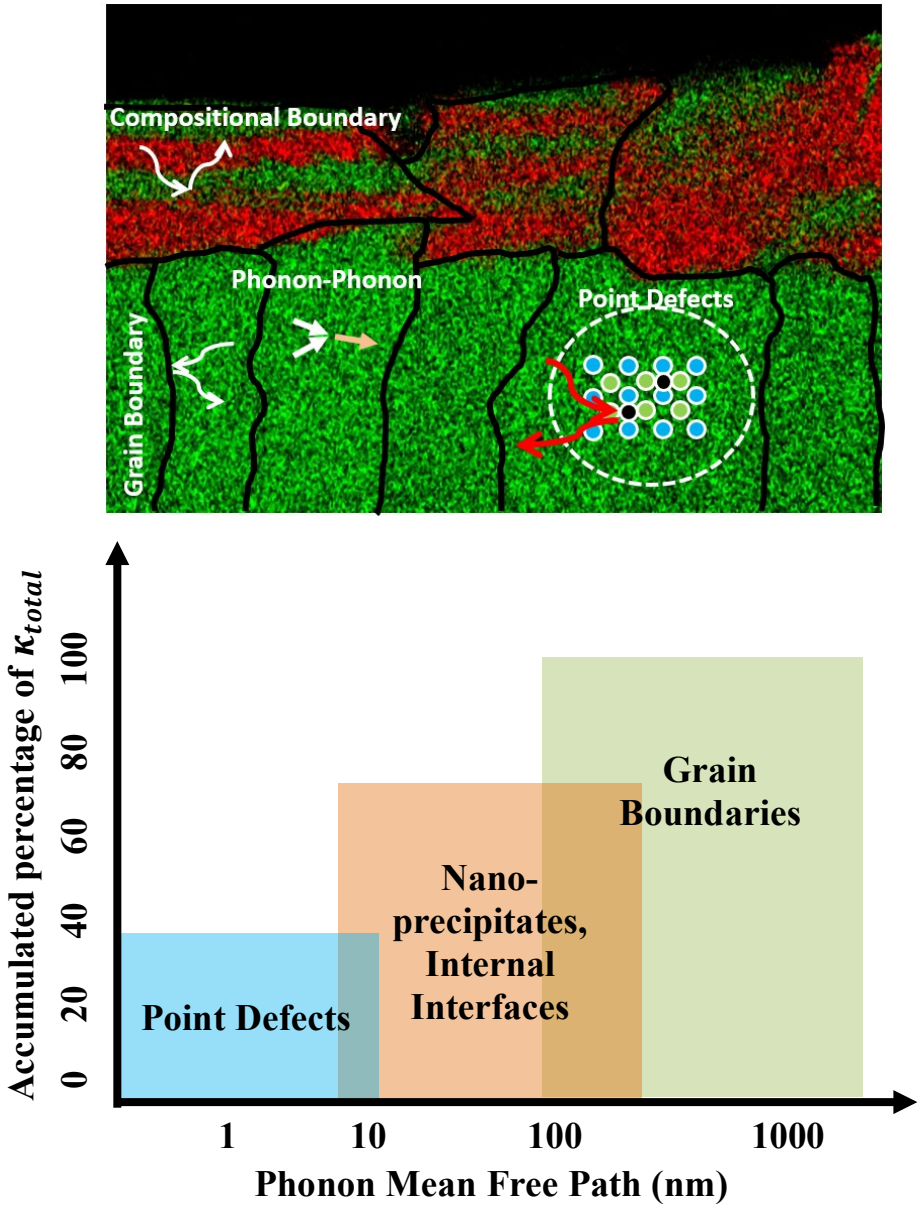


Figure 2.3: (top) Schematic of a micro-structured chalcogenide, and the corresponding phonon scattering processes that can lead to material engineered reduced thermal conductivities. (bottom) Qualitative illustration of the accumulated contributions to reducing the lattice thermal conductivity with respect to MFP, adapted from Xiao and Zhao.[1]

normal mode vibration). The "gray" approximation assumes that all phonons have the same energy and velocity, and can be described by a single scattering time. The "gray" approximation fails at high temperatures because the neglection of the phonon dispersion results in a significant underestimation of phonon lifetimes and scattering rates.[45] Therefore the effects of anharmonicity

and phonon scattering processes are important to understanding how heat transport occurs at higher temperatures.

The works by Klemens, Callaway, and Ziman provide a more rigorous description of thermal conductivity, capturing the dispersive nature of phonons by considering the contribution from each individual phonon as[46–49]

$$\kappa = \frac{1}{3}\sum_j \int_0^{\omega_{max,j}} \hbar\omega D_j(\omega) \frac{\partial f(\omega,T)}{\partial T} v_j^2(\omega)\tau_j(\omega) d\omega, \tag{2.11}$$

where the sum is taken over all branches of the dispersion relation, $\omega_{max,j}$ is the maximum angular frequency of branch $j$, $f(\omega,T)$ is the Bose-Einstein distribution, and $\tau_j$ is defined as the phonon relaxation time. The relaxation time is composed of all intrinsic and extrinsic individual scattering process including phonon-phonon, boundary, and mass-impurity (point defects) scattering and is described by Matthiessen's rule

$$\tau_j^{-1} = \sum_i \tau_{i,j}^{-1}, \tag{2.12}$$

where the summation is over all possible scattering processes (*i*) for each phonon branch (*j*). To bound the scope of this dissertation, I provide a detailed description of phonon-phonon interactions in the following sections, but only briefly discuss the other scattering mechanisms, since they have been shown to be ambiguous in the presence of disorder.[50]

As phonons propagate through a lattice, they may interact in such a way to cause a collision. This collision is dictated by the interatomic potential, which defines the strength of the chemical bonding and constrains the motion of neighboring atoms. A harmonic interatomic potential follows Hooke's law, and maps out a parabolic potential well, leading to an ideal spring with force linearly proportional to displacement from the minimum potential position. Phonons in such an ideal potential do not collide with each other producing an infinite thermal conductivity.

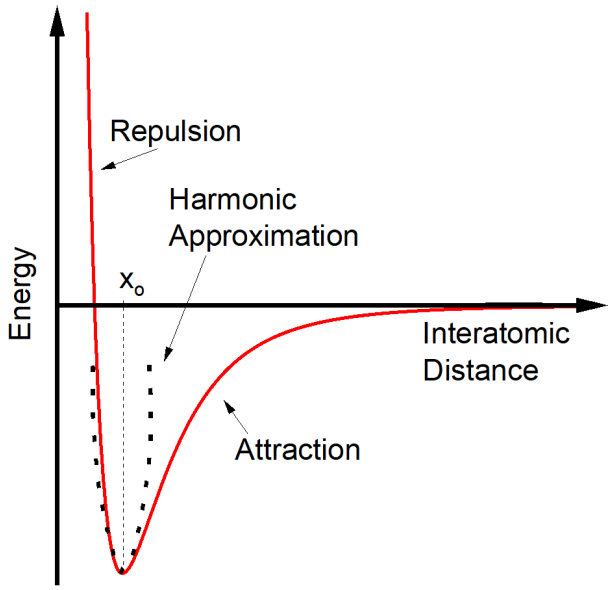


Figure 2.4: An anharmonic generic interatomic potential (red line) compared to a harmonic oscillator model (dotted black line). The equilibrium position is denoted as $x_o$.

Finite thermal conductivities arise from the presence of resistance in the material, which occurs from phonon collisions, or scattering events. There are three types of scattering processes that affect thermal transport and are used in modeling the thermal conductivity in Chapters 4 and 5: phonon-phonon interactions in an anharmonic potential, phonon-impurity, and phonon-boundary scattering. These scattering processes are illustrated in Figure 2.3, depicting a chalcogenide material with compositional boundaries, grain boundaries, and defects that have been intentionally fabricated to maximize phonon scattering to minimize thermal conductivity. In addition, the figure also shows a conceptual illustration of the relative contributions of different forms of disorder (grain boundaries, nano-precipitates, internal interfaces and point defects) on the suppression of the lattice thermal conductivity and their relative length scales.

In order for a resistive phonon-phonon collision to occur, the interatomic potential must be anharmonic (non-parabolic). An example of a generic anharmonic potential compared to a harmonic model is shown in Figure 2.4. In this potential, atoms prefer an equilibrium position

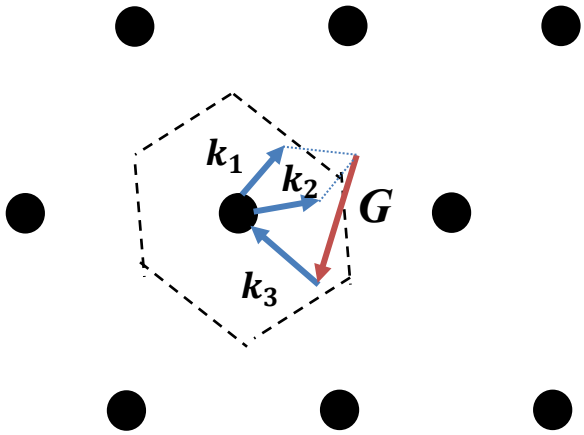


Figure 2.5: Schematic of anharmonic phonon-phonon scattering in wave vector space defined with the first BZ chosen as the primitive cell in reciprocal space (dashed lines). Here, two phonons with wave vector $k_1$ and $k_2$, and frequencies $\omega_1$ and $\omega_2$ collide to form one phonon with wavevector $k_3$ and frequency $\omega_3$.

($x_o$) that occurs at a minimum energy, occurring in the well of the potential. Depending on which direction the atom moves during an oscillation, it will experience repulsive or attractive forces. Anharmonicity represents deviations from a linear force interaction (derivative of the interatomic potential) between neighboring atoms. Anharmonic phonon scattering results in a loss of its phase information, promoting incoherent heat transport. In a crystalline system defined by an anharmonic interatomic potential, the thermal conductivity is maximized at a temperature when anharmonic scattering becomes dominant over other scattering processes in the crystal, known as the "Umklapp peak".

As a note to the reader, I intentionally refrain from differentiating between U*mklapp* (U) and *normal* (N) scattering. This is due to the nuanced concept that a N and U process is arbitrary based on the choice of the primitive cell of the reciprocal lattice, that was demystified by Maznev and Wright.[51] More precisely, Figure 2.5 shows an example of anharmonic scattering, where two phonons, with wave vectors $k_1$ and $k_2$ and frequencies $\omega_1$ and $\omega_2$ collide to produce a new phonon with wavevector $k_3$ and frequency $\omega_3$. The resultant phonon falls outside of the boundary of the defined primitive cell in reciprocal space. Therefore, in order to conserve the

quasi-momentum of the crystal( $\hbar$k, $\hbar$ is the reduced Planck constant) a vector, G, is required to map the resultant phonon back into the defined primitive cell. This requirement results in a reversal of the phonon propagation direction, and therefore contributes to thermal resistance. Note that 'quasi-momentum' of the crystal is used instead of the term 'momentum,' because phonon momentum does not have any mass transfer so it does not exhibit classical momentum. Lastly, in addition to two phonons colliding to form one new phonon, one phonon can also split into two.

Phonons can also collide with impurities within the crystal and boundaries. Impurities introduce random mass fluctuations within the crystal and take the form of point defects and atomic isotopes. Phonon scattering due to impurities follows Rayleigh's law, where the scattering time ($\tau$) varies inversely as the fourth power of the phonon frequency so that short wavelength phonons are scattered more strongly than long wavelength phonons.[48,52] Finally, when the length of physical structures within the material becomes comparable to the phonon MFP, the phonons can scatter at the boundary.[43] These boundaries come in the form of composition boundaries (i.e., periodic layering of material like a superlattice), grain boundaries, and the boundary of the nano-material.

Figure 2.6 illustrates the different temperature dependent trends in thermal conductivity that appear for bulk and thin crystalline and amorphous material. The bulk silicon shows a typical temperature dependance that is commonly observed at T >100 K for crystalline, non-metallic solids. This trend also appears in bulk crystalline chalcogenides, and some large porous, unit cell crystals like skutterudites (unfilled) and single crystal $C_{60}$. Here, phonon-phonon scattering dominates above the Umklapp peak (the temperature where the maximum thermal conductivity occurs) and leads to a decreasing thermal conductivity with increasing temperature ($\kappa(T) \propto T^{-1}$). To the left of the Umklapp peak, impurity/defect scattering and surface boundary scattering dominate. Different phonon physics arises in low dimensional materials. The 100 nm

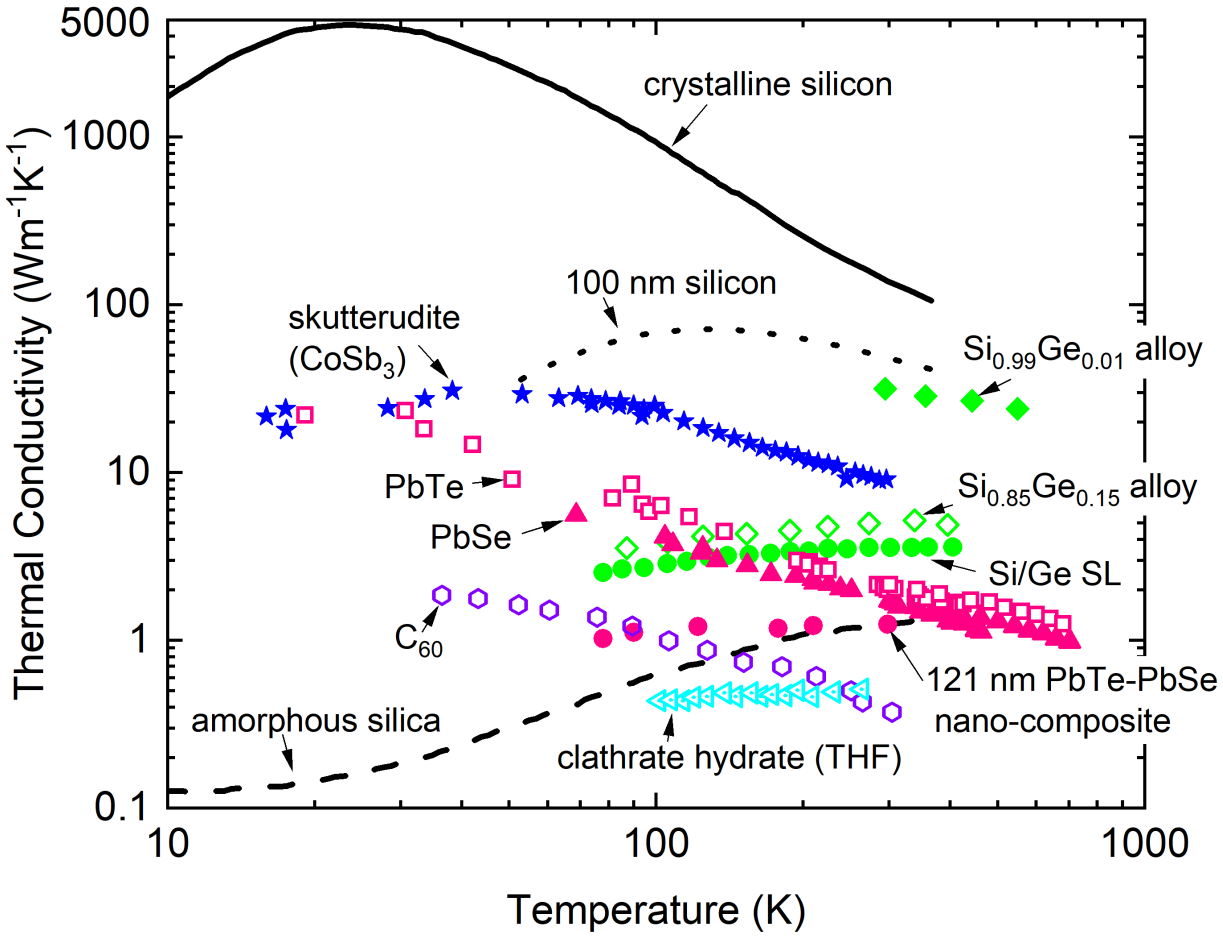


Figure 2.6: Temperature dependent thermal conductivity of bulk single crystal silicon (black solid line),[53] amorphous silica (black dashed line),[54] 100 nm and 20 nm silicon (black open circles),[55] SiGe alloys (diamonds),[56,57] Si/Ge superlattice (green circles), [23] bulk single crystal PbTe (squares)[58] and PbSe (triangles),[59] thin PbTe-PbSe nanocomposite (pink circles),[60] porous crystalline skutterudite ($CoSb_3$) (blue stars),[61] porous crystalline clathrate hydrate encapsulating tetrahydrofuran (THF) (left pointing triangles),[62] and a large single crystal $C_{60}$ (purple hexagons).[63]

and 20 nm crystalline silicon exhibit a decrease in magnitude and do not follow the temperature dependent thermal trend of the bulk Si crystal. The large reduction in magnitude is due to thermal size effects arising from high surface to volume ratios, where long wavelength phonons present in Si are scattered by the limiting dimension of the film (>100 nm or >20 nm).[64] Further, the thin films are dominated by boundary scattering up to higher temperatures, which is reflected by the shift in the maximum thermal conductivity to higher temperatures as film thickness decreases.[55] Furthermore, compositional and structural disorder can also dominate the phonon scattering

mechanisms. In these systems, disorder limits the phonon mean free path and group velocity resulting in an increasing temperature dependent trend in thermal conductivity, which follows the temperature dependent heat capacity according to kinetic theory ($\kappa = {}^{1}/_{3}\, C_v v \lambda$). This trend is characteristic of amorphous materials (e.g., *a*-$SiO_2$) and also crystalline materials with engineered disorder such as superlattices (Si/Ge), alloys ($Si_{(1-x)}Ge_x$), nanocomposites (PbTe-PbSe), and even some classes of porous crystals such as clathrates and skutterudites. Engineered disorder can come in the form of compositional boundaries, grain boundaries, and point defects (mass-impurity scattering through dopants or alloying). Additionally, disorder can also appear in large unit cell material (i.e., porous crystals), that contain periodicity over large length-scales (several nm or greater), that approach and/or exceed the typical length scales of phonon mean free paths (typically < 10 nm). In these large unit cell crystalline systems, it is unclear if phonon-based heat transfer is relevant, or if the long-distance translational symmetry of the atoms produces an amorphous material. In total, the temperature dependent thermal conductivity trend sheds light onto the dominating heat carrying mechanisms in material systems.

#### *2.1.2.3 Phonon Hybridization and Rattling*

Phonon dispersions dictate the allowable quantum mechanical energy states of thermal carriers within a crystal by relating phonon frequency to the phonon wavevector. As discussed previously, phonons can interact with one another in the form of collisions, which cause resistance in the material and establish a finite thermal conductivity. In addition to collisions, phonons can also interact with one another to create hybridization, that can greatly impact phonon scattering rates and also be concomitant with changes in the mode character.[50,65,66] In addition to hybridization, the role of rattling localized vibrational modes introduced by the addition of non-periodic side groups or guest atoms in pores can also drastically affect heat transport processes.

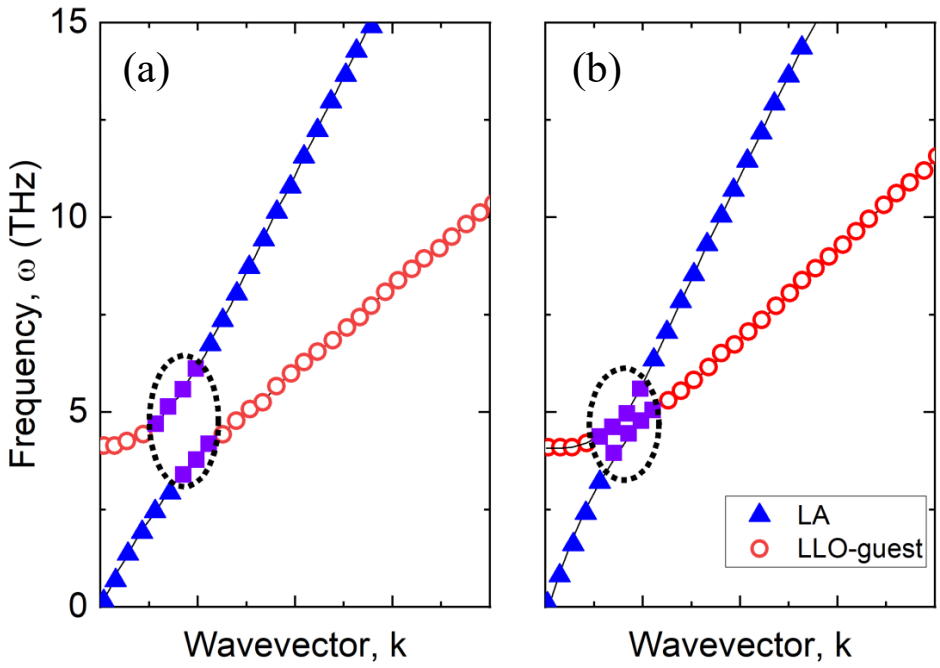


Figure 2.7: Example of optical-acoustic phonon hybridization for an arbitrary crystal showing only the lowest-lying optical mode (LLO) from the guest molecule and the longitudinal acoustic mode. The area circled highlights the avoided crossing where the LLO and LA phonons are indistinguishable (purple squares). (a) Shows the emergence of a large gap at the avoided crossing representative of high coupling between the LO and LA phonons. (b) Shows a much smaller gap indicative of weak coupling.

Hybridization occurs when multiple phonon states with compatible symmetry and similar frequencies/energies couple, resulting in an energy eigenstate that is a linear combination of the individual states. An example of this is optical-acoustic phonon hybridization shown in Figure 2.7 for an arbitrary crystal.[66] When the criteria defined above for phonon hybridization are met, the lowest-lying optical (LLO) and LA branches exhibit an avoided crossing (anti-crossing) resulting in coupling between branches. In quantum mechanical terms, an avoided crossing is a phenomenon in a degenerate system, where two eigenvalues representing the quantum observable cannot become exactly equal (cross), and end up producing lowered energy eigenstates.[67] In a system with coupling, a gap appears at the avoided crossing that is proportional to the coupling strength. In the absence of coupling, crossing occurs and no lowered energy eigenstates are

produced. Within the avoided crossing region in a phonon dispersion, hybridization between the optical and acoustic phonons causes the modes to be indistinguishable and also lowers their energy that results in enhanced phonon-phonon scattering channels. Hybridized modes within the avoided crossing have been shown to significantly contribute to increased scattering rates that drastically reduce thermal conductivity.[66,68]

Rattling modes can appear in materials containing side groups, or guest atoms, such as long chains of molecules attached to polymer backbones and guest molecules adsorbed into a porous crystal.[69,70] In general terms, a side group introduces atoms or molecules in semi-stable positions that produce no predictable long range order. These side groups may introduce both incoherent and coherent effects. Wiggling guest atoms introduce localized incoherent rattling motion (Einstein motion) that can act as additional scattering centers for acoustic phonons within the native material.[71] Additionally, resonant, or "rattling" phonon modes may appear near/from an avoided crossing interaction of low energy optical phonons, introduced from the side group, with energetically compatible acoustic phonons within the main material.[72] This interaction is unique because typically optical phonons have too high an energy to scatter with acoustic phonons. Another result of hybridization is the appearance of flat (low group velocity) modes in the dispersion created by avoided crossing interactions between vibrations of the guest atoms and acoustic phonons from the host matrix.[70] These flat modes can act as additional anharmonic scattering channels to limit thermal conductivity.[69,70,72] Further, it has also been shown that rattling modes contribute to band flattening, which reduces the group velocity of acoustic phonons at the avoided-crossing, rather than shortening phonon lifetime by scattering.[73] The dominating effects of rattling modes due to guest atoms is still very much an open question.

### *2.1.2.4 Locons, Diffusons, and Propagons*

Thermal transport in highly disordered material, like amorphous solids, is not as clearly understood as in crystals, and relies on a modified taxonomy to describe the thermal transport processes. Disordered systems are described by a lack of long-range order due to a break in atomic periodicity. In disordered amorphous material, normal modes still exist, however wavevectors are no longer well defined; therefore a phonon group velocity and mean free path become difficult to define for high frequency vibrations.[74] Experimental measurements for amorphous material show reduced thermal conductivities compared to their crystalline counterparts, in addition to temperature dependent thermal conductivity trends that increase steadily with temperature, without passing through a maximum.[75,76] A theory originally devised by Einstein[77] reframes thermal transport in highly disordered systems by treating atoms as damped, localized independent oscillators, where energy hops from one atom to the next through a random walk, with all atoms vibrating at the same angular frequency $\omega_E$ (Einstein frequency), with uncorrelated phases that transfer energy with one half the period of vibration.[77,78] Slack[79] and Cahill and Pohl[78]extended and formalized Einstein's concepts into a hybrid model aimed at describing the minimum thermal conductivity in amorphous solids by pointing out that in reality, atoms vibrate together forming a spectrum of frequencies (rather than at a single Einstein frequency), with a relaxation time defined from half a period of oscillation. The theory resulted in the following expression

$$\kappa_{min} = (\frac{\pi}{6})^{\frac{1}{3}} k_B \eta^{2/3} \sum_i \upsilon_{s,i} (\frac{T}{\Theta_i})^2 \int_0^{\Theta_i/T} \frac{x^3 e^x}{(e^x-1)^2} dx, \quad (2.13)$$

where $k_B$ is the Boltzmann constant, $\eta$ is the number density of atoms, $\upsilon_s$ is the speed of sound, the summation is performed over the polarization of acoustic waves and $\Theta$ is the Debye

temperature defined as $\Theta_i = v_{s,i}(\hbar/k_B)(6\pi^2\eta)^{1/3}$, where $\hbar$ is the reduced Planck's constant. This dispersionless description of thermal conductivity has proven successful in describing the thermal conductivity in many disordered material,[54,80] however has proven to be limited by its reliance on classical diffusion of phonons in a solids.[81]

The problem with quantifying thermal transport in disordered material through the lens of phonons is that any form of disorder breaks the periodicity of the crystal, therefore making it difficult, and even inaccurate, to define phonon wave vectors and corresponding group velocities.[50] This translates to inconsistencies in the phonon gas model (PGM), which is built on the assumption that the energy of the vibrational modes can be represented as particles that travel and scatter. Alternate theories have been developed that reframe the phonon definition by considering vibrational mode diffusivities.[82,83] In this picture, the vibrational modes are broken into pseudo-particles that describe diffusion, and are differentiated based on their spatial extent (extended or localized) and whether they propagate or not.[74,82] Similar to phonons, propagons are extended propagating vibrational modes that contain well-defined wave vectors and long wavelengths. Diffusons are non-propagating (cannot define a wavevector) delocalized modes. Lastly, locons generally exhibit high frequencies and are localized, non-propagating modes. The full vibrational spectrum contains boundaries which distinguish propagons from diffusons (Ioffe-Regel crossover) and diffusons from locons (mobility edge).[74] From here, various thermal models for describing thermal transport are distinguished by how they treat each class of mode contribution to the overall thermal conductivity. Since propagons exhibit a plane wave propagating character, they can be treated via PGM. Numerical studies from Allen *et al.* on amorphous silicon showed that diffusons overwhelmingly dominate the population of vibrational modes, and that propagons and locons made up only 4% and 3% of the total modes respectively.[82] Generally, it is

true that a high concentration of diffusons dominates the thermal transport of disordered material. In this limit, the diffuson contribution to thermal conductivity predicted by Allen-Feldman (AF) theory[75,84] is a useful tool to model disordered system, as it sums the individual contribution of each mode's volumetric heat capacity and diffusivity. However experimental and theoretical studies have shown that contributions from propagons and locons may also produce non-negligible effects on the thermal conductivity.[75,85,86] Further, Lv and Henry have developed the Green-Kubo modal analysis (GKMA) approach which describes thermal transport via correlation (i.e. different modes are correlated that have different characters), rather than scattering, which allows for an assessment of the mode level contributions to the thermal conductivity.[50,83] This approach is fundamentally different from PGM because it considers the role of disorder on thermal transport to result in a change in the vibrational mode character (i.e. loss of propagating/plane wave character) rather than impurity scattering. In total, while significant progress has been made in understanding the thermal transport in disordered material, there is still ambiguity in the current established frameworks for studying disordered material.

The classification of a material as crystalline or amorphous implies which thermal transport framework should be applied to characterize the thermal carriers of the respective system. However, material scientists and chemists alike have provided engineers interested in microscale heat transport with a complex variety of materials that do not fit neatly into one category. Material that exhibits crystallinity in combination with a high degree of disorder continue to blur the line, and require a flexible framework that can account for the interplay between crystalline and disorder mechanisms of thermal transport.

## 2.2 Mechanical Properties and Thermal Processes (Leibfried and Schlomann)

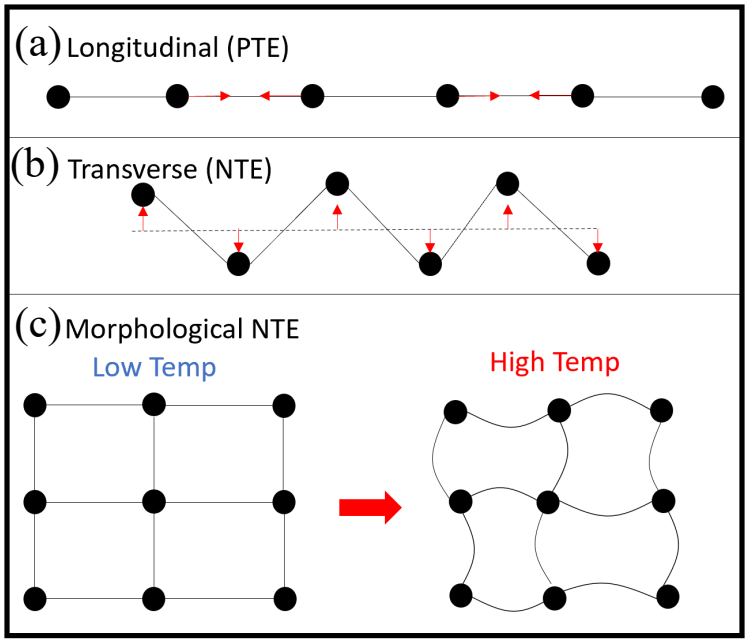


Figure 2.8: Schematic illustration of a lattice where (a) longitudinal phonon modes produce chain lengthening from anharmonicity resulting in positive thermal expansion (PTE) and (b) transverse optical phonon modes oscillating so that their amplitude shortens the chain length leading to negative thermal expansion (NTE) and (c) morphological NTE where the 'bonds/struts' between 'atoms/nodes' lengthen at higher temperature, but separation between the nodes decreases corresponding to an overall volume reduction.

The mechanical and thermal properties of materials are closely related, since both are physical manifestations of the movement of atoms and molecules whose neighborly interactions are defined by a chemical potential. Therefore, measurements of mechanical properties, such as the thermal expansion coefficient and elastic modulus, can help to inform mechanisms dictating thermal processes. This section will illustrate how the mechanical properties of materials affect thermal processes.

Materials often increase in volume with temperature, known as positive thermal expansion (PTE). This occurs by an increase in energy into the system that causes an increase in the equilibrium spacing of the atomic bonds. Ultimately, thermal expansion stems from

anharmonicity, where the equilibrium position defined by the potential, can no longer reside at the minimum of the potential well, and must increase (move to the right), as more energy enters the system (Figure 2.4). This causes atoms to spend more time at distances greater than the original equilibrium position, where repulsion at short distances is greater than attraction forces at far distances. From this atomistic picture, we can see that a matrix of bonded atoms will undergo an increase in volume to compensate for the bond lengthening that is required by the anharmonicity of the system. Materials can also experience negative thermal expansion (NTE), when competing effects to the natural thermal expansion are present. These competing effects come in the form of phonons and morphological effects.[87] Figure 2.8 (a) (b) show a longitudinal and transverse phonon mode in a semi-infinite atomic chain. Longitudinal waves move in the direction of the atoms, and therefore their propagation lengthens the chain as temperature increases; adhering to the classic definition of PTE and bond anharmonicity. Transverse waves on the other hand move orthogonal to the direction of the atoms and act to shorten the chain length, where the amplitude of the transverse wave acts to pull the lattice together leading to large chain shortening. In particular, materials that contain high energy transverse optical modes experience large NTE. Additionally, NTE can also be achieved through a morphological mechanism. For example, Figure 2.8 (c) shows how a material structure could be designed in such a way where contraction upon heating occurs through the reduction of the volume of internal voids, which outweighs the increase in the total volume of the material. [87]

A measure of material stiffness through stress/strain curves provides information about how bonds respond to physical deformation. Figure 2.9 (a) shows a typical stress/strain curve. The linear region represents elastic bond stretching, where there is no permanent deformation to the bonds in response to a load. The slope of this elastic region is equal to the

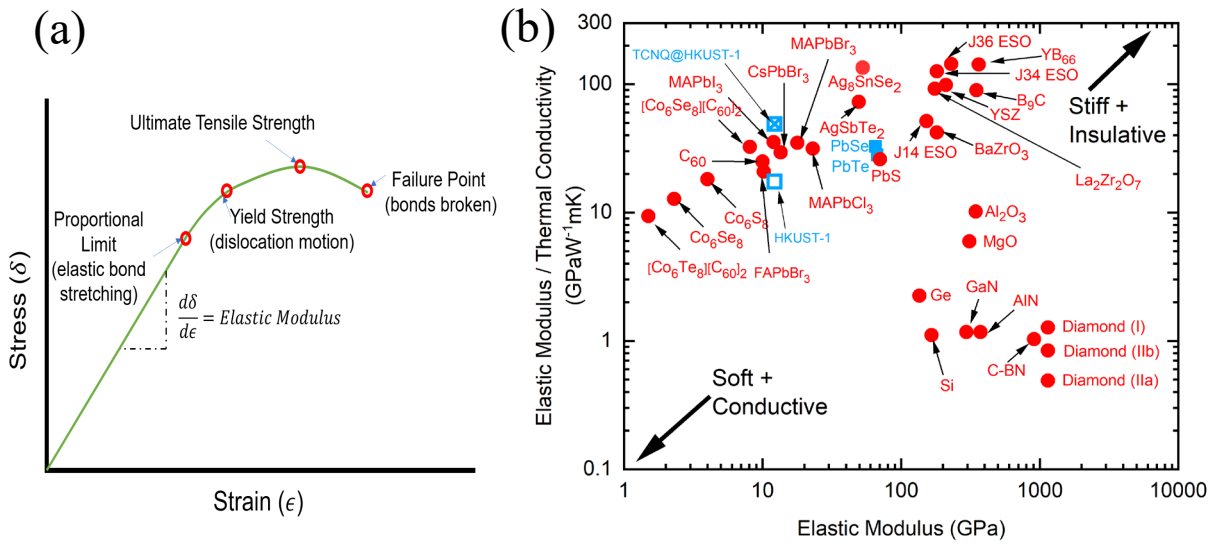


Figure 2.9: (a) Typical stress-strain diagram for a material showing elastic and plastic deformation and how this manifests from the bonds within the material. (b) Plot of the elastic modulus/thermal conductivity vs. elastic modulus of a variety of crystalline material taken from Braun *et al.*[88] (red symbols), in addition to materials investigated in this dissertation (blue symbols).

elastic modulus, which is a measure of a material's stiffness. Beyond the linear regime (past the proportional limit) a material experiences plastic deformation where permanent dislocations occur, eventually reaching total failure, where the material fractures and the bonds break. Figure 2.9 (b) shows how the elastic modulus is generally related to the thermal conductivity. In fact, it was actually Debye[89] who first pointed out that thermal resistivity in dielectric solids occurred from scattering of vibrational modes by changes in the elastic constants. Notably, a soft deformable material with a low modulus usually correlates to a thermal insulator and a stiff material (high modulus) generally correlates to high thermal conduction.[90] This relationship is best described by the Leibfried-Schlomann (L-S) equation, which captures the magnitude of the $T^{-1}$ dependence for thermal conductivity for crystalline material.[91] Leibfried and Schlomann proposed that the lattice thermal conductivity of a crystal at temperatures above the Umklapp peak can be approximated by the following relation when the dominant carriers of heat are acoustic modes and the dominant scattering mechanism is three-phonon interactions between acoustic modes

$$\kappa_{L-S} = A_1 \frac{V^{1/3}\omega_D^3}{\gamma^2 T}, \tag{2.14}$$

where $A_1$ is a constant, $V$ is the volume of the unit cell, $\omega_D$ is the Debye frequency (maximum frequency of vibration), $T$ is temperature, and $\gamma$ is the Gruneisen parameter. Since the Debye frequency is proportional to the group velocity $v = \sqrt{BV^{1/3}/\bar{M}}$ where $B$ is the bulk modulus and $\bar{M}$ is the mean atomic mass, thermal conductivity then scales with the bulk modulus as[92–94]

$$\kappa \propto B^{3/2}. \tag{2.15}$$

## 2.3 Review of Measurements of Thermal Transport in Porous Materials

A porous solid subjected to a thermal gradient transfers heat via two main mechanisms, conduction through the solid scaffolding, and through the fluid in the pores (Figure 2.10 (a)). In this work, we ignore the contribution of radiation across the pores because it becomes negligible for low emissivity material with small pores around room temperature, like the materials which are studied here.[95] However I note at high temperatures, radiative heat transport would become dominant as it increases as $T^4$. Additionally, I adopt a microscale definition of convection, which includes its contribution to the heat transfer picture in the form of a Kapitza resistance. In general, vibrational conduction occurs in the dielectric solid phase by phonons, and conduction by the fluid in the pores occurs through Brownian motion of the fluid particles, where the temperature of the pore is influenced by the solid conductivity, and the thermal boundary resistance occurring at the pore/void (solid/fluid) interface. This section provides a brief overview on heat transfer processes of porous material and summarizes the current literature for disordered and ordered porous material.

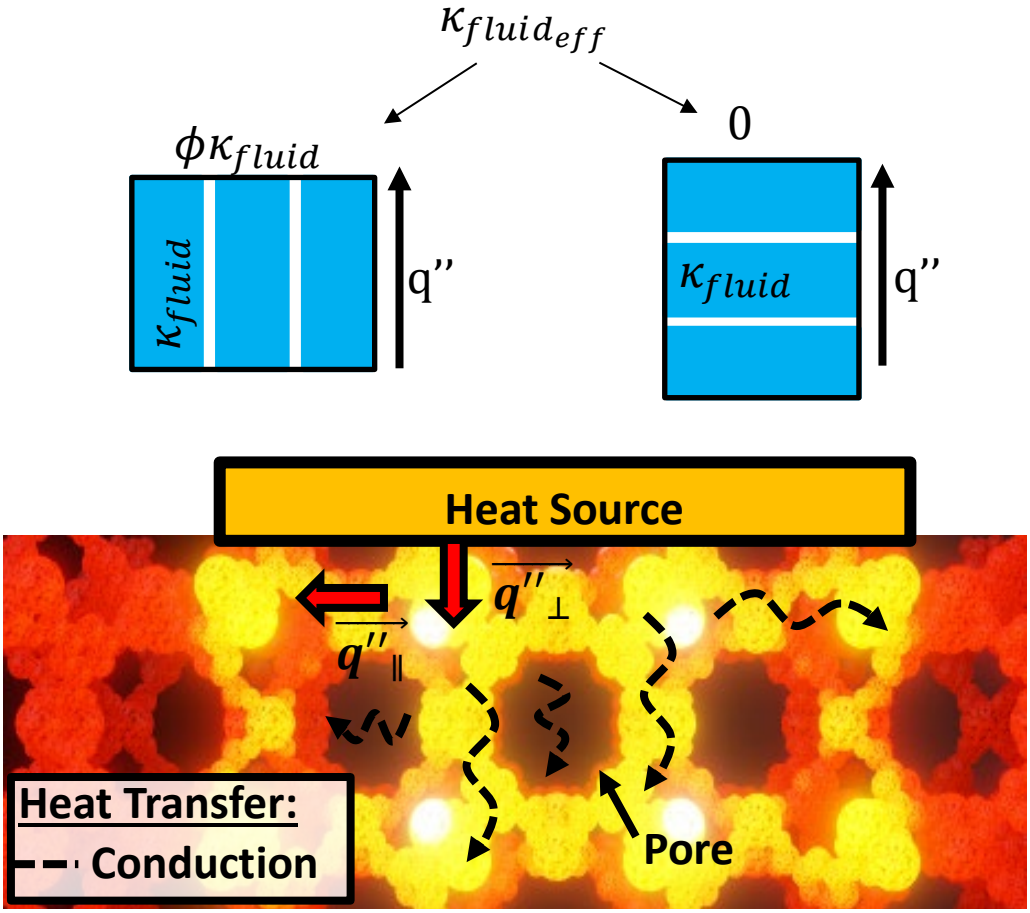


Figure 2.10: (top) Orientation of fluid in a two-phase flow and its effect of $\kappa_{fluid_{eff}}$, where $\phi$ is the void fraction. (bottom) Schematic of thermal transport in an ordered porous material, where the contributions to the thermal conductivity (conduction by the solid and the fluid) are shown in both the cross-plane and in-plane directions (not drawn to scale). This image was constructed with the help of Prof. Chris Wilmer (University Pittsburgh).

Literature on the topic of the effect of pores on the thermal conductivity of porous material is extensive. Early theoretical observation on such systems were provided by Maxwell, where he showed the thermal conductivity of a porous system was related to the thermal conductivity of its fully dense counterpart via,

$$\frac{\kappa_{(Porous)}}{\kappa_{(Dense)}} \approx 1 - \frac{3}{2}\phi, \tag{2.16}$$

where $\kappa$ is the phonon thermal conductivity of the solid phase and $\phi$ is the porosity.[96] Others have shown that the overall thermal conductivity of these porous systems cannot exceed the volume

average of its individual components.[15] Therefore, the apparent thermal conductivity ($\kappa_{app}$) of a porous material can be described as the contributions from a two phase flow (solid and liquid/gas), as the sum of two parallel resistors

$$\kappa_{app} = (1 - \phi)\kappa_{solid} + \kappa_{fluid_{eff}}, \tag{2.17}$$

where $\kappa_{solid}$ is the intrinsic thermal conductivity of the solid matrix material, and $\kappa_{fluid_{eff}} = \phi\kappa_{fluid}$ where $\kappa_{fluid}$ is the thermal conductivity of the fluid filling the pores, and $\phi$ is the void fraction occupied by the fluid. Equation 2.17 is only valid if the fluid is oriented so that it runs parallel to the direction of heat flow, otherwise $\phi\kappa_{fluid} = 0$ (see Figure 2.10 (b)). While useful, this simplified approach for approximating the apparent thermal conductivity of a porous material neglects the complex interactions that can occur between the solid and fluid constituents, where pore geometry can greatly influence the total apparent conductivity.[15] In particular, pores act to contribute interfacial thermal resistance that plays an increasingly important role as the characteristic dimension of the material decreases, where an increase in resistance at interfaces will reduce the conduction in the solid and in the fluid.[97–99]

A natural extension to understanding the thermal transport processes in porous materials is investigating how these processes are affected by the introduction of a guest molecule into the pore, in the form of an adsorbed fluid (liquid or gas) or solid molecule. Matters are complicated further during the introduction of 'guest' molecules within the pores, where interactions between the solid matrix and adsorbate become more involved, and a more complex thermal transport regime is established. Percolation theory would predict the guest to increase the total apparent thermal conductivity of the system due to the increase in the number of heat channels introduced by the guest molecule.[100] Alternatively, kinetic theory ($\kappa = \frac{1}{3}Cv^2\tau$) might predict the

guest molecule(s) could partially fill the pore and act as a defect, which would increase phonon scattering, reducing phonon lifetimes ($\tau$) therefore reducing the total apparent thermal conductivity. The thermal properties of composite multiphase materials have been approximated by a variety of models that account, on varying levels, for both the conductivity of the solid, the disperse material (guest species in the pore), and the interaction between them, and include factors such as pore geometry and anisotropy effects. These include the Maxwell model (Eqn. 2.16)[96], variants of effective medium theory (EMT) [101–103] and differential effective medium theory (DEM).[104] Generally, EMT pertains to defining properties macroscopically by averaging the constituents that comprise the composite while DEM takes the point of view that a composite material can be understood by making infinitesimal changes to an already existing composite. Though useful, a single theory has not yet emerged which captures the thermal trends of infiltrated porous systems, because the impact of guest molecules on the thermal properties of porous media is quite inconclusive. The remainder of this section will present the thermal results of two types of porous solid material reported in the literature, porous disordered solids (i.e. $SiO_2$-based nanostructured films, aerogels, foams, mineral wool, and sintered plastics and oxides) and porous ordered solids (clathrates, skutterudites, zeolite, metal organic frameworks (MOFs), covalent organic frameworks (COFs), and periodic and randomly oriented porous silicon materials) compared to popular EMT and DEM approximations for two phase nanocomposites. The distinction between disordered and ordered porous media in this dissertation, is defined by the crystalline or amorphous properties of the solid matrix material.

Cellulose foams, aerogels and sintered oxides are examples of disordered porous materials. The pores in these materials supplement the intrinsic disorder of the solid matrix material in the form of varying degrees of pore size and distribution heterogeneity. For example,

sintered alumina and zirconia have been shown to exhibit meso and macropores that differ in both size and shape, where the macropores are 100 x larger than the mesopores.[105] Cellulose foams, on the other hand, contain a more ordered pore distribution, where the pores orient as long tubes throughout the material and the pore density decreases by 30% from bottom to top of the foam nanocomposite.[106] In total, porous disordered materials include a vast array of structured and randomly oriented pores whose solid media is amorphous.

Figure 2.11 (a) shows the thermal conductivity of a variety of disordered porous material as a function of porosity. In general, the apparent thermal conductivity decreases with increased porosity for disordered porous material. The thermal conductivity decreases with increasing pore size following a typical effective medium theory, where the apparent thermal conductivity of the material is an average of the higher thermal conductivity material from the solid phase, and the lower thermal conductivity from the fluid phase based on their respective volume fraction. Thus, a higher porous volume fraction will lead to a lower apparent thermal conductivity if the fluid (air) has a lower thermal conductivity than the solid. In line with these trends, the morphology of disordered porous materials is one of interconnected macroscale pores that prove ineffective for mitigating the solid conduction, which results in thermal conductivities that are higher than air.[107] Figure 2.11 (a) showcases a boron-nitride aerogel in vacuum that boasts a thermal conductivity below air, resulting from the ultralow density and engineered structural disorder; in air, the thermal conductivity jumps to 0.02 $Wm^{-1}K^{-1}$.[107] In total, at the macroscopic level, an effective medium approach may capture the thermal trends of porous material. However, at the nanoscale, effective medium theory often fails. For example, fabricating nano-pores that are smaller than the MFP of the gas molecules has been theoretically proposed[99] and experimentally validated[108] to obtain ultra-low thermal conductivities, by taking advantage of the Knudsen effect

where gas molecules located inside the pore scatter strongly at the pore wall, and not with other gas molecules, drastically reducing $\kappa_{fluid_{eff}}$ and therefore $\kappa_{app}$. The heat transport picture is not fully understood in porous material at the nanoscale, and is the topic of on-going research.

Ordered porous material include large unit cell crystals like: clathrates, skutterudites, zeolites, metal organic frameworks (MOFs), and covalent organic frameworks (COFs), in addition to intrinsically crystalline solid material with either periodic or randomly oriented fabricated porosity (i.e., porous silicon). Let us begin with intrinsically crystalline material containing fabricated micropores obtained through etching and lithography, which are a class of ordered porous material heavily reported on in the literature. Nanoscale porous materials of this nature can exhibit strong phonon size effects due to their increased surface areas, and disorder introduced by the pores.[109,110] The impact of pore placement (random or uniformly oriented) on thermal conductivity has been shown to have a drastic effect on thermal conductivity.[111,112] Theoretical investigation into pore placement indicates that when pores are fabricated in a spatially uniform orientation, the thermal transport is prescribed by the porosity and specularity (pore surface roughness) at pore interfaces, however when pores are non-uniformly placed, they can locally increase resistance to phonon transport in the form of phonon bottlenecks, where small sets of pores create high local resistance to phonon transport within the material.[111] Wolf *et al.* showed that the average thermal conductivity of randomly oriented pores was up to 15% lower than that of their aligned counterparts.[112] Indeed, experimental results for crystalline silicon thin films fabricated with random and oriented pores plotted in Figure 2.11 indicate an enhanced reduction in thermal conductivity, which is thought to be due to strong size effects, increased boundary scattering and coherent phononic effects.[109,113]

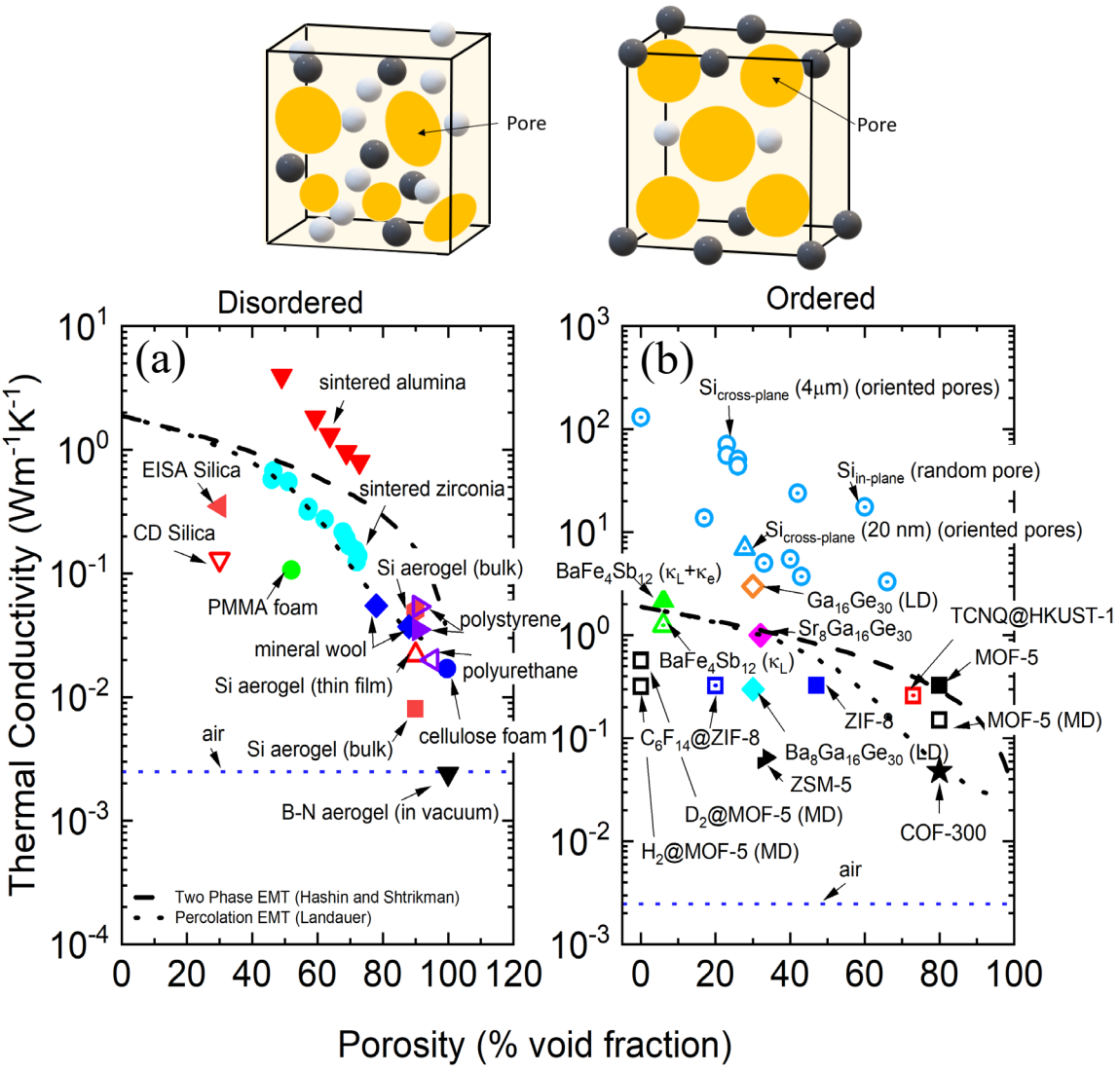


Figure 2.11: The thermal conductivity reported in the literature for disordered (a) and ordered (b) porous material. (a) Disordered porous material include thin[16] and thick[18,114] Si aerogels, a boron-nitride aerogel,[107,115] convectively deposited (CD) silica particles,[116] evaporation-induced self-assembled silica particles (EISA), [116] mineral wool, polystyrene, and polyurethane,[99] and PMMA[108] and cellulose[106] foams. Note that the opaque symbols represent the apparent thermal conductivity and the open symbols represent values for the thermal conductivity of the solid component only. The effective medium approximation by Hashin and Shtrikmann for a two phase system, [117] and Landauer's effective medium percolation theory[118] calculated for sintered zirconia are also plotted for reference. (b) The ordered porous material include MOFs shown as squares (MOF-5,[119,120] pristine and infiltrated ZIF-8,[121] and infiltrated HKUST-1[122]), COFs as stars (COF-300[123]), skutterudites as triangles ($RFe_4Sb_{12}$[124]), clathrates as diamonds ($Sr_8Ga_{16}Ge_{30}$,[125] $Ba_8Ga_{16}Ge_{30}$,[65] and $Ga_{16}Ge_{30}$[65]) and zeolites as right leaning triangles (ZSM-5[123]). Both pristine and infiltrated material are plotted. Infiltrated material are labeled as 'guest@host'. Porous crystalline Si cross plane thermal conductivity for 4 μm (blue circles)[109] and 20 nm (blue triangle)[113] thick films with oriented pores, and the in-plane thermal conductivity for porous silicon with randomly distributed pores (blue circles with dot)[126] are also shown for reference.

The ordered porous large unit cell crystals take advantage of coordination chemistry to form networks with well-defined permanent porosity. In the case of large unit cell crystals, a coordination network is defined by the preferred orientation and bonding of an ion to ligands (i.e. six ammonia ligands can bond to a single $Co^{3+}$ cation in an octahedral geometry).[127] Alternatively, others such as zeolites and COFs are formed from kinetically controlled pathways, where different phases are obtained through prescribed heating times, temperatures, or class of organic molecules used for synthesis.[128] Ultimately the product is a uniform network of linked cavities and pores. Large unit cell crystals like MOFs and COFs contain intrinsic disorder, where the large number of atoms in the unit cell result in an increased phase space for scattering events if low lying longitudinal modes can interact with acoustic modes, thereby reducing phonon lifetimes.[66,129] As shown in Figure 2.11 (b), the heat transfer picture in these porous materials is not easily captured as a function of porosity. Rather, heat transfer in ordered porous material is a result of a complex interaction between propagating lattice-modes and localized molecular-modes, contributing to the total thermal conductivity.[130] The influence and interplay of these competing modes means that both crystalline anharmonic trends and glasslike phonon thermal conductivities emerge among these materials.[15,119] For example, there are a few reports of crystalline temperature dependent heat transport trends ($T^{-1}$) for porous crystalline material such as MOF-5[119] and perovskite-type MOF crystals[131] and the unfilled $CoSb_3$ skutterudite,[132] whose thermal trends are captured by the kinetic theory of gases (Eqn. 2.5) where the mean free path of the lattice modes (phonons) decreases as 1/T as the number of phonons increase at high temperatures. In contrast, reports of glasslike thermal conductivities (increase with temperature up to a plateau) are far more prevalent for this class of material, and have been reported for zeolites,[133–135]filled clathrates,[136–138] and filled skutterudites.[132] Non crystalline behavior is commonly seen in these materials where enhanced

vibrational mode scattering from the guests and small mean free paths dominate the thermal transport. Variations in the temperature dependent thermal trends of porous ordered material is a result of the interplay between propagating and localized modes intrinsic to the solid material, and the interaction of dispersive materials within the pores.

It is common for guest atoms/molecules to inhabit the pores to form host-guest complexes with diverse energy landscapes. Specific engineering of porous material with guest molecules has allowed for precise modifications in the electrical, mechanical and thermal properties of materials. In particular, this strategy has been deployed to develop phonon glass-electron crystals for thermoelectric applications. For example, MOFs have been infiltrated with redox-active organic charge transfer guest molecules to realize tunable electrical conductivity.[139] Skutterudites and clathrates exhibit guest/host interactions where the radius of the pore is much larger than the radius of the guest so that the guest is trapped in a highly anharmonic potential and vibrates with large amplitudes.[140] From a thermal perspective, it is unclear what role the guest has on transport processes. On one end, filling the pores introduces more heat carrying channels that could increase thermal conductivity. On the other, the guest may introduce rattling and hybridization that scatters phonons, or slows them down. In the case of the skutterudites and clathrates, it has been shown that the large vibration of the guest atom acts as a rattling mode that strongly scatters acoustic phonons, which carry the majority of the heat.[65,130] The role of these rattlers on phonon lifetimes and group velocities is not fully understood. For example, in clathrates, the effects of the rattling modes on phonon lifetimes are suggested to be non-resonant (scattering occurs over a wide frequency range),[65] while in skutterudites rattling may appear as a resonant process (scattering occurs over a limited energy region),[129] or not at all, where the guest fully occupies the atomic cages resulting in a coherent optical phonon branch that increases heat

carrying channels.[70] Further, others have argued that the dominant role of the rattler mode in clathrates is to flatten phonon bands, thereby reducing the group velocity, rather than producing new phonon scattering channels.[73] Even more, *ab initio* calculations have shown that the guest molecule in skutterudites produces phonon hybridization that flattens phonon modes leading to increased three-phonon scattering channels, but the anharmonic interaction between the guest and host (rattling) does not play a role in reducing the thermal conductivity.[66] Figure 2.11 (b) plots the apparent thermal conductivity of both pristine unfilled and infiltrated ordered porous material as a function of porosity, where there is not an obvious trend observed.

This chapter summarizes the theories and concepts of macroscopic and microscopic transport and goes into detail about how these processes occur in porous material. A review of the literature on the thermal transport of porous material sheds light on the dominating mechanisms in disordered and ordered porous material and also highlights many of the open questions about how limiting length scales regarding pore size and guest-host interactions effect thermal transport. This sets the stage for the motivation behind the work in this dissertation, which investigates the roles of composition and morphology on both nanostructured solid chalcogenides and highly porous metal organic frameworks.

# Chapter 3

## 3. Experimental Techniques

"The true method of knowledge is experiment."

-William Blake

## 3.1 Time Domain Thermoreflectance (TDTR)

### 3.1.1 Background

Time-domain thermoreflectance (TDTR) is a transient non-contact, optical thermometry technique, which is uniquely poised and commonly used to measure the thermal properties of thin films. The first demonstration of transient thermoreflectance (TTR) to measure thermal transport in thin films was realized over 30 years ago by Paddock & Easley[141] and enhanced over the last three decades by improvements in measurement accuracy by Cahill[54,142] and advancements by Capinski and Maris in both thermometry and picosecond ultrasonics.[29,30] The high spatial and temporal resolution offered by TDTR, which is limited by the pulse width (often < 100 fs directly out of the laser) and laser spot size, make it highly useful for measuring ultrafast nonequilibrium dynamics (electron-phonon coupling, phonon-phonon thermalization)[143–145] as well as heat transport processes such as the thermal conductivity[21,146] and thermal boundary conductance[147,148] of thin engineered materials.

Figure 3.1 shows a schematic of a two-color TDTR set up at the University of Virginia's ExSiTE Lab. TDTR utilizes a pump-probe experimental configuration to both generate surface heating and measure the resulting temperature profile of the sample by monitoring the change in optical reflectivity with temperature, or thermoreflectance ($^{dR}/_{dT}$). This specific pulsed

TDTR system is centered around a femtosecond oscillator that emits sub-picosecond pulses at a repetition rate of 80 MHz, with a wavelength centered at ~800 nm (bandwidth of 10.5 nm). The output is split into a pump and probe path that are coaxially focused on the surface of the sample by an objective lens (typical pump and probe radii that are used in our two-color system are $1/e^2$ pump radius $\approx 20\ \mu m$, probe radius $\approx 9\ \mu m$). The pump path is electro-optically modulated with a square wave, generally between 1-10 MHz. The use of pump modulation is important, because it provides a reference frequency to allow for lock-in detection which increases the signal to noise ratio (SNR).[149] The modulated pump beam heats a metal transducer layer (typically aluminum or gold) which must be in contact with the sample. Typically, the metal transducer is deposited directly on top of the sample. The effectiveness of this approach requires that the surface roughness of the sample is optically smooth (ideally surface roughness < 15 nm).[150] Because solution processed materials tend to be optically diffusive to visible light, the sample fabrication procedure can be adjusted by depositing the thin film metal transducer on top of a glass substrate (which is transparent to the pump and probe wavelengths). Then, the solution processed films can be deposited on the metal side of the metal/glass substrate. In this sample configuration, bi-directional heat conduction must be accounted for in the analysis.[149] More detail is provided on this topic is Section 3.1.2.2. Requirements for the transducer are a large thermoreflectance coefficient ($\beta = \frac{\partial R}{\partial T}$) at the probe wavelength, good adhesion to the sample or substrate, and a high thermal conductivity to minimize the measurement sensitivity to the metal layer.[151] Additionally, the diffusivity ($\alpha = {}^{\kappa}/_{C_v}$) controls the time it takes energy to diffuse ($t_{thermalize}$) through a metal film of thickness ($d$) according to

$$t_{thermalize} = \frac{d^2}{\alpha} = \frac{(100e-9)^2}{1e-5} \sim 100ps. \tag{3.1}$$

Therefore, a high transducer thermal conductivity ensures that the majority of the temperature gradients in a TDTR experiment are not in the transducer. The thermalization time dictates when it is appropriate to fit the thermal model to the data. Consequently, the TDTR measurements of thermal conductivity and thermal boundary conductance begin at 500 ps for the sample systems studied here to ensure the majority of the thermal gradients sensed during a TDTR experiment not driven by those in the metal transducer.

The interaction of the pump with the transducer creates both DC (steady-state) heating event, and a small modulated heating event at the sample surface. While the heating events are heavily dependent on the sample material properties, typically the power absorbed by the sample is on the order of a few milliwatts, which corresponds to DC heating that is on the order of a few Kelvin, and a much smaller (~10-100 mK) modulated temperature rise ($\Delta T$) .[152] The reflectivity ($\Delta R$) of the metal transducer changes linearly with the change in the surface temperature ($\Delta T$) due to the modulated heating event such that

$$\Delta R = \beta \Delta T, \tag{3.2}$$

and is monitored temporally by the probe beam. The thermoreflectance coefficient ($\beta$) is a material property of the transducer that depends on the illumination wavelength and surface properties. Al is a good choice as an optical transducers for TDTR because it has a high thermoreflectance coefficient at the probe wavelength ($\beta = 1.8x10^{-4}K^{-1}$). [153,154] The probe is delayed in time by a translational mechanical delay stage from -15 ps $\leq t \leq$ 5.5 ns (where here $t$ is the relative time delay of the probe to the pump), and its reflected intensity from the sample is measured by a photodetector or balanced photo-diode. Additionally, the change in reflectivity of the probe pulses

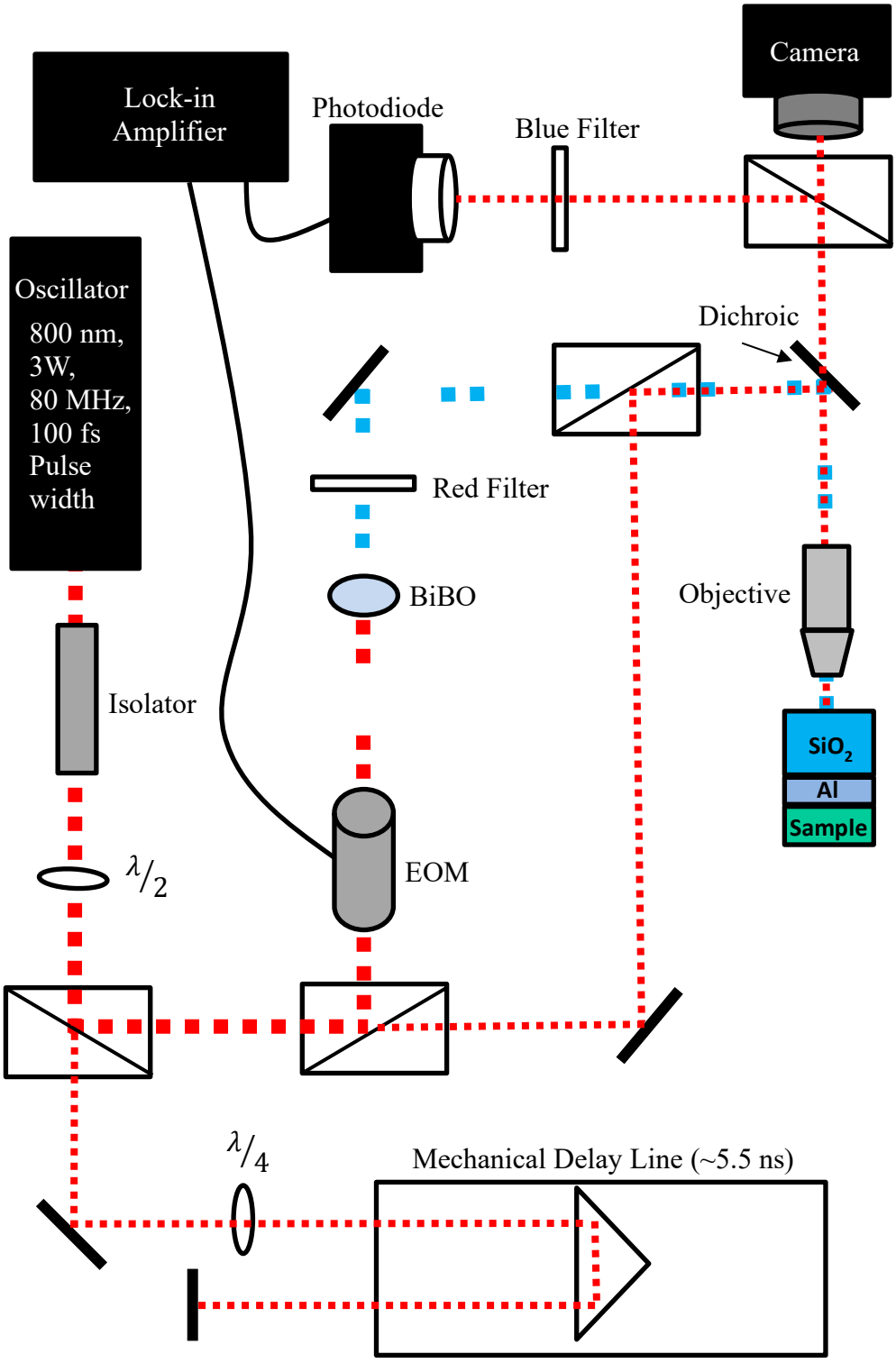


Figure 3.1: Two color time-domain thermoreflectance (TDTR) schematic.

due to pump heating is very small (on the order of $10^{-4}$ – $10^{-6}$),[155] therefore a lock-in amplifier is synchronized to the modulation frequency of the pump beam to enhance and demodulate the signal to provide amplitude (of the voltage) and phase data in the form of an in-phase ($V_{in}$) and out-of-phase ($V_{out}$) signal. In total, the lock-in output corresponds to a change in reflectance resulting from the temperature event produced by the pump. This representation of a thermal decay is directly related to the sample thermal properties, which are then obtained by fitting an appropriate thermal model, as will be discussed in detail in the next section.[153,156,157] Two variations of the TDTR systems exist at the UVA ExSiTE lab, the two-color and the two-tint arrangements.[149,158,159] Each arrangement optimizes the SNR by mitigating diffuse scattering from the pump pulse from making its way back into the detector. For the two-color system, shown in Figure 3.1, the 800 nm pump light is frequency doubled using a BiBO (bismuth Triborate, $BiB_3O_6$) crystal after it passes through the EOM. This converts the back end of the pump to 400 nm light which is easily filtered from the 800 nm probe light and kept from leaking into the detector. On the other hand, the two-tint TDTR system employs long pass sharp edge and narrow bandpass filters to spectrally isolate the pump and probe beams. The pump is then reflected to the sample from a polarizing beam splitter and filtered from the probe line back into the detector to avoid leakage into the detector. Figure 3.2 shows representative data for the magnitude ($\sqrt{V_{in}^2 + V_{out}^2}$) for two typical calibration samples, a high thermal conductivity material ($Al_2O_3$), and a low thermal conductivity material ($SiO_2$). The data are collected at a negative delay time in order to fully resolve the temperature rise time due to the interaction of the optical energy of a single pulse with the metal transducer. Note that the data in the figure have been shifted by +15 ps to allow for the use of a log scale on the x-axis; therefore, the data plotted from 1-15 ps are considered the '*pre t=0*' signal, which is the signal that is generated before the arrival of the pump pulse. The noise floor, or the average amplitude of

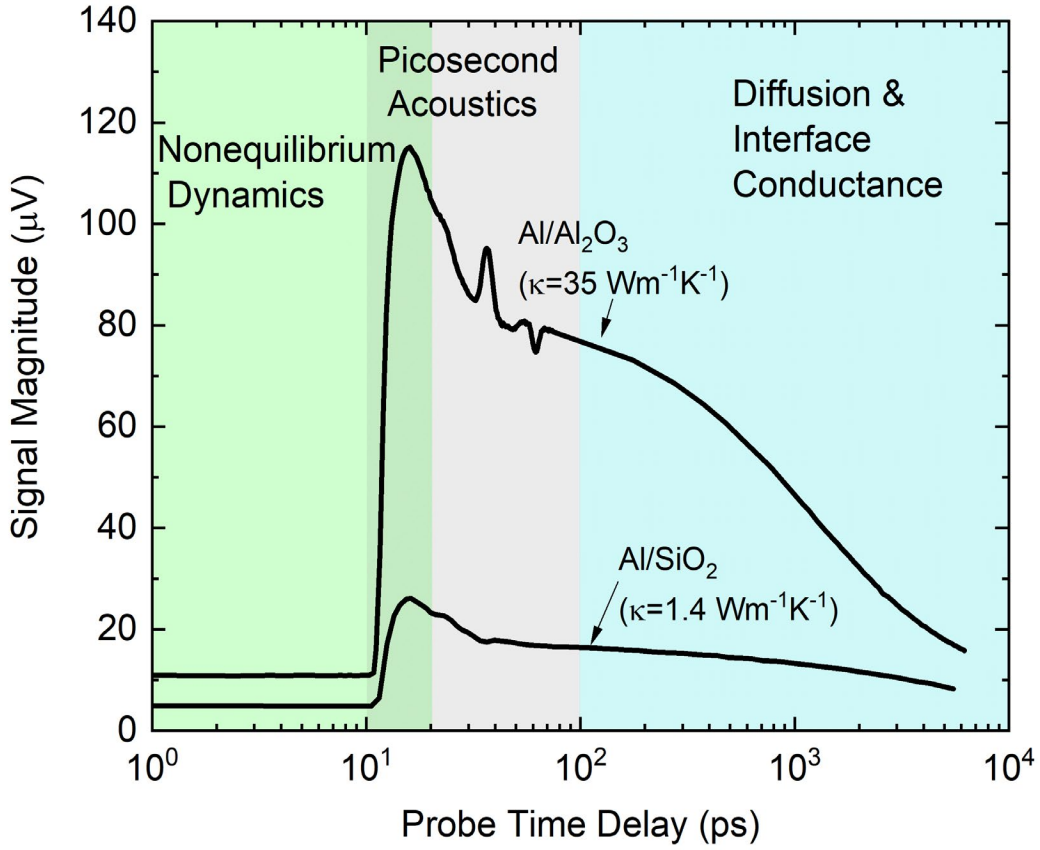


Figure 3.2: Representative TDTR data for two typical calibration samples, a high thermal conductivity material ($Al_2O_3$) and a low thermal conductivity material ($SiO_2$). The data are plotted as the magnitude of the TDTR signal vs. the probe delay time. Note that the plot has been shifted by +15 ps to allow for the use of a log scale.

the signal oscillations for a given time delay is about ± 0.1 μV. In order to maintain a high SNR throughout the scan, a '*pre t=0*' signal magnitude of 10-15 μv is preferred, which can be obtained by adjusting the pump power. This ensures that the lowest SNR throughout the scan will be 100-150, since the TDTR signal is lowest in this pre t=0 regime.

Illustrated in Figure 3.2, once the pump pulse arrives at the sample, the TDTR signal becomes composed of three temporal regimes which are indicative of how energy is transferred within the medium: non-equilibrium dynamics, picosecond acoustics, and diffusion. Nonequilibrium dynamics occurs at early times (in the first few ps), where the optical energy from the pump pulse is absorbed by electrons in the metal transducer to form the large rise in signal

magnitude. These hot electrons thermalize and quickly transfer their energy to phonons and electrons within the lattice. Here, processes such as electron-electron and electron-phonon coupling can be studied.[160–163] As it is aptly named, the picosecond acoustic region persists to 10's of picoseconds and is useful for measuring the transducer thickness. When the impulse from the pump reaches the metal film, the surface is rapidly heated leading to prompt thermal expansion. This rapid expansion produces a high frequency acoustic mechanical strain wave that traverses at the sound speed of the material, and partially reflects off of any interfaces that it encounters. The stronger the acoustic mismatch between the materials at the interface, the stronger the reflection. The reflected portion of the wave is then sent back in the direction of the sample surface, where it is optically detected by the probe. Together, propagation time and the amplitude of the acoustic echo measured by the probe provide information about the transducer thickness and the quality of the bonds at the transducer/sample interface. [164–166] Examples of these acoustic echoes are shown in Figure 3.2 for both $Al_2O_3$ and $SiO_2$, where the picosecond acoustic signal is much larger for the sapphire, due to the higher acoustic mismatch between the $Al/Al_2O_3$ interface. Finally, at longer times, diffusive processes can be examined where the energy from the pump pulse has had sufficient time to thermalize and transfer to the film. The data collected in this regime are fit to the solution of the heat diffusion equation for a multilayered structure to derive the relevant thermal parameters.

The interaction of the pump with the sample results in two surface temperature events, a modulated AC heating event (on the order of ~10-100 mK),[152,167] which is what the probe temporally monitors, and a demodulated DC steady state temperature rise (which can range to a few degrees to tens of degrees Kelvin).[152] The steady state temperature rise is a function of the average power absorbed by the transducer during the laser heating event, and the corresponding

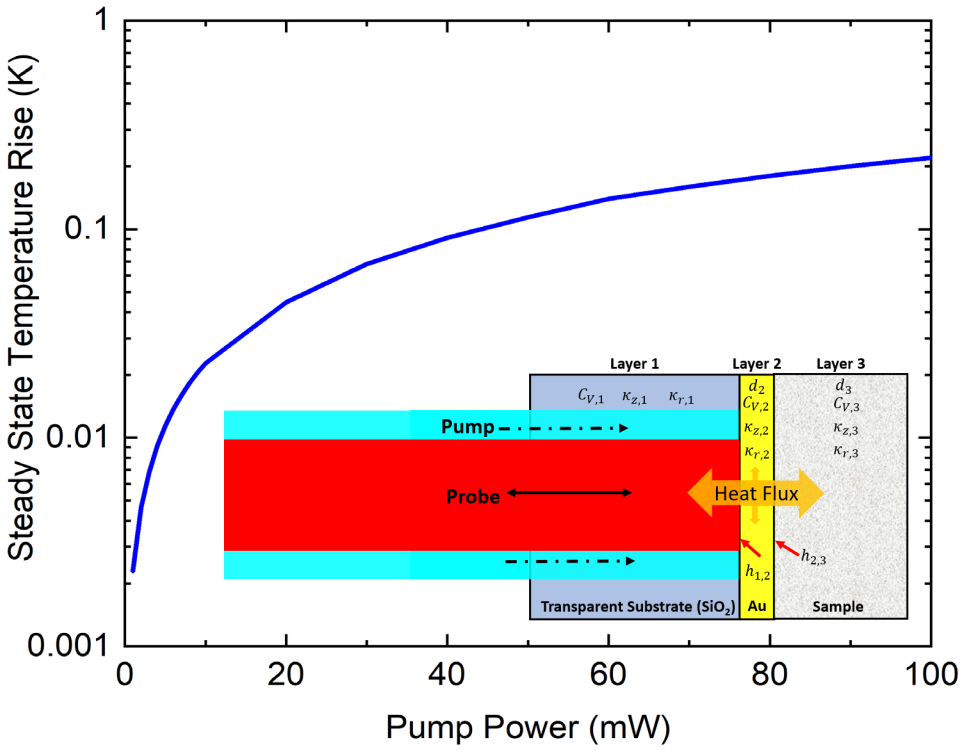


Figure 3.3: Room temperature steady state temperature rise predicted by the multi-layer heat diffusion model from Braun *et al.*[152] for a sample with bi-directional heat flow (bulk $SiO_2$ / 80 nm Au / 400 nm HKUST-1 ($\kappa$~1Wm$^{-1}$K$^{-1}$)), where $\kappa_{sink} = \kappa_{SiO2} = 1.4\ Wm^{-1}K^{-1}$, the pump power is varied from 1-100 mW, $\alpha_{Au,800nm} = 0.02$ and $r_o$=22 µm. The inset shows the sample geometry.

thermal properties of the heat sink in contact with the transducer. Both of these events occur at the surface of the sample simultaneously, and can be mathematically decoupled.

A common analytical model used to estimate the upper bound steady state temperature rise was defined by Cahill[153] and extended by Schmidt[168] as

$$T_{steady\ state} = \frac{P_{pump}\alpha_t}{\kappa\sqrt{2\pi r_o^2 + 2\pi r_1^2}}, \tag{3.3}$$

where $P_{pump}$ is the incident power of the pump, $\alpha_t$ is the absorptivity of the transducer layer at the pump wavelength (~0.02 for Au and ~0.10 for Al at 800 nm),[169] $r_o$ and $r_1$ are the respective $\frac{1}{e^2}$ radii of the probe and pump spot sizes, and $\kappa$ is the thermal conductivity of the sample. This

expression is derived for an isotropic bulk material and also does not account for bi-directional heating. Braun *et al.*[152] provide a rigorous calculation for the steady state temperature rise which is more applicable to the inhomogeneous, nano-sized material studied via TDTR in this dissertation. This model accounts for a pulsed Gaussian surface heating source impinging on a multilayer sample using the appropriate initial and boundary conditions applied to the solution to the radially symmetric heat diffusion equation.[152] This model shows that gold and aluminum transducers reduce the steady state temperature rise by orders of magnitude in comparison to a transducer-less measurement, by providing rapid radial heat dissipation, and that a bi-directional sample scheme (i.e. $SiO_2$/transducer/film) can also significantly reduce the steady state temperature rise.[152] Figure 3.3 shows the predicted steady state temperature results from the heat diffusion model applied to a low thermal conductivity, thin MOF sample configured in a bi-directional heating geometry. The multi-layer diffusion model predicts a steady state temperature rise of less than 1K for pump powers less than 100 mW (relevant to the pump power ranges used in TDTR). The results show that the steady state temperature rise remains small in this circumstance, so that it is appropriate to increase the pump power to increase the SNR without having to account for DC temperature rise effects in the thermal model to analyze the raw TDTR data.

TDTR uses an optical probe that applies a modulated train of heat pulses at one boundary of the sample and then measures the temporal temperature decay with an optical probe. A TDTR measurement is sensitive to the diffusivity (or effusivity)[170] of a sample and measures the change in reflectance over time after a pump pulse, which is linearly proportional to the surface temperature. The thermal properties of the material are solved for by applying the cylindrical heat diffusion to a multilayer structure in the frequency domain, and then the lock-in response is used

to reconstruct the solution in the time domain. The heat equation is valid here because the thermal penetration depth of the modulated laser pulse is typically much greater than the effective MFP of phonons of the interrogated material, so transport is diffusive. Secondly, the heat transport can also be assumed to be one dimensional, due to the large aspect ratio of the sampling system, where the spot size is much larger than the thermal penetration depth so that the measurement is not sensitive to radial transport.[29,171] In order to fit these requirements, the thermal penetration depth of a TDTR measurement is controlled by requiring a large modulation frequency (1-10 MHz) onto the pump beam. The penetration depth at these modulation frequencies is on the order of a few tens of nanometers to a few micrometers, and is in a regime where the thermal wave is small compared to the total film thickness, but long enough to directly measure the heat diffusion at nanometer length scales. A simplified analytical expression for the thermal penetration depth ($l_z$) is estimated by[172]

$$l_z = \sqrt{\frac{2\kappa}{C_v f}}, \tag{3.4}$$

where $f$ is the modulation frequency of the pump beam. Consistent with the discussion of DC heating above, this simplified analytical expression is known to break down (often over predicting $l_z$) for modulated heating events and applied to multi-layered samples.[167] To this end, Braun and Hopkins [167] describe a more rigorous form that models the spatial and temperature distributions during a modulated heating event from the heat diffusion equation. In total, an accurate understanding of the thermal penetration depth is critical for TDTR measurements because it defines the measurement volume and determines the sensitivity of the measurement to radial and cross plane transport.

In addition to controlling the thermal penetration depth, the modulated heating event induced by the pump pulses in a TDTR measurement creates a temperature rise at the sample

surface. The temperature response of the material is phase lagged with response to that of the heating event, and this phase lagged oscillatory temperature response is extracted by the lock-in amplifier by mixing the signal output from the detector with a reference wave having a defined phase (the pump) and reported as a complex function of $X + iY$ where X is the in-phase ($V_{in}$) and Y is the out-of-phase ($V_{out}$) component. Either the amplitude or the phase data can be analyzed from the lock-in response. Figure 3.4 shows representative TDTR data, and the simulated response (fits) for a 50 nm thick amorphous $TiO_2$ thin film from DeCoster *et al.*[21] The ratio of the real (in-phase) and imaginary (out-of-phase) components of the lock-in response are used here because it eliminates the need to know the precise thermoreflectance coefficient of the metal film and the gain of the electronic components, and it produces higher SNR and removes the need for normalization.[116,153] This ratio is compared to a simulated lock-in response ($S^{sim}$) derived by applying the transfer function defined in frequency space calculated by solving the heat equation for a multilayered system.[149] The simulated lock-in response, plotted as a solid red line in Figure 3.4 is solved with an initial guess for the properties for each material in layer ($n$) which includes: the heat capacity ($C_{v,1}, C_{v,2}, \dots, C_{v,n}$), thermal conductivity ($\kappa_1, \kappa_2, \dots, \kappa_n$), thickness ($d_1, d_2, \dots, d_n$), and thermal boundary conductance ($h_{1,2}, \dots, h_{n-1,n}$). Typically, this iteration allows for one to two free parameters to perform the fitting. As an example, Figure 3.5 shows a schematic of two common sample geometries with insulated and conductive boundaries and the corresponding parameters defined in each layer. The simulated response is then compared to the experimental response, and a least square minimization routine is used to iterate different guesses for the free variable (thermal property of interest), until a minimum is found in the quantity

$$\mathrm{E} = \int [S^{exp}(t) - S^{sim}(t)]^2 dt. \tag{3.5}$$

I refer the interested reader to the following references, where the specifics of this procedure have been comprehensively described.[116,144,149,153,156,168,170]

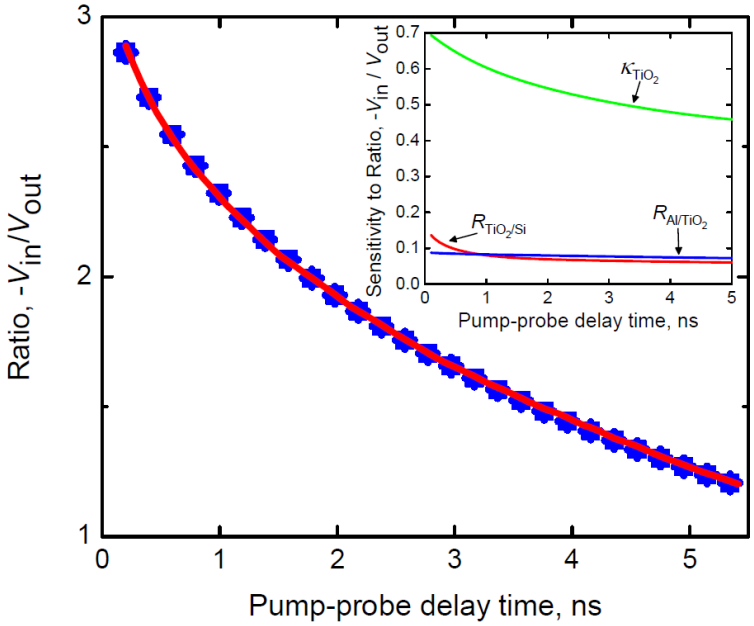


Figure 3.4: Representative TDTR data (blue symbols) and simulated response of the fitted three temperature heat model (red line) for amorphous $TiO_2$ films reprinted with permission from DeCoster *et al.* 2018.[21] Shown here is a measurement performed on a 50 nm thick film of $TiO_2$ grown on silicon, fit to the ratio ($-V_{in}/V_{out}$) of the lock-in detection system. The error bars on the data are representative of scan-to-scan variability. The inset contains the corresponding sensitivity analysis at a modulation frequency of 10 MHz, described in more detail in the next section. These sensitivities demonstrate the measurement is primarily sensitive to the thermal conductivity of the film, $\kappa$, and not the thermal boundary conductance, $h_k$, at the metal/film or film/substrate interface.

### 3.1.2 Porous Media

This section describes the feasibility for TDTR to perform measurements on porous material. It provides both a discussion on the physical measurement, and also a description for how to optimize the measurement for samples that are not intrinsically accessible to standard TDTR measurements due to high surface roughness.

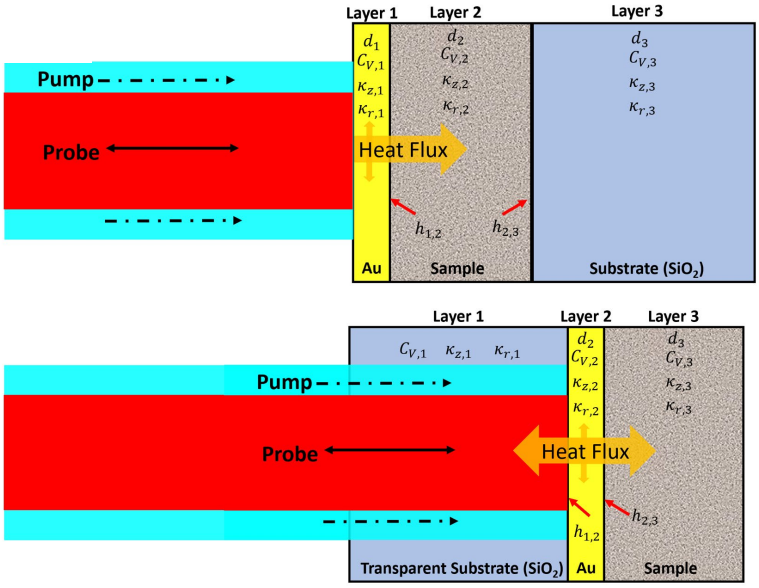


Figure 3.5: Sample schematic of a layered structure with (top) insulated boundary conditions where the optical energy is directly deposited on the transducer, and (bottom) a sample with a conductive boundary condition where the optical energy is deposited in the metal transducer layer and bi-directional heat flow occurs into the transparent substrate and the sample. The input parameters to the thermal model associated with their respective layer are also shown.

TDTR measurements require that the sample surface be reflective and smooth (less than 15 nm RMS roughness), so that a transducer layer can be deposited directly on top of the sample (Figure 3.5 (a)). Many porous and solution processed nanocomposites do not fulfill such requirements and necessitate an improvised sample geometry to successfully obtain TDTR measurements. In order to overcome the high surface roughness of the porous, solution processed samples studied here, I use the technique pioneered by Ge *et al.*[97] and Schmidt *et al.*,[168] which is illustrated in Figure 3.5 (b). In this geometry, rough porous media were directly in contact with the metal side of an $SiO_2$ glass substrate coated with a thin metal film (Al or Au). In contrast to traditional TDTR, the probe pulse is reflected by the metal transducer after passing through the glass substrate layer and experiences bidirectional heat transfer into both the $SiO_2$ substrate and the sample. The analysis of the TDTR data is then fit to a thermal model derived from the solution

to the heat equation in which a modulated source is deposited in between two other conductive materials. Schmidt *et al.*[168] and Hopkins *et al.*[116] discuss in detail how to apply the algorithms developed by Carslaw and Jaeger[173] and Feldman[174] to describe the heat transfer in a composite slab with bidirectional heat flow. Important conclusions from these works include that radial heating is negligible (and therefore heat transport can be approximated as one dimensional) at large pump modulation frequencies ($f$=1-20 MHz) for most material, which in an important approximation that simplifies analysis. Further, low thermal diffusivity ($\kappa/C_v$ =$10^{-4}$-$10^{-6}$ m$^2$ s$^{-2}$) material can be approximated by one-dimensional transport at even lower pump modulation frequencies (~0.1 MHz).[116] This is an important concept since varying the pump modulation frequency can cause the TDTR signal to increase in sensitivity to different aspects of thermal transport within a material.[149,175,176] An additional conclusion is that the bidirectional thermal model is very sensitive to the thermal conductivity of the cover glass and the thermal boundary conductance between the metal film/cover glass ($\kappa_1$ and $h_{1/2}$ in Figure 3.5 (b)). Therefore, it is important to measure these values experimentally before sample deposition to reduce the number of free parameters in the thermal model. In total, this approach allows for the interrogation of samples that otherwise would not be good candidates for TDTR.

For the purposes of the thin film material studied via TDTR in this dissertation, I focus on the microscale picture of thermal transport, where heat transfer by conduction dominates. This assumption can be justified by comparing the time scales between conduction, convection, and radiation, to the experimental time scales accessible in TDTR. The approximate time interval ($\tau$) for the heat transport processes reported here are defined from energy balances and fluxes and applying a limiting characteristic length ($l_{ch}$) such as the thermal diffusion length, diameter of the pore, thickness of the material, etc. From here the time intervals can be represented as

$$\tau_{Conduction} = \frac{l_{ch}^2 C_v}{\kappa} = \frac{(100e^{-9}m)^2 \, x \, 1e^6 \, Jm^3/_K}{1 \frac{W}{mK}} \sim 10 \, ns \tag{3.6}$$

$$\tau_{Convection} = \frac{l_{ch} C_v}{h} = \frac{100e^{-9}m \, x1e^6 \, Jm^3/_K}{100 \, Wm^2/_K} \sim 1 \, ms \tag{3.7}$$

$$\tau_{Radiation} = \frac{l_{ch} C_v}{4\varepsilon\sigma T^3} = \frac{(100e^{-9}m)1e^4 Jm^3/_K}{4x0.1x5.67e^{-8}W/_{m^2K^4}x300K} \sim 2 \, ms, \tag{3.8}$$

where it becomes evident that free convection and radiation processes are relatively slow in comparison to conduction. Next, consider the three time scales relevant to TDTR: first is the time scale between successive pulses which is dictated by the repetition rate of the oscillator ($\tau_{rep-rate}$), second is the pump-probe delay time ($\tau_{pump-probe}$) which is the time interval where the thermal decay from the pump pulse is monitored, and third is the out-of-phase time interval ($\tau_{out}$) that is determined by the pump modulation frequency ($f = 1 - 10MHz$). The following time intervals can be defined for the TDTR experiment used at the University of Virginia's ExSiTE Lab,

$$\tau_{rep-rate} = 12.5 \, ns \tag{3.9}$$

$$\tau_{pump-probe} = 10 \text{ ps} – 5 \text{ ns} \tag{3.10}$$

$$\tau_{out} = \frac{1}{f} = 300 \text{ ns} – 3 \text{ µs}. \tag{3.11}$$

The extremely fast time intervals achieved by the transient technique indicates that contributions from the slow convective and radiative processes will likely not contribute to the thermal effusivity or thermal diffusivity measurements because TDTR monitors the heat transfer properties of a sample before the effects of non-conductive heat transport can contribute. In fact, Hopkins *et al.*[16] showed that the thermal decay in a porous film measured via TDTR is related to the reduced thermal conductivity, and the bulk heat capacity, of the solid matrix material; and therefore the thermal conductivity obtained from a TDTR measurements on porous media represents only the solid portion or the media, not the total effective medium (solid and air components).

Further justification of the claims above are required. TDTR is an experimental technique that temporally monitors the change in a sample's thermoreflectance (i.e., the surface reflectance changes linearly in proportion to temperature when the temperature perturbation is small) with respect to a heating event. In the bidirectional sample geometry, the laser pulse passes through the glass substrates and is partially absorbed in the first few nm's of the metal film before it is transduced to thermal energy that propagates through the backside of the metal film and into the adjacent sample layers (i.e., MOF). For large pump modulations frequencies (8-10 MHz) the TDTR data represent the thermal effusivity ($\sqrt{\kappa C_v}$) of the porous material.[175] Therefore, when the thermal mass on the free surface of the metal side of the substrate is low (like a gas), the measurement loses sensitivity to the thermal boundary conductance between the metal/sample, and the overall TDTR signal is reduced.[116] The presence of any thermal mass (like a porous solid film), increases the TDTR signal. In fact, it has been shown that TDTR has the sensitivity to be able to measure thermal conductivities of samples with thermal effusivity as low as 147 J $s^{-1/2}$ $m^{-2}$ $K^{-1}$.[16]

The discussion provided in this section has provided theoretical evidence that TDTR measurements are not sensitive to heat transferred through the solid pore/air interface for two reasons: the temporal scale of the TDTR measurement (5 ns) is generally much faster than the thermal decay time that corresponds to typical solid/air interfaces (milliseconds to seconds), and the TDTR measurement loses sensitivity to thermal properties of interest when the thermal mass is very low. To show this empirically, Figure 3.6 plots TDTR collected on a thin pristine, activated, HKUST-1 MOF film collected where the sample was staged in an ambient environment and under

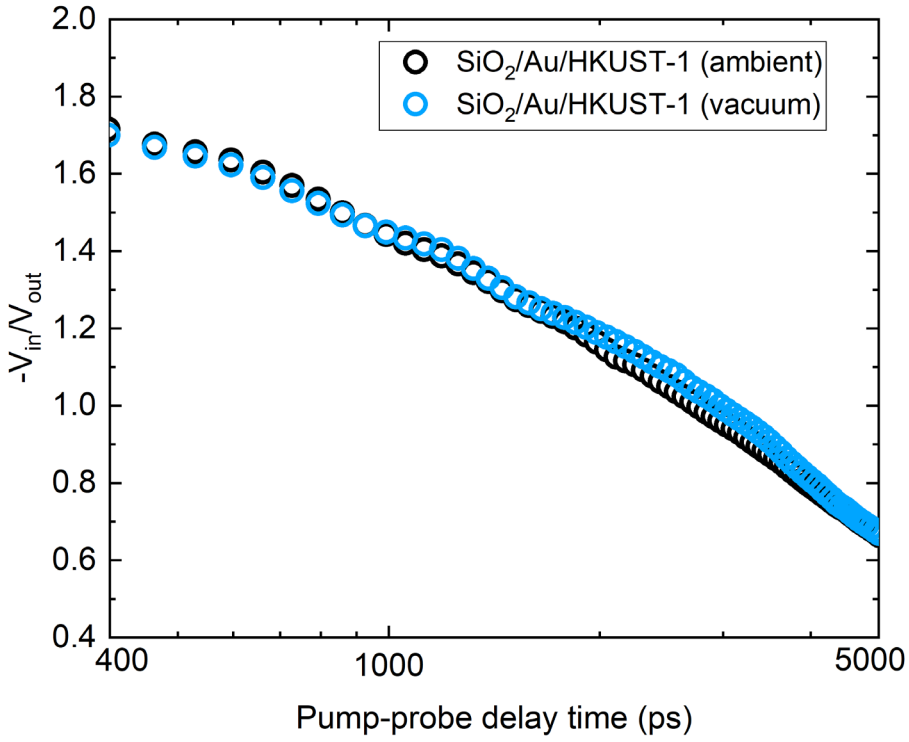


Figure 3.6: TDTR data collected on a 400 nm HKUST-1 sample within three hours of activation in an ambient environment and under vacuum (1.4e$^{-6}$ mbar).

vacuum at a pressure of 1.64 e$^{-6}$ mbar (which is sufficient to remove the contribution from air[18]). The data overlap quite consistently, empirically showing that air in the pores has a negligible contribution, since no change occurs in the measured thermal conductivity (thermal effusivity). This result provides sound evidence that the heat transfer coefficient between the solid and air is insignificant and that the heat transferred to the porous material from the metal transducer occurs only though the solid matrix. Therefore, the thermal effusivity of a porous material measured by TDTR represents the bulk heat capacity of the solid, and the solid matrix of the film (not the effective solid/air medium).[16]

### 3.1.3 Sensitivity and Uncertainty

TDTR data analysis is reliant on the fitting of the thermal model to the raw data output from the lock-in amplifier detection system. A high fidelity TDTR measurement of a certain material parameter is then reliant on how strongly the thermal model depends on the parameter of interest. Specifically, an accurate TDTR measurement occurs in a regime with high sensitivity to the parameter of interest (i.e., thermal conductivity, thermal boundary conductance) and low sensitivity to other parameters in the system that may be measured independently (i.e., pump/probe spot size, transducer thickness, sample thickness) or taken from the literature (e.g., heat capacity). The sensitivity of a TDTR measurement to a parameter of interest *(x),* described by Costescu *et al.*[177] is quantified by

$$S_x = \frac{\partial(^{-V_{in}}/_{V_{out}})}{\partial \ln(x)}. \tag{3.12}$$

A sensitivity analysis was performed on every material system studied in this work in order to tune the TDTR experimental configuration (i.e., spot size modulation frequency) in order to maximize the sensitivity to thermal parameter of interest. In order to elucidate the concept further, I present a distinctive example, relevant to the materials studied in Chapter 5, of a three-layer stack with bidirectional heat flow (Figure 3.5 (b)). In this system, the heat conduction model requires knowledge of the heat capacity, thermal conductivity, and thickness of all of the materials making up the sample stack, as well as the thermal boundary conductance between each layer. An accurate and precise fit of the model to the data requires one (at most two) free fitting parameters, therefore all other variables must be measured externally or obtained through the literature. The thermal conductivity of the transducer is measured by four-point probe and literature values are typically assumed for the heat capacities of the metal transducer and the substrate (typically $SiO_2$).[178] In the case of bi-directional heat transport, the thermal conductivity of the glass substrate and thermal

boundary conductance across the glass/metal interface is measured using TDTR before the solution processed film is deposited. It is extremely important to characterize the metal/glass substrates before the samples are deposited onto them, because the TDTR measurement will be highly sensitive to a large resistance that may occur between the glass/metal interface. The thickness of the metal layer is measured by picosecond acoustics[179] (when appropriate) and profilometry, and the thickness of the films are typically confirmed through SEM. Once the known and unknown parameters are identified, a sensitivity analysis can be performed. Figure 3.7 shows the sensitivity analysis of the TDTR signal to the thermal conductivity and the heat capacity of a 200 nm HKUST-1 metal organic framework sample deposited on both $Au/SiO_2$ and $Al/SiO_2$ substrates at a pump modulation frequency of 8.8 MHz. The figure shows that by careful tuning of experimental parameters (modulation frequency, spot size, and what parts of the TDTR signal I fit the data to ($V_{in}$ vs. $-V_{in}/V_{out}$)), I can take advantage of the TDTR experimental configuration to measure both the thermal conductivity and heat capacity of this particular sample, at a single modulation frequency. Figure 3.7 (a) plots the sensitivity of the heat capacity and thermal conductivity of the material system fit to the in-phase ($V_{in}$) TDTR signal, and Figure 3.7 (c) plots the sensitivity fit to the ratio ($-V_{in}/V_{out}$). In these plots, high sensitivity to a parameter is identified by both the magnitude and the temporal profile. Multiple parameters can be measured with high sensitivity, if they both have relatively high (non-zero) magnitudes and differing temporal profiles.

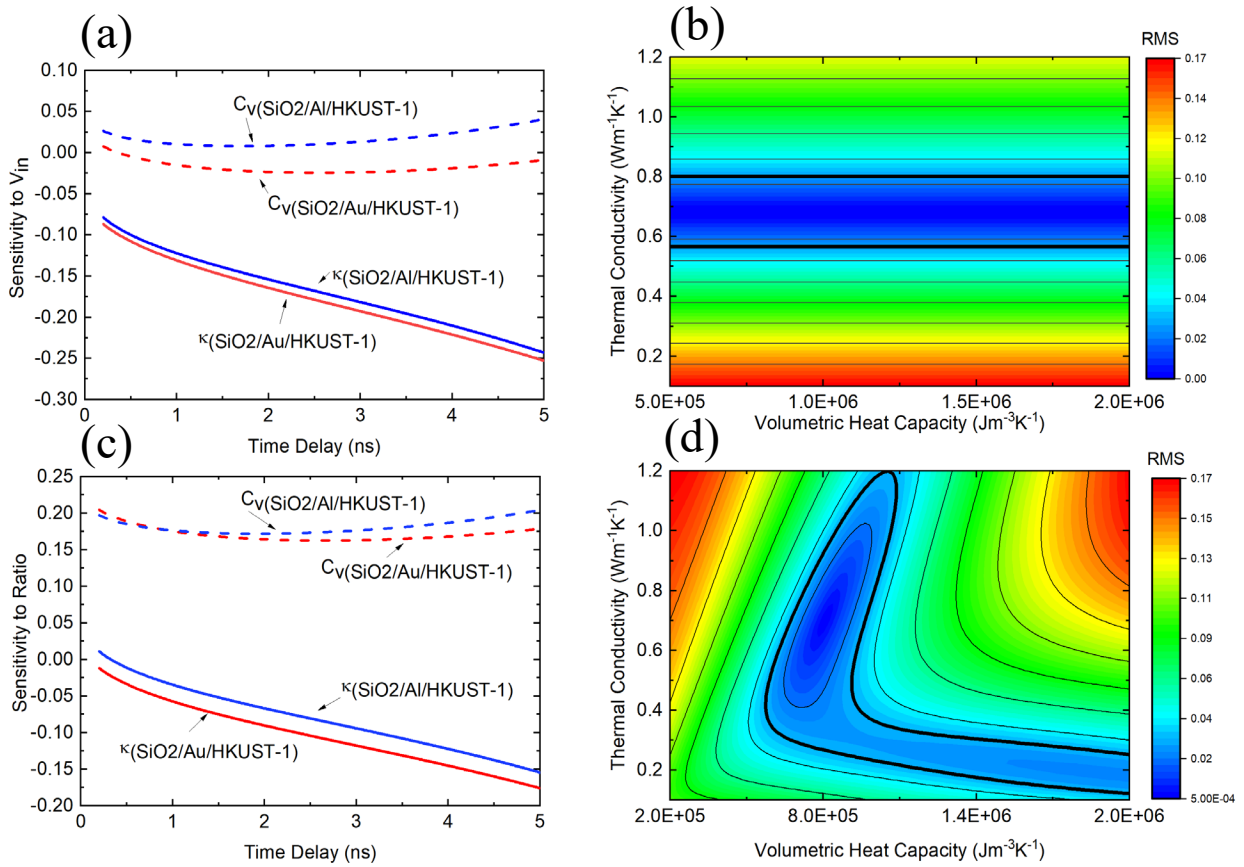


Figure 3.7: Sensitivity plots for the thermal conductivity and heat capacity of a 200 nm pristine metal organic framework deposited on both $Al/SiO_2$ and $Au/SiO_2$ substrates, to the (a) $V_{in}$ (in-phase) component of the TDTR signal, and to the (c) ratio ($-V_{in}/V_{out}$) of the TDTR signal at 8.8 MHz modulation frequency. The contour plots show the residual (the model fit compared to the obtained thermal decay curve described by Eqn. 3.13) for a single TDTR scan fit to (b) the $V_{in}$ and (d) the ratio. The plots show that the $V_{in}$ signal is insensitive to heat capacity. The thick black contour line represents an error of 3% which indicates a 'good' fit of the thermal heat transport model to the TDTR data.

The sensitivity analysis can be developed further by calculating the normalized residuals[180] ($Z$) resulting from the model's fit relative to the obtained thermal decay curve ($r$) for a single TDTR scan, from the relevant material system given perturbations in alternative parameters (such as the thermal conductivity ($\kappa$) and volumetric heat capacity ($C_v$)), via

$$Z = \left(\frac{\sum_{x_o}[r(x_o;\kappa_{exact},C_{v,exact})-r(x_o;\kappa_{perturbed};C_{v,perturbed})]^2}{\sum_{x_o} r(x_o;\kappa_{exact})^2}\right)^{1/2}. \quad (3.13)$$

Figure 3.7 (b) and (d) show the normalized residuals resulting from perturbing the thermal conductivity and volumetric heat capacity to the in-phase and ratio respectively. The contour plots indicate the range of values that would receive a 'good' fit given the value used for the heat capacity or thermal conductivity. The thick black contour line represents a 3% residual error,[43] where all values inside that contour line represent the acceptable range of thermal conductivities based on a single heat capacity value resulting from a good fit of the thermal model to the data. For this particular example, Figure 37 (b) shows that the in-phase component of the signal is insensitive to the heat capacity of the MOF, while Figure 37 (d) shows that the ratio ($-V_{in}/V_{out}$) has sensitivity to both the thermal conductivity and the heat capacity. Therefore, by performing an iteration procedure where the in-phase signal is fit first for the thermal conductivity (since the input value for the heat capacity will not affect the result for the thermal conductivity) and then using the output from that fit as the input to the thermal model that is fit to the ratio for heat capacity, allows for the simultaneous measurement of the thermal conductivity and heat capacity at a single modulation frequency. The ability to measure both the thermal conductivity and heat capacity of a material is extremely important because it validates the accuracy of the thermal model for characterizing the thermal properties of a new material.

A high sensitivity to the measured material parameter ensures accurate and precise measurements of thermal properties of interest. The uncertainty of the TDTR measurement then stems from careful consideration of sources of error within the measurement procedure, and within the sample characterization. To mitigate the propagation of error due to the measurement procedure, we perform daily calibrations on standardized samples of amorphous $SiO_2$, $Al_2O_3$, Si and quartz to ensure proper beam alignment across the optical table and stage. Additionally, I use large pump and probe spot sizes (~10 μm for the probe, and ~20 μm for the pump) and large

modulation frequencies (1-10 MHz), so that slight error in the spot size measurement does not significantly propagate into the reported thermal conductivity measurement. It has been shown previously that spots sizes of this magnitude are large enough that a 20% error in the spot size measurement results in no more than 1% error in the reported thermal conductivity measurements.[181]

The main source of error in the reported TDTR measurements in this dissertation stem from uncertainty in material parameters of the sample itself. Specifically, the uncertainty of the transducer thickness is the most significant, where a 5% error in the transducer thickness propagates to a ~10% error in the thermal conductivity. To bound this uncertainty, the thickness of each transducer layer is quantified by either picosecond acoustics[182] or profilometry , which produce accurate thicknesses to within ± 3 nm for an 80 nm thick transducer layer. The error bars reported for each TDTR measurement reported in this work are therefore representative of the ± 3 nm of uncertainty in the transducer layer thickness. Additional contributions to the measurement uncertainty stem from scan-to-scan variability from multiple TDTR scans taken at different locations on a single sample, and also repeat measurements at the same spatial location. The uncertainties reported in this dissertation represent the root sum of squares of three to seven TDTR scans that were both repeated at as single spot and rastered over sample surface. It is important to note that the samples studied in Chapters 4 and 5 both have a tendency to degrade in ambient conditions, due to oxidation and hydration respectively, and therefore exhibited different levels of quality depending on their variable storage conditions.

## 3.2 Pump-Probe Brillouin Scattering

### 3.2.1 Background and Data Analysis

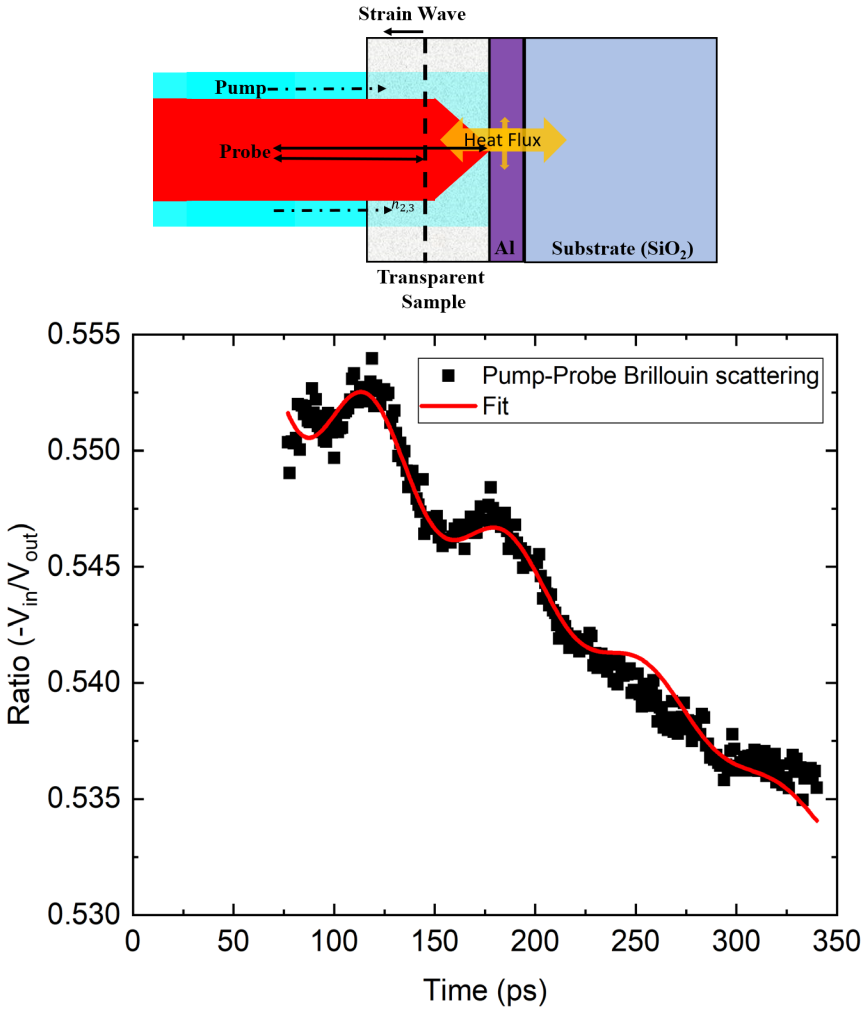


Figure 3.8: (top) The sample geometry needed for pump-probe Brillouin scattering measurements. (bottom) Example data of pump-probe Brillouin scattering data and fit (Eqn. 31).

Brillouin scattering is a mature, antiquated technique that has been commonly used to study the velocity and attenuating response of acoustic waves in both solids and liquids.[183–186] The picosecond temporal resolution of TDTR creates a unique opportunity to perform pump-probe Brillouin scattering measurements on thin transparent films to measure the elastic constants, which can be related to the thermal conductivity of materials as previously discussed (Chapter 2.2).[187]

This method has been used to study phonons in the Brillouin frequency range, where the specific phonon frequency ($v$) that is monitored is given by Thomsen *et al*.[188] as

$$v = (\frac{2nv_g}{\lambda_o}) \sin(\frac{\psi}{2}), \tag{3.14}$$

where $n$ is the refractive index of the transparent sample material, $\psi$ is the scattering angle, $\lambda_o$ is the wavelength of the probe, and $v_g$ is the sound velocity of the transparent sample material. The phonon frequency probed in this work is ~10 GHz.

Pump-probe Brillouin scattering measurements are achieved through a slightly different sample geometry as compared to a traditional TDTR measurement. Specifically, the sample is flipped around so that the pump/probe beams pass through the sample first before depositing their energy into the metal transducer layer. This requires that the sample must be at least partially transparent to the optical pulse wavelengths. In this geometry the deposition of energy by the pump into the transducer creates an ultrafast temperature rise that leads to rapid thermal expansion of the Al transducer layer, resulting in a coherent acoustic wave traveling into the materials in contact. This coherent acoustic wave causes a subtle change in the refractive index associated with the pressure gradient that it creates as it propagates through the media, reflecting off of any interfaces it encounters. The probe then detects both the temperature rise created by the ultrafast laser heating, and the strain wave produced in the sample in the form of coherent lattice motion.[189] Specifically, the probe beam monitors the change in reflection due to the constructive and destructive interference between the pressure gradient wave front associated with the acoustic wave propagation and the thermo-reflection. The constructive and destructive interference leads to periodic oscillations in the temporal reflected signal, whose intensity can be described via

$$I(t, T_w) = A * \exp(-\Gamma t) * \cos\left(\left(\frac{2\pi}{T_w}\right) t - \delta\right) - B * \exp\left(-\frac{t}{\tau}\right), \quad (3.15)$$

where A, B, and $\delta$ are scaling factors, Γ is the damping term for the acoustic wave front due to the energy dissipation, and $T_w$ is the period of the pressure front. The first term of the equation describes the damping of the acoustic wave front, the second term captures the period of the pressure front, and the third term in the equation ($\exp\left(-\frac{t}{\tau}\right)$) is the thermal decay associated with traditional thermoreflectance at the surface of the metal transducer. An example of pump-probe Brillouin scatting data compared to the fit described by Eqn. 3.15 is shown in Figure 3.8. At normal incidence, the inverse of the period (or frequency, $f$) can be related to the sound speed of the partially transparent material via,

$$\frac{1}{T_w} = f = \frac{2n v_g}{\lambda_o}, \quad (3.16)$$

where $n$ is the index of refraction, $\lambda_o$ is the wavelength of the probe, and $v_g$ is the velocity of the coherent wave-front (or group velocity). The bulk modulus ($B$) is then related to the group velocity ($v_g{}^2$) and density of the film ($\rho$) by,

$$B = v_g{}^2 \rho. \quad (3.17)$$

In short, pump-probe Brillouin scattering measurements allow for the indirect measurements of mechanical properties of thin films (as long as the material is somewhat transparent to the pump/probe wavelength(s)).[164] These mechanical properties are directly related to thermal conductivity as described previously in Chapter 2.2.

### 3.2.2 Uncertainty

In general, the uncertainties for pump-probe Brillouin scattering measurements can be quite large, due to an intrinsically low SNR that leads to a high variance in the measurement.

For the pump-probe measurements taken here, at a modulation frequency of ~10 MHz, the fluctuations in signal of the lock-in amplifier response when the pump probe is blocked is on the order of ~0.2 μV for the in-phase and out-of-phase signals. An incident pump beam of a nominal power of ~15 mW (power levels must be low to reduce damaging the sample) on the sample generates a signal level of ~3 μV for both the in-phase and out-of-phase signals at a +1 ps time delay. Note that the true signal is dependent on the sample properties (thickness, opacity, thermal conductivity, etc.), and the pump powers that will vary from sample to sample. The majority of the signal comes from the thermal background, therefore subtracting this contribution (i.e., the third term in Eqn. 3.15) leaves a small signal of ~0.08 μV that contains components of the period of the pressure front, which is the parameter under investigation. Therefore, the SNR for the pump-probe Brillouin scattering is approximately 0.4 (assuming a noise floor of ± 0.1 μV), which is quite small compared to the SNR for TDTR that is typically better than 100-150.

The low SNR contributes to a high variance in the measurements where the uncertainty is then quantified using standardized error analysis methodologies founded on statistical parameters that describe the measurement in the context of its associated noise.[190] First, the sample mean is calculated from multiple measurements ($n$) as

$$\overline{T_w} = \frac{1}{n}\sum_{k=1}^{n} T_{w,k}, \tag{3.18}$$

and the standard deviation of the mean is defined as

$$\sigma_{\overline{T_w}} = \frac{1}{n-1}\sum_{k=1}^{n}(T_{w,k} - \overline{T_w})^2, \tag{3.19}$$

so that experimental results are expressed as

$$\overline{T_w} \pm \sigma_{\overline{T_w}}. \tag{3.20}$$

Added uncertainty from the index of refraction and the material density, that were obtained through the literature, combine linearly in Eqns. 3.18 - 3.19, and serve to increase the total error quadratically.[190] In total, the low SNR which leads to high scan-to-scan variability, combined with uncertainty in the index of refraction and density of the film results in approximately 80% uncertainty for the elastic modulus measurements obtained through pump-probe Brillouin scattering measurements reported in this work.

## 3.3 Summary

In this chapter, I provided an overview of the experimental techniques used to measure the thermal and mechanical properties of thin films studied in this dissertation. This chapter contains an overview of sample geometry considerations and measurement uncertainties in our TDTR measurement. Here, we see how a single pump-probe thermometry technique can be configured to measure both the thermal and mechanical properties of a sample via TDTR and pump-probe Brillouin scattering, respectively.

# Chapter 4

## 4. Composition and Morphology Effects on Thermal Conductivity of Nanostructured Chalcogenide Material

Parts of Chapter 4 were published in *Advanced Functional Materials, (2019) 1904073* DOI: 10.1002/adfm.201904073

### 4.1 Motivation

The overarching theme of this dissertation is to develop an enhanced understand the role of intentional compositional and morphological disorder (including for example: secondary phases, defects, nano-precipitates, and adsorbates) on the thermal transport properties of nano materials. In this chapter, I examine the effects of engineered disorder in the form of point defects, nano-precipitates, internal interfaces and grain boundaries in chalcogenides. Nanostructured chalcogenides are pursued for their thermoelectric applications through enhancements to the power factor ($S^2\sigma$) with simultaneous reductions to the contribution of the lattice thermal conductivity.[2,3] Lead selenide (PbSe) and lead telluride (PbTe) are promising semiconducting materials for this application[191] due to their intrinsically high figure of merit (*ZT*). Therefore, significant efforts have focused on improving the thermoelectric properties of bulk and nanostructured PbTe- and PbSe-based materials.[192–196] An improved Seebeck effect has been measured in atomic layer deposition (ALD) grown lead-rich n-type PbTe/PbSe nanolaminates in both the cross and in-plane directions, which was attributed to changes in the electronic density of states from the nanostructuring and off-stoichiometry.[197] Additionally, first-principles calculations have shown that nanostructures separated by less than ~20 nm could favorably scatter phonons within pure PbSe and PbTe.[198] Taken together, nanostructuring and chemical modification to PbSe- and PbTe-based films with defect and interface length scales less than or on the order of a few 10's of nanometers may

therefore present an opportunity for enhanced thermoelectric performance. This hypothesis is assessed through a detailed experimental study of the phonon scattering mechanisms and thermal transport properties of a series of ALD grown PbTe-PbSe nanostructured thin films.

Here, I examine the impact of limiting length scales on phonon heat transport mechanisms within thermoelectric PbTe-PbSe nano systems. I study the thermal transport processes in a series of ALD deposited, Pb-rich, PbTe-PbSe nanostructured thin films. The ALD method of growth allows for layering during deposition that results in polycrystalline thin films with laminate and alloy features throughout the film thickness.[197] The various nanostructures (grain boundaries, PbTe-PbSe layering, and compositional defects) result in thermal conductivities of these polycrystalline films that follow disorder-like trends in their thermal conductivities, which are preferential for thermoelectric applications. These low phonon thermal conductivities are attributed to the various point and planar defects that are inherent to the growth of these ALD-grown films.

It is well known that nanostructuring in thin films and superlattices (SL's) at a few to 10's of nanometer length scales can significantly reduce thermal conductivity relative to their bulk counterparts.[5–7,199–205] This is consistent with other phonon dominated systems where size effects emerge at the microscale.[9,206–211] Electron dominated systems, in contrast, are more often unaffected by size until limited at the nanometer scale.[10,209,212] Generally, in systems where the average mean free path of phonons is longer than the limiting dimension of the sample, the heat transport fails to follow Fourier's law and can instead be described by semi-ballistic phonon transport (Figure 2.1); in this regime, the wave nature of phonons can appear, possibly preserving coherence.[11,201,213–215]

The interplay of quantum size effects from coherent transport (where a reduced Brillouin zone introduces phonon band gaps that reduce the phonon group velocity and the phonon scattering phase space) and incoherent size effects (where phonons scatter diffusively at internal interfaces) has been extensively studied in many material systems including: Si/Ge, GaAs/AlAs, BiTe/SbTe, and SrTiO3/CaTiO3 superlattices.[5,29,201,214–216] In these systems, the periodicity of the superlattice is thought to affect the thermal conductivity in one of two ways: i) it creates well defined internal boundaries that increases phonon boundary scattering (i.e., incoherent) or ii) the phonons see the periodicity of the SL as a new material resulting in a modified phonon dispersion (i.e., coherent).[31,213–215] The thermal conductivity trends in periodicity and film thickness can be indicators of coherent-phonon transport impacting thermal transport. This is because there are many characteristic lengths that are involved in describing the wide spectrum of phonon wave packets responsible for phonon transport (i.e. the spatial coherence length, the associated wavelength of the normal mode, the mean free path of the wave packet in the material and characteristic lengths defined by the material (length)).[31] For example, if periodic interfaces within a material destroy phonon coherence by diffusively scattering phonons (Casimir picture), the thermal conductivity is then expected to be independent of the number of periods and coherent interference effects can be ignored so that the material can be treated as a composite. However, when phonon transport is coherent, the material should be treated as one homogeneous material and interference effects then contribute to modification of the phonon dispersion.[215] In the case of this study, we find that while the thickness dependent trends in the PbTe-PbSe samples' thermal conductivities are similar to those found in alloys and SL's dominated by long wavelengths, possible coherent phonon transport,[201,202,215,217] my samples' thermal conductivity thickness trends

are dictated by spatially varying defect densities, where thicker films result in higher quality samples.

In this work, I report on the cross plane thermal conductivity of PbTe-PbSe nanostructured, polycrystalline thin films. I measure the thermal conductivity over a range of temperatures using TDTR; with a combination of atomic force microscopy (AFM), scanning electron microscopy (SEM), transmission electron microscopy (TEM), x-ray diffraction (XRD), energy dispersive x-ray (EDS) spectroscopy, and Raman spectroscopy, the results show that the phonon thermal transport processes in these ALD-grown films are determined by: i) thickness varying crystalline quality, where structural defect densities increase in thinner films due to the ALD growth mode of these materials; ii) point defects inherent in the ALD growth process (e.g., oxygen defects); and iii) compositional-driven defects, such as point defects and phase boundaries between the PbTe and PbSe. The full details of this work have been published in *Advanced Functional Materials*.[146]

## 4.2 Experimental Detail and Sample Characterization

Collaborators at Old Dominion University (ODU) fabricated a series of ALD PbTe-PbSe control and nanocomposite samples, where they controlled for the film thickness, composition, stoichiometry, uniformity and conformity of the multilayers. ALD conditions were optimized during the fabrication of the nanocomposites to promote the creation of internal interfaces between layers (corroborated by HR-TEM). The samples that were fabricated are shown in Table 4.1, where the targeted layer thickness (*d*) represents the total thickness of the smallest repeating unit within the film (i.e., layer thickness of 20 nm corresponds to 10 nm of PbTe followed by 10 nm of PbSe).

The fabricated films were characterized using a multitude of techniques including: field emission scanning electron microscopy (FE-SEM), atomic force microscopy (AFM), transmission electron microscopy (TEM), X-ray diffraction (XRD), energy-dispersive X-ray spectroscopy (EDS) and Raman spectroscopy to understand the crystallinity, composition, microstructure, and morphology of the samples and get better insight into the defects and phases that are produced in the ALD growth. The following section provides a snap shot of the findings from the characterization techniques while also pointing out conclusions in qualitative trends that are corroborated by multiple techniques. A full description can be found in the Supporting Information in the published manuscript.[60] Taken in total, the characterization indicates that the nanocomposite films are highly disordered in both crystallinity and composition, where the disorder scales with the total thickness due to the ALD growth mode.

Table 4.1: ALD grown PbTe and PbSe control films and PbTe-PbSe nanocomposites, with targeted multilayers thickness (*d*) of PbTe and PbSe set to 4 nm (2 nm PbTe followed by 2 nm PbSe), 12, and 20 nm.

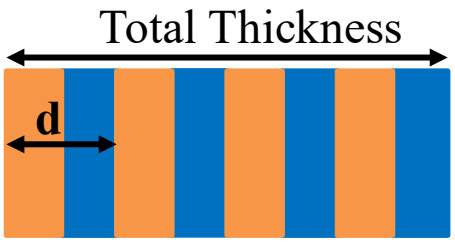


| Material | Targeted repeat layer thickness during growth (*d*) [nm] | Total Thickness [nm] | Thickness Std. Dev. [nm] | Thermal Conductivity [$Wm^{-1}K^{-1}$] |
|---|---|---|---|---|
| **Control** | | | | |
| PbSe | - | 127 | - | 2.32 ± 0.10 |
| PbSe | - | 96 | - | 2.40 ± 0.09 |
| PbSe | - | 60 | - | 2.24 ± 0.17 |
| PbSe | - | 25 | - | 2.53 ± 0.28 |
| PbTe | - | 105 | 12 | 1.25 ± 0.36 |
| PbTe | - | 77 | 1 | 1.28 ± 0.06 |
| PbTe | - | 33 | 7 | 0.79 ± 0.35 |
| PbTe | - | 25 | 6 | 0.97 ± 0.11 |
| **Nanocomposite** | | | | |
| PbTe-PbSe | 20 | 121 | 21 | 1.05 ± 0.37 |
| PbTe-PbSe | 20 | 135 | 11 | 1.03 ± 0.09 |
| PbTe-PbSe | 12 | 196 | 6 | 1.31 ± 0.08 |
| PbTe-PbSe | 12 | 188 | 15 | 1.05 ± 0.10 |
| PbTe-PbSe | 12 | 73 | 15 | 0.74 ± 0.29 |
| PbTe-PbSe | 12 | 60 | 15 | 0.77 ± 0.28 |
| PbTe-PbSe | 12 | 26 | 1 | 0.45 ± 0.06 |
| PbTe-PbSe | 4 | 243 | 28 | 1.32 ± 0.07 |
| PbTe-PbSe | 4 | 226 | 26 | 1.26 ± 0.15 |

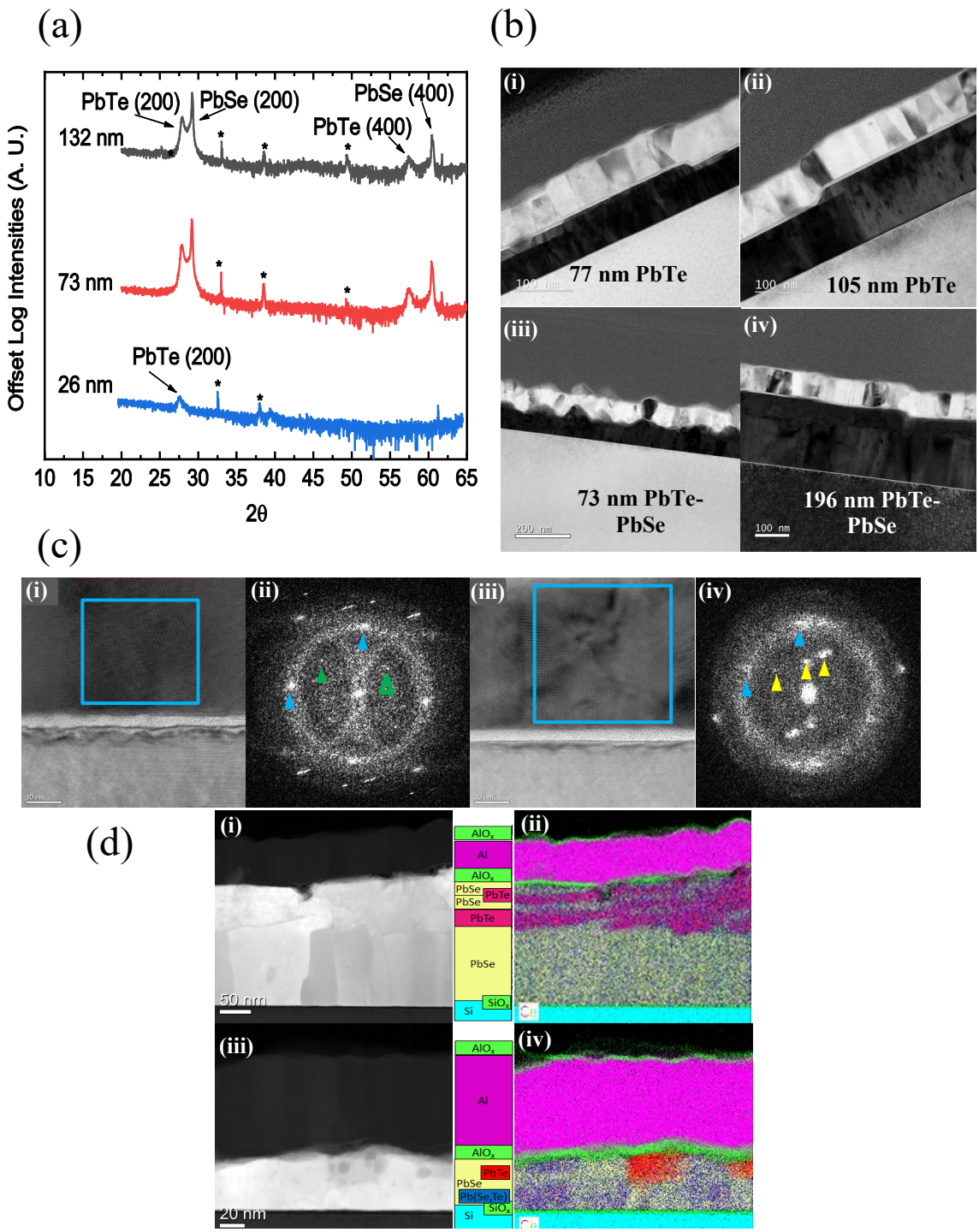


Figure 4.1: (a) X-ray Diffraction (XRD) of the PbTe-PbSe nanocomposite samples for different total thicknesses. The additional peaks in the spectra labeled by stars are indicative of secondary lead oxide phases. Note the 26 nm sample only has a clear peak for the PbTe phase and not the PbSe, and the peaks are non-existent due to the reduction in the measurement volume. (b) HR-TEM data for (i) 77 nm PbTe with an average grain size of 143 nm ± 31 nm; (ii) 105 nm PbTe with an average grain size of 193 nm ± 64nm; (iii) 73nm PbTe-PbSe nanocomposite with an average grain size ≤100 nm; and (iv) 196 nm PbTe-PbSe with and average grain size ≥150 nm. (c)

(i) HR-TEM and (ii) FFT from the 188 nm PbTe-PbSe film section of the HR-TEM that shows inter planar spacings of 0.309 (blue arrows), 0.432 (solid green arrow) and 0.552 (hollow green arrow) nm. The 0.309 and 0.432 nm spacing relate to the 002 and 011 planes of PbSe. (iii) HR-TEM and (iv) FFT from the 55 nm PbTe-PbSe film that shows inter planar spacings of 0.312 nm (blue arrows), which is in between the 002 spacing of PbSe and PbTe. Reciprocal space peaks indicated by yellow arrows result from Moiré fringes. No superlattice periodicities were observed in either FFT. The blue squares show the area in which the FFT was taken. (d) EDS data for (i)(ii) 188 nm thick and (iii)(iv) 60 nm thick PbTe-PbSe films, where (i)(iii) show the EDS HAADF cross sectional image, (ii)(iv) show the distribution of Al (pink), O (green), Te (red), Se (yellow), Pb (blue), and Si (aqua). We include a schematic to the left of each EDS image to further exemplify the morphology of the samples, where we see two wavelengths of layering at the top of the 188 nm sample, while the 60 nm sample exhibits a granular structure.

Figure 4.1 shows the XRD, TEM (and corresponding FFT image analysis), and EDS data for a thin and thick PbTe-PbSe nanocomposite. In Figure 4.1 (a), the XRD data are plotted as a function of total thickness and show evidence of peak broadening as the total thickness is reduced, corresponding to a reduction in film quality. Since peak broadening in XRD can be due to three mechanisms – broadening that is intrinsic to the XRD instrument, contributions from inhomogeneous strain, and the size of the ordered crystalline domains – I carry out a Williamson-Hall analysis to more fully understand the peak broadening as a function of compositional repeat layer (*d*) and total thickness. The results plotted in Figure 4.2 qualitatively show that the domain sizes for the PbTe layers increase with *d*, while the approximate domain size for the PbSe layers remain relatively constant, reaching saturation early. Interestingly, we also see this same trend as function of total thickness. In the nanocomposites with the smallest compositional repeat thickness (4 nm), the PbTe domain size is reduced by nearly 80 % compared to the largest period thickness. In addition to broadening, the XRD data indicate the presence of polycrystalline PbTe and PbSe in the PbTe-PbSe nanocomposites, where the growth direction is predominantly along the <200> crystallographic direction (Figure 4.1 (a)) as indicated by the predominance of this peak, where the large linewidths are indicative of poly- rather than single crystallinity.

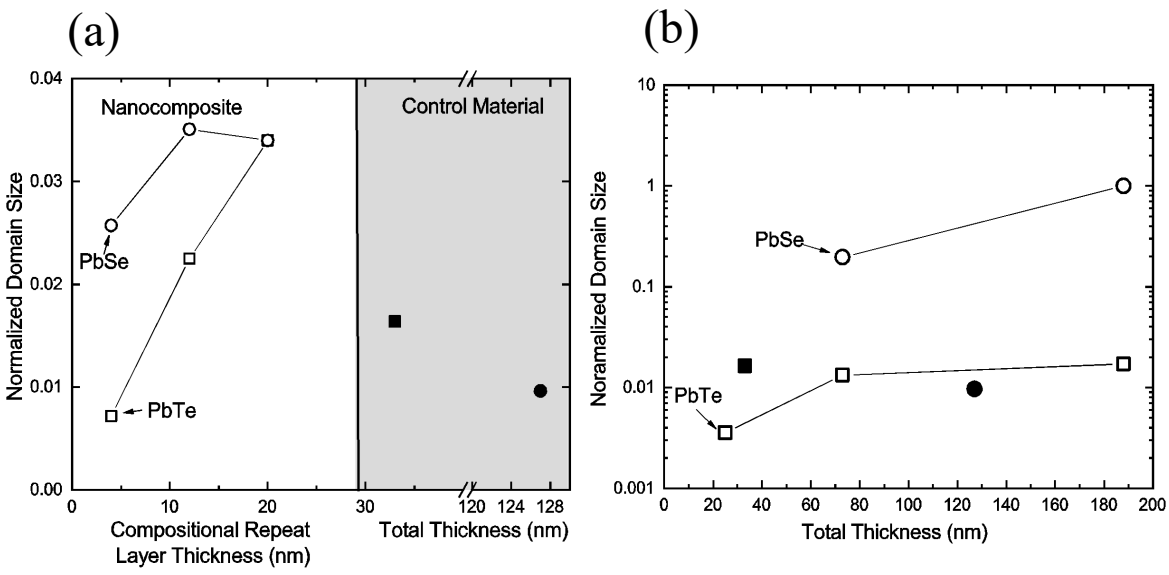


Figure 4.2: The results for the Williamson-Hall analysis applied to the XRD for the nanocomposite samples. (a) Shows the resulting normalized domain sizes for the samples as a function of compositional repeat layer thickness (*d*). The results from the PbTe (solid square) and PbSe (solid circle) are shown in the shaded region for reference. (b) Shows the normalized domain sizes as a function of total thickness, where again the parent material is shown as solid symbols.

Additionally, it is important to elaborate on the role of the lead oxide, the features which are indicated by asterisks, that are present in the XRD in Figure 4.1 (a). Additional characterization by EDS (Figure 4.1 (d) and Figure 4.3) show the presence of $PbO_x$ both at the front and backside surfaces and within the films. The EDS data in Figure 4.3 shows that the Pb is distributed homogeneously throughout the film (except for the Se rich grain in the thin sample), but the Se and Te are not in a periodic pattern. The $PbO_x$ stoichiometries that are internal to the material will play a large role, acting as point defects to scatter phonons and reduce the thermal conductivity of the films. The resolution of the EDS makes it hard to confirm if a periodic nanocomposite structure truly is present, therefore we rely on the FFT of the TEM to investigate any periodicity. Figure 4.1 (b) shows high resolution TEM of a thick and thin PbTe control film and nanocomposite, where the oriented grains are clearly visible. Indexing of the inter planar spacings of the FFT of the HR-TEM in Figure 4.1 (c) shows the resulting interplanar spacing and

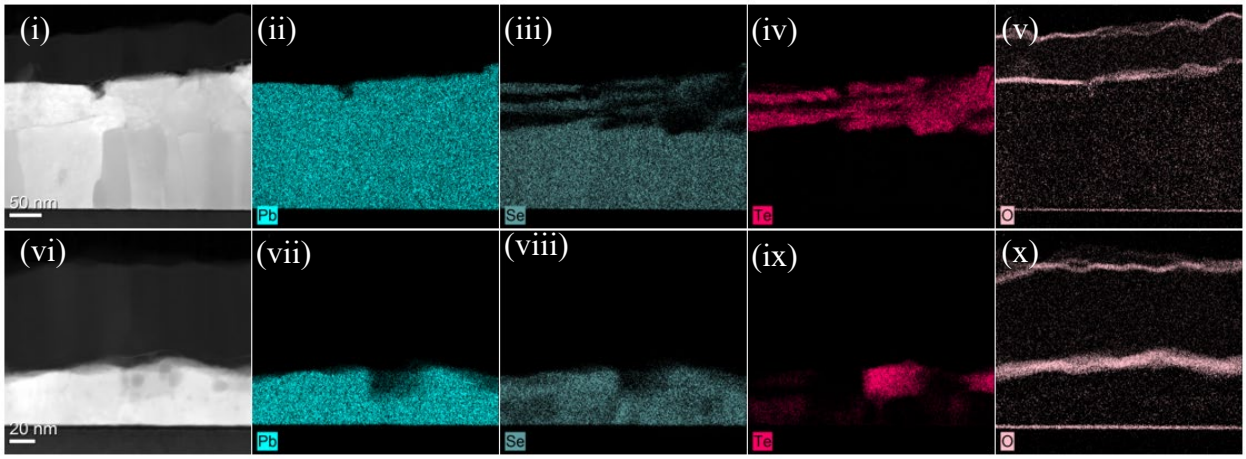


Figure 4.3: EDS data for (top panels) 188 nm thick and (bottom panels) 60 nm thick PbTe-PbSe films, where (i)(vi) show the EDS HAADF cross sectional image, (ii)(vii) show the distribution of Pb species, (iii)(viii) show the distribution of Se species, (iv)(ix) show the Te species and (v)(x) show the oxygen species which act as point defects in the films.

indicates that no nanocomposite periodicities with length scales on the order of the target layering length scales during growth (Table 4.1) are observed. Therefore, the ALD growth does not result in superlattice periodicities in either sample. Together, the TEM and EDS illuminate the morphology of the Pb, Te, Se and O within the films and show evidence of nanocomposite grains of PbTe and PbSe within both films, with some rough periodic layering occurring in the thicker sample.

HR-TEM micrographs shown in Figure 4.4, depicting the cross sections of the ALD synthesized nanocomposites, corroborate the polycrystallinity shown by the XRD. Additionally, the apparent columnar morphology in the thin films is indicative of Volmer-Weber growth, where the grains from individual islands have conglomerated to form a cohesive film. Volmer-Weber growth induces roughness into the nanocomposite interfaces, as measured by EDS, and HR-TEM (Figure 4.3-Figure 4.4). Typically, the surface roughness of a polycrystalline film is not constant, but instead is a function of the film thickness and increases with grain growth as the film grows.

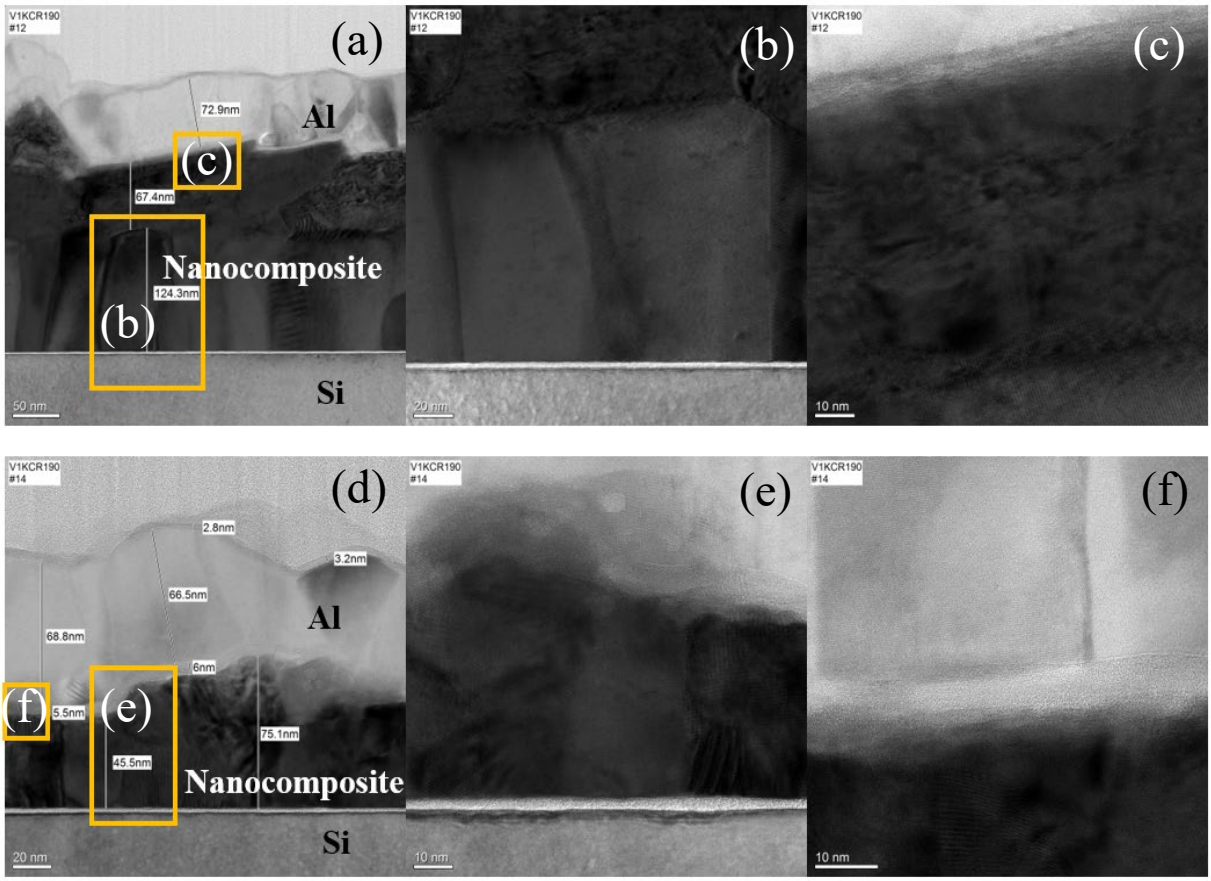


Figure 4.4: TEM data for (Top) 188 nm nanocomposite. The square boxes in (a) are indicative of the zoomed in areas that are shown in (b) and (c). TEM data for (bottom) 60 nm nanocomposite where the square boxes in (d) are indicative of the zoomed in areas shown in (e) and (f).

AFM measurements of the PbTe-PbSe nanocomposite structure grown at 150ºC on a planar Si substrate with a total thickness of 121 nm found an 11.4 nm RMS surface roughness, which is significant for ALD, and is expected to scale with thickness during Volmer-Weber growth. Beyond inducing roughness, Volmer-Weber growth also creates numerous grains and grain boundaries with preferred columnar orientations that run perpendicular to the internal interfaces, as shown in detail by the TEM cross-sectional image in Figure 4.4.

Raman spectra for thick and thin parent materials and accompanying nanocomposites of varying thicknesses are displayed in Figure 4.5. Spectra are scaled to allow for comparison. In some cases, the background signal originating from the 2$^{nd}$ order acoustic overtones of Si has been

removed via subtraction.[218] Mode positions are consistent with expectation for the films.[219] The linewidths of the peaks vary significantly depending on total film thickness for both the PbTe control films and the nanocomposites whereas no substantial change occurs to the PbSe controls. These variations in linewidth with thickness further corroborate the reduction in film quality with reduced thickness that occurs as a consequence of the Volmer-Weber growth. Raman spectroscopy further highlights the reduction in film order with thickness.

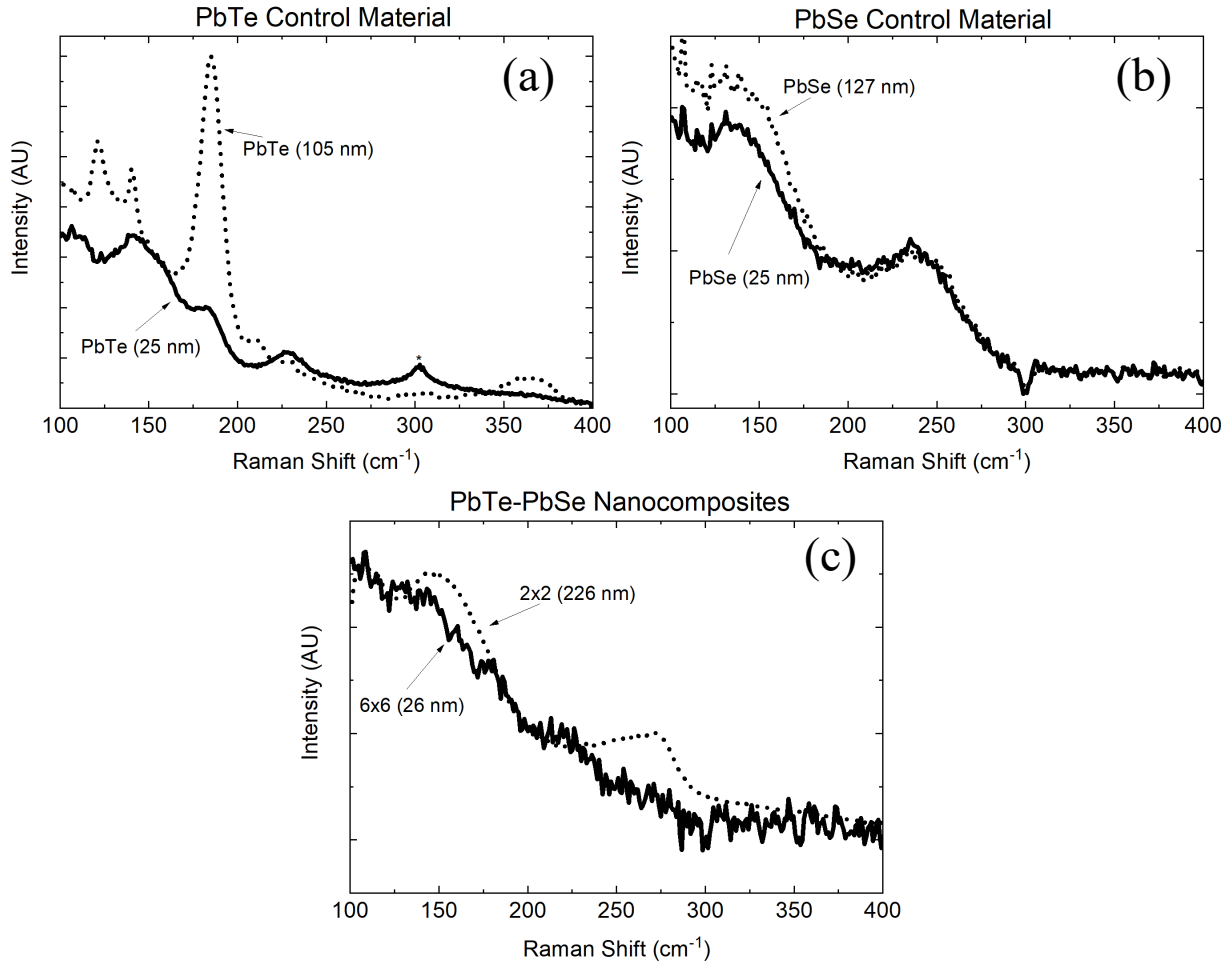


Figure 4.5: Raman spectra of a thin and thick film for: (a) PbTe, (b) PbSe and (c) nanocomposites. Linewidth increases in the thinner PbTe and nanocomposite films owing to increased disorder.

## 4.3 Thermal Conductivity and Phonon Scattering Processes of ALD Grown PbTe-PbSe Thermoelectric Thin Films

### 4.3.1 Results

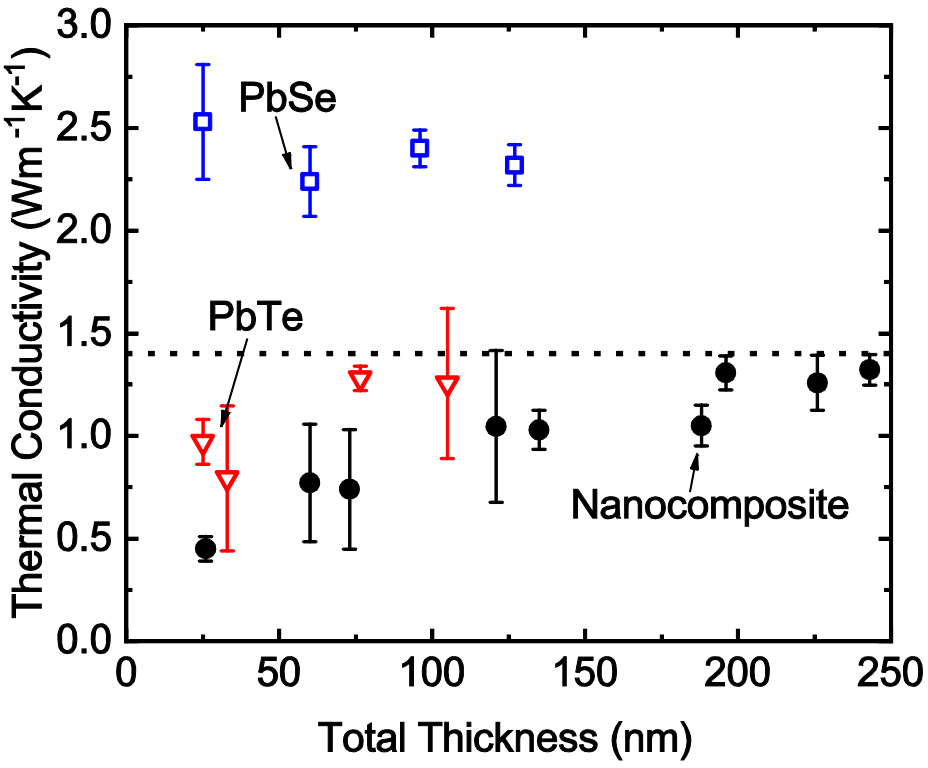


Figure 4.6: Thermal conductivity results for the PbTe (blue squares) and PbSe (red triangles) control and PbTe-PbSe nanocomposite (opaque circles) materials vs total sample thickness. The dotted line represents calculations using Eqn. 4.1 (a series resistor model).

The thermal conductivities of the PbTe-PbSe nanostructured thin films, as well as the control ALD-grown thin films of PbTe and PbSe were measured with TDTR as a function of total thickness and compositional repeat layer thickness ($d$). The samples and thicknesses are listed in Table 4.1, along with the measured thermal conductivities. The thermal conductivities as a function of total film thickness are plotted in Figure 4.6, and as a function of $d$ in Figure 4.7 for the various PbTe-PbSe thin films. Note that the error bars reported with each experimental measurement consist of the propagation of ± 3 nm of uncertainty in the thickness of the transducer

layer, as well as scan-to-scan variability from an average of five TDTR scans that were spatially rastered across the sample surface. Differences in the magnitude of the reported uncertainty from sample to sample is related to differences in the sample quality achieved during fabrication, where inspection of the characterization data indicate that individual samples display different levels of compositional and morphological heterogeneity (Section 4.2). As previously mentioned, there is no evidence of consistent superlattice-like layering in the ALD-grown samples, however, compositional segregation and heterogeneity on the order of 10's of nanometers is observed, along with grain boundaries on this length scale. Figure 4.6 shows that the thermal conductivities of these PbTe-PbSe films increase with total film thickness, which is discussed in more detail below. Additionally, Figure 4.7 shows no apparent trend in target PbTe/PbSe layer thicknesses (*d*), which is most likely due to the diffusive spatial gradation of the chemical composition between the two nanolaminate compounds. Note, period independence in the thermal conductivity of PbTe/PbSe superlattices has been observed previously in MBE-grown $(PbTe)_{1-x}/(PbSe)_x$ nanodot superlattices (NDSLs) over a wide range of periods from 5 – 50 nm.[220] This periodic independence was partially ascribed to the fact that the nanodot layers in these aforementioned NDSLs did not form well defined layers. This is consistent with our current ALD-grown samples, and the lack of observable superlattice-like layering in our films.

In general, the thermal conductivities of the nanostructured films are lower than those of the control thin films. The control PbSe films do not exhibit size effects, while the PbTe controls seem to experience size effects over the thickness range studied (a 40% increase in thermal conductivity when the film increases from 25 to 120 nm). This reduction is not a traditional size effect (increased boundary scattering), but due to the thickness-varying structural defects that occur during ALD growth of the PbTe layer. My thermal conductivity results suggest that this

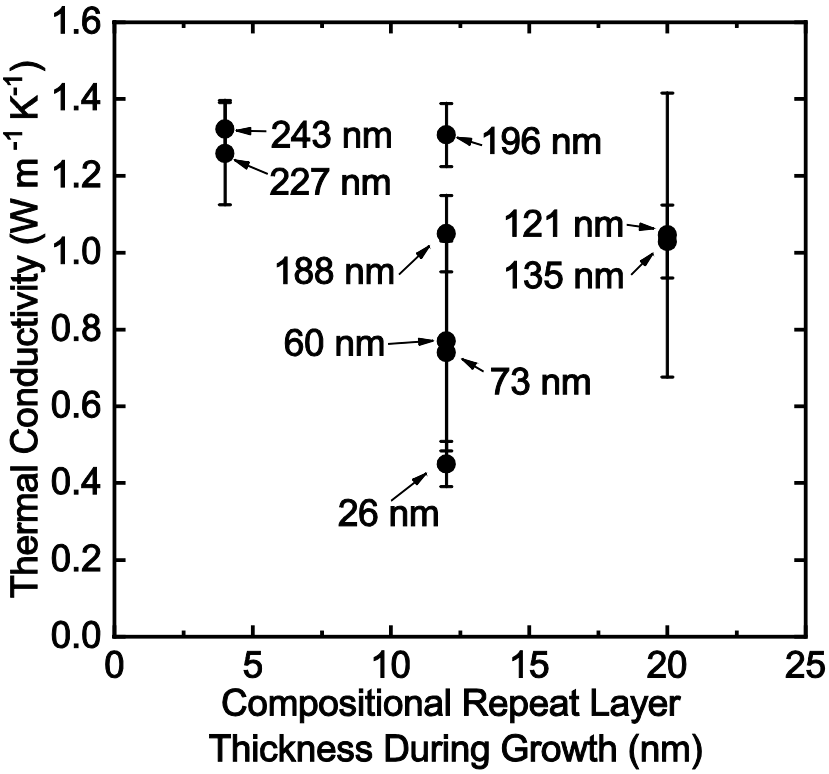


Figure 4.7: Thermal conductivity results for the PbTe-PbSe nanocomposite material as a function of the intended compositional repeat layer thickness (*d*) targeted during the ALD growth. The characterization via TEM and EDS does not show any evidence of layering or superlattice-like structures on these length scales in the resulting nanocomposites. The annotations show the total thickness of the sample.

same thickness-varying film quality is not occurring in the PbSe layers. Additionally, the thermal conductivities of the thick PbTe-PbSe nanostructured films (≥ 121 nm) are relatively constant with total thickness, but still show a reduction in thermal conductivity compared to the control films. Increased phonon scattering due to varying compositional point defects (i.e., Te and Se) and compositional phase boundaries between the PbTe and PbSe (or other planar defects originating from the compositional variation, like dislocations) is likely contributing to the relatively reduced thermal conductivity of the nanostructured films in this thickness regime (c.f., TEM and EDS analysis in Figure 4.1), where film quality has been maximized. However, in the thin film regime, the Volmer-Weber growth occurring during the ALD fabrication, plays a major role in further reducing the thermal conductivity of the nanostructured films as the sample thickness is reduced

and concomitantly the sample quality is degraded. Thus, the reduction in thermal conductivity of the nanostructured thin films compared to the parent materials is due to compositional effects (point and planar defects driven by the spatially varying chemical composition). The film thickness dependent thermal conductivity of the nanostructured film and PbTe control film is driven by an increase in microstructural quality with increased film thickness.

First principles calculations have shown that a large portion of heat conducted in PbTe and PbSe is carried by phonons with a distribution of mean free paths that are ≤10 nm.[198,221] If these phonons scatter diffusively at the compositional phase boundaries in the nanostructured films (as suggested by the lack of trend in thermal conductivity vs. target layer thickness during growth, shown in Figure 4.7), then the dominant heat transport picture can be described by a coherence length and mean free path that are smaller than the period thickness.[222] Assuming relatively negligible thermal boundary resistances at the compositional interfaces, the thermal conductivity of the nanostructured films would be a weighted average of the thermal resistivities of the two parent materials represented as a series resistor analog according to[29]

$$\frac{1}{\kappa_{nanostructure}} = \frac{1}{d_1+d_2}\left(\frac{d_1}{\kappa_1}+\frac{d_2}{\kappa_2}\right), \tag{4.1}$$

where, $d_1$ and $d_2$ are the thicknesses of the parent materials and $\kappa_1$ and $\kappa_2$ are the thermal conductivities of the respective parent materials. I take the intrinsic thermal conductivities of the parent material to be the values measured for the thinnest samples (25 nm), and plot the result of Eqn. 4.1 in Figure 4.6 as a dotted line. This model sets the upper bound on the thermal conductivity of a theoretical PbTe/PbSe superlattice with a period thickness of 50 nm, when boundary and defect scattering are not playing a role. The reduction of thermal conductivity below this threshold suggests that additional scattering mechanisms are playing a role in reducing the thermal transport

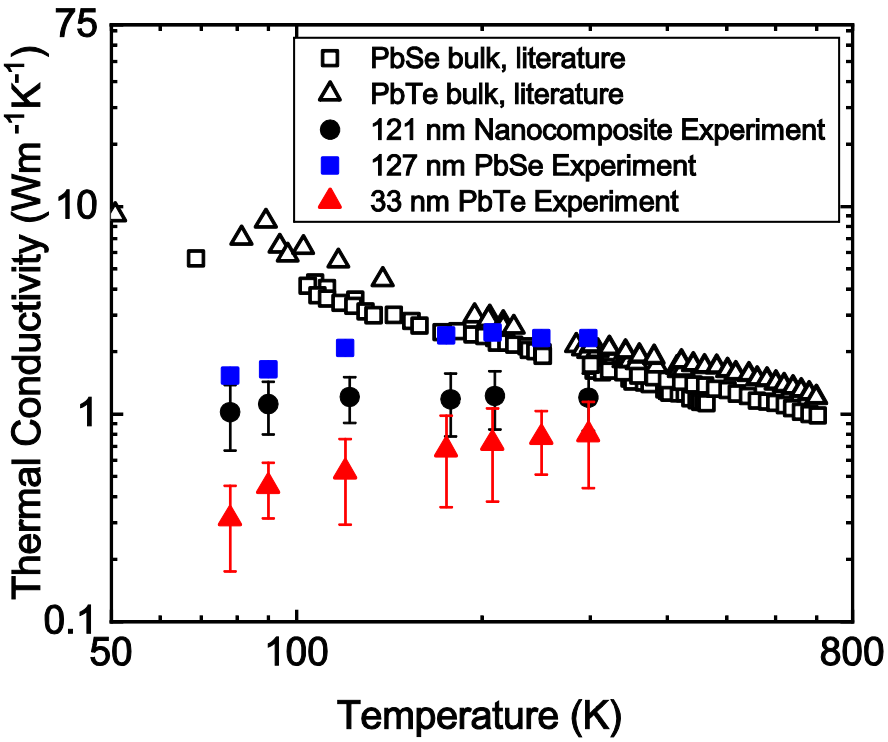


Figure 4.8: Thermal conductivity vs. temperature for PbSe (127 nm sample thickness), PbTe (33 nm sample thickness), and a PbTe-PbSe nanocomposite (121 nm sample thickness) with a 20 nm compositional period thickness. Data collected on bulk samples are taken from the literature for PbSe[223] and PbTe.[224] The temperature-dependent thermal conductivity trends in our ALD-grown samples indicate that the phonon scattering processes are driven by extrinsic defect scattering processes as opposed to phonon-phonon scattering processes intrinsic to the PbTe or PbSe phonon spectra.

below that of the control materials, which are due to the spatially varying compositional variations of PbTe and PbSe leading to both chemical heterogeneity of Se and Te and PbTe/PbSe phase boundaries, as discussed in detail in Section 4.2.

To gain further insight into the phonon scattering mechanisms driving the thermal conductivity in these ALD-grown PbTe-PbSe thermoelectric films, I measured the thermal conductivity of the highest and lowest thermal conductivity control films (127 nm thick PbSe film and 33 nm thick PbTe film – c.f. Figure 4.6 and Table 4.1), and the thermal conductivity of a 121 nm thick PbTe-PbSe nanostructure film as a function of temperature from 77 – 298 K. Figure 4.8 shows the temperature dependent trends of these three ALD grown samples, compared to

experimental data for bulk samples of PbSe[223] and PbTe[224] from literature. The thin film control and nanostructured films show an increase in thermal conductivity with an increase in temperature. This is in contrast to the temperature dependent thermal conductivity of their bulk counterparts, which show a $1/T$ trend that is typical of increased Umklapp scattering in crystalline solids. From our TEM and EDS data previously discussed (Figure 4.1 (c),(d) and Figure 4.3), these thermal conductivity trends are reasonable given the high levels of chemical point defects in the samples (e.g., Pb-O defects in the control and nanostructured samples) and structural defects from the Volmer-Weber growth process. Thus, the phonon scattering and resulting thermal conductivities in these ALD-grown PbTe-PbSe thermoelectric materials are driven by extrinsic defect scattering processes as opposed to phonon-phonon scattering processes intrinsic to the PbTe or PbSe phonon spectra.

From a classical kinetic theory perspective of thermal conductivity, the thermal conductivity trend of the PbTe-PbSe nanocomposite thin films is dominated by the temperature dependent heat capacity term:

$$\kappa = \frac{1}{3}\sum_i C_{v,i} v_i l_i. \tag{4.2}$$

The summation is performed over all the available vibrational modes ($i$), $C_{v,i}$ is the heat capacity, $v_i$ is the group velocity, and $l_i$ is the phonon mean free path. This trend in thermal conductivity implies that three phonon scattering plays a minor role in the thermal conductivity of these films, even in the control materials, since there is no evidence of the temperature dependent thermal conductivity trends expected from phonon-phonon scattering, as previously mentioned. Further, the temperature dependent thermal conductivity trend of the nanostructure film is reduced compared to the PbSe control film with a similar thickness, consistent with a reduction in $l_i$ from

the various additional phonon scattering mechanisms in these nanostructures, as previously discussed.

### 4.3.2 Discussion

Previous works have shown that nanostructuring of PbTe, ranging from artificially designing defects, nano-precipitates, and grain boundaries, is effective to reduce the lattice thermal conductivity.[44] Figure 4.1 summarizes the characterization data to show that the film quality improves with increased total thickness. Further, the HR-TEM data shown in Figure 4.4 show the morphology of the 188 nm and 60 nm nanocomposites, where the internal compositional layers are difficult to see, however the oriented columnar grains of the ALD growth are easily distinguishable. The decrease in grain boundary density with increasing film total thickness plays a key role in the observed thermal trends, due to the effects of decreased defect scattering.

It proves interesting to compare the mean free path (MFP) spectra calculated by Tian *et al.*[198] of PbSe, PbTe, and a PbSeTe alloy to the experimentally measured control materials and nanocomposite thin films. Figure 4.9 shows the calculated MFP spectra as lines, and the experimentally measured nanocomposite films plotted by their total thickness as symbols. The parent materials are also included in this figure for reference and are plotted by their total thickness. Based on the calculations from Tian *et al.*,[198] short wavelength phonons ranging from 1-10 nm contribute to the majority of the heat carrying phonons in PbSe and PbTe, while phonons with MFP's greater than 10 nm do not contribute substantially to the total thermal conductivity. Figure 4.9 also shows that the calculated MFP spectra of the parent materials and alloy over-predict the contribution to the thermal conductivity of our nanocomposites. Interestingly, the MFP spectra predict that limiting length scales ranging from 1-10 nm should result in an increasing trend to thermal conductivity in this regime. It appears that an increased interface density introduced by

the 4 nm periodicity of the nanocomposite compared to the 12 nm and 20 nm periodicity does not further decrease the thermal conductivity of the material.

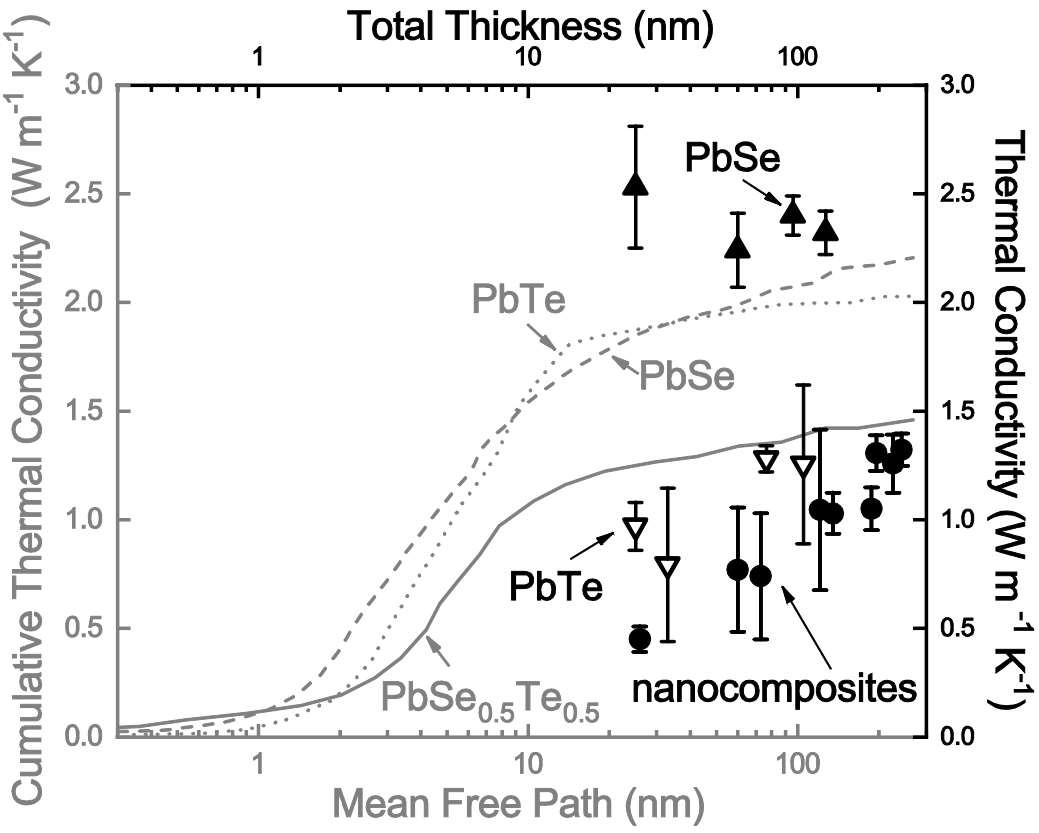


Figure 4.9: The cumulative thermal conductivity with respect to phonon mean free path at 300K. The phonon MFP spectra are plotted as lines and were calculated by Tian *et al.*[198] The data that are overlaid on the spectra as symbols are individual measurements of thermal conductivity of PbTe-PbSe nanocomposites and parent material plotted against their total thickness.

## 4.4 Conclusion

In conclusion, the ALD growth of the PbTe-PbSe thermoelectric samples in this work resulted in non-epitaxial films grown directly on native oxide/Si substrates, where the Volmer-Weber mode growth promoted the growth of grains with a preferred columnar orientation, secondary oxide phases that acted as point defects within the films, and increased microstructural quality with increased film thickness. The phonon thermal transport processes in these ALD-grown films are determined by: i) thickness varying crystalline quality, where structural defect

densities increase in thinner films due to the ALD growth mode of these materials; ii) point defects inherent in the ALD growth process (e.g., oxygen defects); and iii) compositional-driven defects, such as point defects and phase boundaries between the PbTe and PbSe. While nanoscale superlattice structures are not observed in these PbTe-PbSe systems, the compositional variation and resulting point and planar defects give rise to additional phonon scattering events that reduce the thermal conductivity below that of the corresponding ALD-grown control PbTe and PbSe films. Temperature dependent thermal conductivity measurements further support these findings that the phonon scattering and resulting thermal conductivities in these ALD-grown PbTe-PbSe thermoelectric materials are driven by extrinsic defect scattering processes as opposed to phonon-phonon scattering processes intrinsic to the PbTe or PbSe phonon spectra. The implication of this work is that polycrystalline, nanostructured ALD composites of thermoelectric PbTe-PbSe films are effective in reducing the phonon thermal conductivity, and hereby represent a pathway for further improvement of the figure of merit (ZT), enhancing their thermoelectric application potential.

# Chapter 5

## 5. Composition and Morphology Effects on Thermal and Mechanical Properties of Porous Crystalline Solids with Guest Molecules

Parts of Chapter 5 were published in *Nature Communications, (2020) 4010* DOI: 10.1038/s41467-020-17822-0 and a mature manuscript has been submitted to *PNAS* under the title: Hybridization from Guest-Host Interactions Reduce the Thermal Conductivity of Metal Organic Frameworks (MOFs).

### 5.1 Motivation

MOFs have a vast variety of applications ranging from gas storage, separation, catalysis and recently, thermoelectrics (TE).[139,225–227] Their versatility stems from highly selective chemical and mechanical modifications that are achieved by choice of MOF building blocks (metal node and ligand), their extremely high porosity/surface area and the ability to introduce specific guest molecules into the pores of the framework.[226–230] In particular, tailoring of additional properties such as electrical conductivity and thermopower have been achieved by infiltrating MOF pores with specialized guest molecules.[139,226,227] While the thermal properties of MOFs have been investigated on idealized structures using molecular simulations,[231–234] experimental inquiry of infiltrated MOFs are deficient, and critically important for realizing efficient gas adsorption and thermoelectric material. [119,226,227,235–237]

MOFs are well suited for gas storage and gas separation applications. Gas adsorption is an exothermic process therefore, fuel tanks can undergo a significant temperature rise that would greatly affect the efficiency of adsorption rates that can lead to lower sorbent gas storage capacity if not properly mitigated. Therefore, a guest-host induced change in the thermal conductivity upon sorption will control the achievable concentration of gas storage available to MOF material.

Additionally, MOFs may emerge as a viable thermoelectric material due to their intrinsically low thermal conductivity and "emergent" electrical properties upon infiltration. Specifically, significantly enhanced charge transport has been achieved upon infiltration of electrically conductive guest molecules into the pores.[227,238] Understanding the role of guest species on the thermal transport properties of porous crystals, such as MOFs, is critical for realizing an efficient TE material.[139]

In a porous crystal containing adsorbed guest molecules there are, in general, two main mechanisms that influence overall heat transfer. First is thermal transport through the solid scaffolding. While MOFs can be modestly electrically conductive,[239] the primary energy carriers are phonons because the electrical conductivity is too low to make any substantial contribution to thermal conductivity. Second is thermal transport through the guest-host interaction.[240] Thermal transport through the guest-host interaction is complex, and not well understood because competing effects can impact the thermal conductivity. For example, an effective medium approximation suggests that MOF infiltration should increase the total thermal conductivity, since an adsorbed molecule increases the number of atoms per unit volume serving to increase both the density while enhancing the total number of channels that heat can flow through the material system. Alternatively, the addition of any extrinsic species in the form of a guest molecule within the pore could lead to impurity scattering or changes in mode character (i.e., loss of plane wave/propagating character) which would imply a reduction in thermal conductivity.[50,241] Further, in this picture, the guest molecules can also be thought of as 'rattling' atoms that introduce strong localized modes producing increased scattering rates of MOF phonons, decreasing heat transfer.[242,243] In short, the physical mechanisms driving heat flow processes in porous crystalline material undergoing infiltration require additional examination.

MOFs offer limitless compound and network combinations due to the choice of the organic linker and metal ion. Currently, the microscopic mechanisms driving thermal transport in MOFs are not well understood, and it has been an open question as to whether the introduction of adsorbates helps or hinders heat transfer. In Chapter 5, I elucidate the role of the infiltrated guest molecules on the thermal conductivity of metal organic frameworks in a range of energy landscapes by varying the adsorbate phase (solid, liquid, gas), molecular weight, and adsorbate/MOF bonding environment (coordinated vs. uncoordinated). In addition, since MOFs consist of well-defined pores that exhibit different geometries (squared, rectangular, triangular, and window-connected cages),[244] I selected two compositionally different MOFs (HKUST-1 and ZIF-8) with differing pore morphologies (rigid square pores vs. flexible window connected cages) to study how composition and morphology impact the thermal properties of MOFs in the presence of adsorbates.

## 5.2 Experimental Details and Sample Characterization

Two different types of MOFs were investigated in the work presented here including, thin films and thick samples of HKUST-1, and thin films of ZIF-8. A schematic of the building blocks (metal nodes and organic linkers) is shown in Figure 5.1. HKUST-1 was infiltration with gas ($N_2$), liquid (methanol, ethanol, DI-water), and solid (TCNQ, $F_4$-TCNQ, $H_4$-TCNQ) molecules, and ZIF-8 was infiltrated only with the gas and liquid adsorbates, the details of which are provided in Table 5.1. Due to experimental constraints, gas infiltration occurred only at ambient pressure (~0.1 MPa), therefore the liquid guests served as a substitute for performing challenging *in situ* thermal conductivity measurements at very high pressures, where pores filled with liquid adsorbates have similar densities to saturated pores containing gaseous adsorbates.[235] The solid molecules were chosen because they have been shown to promote emergent electrical

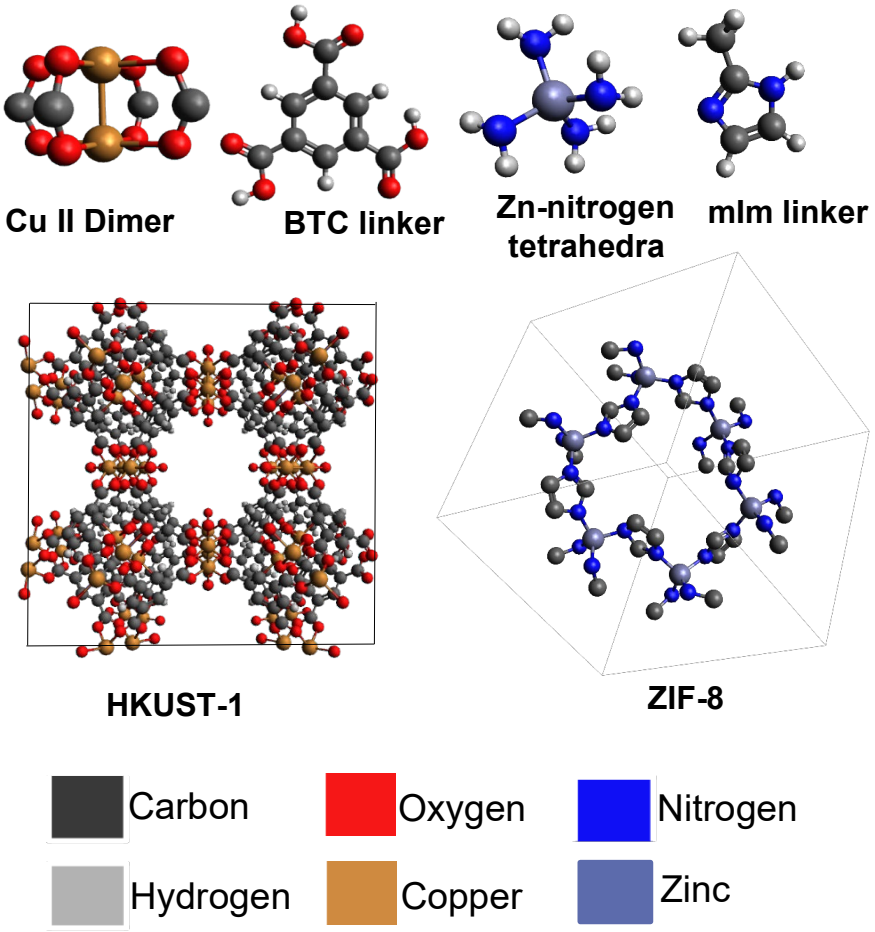


Figure 5.1: Schematic of the MOF metal nodes and organic linkers and a single unit cell. (Left) HKUST-1 face center cubic unit cell is composed of di-copper paddlewheel secondary building units that coordinate to eight oxygens corresponding to four 1,3,5 benzenetricarboxylic acid (BTC) linkers and exhibits a large, rigid 9 x 9 Å square pore with access to the open metal sites on the Cu atoms.(Right) ZIF-8 self assembles into a cubit unit cell with a sodalite topology that is composed of $Zn^{2+}$ metal nodes that are tetrahedrally coordinated to hydrophobic 2-methylimidazole (mIm) linkers. ZIF-8 exhibits flexible cage-like pores that are approximately 11.6 Å in diameter. ZIF-8 does not contain open metal sites.

properties in HKUST-1, and due to their charge accepting nature, they create differing degrees of orbital overlap between the guest and host.[227] Altogether, the adsorbate/MOF combinations chosen for this investigation cover a variety of strong and weak guest/host interactions ranging from full coordination to weak van der Waals interactions that are relevant for designing these MOFs towards efficient thermoelectric and gas storage applications.

The differences in composition and morphology of these MOF's are outlined in Table 5.1, which show how these particular MOFs provide a unique material system to study the roles of pore composition, and pore morphology on the thermal processes in porous crystalline material. In general, MOFs are fabricated by coordination chemistry that combines appropriate stoichiometries of metal nodes with organic linkers which self-assemble into a porous crystalline, three-dimensional scaffolding. HKUST-1 contains a rigid framework composed of Cu (II) paddle-wheel units coordinated by four oxygen from 1,3,5 benzenetricarboxylic acid (BTC) linkers.[245] HKUST-1 is unique in that instead of using a single metal atom to form the node within the scaffolding structure, it relies on a secondary building unit (SBU), where two $Cu^{2+}$ atoms bond to form a copper dimer (with a coordination number of six (octahedral)). Each Cu atom within the dimer then forms four coordinating bonds with the BTC linker, so that the first coordination sphere of the SBU is unsaturated forming an open metal site (OMS).[245] This means that each Cu atom contains a pair of free electrons that are free to interact with any adsorbate species in close proximity. The SBU's and organic linkers arrange themselves into a cubic (*Fm-3m*) structure that exhibits permanent porosity in the absence of guest molecules.[245] It contains a system of large square shaped pores measuring approximately 9 x 9 Å, that are connected by open channels with diameters on the order of 3 - 4 Å.[245,246] The pores also exhibit different levels of polarity based on their exposure to OMS.[245]

ZIF-8 (zeolitic imidazolate framework-8), is the second MOF material investigated. It is a non-OMS MOF (the coordination sphere is fully saturated) that also exhibits permanent porosity. ZIF-8 contains a cubic unit cell (*I4m3*) that is composed of zinc cations tetrahedrally coordinated by four hydrophobic 2-methylimidazole (mIm) linkers resulting in a porous structure with large cages (diameter ~11.6 Å) interconnected by narrow 6-ring windows (~3.4 Å).[247] Unlike

the more rigid structure in HKUST-1, ZIF-8 exhibits a flexible framework that can dramatically adjust its pore size through a structural transformation of the mIm likers, to accommodate guest molecules while maintaining its crystallinity.[248,249] ZIF-8 crystalizes into the zeolite sodalite topology that contains flexible narrow pore apertures that can swing open by reorientation of the mIm linkers and expand when infiltrated with guest molecules.[249,250] HKUST-1 and ZIF-8 exhibit comparable bulk densities, porosities, and pore volumes and they both assemble into cubic unit cells, however their pore compositions and morphologies are quite different. HKUST-1 contains small square pores that are mechanically rigid and have access to OMS. ZIF-8 does not contain an OMS property and has slightly larger, flexible, hexagonal pores that expand and deform to accommodate guest molecules.

All samples were fabricated directly on the metal side of either Al/$SiO_2$ or Au/$SiO_2$ substrates where 65-80 nm of Au, or 80 of Al was electron-beam evaporated onto bulk amorphous $SiO_2$ substrates at a base pressure of $1x10^{-6}$ Torr. The thermal conductivity of the $SiO_2$ and the thermal boundary conductance between the metal/$SiO_2$ interface was measured with TDTR before the MOF's were deposited (Table A 1). Thin film and thick polycrystalline HKUST-1 MOFs were prepared at two separate institutions, Karlsruhe Institute of Technology (KIT) and the University of Virginia (UVA), using a layer-by-layer (LBL) liquid phase epitaxy (LPE) technique[251] and a solution shearing[252,253] fabrication process, respectively. Thin film ZIF-8 were fabricated at North Carolina State University (NCSU) using chemical vapor deposition (CVD). The fabrication techniques used to synthesize all the MOF samples are described in detail in Section 5.2.1. All pristine (un-infiltrated) MOF samples were thermally activated both before infiltration, and before TDTR measurements were acquired. The activation procedure followed heating the HKUST-1 films to 145$^{o}$C and the ZIF-8 films to 100$^{o}$C, under vacuum (c.f. Section 5.2.1), which has been

shown to be an effective technique to remove both pre-coordinating solvent molecules and unwanted guest molecules (such as $H_2O$ and CO) that would otherwise prevent the pores from interacting with the intended adsorbates, while maintaining the crystallinity and porosity.[121,254–258] I also found that activation of the HKUST-1 samples within approximately 12 hours of acquiring TDTR measurements was extremely important, due to the presence of adsorbed water vapor. After this time interval, the HKUST-1 would adsorb ambient water vapor into its pores, which would significantly affect the TDTR measurement. Figure 5.2 shows a time series of TDTR measurements collected on the same thick HKUST-1 sample following activation. The sample was exposed to ambient environment conditions while TDTR measurements were taken over the course of minutes to days, following sample activation. The results show that the thermal conductivity is strongly affected by the introduction of an adsorbate, and acts as a good indicator for marking the transition from a pristine activated, to an un-activated state. Both pristine activated ZIF-8 and HKUST-1 samples were infiltrated with liquid (ethanol, methanol, and water) and gas ($N_2$) guest molecules. Additionally, the HKUST-1 samples were infiltrated with solid guest molecules (TCNQ, $F_4$-TCNQ, and $H_4$-TCNQ), the full details of which are provided in Section 5.2.1. I measured the thermal conductivities of the various HKUST-1 and ZIF-8 samples in activated pristine and loaded forms with TDTR.[153,157]

Table 5.1: Composition and morphology of HKUST-1 and ZIF-8 MOFs measured at room temperature for HKUST-1[235,245,259,260] and ZIF-8[261,262] from previous reports. The adsorbates for each MOF are also listed. *The range in pore volume reported in the literature for HKUST-1 is attributed to different preparation procedures.[259] The pore morphology shows the pore size and geometry, and also indicates the presence of an open metal site (OMS).

| | MOF | SURMOF HKUST-1 | HKUST-1 | ZIF-8 |
|---|---|---|---|---|
| Composition | Chemical Composition | $[Cu_3(BTC)_2]$ | | $[Zn(mIm)_2]$ |
| | Adsorbate | $N_2$ (g), methanol (l), ethanol (l), water (l), TCNQ (s), $F_4$-TCNQ (s) | $N_2$ (g), methanol (l), ethanol (l), water (l), TCNQ (s), $F_4$-TCNQ (s), $H_4$-TCNQ (s) | $N_2$ (g), methanol (l), ethanol (l), water (l) |
| Morphology | MOF Thickness (nm) | 200-400 | 5500 | 280 |
| | Unit Cell (space group) | Cubic (F*m*-3*m*, $a_o$=26.3 Å, V=18,280 Å$^3$) | | Cubic (I43*m*, $a_0$=17.0 Å, V=4,905.2 Å$^3$) |
| | Molecular Mass (g mole$^{-1}$)/ Density (g cm$^{-3}$) | 658.9/0.96 | | 229.6/0.95 |
| | Pore Morphology (Å) | 9 x 9 square with OMS | | 11.6 (diameter) floppy cage, non-OMS |
| | BET Surface Area (m$^2$g$^{-1}$)/ Pore Volume (cm$^3$ g$^{-1}$) | 1805/0.33-0.69 * | | 1812/0.65 |
| | Porosity (%) | 40.7-67.8 | | 58.8 |

## 5.2.1 Sample Fabrication

### *5.2.1.1 Layer-By-Layer LPE Thin Film SURMOF HKUST-1*

Polycrystalline HKUST-1 surface-anchored MOF (SURMOF) thin films were self-assembled onto the metal side of $Au/SiO_2$ glass substrates using layer-by-layer liquid phase epitaxy, the details of which have been previously described.[235,263] The Au substrates were treated with an MHDA-SAM layer to improve adhesion. In brief, the substrates were pretreated by $O_2$ plasma cleaning. The MOF precursors were then iteratively hand sprayed onto the substrate using an LBL, LPE technique. A metallic, copper acetate solution (1.0 mM) was sprayed for 15 s, followed by a 25 s spray sequence of the polymeric BTC linker (0.2 mM). Residual reactants were washed away with a 5 s rinsing step with pure ethanol after every individual spray sequence. A single LBL cycle is defined as both the application of a single round of the metallic and polymeric linker constituents. A total of 125, 150, and 200 cycles resulted in 250 nm, 300 nm, and 400 nm thick films respectively. Following the completion of all cycle depositions, the MOFs were chemically activated by ultrasonication in dicholormethane for two min to remove residual solvents from the pores, and characterized by XRD (Figure 5.4). These samples were then periodically reactivated by heating at 145 $^oC$ for 12 hours under a vacuum of $3.4x10^{-6}$ mbar prior to loading with guest molecules or acquiring TDTR measurement.

The thin films were infiltrated with gas, liquid, and solid adsorbates. An activated pristine 400 nm thin film HKUST-1 was infiltrated with 99.996% pure $N_2$ (g) acquired from Praxair, under an approximate flow rate of 0.002 $m^3/s$, using a Linkam stage that acted as a controlled gas chamber while providing an optical window to perform TDTR measurements. The pristine activated thin films of HKUST-1 were loaded into the Linkam stage while $N_2$ gas flowed

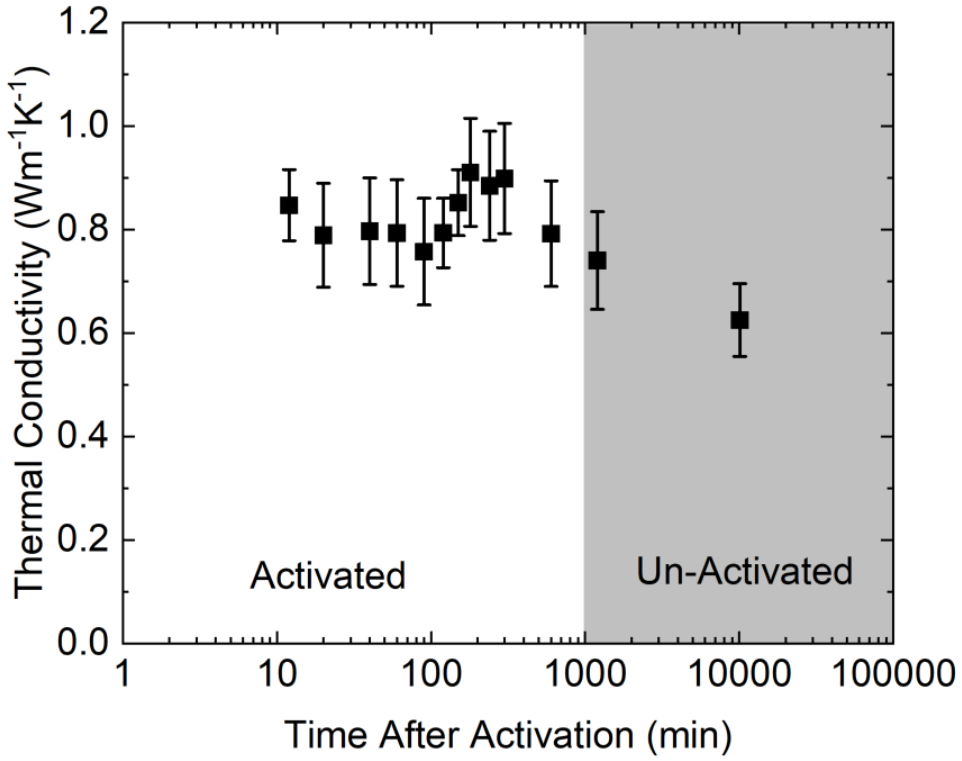


Figure 5.2: Time series of TDTR acquired measurements on a thick HKUST-1 sample after activation by heating at 145 ºC for 12 hours under a vacuum of $3.4 \times 10^{-6}$ mbar. Measurements were taken in ambient conditions.

through the chamber for an hour at ambient air pressure ($P_{gauge}$ = 1 atm). Liquid adsorbates were introduced to activated thin films HKUST-1 samples ranging from 200-350 nm. The individual SURMOF samples were cut into four sections, three of which were infiltrated with either methanol, ethanol, or DI-water. Only the SURMOF assembled on Au was submerged in water so as to reduce the effects of oxidation likely to occur with the Al in the Al/silica substrates. The thermal conductivities of the pristine and infiltrated HKUST-1 thin films, for a range of film thicknesses, were then measured using TDTR (Table A 1). Lastly, loading of pristine HKUST-1 SURMOF thin films (250-400 nm) with the solid guests (TCNQ and $F_4$-TCNQ) was done following the procedure described by Talin *et al.*[139] The activated pristine SURMOFs were placed in 2 mM of TCNQ ($F_4$-TCNQ) dissolved in acetonitrile for 72 hours. After soaking, they were removed from the loading solution, rinsed with pure acetonitrile (to remove residual loading

molecules) and dried by a $N_2$ flux. XRD data were collected for both sets of guest molecules, showing the polycrystallinity of the SURMOF is maintained (Figure 5.4). Loading with $H_4$-TCNQ was not achieved within the thin HKUST-1 because the $H_4$-TCNQ was very volatile and would not stay infiltrated within the pore long enough to acquire measurements.

#### *5.2.1.2 Solution Shearing of Thick HKUST-1*

Solution shearing is a high throughput method for fabricating thick HKUST-1 samples, where the MOF self assembles behind the leading edge of a coating blade that is moved across the substrate surface.[264] The solution-shearing device used at UVA to fabricate the MOFs was assembled as described in the work of Ghorbanpour *et al.*[253] Before the precursor solution was sheared, the Trichloro(octyl)silane (OTS)-functionalized coating blade was washed with toluene, acetone and isopropyl alcohol and dried with in-house air. The substrate stage was heated to the desired temperature. The blade was held in place with a top vacuum stage and an 80 nm Au/$SiO_2$ substrate was attached to the bottom vacuum stage. The blade angle and the gap between the blade and the substrate stage were approximately set to 1° and 100 μm respectively, by controlling the micro-manipulating assembly. 5-10 μL of the precursor solution of HKUST-1 was injected into the smallest gap between the edge of the blade and the substrate in accordance with the dimensions of the substrate and solution concentration. The solution was deposited on the gold side of the substrate as the blade moved along the substrate. After the blade passed the substrate, samples were taken off from the bottom stage for further analysis by XRD and SEM (see Section 5.5.2, Figure 5.4). The resulting MOFs were approximately 5.5 micrometers thick.

The thick HKUST-1 samples were infiltrated with gas, liquid, and solid adsorbates in a similar fashion as the thin films. Freshly made activated pristine HKUST-1 were exposed to $N_2$

(g) under an approximate flow rate of 0.002 $m^3/s$, using a Linkam stage that acted as a controlled gas chamber while providing an optical window to perform TDTR measurements. The pristine activated thick HKUST-1 was loaded into the Linkam stage while $N_2$ gas flowed through the chamber at atmospheric pressure ($P_{gauge}$ = 1 atm) for one hour. The liquid adsorbates included methanol, ethanol, or DI-water. Individual HKUST-1 samples were fully submerged in respective solutions of 99.8% methanol, and 96% ethanol for an hour, and measured with TDTR directly after soaking. The soaking time was reduced to 20 min for the HKUST-1 sample infiltrated with DI-water, to avoid sample degradation. The infiltration with the solid adsorbates followed a slightly different procedure. After the HKUST-1 samples were fully grown on the substrates, they were moved to the $N_2$-filled glovebox. The HKUST-1 samples were then transferred to the vacuum oven and heated at 180 °C for 12 hours. After the heat treatment, the samples were cooled down for an hour inside the glovebox. Finally, the cooled HKUST-1 samples were transferred to the saturated TCNQ/$F_4$-TCNQ/$H_4$-TCNQ solution (individually) for 72 hours.

#### *5.2.1.3 Chemical Vapor Deposition (CVD) of Thin Film ZIF-8*

Thin film ZIF-8 MOFs were fabricated at North Carolina State University (Dr. Parson's Lab) using the chemical vapor deposition (CVD) technique described by Stassen *et al.*[265] The CVD technique used here relied on the reaction of the vaporized MOF ligand precursors on a nearby metal oxide substrate to form uniform thin film ZIF-8 MOFs.

Substrates of 80 nm of Au that was evaporated on $SiO_2$ were $O_2$ plasma cleaned followed by deposition of a 4.6 nm layer of alumina on the metal side of the Au/$SiO_2$ sample. This layer of alumina provided an adhesion layer for an approximately 16.7 nm thick layer of zinc oxide deposited via ALD. The metal oxide layer was then exposed to a MOF linker precursor vapor (2-

methylimidazole) at ~100°C for 24 hours to induce a vapor-solid reaction. This resulted in a transformation of the solid metal oxide film into a homogeneous, highly crystalline ZIF-8 framework as confirmed through XRD (Figure 5.8). It has been shown that the oxide-to-MOF conversion efficiency of this technique is complete when the metal oxide precursor film is < 10 nm, so that no residual zinc oxide remains at the interface between the ZIF-8 film and the substrate.[265] A 100% conversion of the 16.7 nm ZnO layer would produce a ZIF-8 film with a nominal thickness of 283 nm. The SEM images (Figure 5.8) indicate that the ZIF-8 film is approximately 280 nm, confirming a high metal oxide-to-MOF conversion rate.

All pristine ZIF-8 films were activated before TDTR measurement by heating at 100ºC in vacuum ($1.6 \times 10^{-4}$ mbar) for two hours. The pristine activated thin film (280 nm) ZIF-8 was cut into four sections, three of which were infiltrated with either methanol, ethanol, or DI-water. The pristine activated ZIF-8 film was also exposed to $N_2$ gas within a Linkam stage gas chamber, under an approximate flow rate of 0.002 $m^3/s$, for 1 hour at ambient pressure ($P_{gauge} = 1$ atm).

## 5.2.2 Characterization

### *5.2.2.1 HKUST-1*

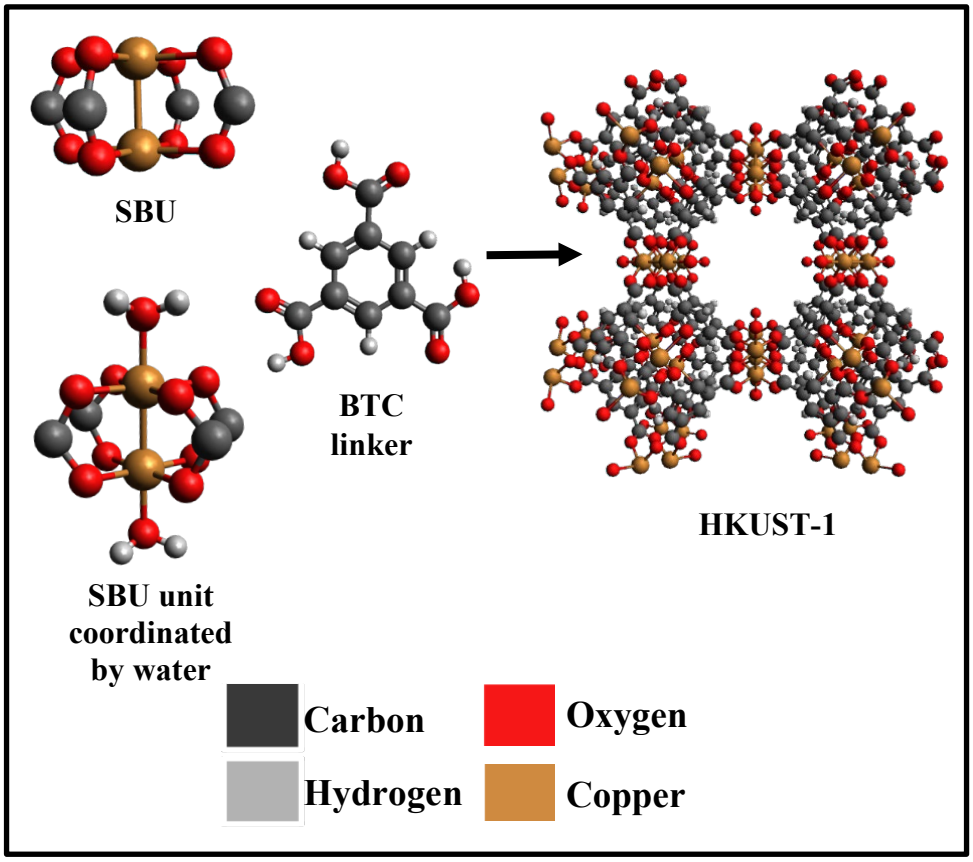


Figure 5.3: The building blocks of HKUST-1 include a secondary building unit (SBU) acting as the 'node' within the MOF scaffolding, consisting of a Cu II paddle-wheel dimer that is coordinated by four BTC linkers through eight oxygens. The OMS is achieved during fabrication through solvent exchange, where water coordinates to the SBU and is then removed through activation once the MOF has self-assembled.

HKUST-1 is a highly porous MOF that exhibits a face-centered-cubic unit cell (*Fm*-3*m* space group) containing a 3D network of large, rigid, square-shaped pores (9 x 9 Å).[245] HKUST-1 MOFs contain open mental sites (OMS), also known as coordinated unsaturated sites (CUS). These OMS stem from the formation of larger secondary-building units (SBUs), where dicopper paddle-wheel SBU's form an octahedral unit and bond to four benzene-1,3,5-tricarboxylic acid (BTC) ligands that leave the coordination sphere unsaturated (Figure 5.3).[245]

From a chemical perspective, the OMS is achieved through solvent exchange, where water molecules coordinate to the SBU, and are then removed by thermal activation after the MOF has self-assembled.[266] This property does not affect the integrity of the framework network (from collapse), and preserves the crystallinity and porosity.[267] OMS are a desirable feature in MOFs intended for gas storage because they provide strong binding sites, which leads to an increased interaction with adsorbate molecules in comparison to MOFs lacking OMS.[267] Therefore, HKUST-1 offers an intriguing system to study the role of different adsorbate interactions, on the thermal properties.

The thin and thick HKUST-1 MOF's were characterized using: SEM, profilometry, and XRD to confirm their composition and to characterize differences in their morphologies (Figure 5.4 (a)-(d)). Additionally, nitrogen isotherm measurements were performed on activated thin and thick HKUST-1 samples at 77 K, and a DFT model was used to calculate the BET surface area and total pore volume for each respective sample, which are reported in Table 5.2. The results indicate that the BET surface areas and pore volumes are within the range of previously reported HKUST-1 samples.[245,246] The lower BET surface area for the thicker sample may imply a smaller percentage of open metal sites, due to a higher degree of coordinated water molecules, where perhaps the desorption of coordinated water adsorbates during activation does not occur as efficiently compared to the thin films.[266,267] Further, the difference in BET surface area could also be indicative of a difference in defects present in the material due to incomplete coordination of the BTC ligands to the SBU's, where Bently *et al.* concluded that increased defects leads to stronger binding between the OMS and water molecules.[266] The SEM and XRD data shown in Figure 5.4 (a)(b) and (c)(d) respectively, show that the surface anchored thin films result in low surface roughness, highly oriented growth. This is in contrast to the thick MOFs that demonstrate

elevated surface roughness and high polycrystallinity. The SEM also illustrates the difference in surface roughness, where the LPE method produces very smooth surfaced films (<10 nm RMS), and the solution shearing method promotes high surface roughness (~1 μm RMS), as confirmed through profilometry.

Table 5.2: The calculated BET surface area and total pore volume derived from nitrogen isotherm measurements for a thin and thick HKUST-1 sample.

| | **BET Surface Area ($m^2g^{-1}$)** | **Total Pore Volume ($cm^3g^{-1}$)** |
|---|---|---|
| 300 nm SURMOF HKUST-1 | 1805 | 0.60 |
| 5.5 μm HKUST-1 | 1450 | 0.61 |

Pristine and infiltrated HKUST-1 samples were characterized to investigate the guest-host interaction. Due to the limitation in sample stability for the gas and liquid infiltrated HKUST-1 samples, characterization via spectroscopy and mechanical measurements was not possible in this work. Characterization of the HKUST-1 samples infiltrated with solid guests was performed with XRD, FTIR, and Raman, to specify the morphology of each sample and confirm the presence of different degrees of guest coordination with the framework. Additionally, nanoindentation and pump-probe Brillouin scattering was performed on thick and thin film samples respectively to measure effects of the adsorbate on the elastic modulus.

Although direct evidence for the guest-host interaction for gas and liquid adsorbates in this work is lacking, previous investigations provide compelling evidence for the expected nature of some specific adsorbate/MOF interactions. In particular, it is expected that the adsorption of dinitrogen gas into HKUST-1 at low pressure (≤ 0.1 MPa) follows a diffusion pathway where the gas diffuses first through the gas-MOF interface followed by diffusion within the

interconnected network of pores and channels; likely exhibiting a nonuniform spatial distribution similar to what was reported by Babaei, McGaughey, and Wilmer for methane adsorption in HKUST-1.[268] Previous work has shown that $N_2$ gas experiences weak unspecific van der Waals interactions within the pores, in addition to stronger interactions from the coordinatively unsaturated sites ($Cu^{2+}$) within the MOF, that act as preferential adsorption sites.[269] While it is known that nitrogen weakly interacts with $Cu^{2+}$ ions,[270] cupric-nitrogen complexes in HKUST-1 have only been observed at temperatures lower than 200 K.[269] Therefore, it is likely that the dinitrogen adsorbate at room temperature and low pressures studied here, only experiences weak van der Waals interactions with the HKUST-1 framework. nitrogen adsorption isotherms at room temperature on HKUST-1 indicate that less than 1 mmol $g^{-1}$ of $N_2$ is adsorbed at the pressures and temperatures studied here.[259]

The interaction of the liquid polar adsorbates (water, methanol, and ethanol) with the HKUST-1 is not fully known. Prestipino *et al.* reported that $H_2O$ (g) present in the pores of HKUST-1 chemically binds to the Cu(II) sites, resulting in significant modifications to the first coordination sphere.[254] It is likely that the introduction of the polar liquid guest molecules (methanol, ethanol) creates similarly complex guest-host interactions. While it is not possible to assess the significance of these different interactions without direct characterization, it can be postulated that the liquid guests may behave in a similar manner to gas adsorbates at saturation loading under high pressures, where the density between pores filled with liquids vs. saturated gas are roughly equivalent.[235] According to adsorption isotherms, of the 67.8% porosity that is accessible to adsorbates in HKUST-1, water is estimated to fill 82% of the void fraction of pores, while the methanol and ethanol are estimated to fill 100% of the void fraction.[260] Nevertheless, there may

exist differences between the gas and liquid adsorbates within HKUST-1 that are not captured by the previous description.

Finally, the HKUST-1 samples infiltrated with solid guest adsorbates were characterized with: SEM, XRD, Raman, and FTIR spectroscopy to understand the effects of the adsorbate on the morphology of guest@HKUST-1 system. Additionally, pump-probe Brillouin scattering and nanoindentation measurements demonstrate the role of infiltration on the elastic modulus of the MOF samples, which further elucidates the fundamental role of guest-host interactions on the stiffnesses of the MOFs. Figure 5.4 shows the characterization results for a subset of thin and thick HKUST-1 samples that specify the morphology of each sample, and confirm the presence of different degrees of solid guest coordination with the framework. The XRD in Figure 5.4 (c)-(d) confirms that infiltration with the solid guests does not affect the MOF's crystalline structure (face centered cubic). Additionally, it has been reported that the XRD peak occurring at $2\theta \simeq 5.7$ is a diagnostic for the guest molecules binding to the open metal sites of the framework.[238] Indeed, Figure 5.4 (d) shows the emergence of a peak at $2\theta \simeq 5.9$ in the solid guest infiltrated cases for the thick MOFs, that is absent for the pristine HKUST-1 samples. I note, that the thin film TCNQ@HKUST-1 shows a feature at $2\theta \simeq 5.87$, however this feature is quite weak in the $F_4$-TCNQ@HKUST-1 diffractogram.

FTIR spectra for powder forms of TCNQ and $F_4$-TCNQ molecules are compared to the infiltrated forms (TCNQ/$F_4$-TCNQ@HKUST-1) and the pristine MOF in Figure 5.4 (e). The red shifts of the nitrile peak of 13 $cm^{-1}$ for $F_4$-TCNQ/$F_4$-TCNQ@HKUST-1 (from 2225 $cm^{-1}$ to 2212 $cm^{-1}$), 24 $cm^{-1}$ for TCNQ/TCNQ@HKUST-1 (from 2223 $cm^{-1}$ to 2199 $cm^{-1}$) and broadening of the nitrile stretch indicate the degree that the guest molecules are interacting with the coordinating $Cu^{2+}$ sites of the paddle-wheel units in the framework.[238] Further, Raman spectra in

Figure 5.4 (f) from the thick samples show that the bonding environment within the pore between the TCNQ, $F_4$-TCNQ, and $H_4$-TCNQ is quite different from species to species, where new features appear in the $F_4$-TCNQ, and $H_4$-TCNQ infiltrated MOFs that are not present in the TCNQ system. Moreover, the feature at ~507 $cm^{-1}$ that represents the Cu-O stretch is blue shifted (higher energy) for the $F_4$-TCNQ, and broadened in the $H_4$-TCNQ spectrum, demonstrating different interactions of the guest molecule in the first coordination sphere of the $Cu^{2+}$ sites. The aromatic alkene (C=C) stretch at ~1463 $cm^{-1}$ is red shifted for the infiltrated guests, which is also strong evidence of guest coordination with the MOF.[238] It is worth noting that others have also reported coordination occurring between the TCNQ and TCNQ derivatives with the OMS of HKUST-1.[227,238,271] In summary, infiltration of the solid guest molecules may result in different polymorphs, as it has been shown that subtle geometrical changes for the nitrile arrangements around the Cu centers can occur.[272] Despite this, the congruency of features between the thin and thick samples indicate that the morphology is relatively consistent between samples.

Mechanical measurements of the elastic constants of pristine (in activated and un-activated forms) and TCNQ infiltrated HKUST-1 using nanoindentation and pump-probe Brillouin scattering are reported in Figure 5.4 (g) and compared to the harmonic lattice dynamics (LD) calculations (discussed in detail later, in Section 5.3) and previous nanoindentation results from 1 μm surface-anchored HKUST-1 film prepared using LPE from Bundschuh *et al.*[273] The experimental and LD results presented here indicate that no discernable change in the elastic modulus is observed between the pristine HKUST-1 and infiltrated TCNQ@HKUST-1, within uncertainty. This is a rather surprising result since both an increase in the density of the system due to the addition of guest molecules, and an increase in guest/host bonding would typically lead

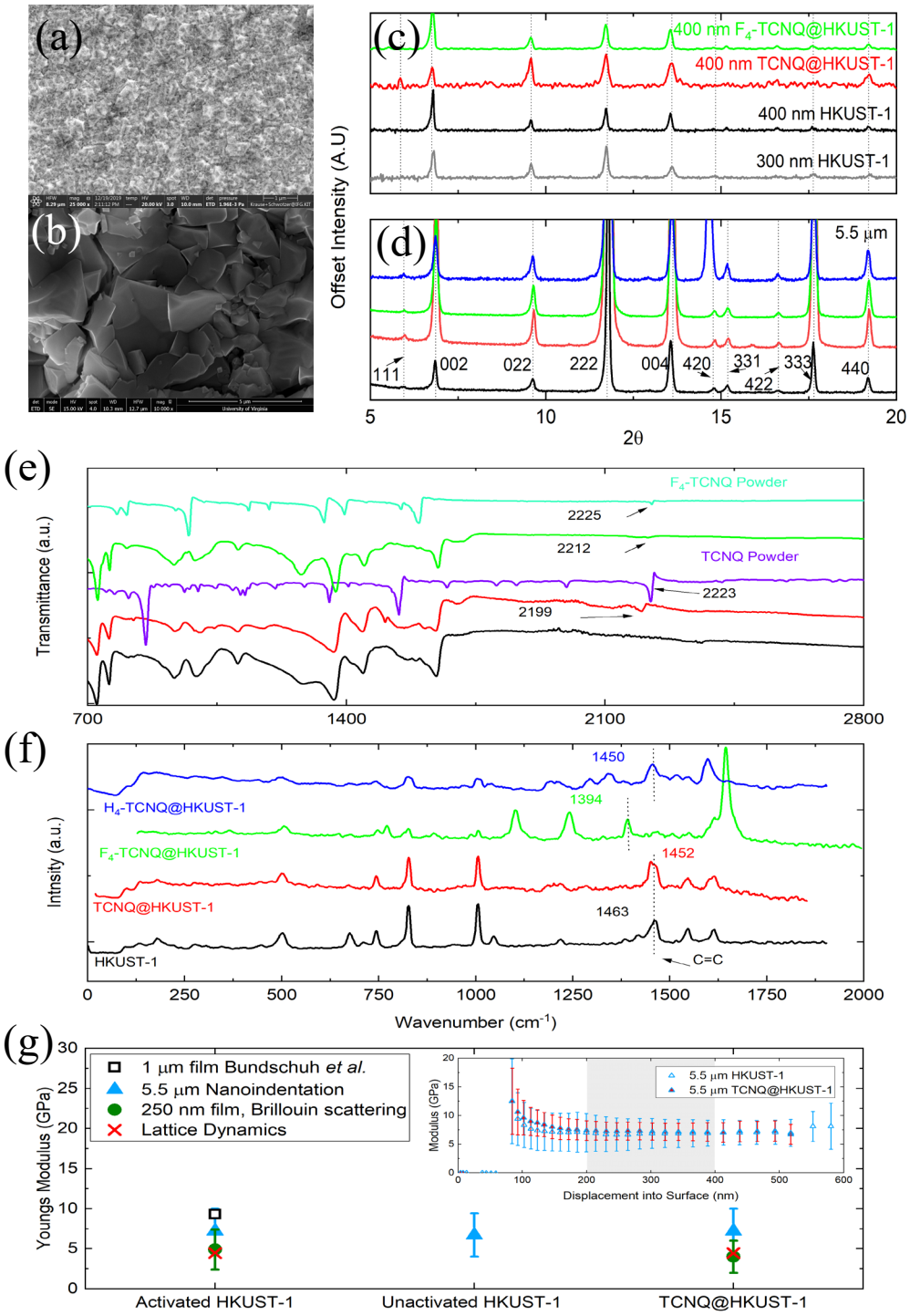


Figure 5.4: Characterization of HKUST-1 samples. (a) Planar SEM images for the 400 nm pristine polycrystalline HKUST-1 SURMOF thin films fabricated by LBL-LPE from KIT and (b) 5.5 $\mu$m thick polycrystalline HKUST-1 samples fabricated using solution shearing at UVA. (c) XRD data for $F_4$-TCNQ@HKUST-1 (green), TCNQ@HKUST-1 (red) and HKUST-1 (black) 400 nm thin films and (d) and XRD for the $H_4$-TCNQ@HKUST-1 (blue), $F_4$-TCNQ@HKUST-1 (green),

TCNQ@HKUST-1 (red) and HKUST-1 (black) 5.5 $\mu$m thick MOF samples. There is little evidence of excess TCNQ, $F_4$-TCNQ and $H_4$-TCNQ that did not diffuse into the pores. (e) FTIR spectra for 5.5 $\mu$m thick pristine (black), TCNQ@HKUST-1 (red) and $F_4$-TCNQ@HKUST-1 (green) MOFs compared to TCNQ (purple) and $F_4$-TCNQ (aqua) molecules in powder form. The respective nitrile stretch is labeled in the spectra, the magnitude of the red shift occurring from the guest species in powder form to infiltrated form shows the degree that the TCNQ/$F_4$-TCNQ interacts with the coordination sites of the framework. (f) Raman spectra for the 5.5 $\mu$m thick pristine (black), TCNQ@HKUST-1 (red), $F_4$-TCNQ@HKUST-1 (green) and $H_4$-TCNQ@HKUST-1 (blue) MOFs. The C=C stretching frequency is labeled. The shift of the C=C stretching frequency upon infiltration and the additional peaks occurring between 1101 – 1343 $cm^1$ indicate the TCNQ and $F_4$/$H_4$-TCNQ derivatives coordinate to the $Cu^{2+}$ ions in the framework. (g) Young's modulus for 400 nm and 5.5 μm pristine and TCNQ@HKUST-1 samples measured by pump probe Brillouin scattering and nanoindentation respectively. The results are compared to the lattice dynamics derived Young's modulus using a Poisson ratio of 0.49, and also to nanoindentation results for a 1μm HKUST-1 film from Bundschuh *et al.*[273] The inset shows the full range of indenter displacement on the 5.5μm pristine and TCNQ@HKUST-1 samples, however only data in the shaded region was used for analysis.

to an increased degree of resistance toward deformation (increased elastic constants). Instead, no measurable change is observed, suggesting that the unit cell deformation upon infiltration/adsorption may compete with density and bonding effects. Therefore, these measurements show that mechanical softening is negligible upon infiltration of HKUST-1, and therefore a loading dependent structural change can be ruled out from affecting the thermal conductivity.

In addition to the characterization detailed above, raw TDTR data and the corresponding fits are shown in Figure 5.5. A modified sample geometry was employed in this study, as discussed in Section 3.1.2, where the laser pulse propagates through the $SiO_2$ substrate first, so that the thermal model plotted in Figure 5.5 accounts for bi-directional heat flow considering a multilayer analysis.[116] The heat conduction model requires knowledge of each layer's heat capacity, thermal conductivity, thickness, and the thermal boundary conductance (TBC) between each layer. Literature values were assumed for the heat capacity of the gold and silica,[171] the heat capacity for the pristine and the TCNQ@HKUST-1 were measured following

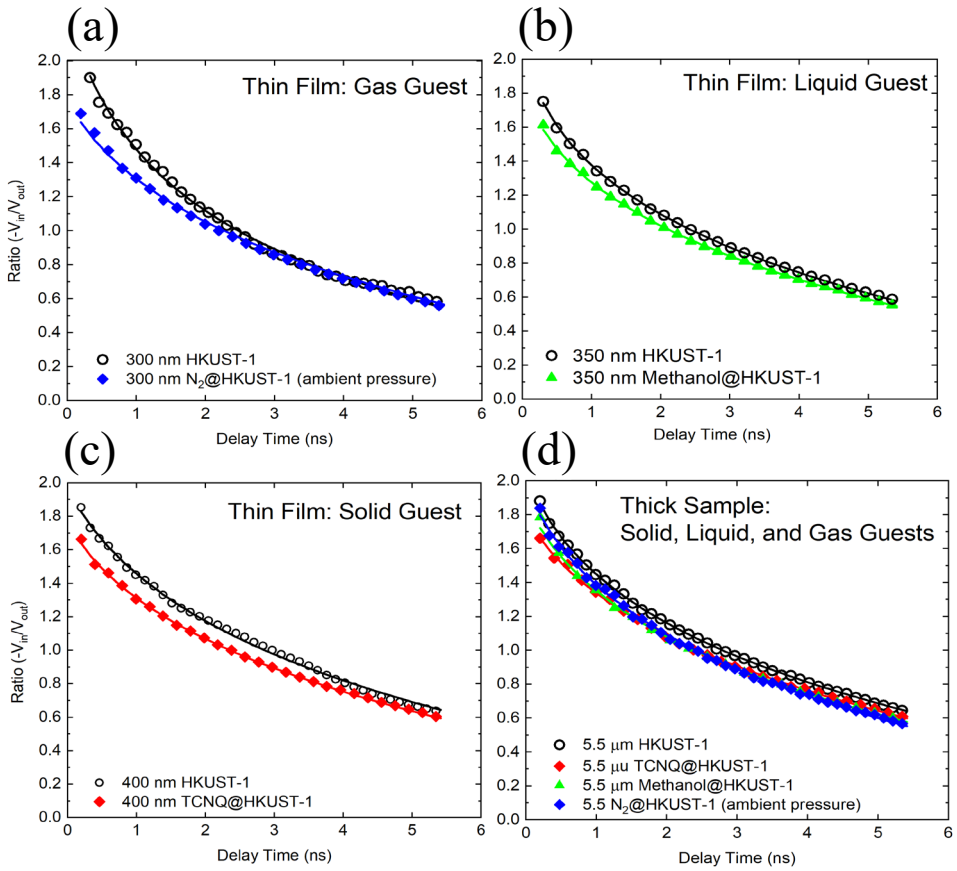


Figure 5.5: Representative data for a TDTR scan on (a) a 400 nm thick HKUST-1 SURMOF deposited on an Au/$SiO_2$ substrate and also infiltrated with a solid guest molecule (TCNQ) and (b) a 350 nm HKUST-1 SURMOF deposited on a Al/ $SiO_2$ and infiltrated with a liquid guest molecule (methanol), (c) a 300 nm HKUST-1 deposited on a Al/SiO2 substrate and infiltrated with a gaseous guest molecule ($N_2$), and (d) 5.5 µm thick HKUST-1 infiltrated with the same respective guest molecules. All data shown here were measured at a pump modulation frequency of 10 MHz, and analyzed with a four-layer model. The data for all other adsorbates is excluded for clarity.

the discussion in Section 3.2.2. Further, the heat capacity for $F_4$-TCNQ@HKUST-1 and $H_4$-TCNQ@HKUST-1 used in the TDTR analysis were calculated from lattice dynamics, and since TCNQ (204.19 g/mol) and $H_4$-TCNQ (208.22 g/mol) are similar molecules with molecular weights differing by ~2%, I applied effective medium theory to calculate the required density to derive the volumetric heat capacity with the assumption of one guest molecule per pore. Additionally, effective medium theory was also applied to the infiltrated MOFs with methanol, ethanol and

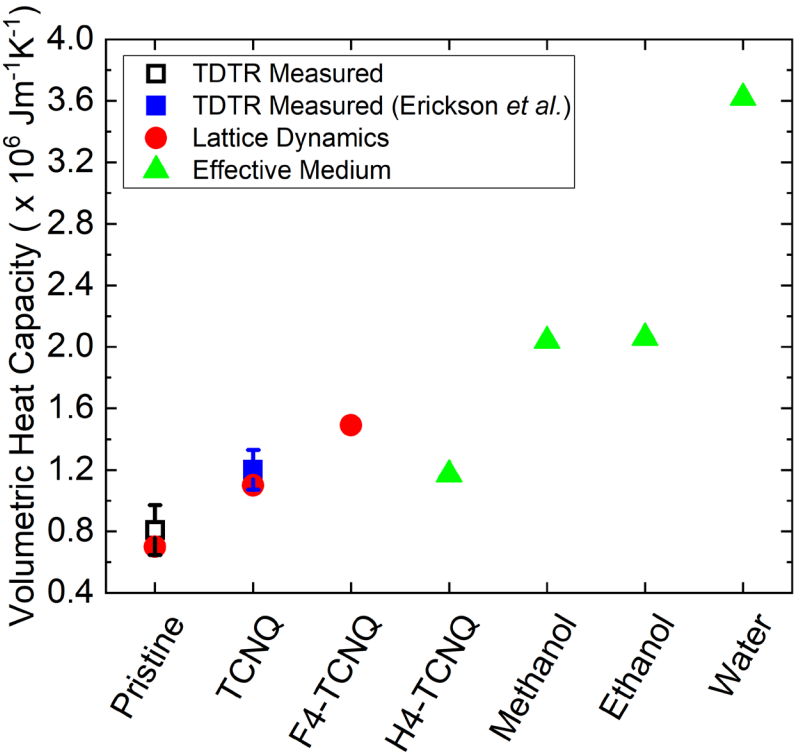


Figure 5.6: Volumetric heat capacity for the pristine and guest@HKUST-1 samples measured via TDTR. The TDTR measured heat capacities for the pristine and TCNQ@HKUST-1 match up quite well. The TCNQ@HKUST-1 heat capacity was obtained from Erickson *et al.*[274] Due to the low concentration of $N_2$ (g) molecules predicted to reside in the pores, and the low molecular weight, the pristine value for heat capacity was assumed for the $N_2$@HKUST-1 TDTR analysis.

water, to calculate the required densities and heat capacities. I assumed the pores were fully saturated when infiltrated with methanol and ethanol, and 82% saturated with water, according to previously reported adsorption isotherms at a porosity void fraction of 0.7.[260] Lastly, due to the low adsorption concentration predicted from nitrogen adsorption isotherms in HKUST-1 at room temperature under low pressure,[259] the pristine value for heat capacity was used for the $N_2$@HKUST-1. Figure 5.6 details the volumetric heat capacities that were used in the thermal model analysis for all the HKUST-1 samples measured with TDTR. I experimentally measured the room temperature thermal conductivity of the $SiO_2$ and the TBC between the 65-80 nm Au and $SiO_2$ ($G_{Au/SiO2}$) on each substrate before the MOF's were deposited using the standard TDTR sample geometry, where the laser pulse is incident on the air/metal side of the metal/glass sample

(Table A 1). Further, the heat model is very sensitive to the thickness of the metal film transducer, which was measured via profilometry. The room temperature thermal conductivity of the Au was obtained using four-point probe ($\kappa_{Au} = 312$ $Wm^{-1}K^{-1}$) and the thicknesses of the thin film SURMOFs were confirmed through SEM after deposition onto the substrates.

#### *5.2.2.2 ZIF-8*

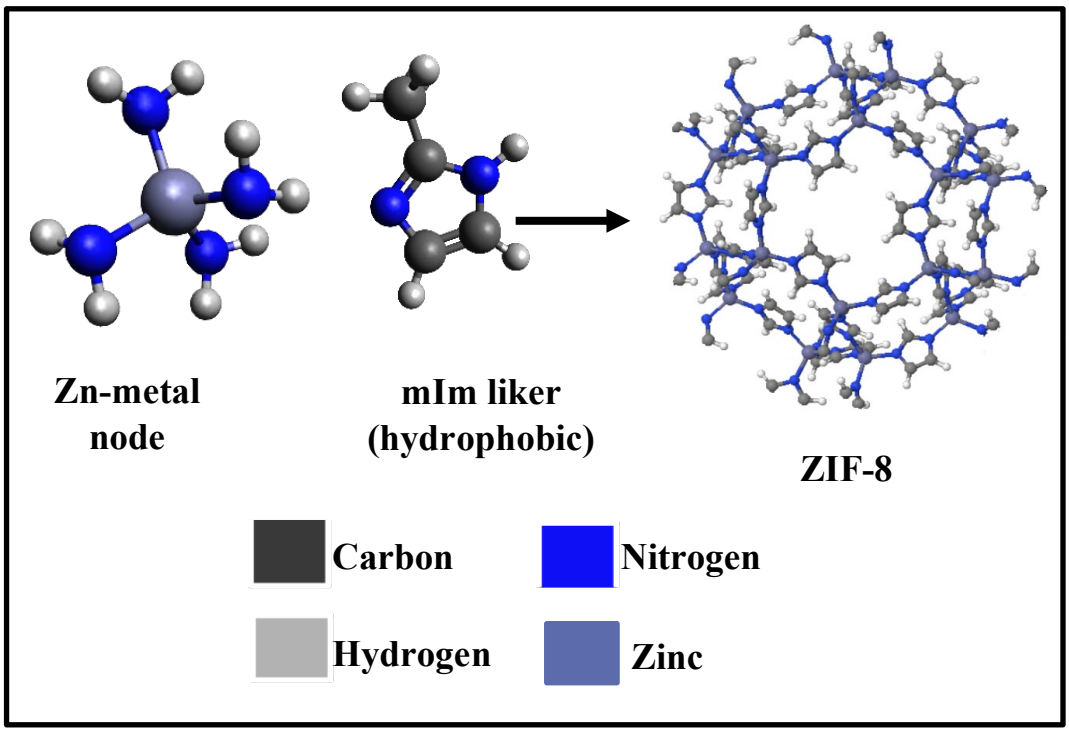


Figure 5.7: The metal node ($Zn^{2+}$ cations) fully tetrahedrally coordinated to four hydrophobic mIm linker ligands to form the ZIF-8 MOF.

ZIF-8 contains a cubic unit cell that forms a SOD zeolite-like topology with a space group of *I*-43*m* (Table 5.1).[262] It is composed of Zn atoms that are tetrahedrally coordinated by four N atoms of 2-methylimidazolate (ligands) to form flexible cage-like pores. Figure 5.7 shows the coordination of the ligands fully saturate the coordination sphere of the $Zn^{2+}$ nodes so that ZIF-8 does not contain OMS, in contrast to HKUST-1.[262,267] It is interesting to note that MOFs that do not contain OMS typically contain somewhat lower porosity compared to OMS-MOFs, which

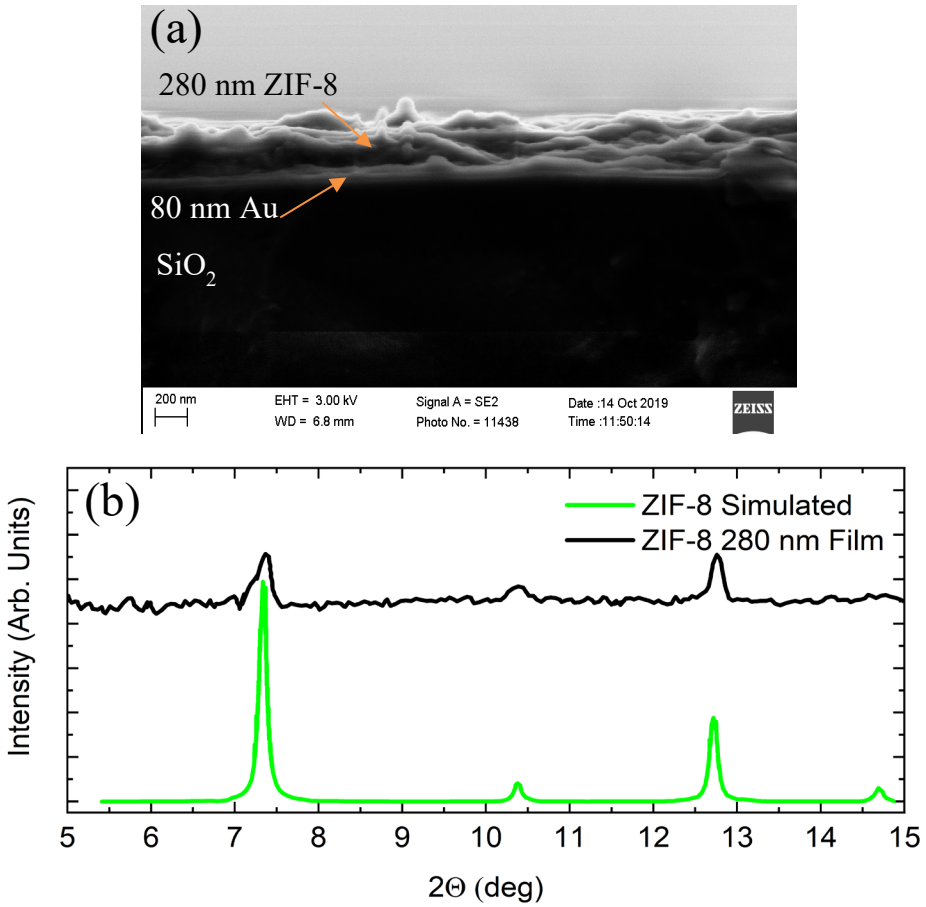


Figure 5.8: (a) SEM micrographs of the 280 nm ZIF-8 film with the substrate (80 nm Au/$SiO_2$) and ZIF-8 MOF layers distinguished. (b) XRD pattern on the 280 nm ZIF-8 thin film is consistent with simulations.

leads to lower gas uptake and also lower heats of adsorption at low loading.[275,276] These observations of larger heat of adsorption experienced in OMS-MOFs is evidence for the stronger adsorbate-MOF interactions. While HKUST-1 (OMS MOF) and ZIF-8 (non-OMS MOF) contain similar porosities, this generalized trend indicates that the nature of an open metal site may promote very different adsorbate-host interactions in ZIF-8 compared to the HKUST-1.

ZIF-8 thin film was characterized using SEM and XRD to confirm both the conversion efficiency of the ALD deposited metal oxide layer during fabrication (Section 5.2.1.3) by measuring the thickness of the ZIF-8 film, and the crystallinity. The SED images shown in

Figure 5.8 (a)(b) show the 280 nm ZIF-8 film deposited on the metal side of an Au/$SiO_2$. The thickness of the ZIF-8 film reveals a 99% conversion efficiency from the 16.7 nm ZnO layer that was deposited onto the substrate. The SEM images also confirm good adhesion of the ZIF-8 film to the Au layer. Since the conversion efficiency of the ZnO layer was not 100%, there may exist a thin layer of ZnO between the Au interface and the ZIF-8 film. Assuming a thin film ZnO thermal conductivity of 2.3 $Wm^{-1}K^{-1}$,[277] and a layer thickness of ~3 nm, the Kapitza resistance for this layer is negligible, and does not need to be considered in the TDTR data analysis. Further, XRD patterns (Figure 5.8 (c)) were also collected on the ZIF-8 thin film directly after fabrication and confirms the expected crystallinity. The XRD pattern for the sample indicates polycrystalline growth without a preferred orientation, since the highest intensity peaks occur at both a $2\Theta \approx 7.33^{o}$ and $2\Theta \approx 12.76$. This indicates that the predominate crystal orientation is not in the [110] direction, as suggested by the simulation. Indeed, others have shown that a decrease in the amplitude for the diffraction peak occurring at $2\Theta \approx 7.33^{o}$ may result from slight hydrothermal degradation due to film exposure to water during processing and moisture in storage.[121]

The thermal conductivity ($\kappa$) and volumetric heat capacity ($C_v$) for the ZIF-8 thin film in this work were both measured with TDTR. In order to understand the sensitivity of the measurement to each parameter of interest, a sensitivity analysis[177] was performed to the ratio ($-V_{in}/V_{out}$) at two pump modulation frequencies (1.4 MHz and 8.8 MHz). The results of the sensitivity analysis are shown in Figure 5.9 (a) and show that at a pump modulation frequency of 1.4 MHz, the TDTR measurement is most sensitive to the thermal conductivity ($\kappa$) of the ZIF-8 MOF, and has virtually no sensitivity to the MOF's heat capacity. At a pump modulation frequency of 8.8 MHz however, the signal is approximately equally sensitive to both material parameters. Therefore, data collected at 1.4 MHz was fit for $\kappa$, since the thermal model is not sensitive to the

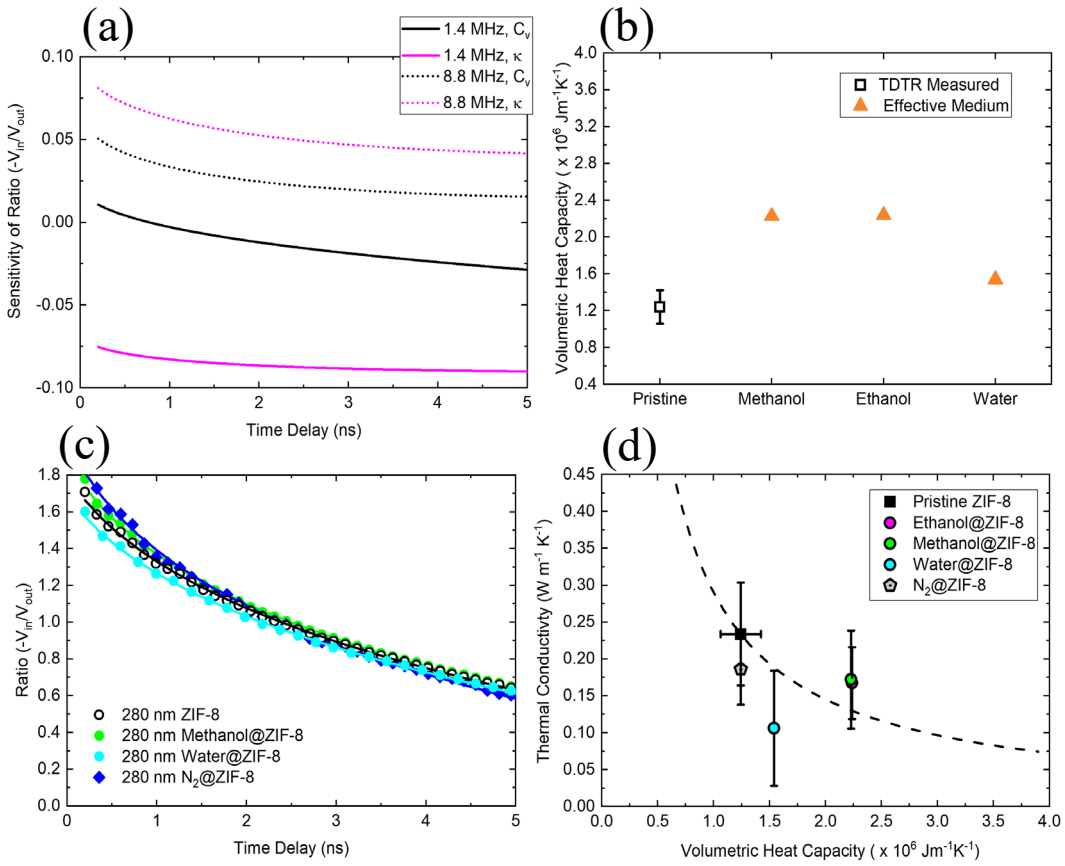


Figure 5.9: (a) Sensitivity analysis of ZIF-8 volumetric heat capacity ($C_v$) and thermal conductivity ($\kappa$) performed at a modulation frequency of 1.4 MHz and 8.8 MHz, fit to the ratio. (b) TDTR measured heat capacity for the ZIF-8 film and calculated effective medium heat capacity for the guest@ZIF-8 samples. (c) Representative raw TDTR data (symbols) and fits (lines) taken at a modulation frequency of 8.8 MHz, for the 280 nm ZIF-8 film in pristine activated form and infiltrated with a liquid (methanol, and water) and gaseous ($N_2$) guest species. The other adsorbates are left off for clarity. (d) The experimentally measured thermal conductivity of pristine and infiltrated ZIF-8 as a function of volumetric heat capacity. The dotted line indicates the corresponding thermal conductivity required to maintain the equivalent thermal effusivity measured for the pristine ZIF-8 as the volumetric heat capacity is increased.

heat capacity in this regime. Then the resulting $\kappa$ measured at 1.4 MHz, was used as an input to the thermal model to fit for both the heat capacity and thermal conductivity at 8.8 MHz This fitting procedure was iterated until the values between the fits at 1.4 MHz and 8.8 MHz converged. The measured volumetric heat capacity for the pristine activated ZIF-8 film is shown in Figure 5.9 (b). The heat capacities for the ZIF-8 infiltrated with methanol, ethanol, and water were calculated using effective medium theory. Due to ZIF-8's high affinity towards alcohols,[234] the volumetric

heat capacity for ethanol and methanol infiltrated ZIF-8 were performed under the assumption of fully loaded pores at a pore void fraction of 0.59.[261,262] Since ZIF-8 is inherently hydrophobic due to the organic imidazolate linkers,[278] the effective medium calculation assumed only a very small water uptake would occur; in accordance to reported water adsorption isotherms of ZIF-8 (~0.5 mmol/g),[234] and therefore the water@ZIF-8 contains a volumetric heat capacity that is closer to the measured pristine ZIF-8 value. The pristine value for the heat capacity was used for the $N_2$@HKUST-1 due to the similarity in density between $N_2$ (g) and ambient air. Representative TDTR data are shown in Figure 5.9 (c) for the ZIF-8 film in pristine, activated form and infiltrated with liquid (methanol and water) and gaseous ($N_2$) adsorbates.

TDTR measures the thermal effusivity ($\alpha_{eff} = \sqrt{\kappa C_v}$) of the ZIF-8. Therefore, in order to accurately measure the thermal conductivity, the volumetric heat capacity must be known. If the effusivity were to stay the same from sample to sample, an increase of the heat capacity to the thermal model would result in a reduced thermal conductivity according to

$$\kappa = \frac{\alpha_{eff}^2}{C_v}. \tag{5.1}$$

The strong overlap in the raw TDTR data from sample to sample (except for the water@ZIF-8 at early times), indicates that the thermal effusivities are similar, despite an increase in the heat capacity. Figure 5.9 (d) shows the TDTR measured thermal conductivity results for the ZIF-8 films as a function of volumetric heat capacity, and also shows the thermal conductivity required to maintain a constant thermal effusivity equivalent to the pristine ZIF-8 sample (539 J $s^{-1/2}$ $m^{-2}$), as a dashed line. Here, it is evident that the thermal conductivity trends for the infiltrated ZIF-8 species follow the dashed trendline representative of a constant thermal effusivity, however within uncertainties, no discernable change in the thermal conductivity can be determined. This shows

the limitations of the TDTR measurement, where uncertainties within the assumed volumetric heat capacity can make it difficult to tease out the effects of adsorbates on the thermal conductivity.

## 5.3 Results: The Effects of Adsorbates on Thermal Processes of HKUST-1

This section discusses the effects of gas, liquid, and solid adsorbates on the thermal transport processes of HKUST-1 that span a range of guest-host/adsorbate-MOF interactions including weak van der Waal interactions ($N_2$), a mix of coordinated and uncoordinated interactions (water, methanol, ethanol), and full coordination producing different degrees of orbital overlap (TCNQ, $F_4$-TCNQ, $H_4$-TCNQ). The experimental results of thermal conductivity of the liquid and solid guest@MOF samples are supported by molecular dynamics (MD) simulations and MD-derived spectral energy density (SED) calculations to elucidate the role of the guest-host interaction on thermal transport processes of infiltrated HKUST-1. Further, harmonic lattice dynamics (LD) was performed on the solid@HKUST-1 systems to capture the effects of bond strength of the guest/host interaction on thermal processes within the MOF. The molecular structures of the HKUST-1 building block and guest molecules are detailed in Figure 5.10.

Before infiltration, the HKUST-1 pristine framework is electrically neutral; it has a partially positive charge on the $Cu^{2+}$ atoms which is balanced by the partially negative localized charge on the carboxylate units within the BTC linker of the polymeric crystal lattice.[269] This neutrality is preserved upon infiltration with the liquid and gaseous adsorbate species, since they all contain neutral formal charges. However, this is not the case for the solid adsorbates, which are charge-accepting molecules that coordinate to differing degrees to the OMS of the HKUST-1 pore. HKUST-1 was infiltrated with three charge-accepting molecules, listed here in order of decreasing guest/host bond overlap: tetracyanoquinodimethane (TCNQ), 2,3,5,6-tetrafluoro-

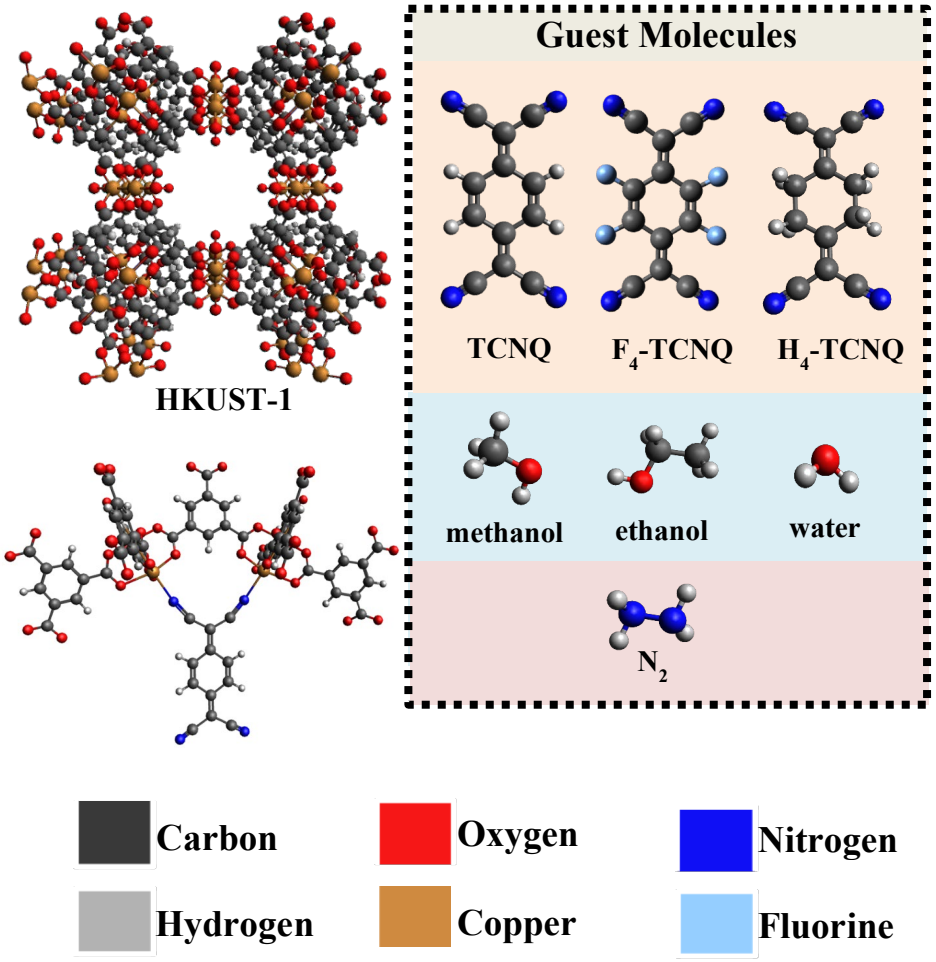


Figure 5.10: Schematic of the building blocks and guest molecules of the guest@HKUST-1 system including: The Cu II dimer metal node (note that the Cu II dimer shows the $Cu^{2+}$ coordinated to eight oxygens from four separate BTC molecules), BTC linker, and TCNQ, $F_4$-TCNQ, $H_4$-TCNQ, methanol, ethanol, and $N_2$ adsorbates. The bottom left illustration captures the coordination between the OMS and TCNQ guest molecule within the HKUST-1 pore.

7,7,8,8-tetracyanoquinodimethane ($F_4$-TCNQ), and (cyclohexane-1,4-diylidene)dimalononitrile ($H_4$-TCNQ). These guest molecules have previously been shown to enhance the electrical conductivity of the guest@MOF system more than six orders of magnitude, by introducing covalent and noncovalent interactions which create continuous charge transport pathways through long range order of the donor bridge acceptor sites, and mixing between the electronic excited and ground states.[225,227] TCNQ, $F_4$-TCNQ, and $H_4$-TCNQ are strong π-acids that accept electrons from

the Cu(II) dimers of the HKUST-1. Talin *et al.* showed that loading of the TCNQ guest species into the HKUST-1 results in approximately eight molecules per unit cell, or one molecule per pore.[238] Additionally, there exists strong evidence of coordination occurring between the terminating nitrile groups of TCNQ (which are *cis* to each other) and the OMS of the MOF, which is thought to be responsible for the emergence of electronic conductivity upon infiltration (Figure 5.10).[227] Since the degree of charge transport is closely related to the crystal binding energy, I use the predicted metric for donor/acceptor electronic coupling from Allendorf *et al.* to qualitatively rank the degree of guest/host orbital overlap between each guest species.[227] TCNQ provides the largest coupling with the MOF, owing to a high degree of orbital overlap between the TCNQ and the Cu d($z^2$) orbitals within the metal node of the MOF. Fluorination of TCNQ results in added tuning, where an increase in electronegativity causes an overall reduction in electrical conductivity by disrupting *d* orbital overlap between the guest and host.[227] Lastly, $H_4$-TCNQ produces the least charge transport of all guest molecules, due to the lack of a conjugated $\pi$ network, and therefore has the smallest orbital overlap.

To support the thermal conductivity measurements, the HKUST-1 SURMOF thin films (250 – 400 nm) and thick polycrystalline samples (5.5 μm) of pristine and infiltrated HKUST-1 were extensively characterized with scanning electron microscopy (SEM), X-ray diffraction (XRD), infrared spectroscopy, nanoindentation and pump-probe Brillouin scattering (see Section 5.2.2.1, Figure 5.4) to examine the structural and mechanical properties, and the coordination environment. Further, I offer an interpretation of the experimental results with atomistic MD, SED, and LD simulations, performed by my collaborator (Dr. Hasan Babaei), to ascertain the guest-host interactions on thermal conductivity, vibrational mode character, and scattering rates. Due to the complex interplay of order and disorder in these large unit cell crystals

with addition of a guest, I frame my interpretation of the simulated and experimental results from a disordered framework perspective. I presume that a combination of extended (phonon-like propagating modes known as propagons, and non-propagating diffusons) and localized (locons) modes are present in the MOF systems.[50,82,279] Ultimately, the results show that the thermal transport in these infiltrated porous crystalline systems is not influenced by a loading dependent structural change, but rather an increase in extrinsic vibrational scattering introduced by adsorbate-MOF collisions, as well as adsorbate induced modifications to the vibrational structure resulting in hybridization with low frequency modes and concomitant increase in mode localization. The infiltrated MOF materials have a higher degree of localized modes at all frequencies compared to the un-infiltrated pristine states that are not significantly affected by the mass or bonding strength of the guest species.

In Figure 5.11, the measured thermal conductivity is plotted as a function of thickness for activated pristine and infiltrated samples. For clarity, where multiple MOFs of the same thickness were measured, the figure reports the averaged value (refer to Appendix A: Table A 1, for full sample details). The results show that infiltrated HKUST-1 samples experience a reduction in thermal conductivity, regardless of the composition or bonding morphology of the adsorbate. Additionally, the lack of dependance of the thermal conductivity on sample thickness suggests that the heat carrying mean free paths of propagons are much less than the film thicknesses or grain sizes (~300 nm confirmed from the XRD (see Section 5.2.2.1)), which is consistent with prior reports on the mean free paths in these systems.[73,280] Further, the lack of a classical size effect also signifies that the dominant vibrational modes that contribute to the thermal conductivity of the material may be non-propagating (e.g., diffusons).[42,50]

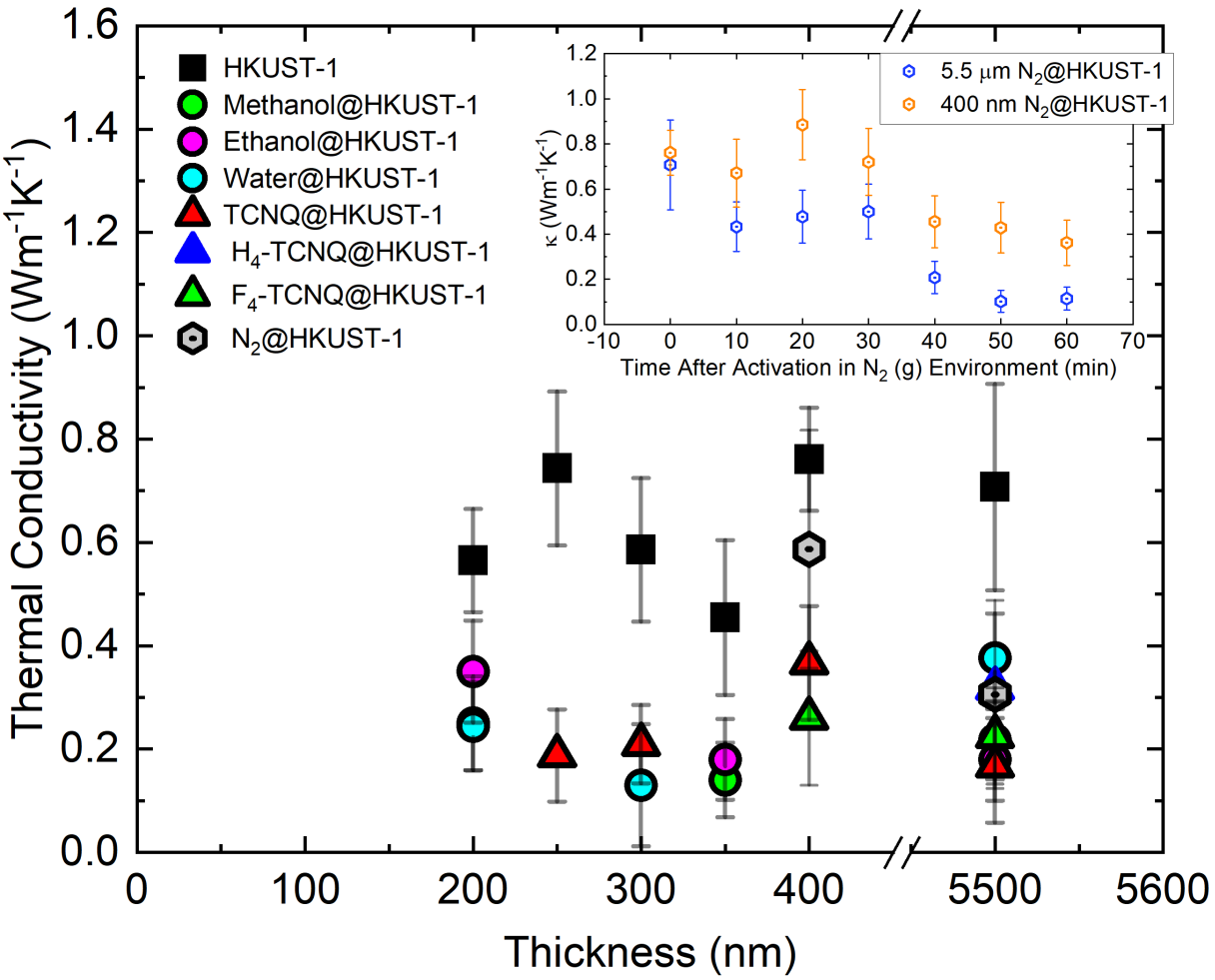


Figure 5.11: Experimentally measured thermal conductivity vs. thickness, of activated pristine and infiltrated HKUST-1. These results show the averaged thermal conductivity when multiple samples were measured. Table A 1 lists the details of all of the individual samples. The inset shows a time series of the thermal conductivity of $N_2$@HKUST-1 for the 400 nm thin and thick samples subject to an $N_2$ (g) rich environment at ambient air pressure for an hour. All error bars represent an uncertainty of ± 3 nm in the transducer layer thickness and scan-to-scan variability from three to seven measurements taken at different locations on the sample surface.

The inset in Figure 5.11 shows the time series for the thermal conductivity of HKUST-1 during infiltration with $N_2$ (g). As the gas is allowed time to diffuse into the 400 nm thin and 5.5 µm thick MOF pores, an evident trend emerges where the reduction in thermal conductivity is more significant over longer times. This is likely due to the presence of a higher concentration of adsorbed gas in the MOF at longer time intervals. Previous reports of nitrogen

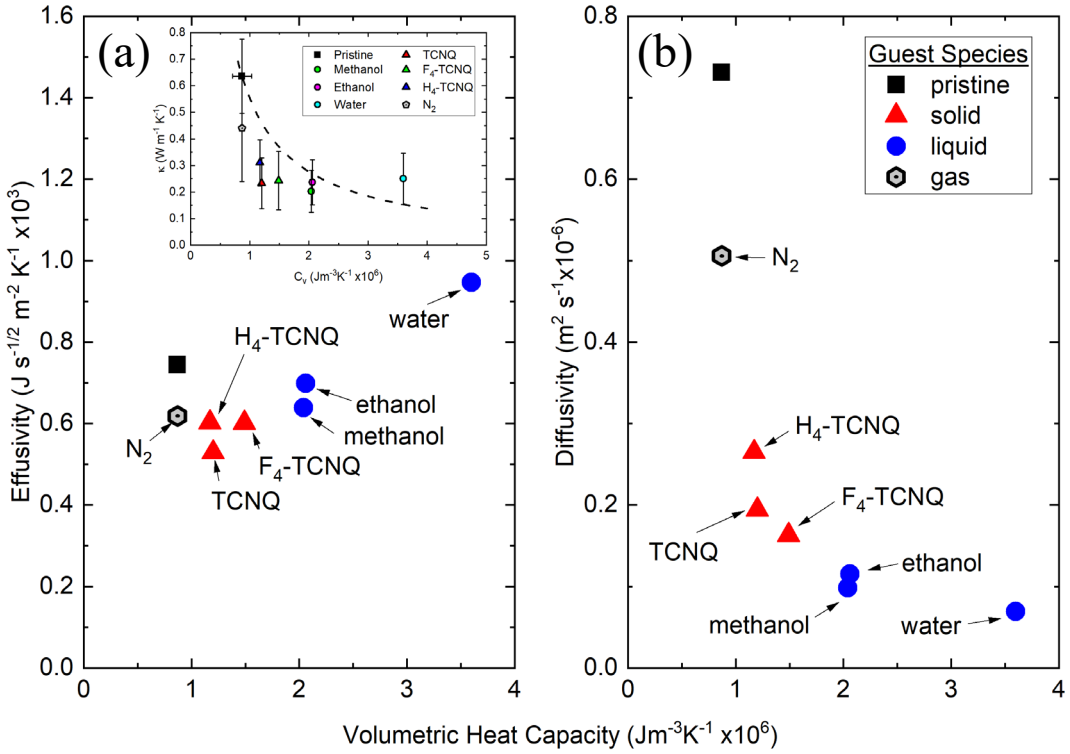


Figure 5.12: (a) Thermal effusivity ($\sqrt{\kappa C_v}$) and (b) thermal diffusivity ($\kappa/C_v$) for the pristine and guest infiltrated HKUST-1 films. The inset in (a) shows the thermal conductivity vs. the volumetric heat capacity for each infiltrated species measured with TDTR. The dotted line represents the thermal conductivity value that would provide the equivalent thermal effusivity of the pristine activated HKUST-1 as a function of volumetric heat capacity described by Eqn. 5.1.

adsorption isotherms of HKUST-1 exhibit a type-I isotherm trend, according to IUPAC classification.[259,281] This indicates that adsorption of nitrogen is limited by the accessible micropore volume, rather than by the internal surface area of the HKUST-1, which is a common characteristic for the adsorption of gases in microporous solids, whose pore sizes are not much larger than the molecular diameter of the adsorbate (such as HKUST-1).[282] Paired with nitrogen adsorption isotherms, the sensitivity of the thermal conductivity of HKUST-1 to the presence of adsorbates could provide an avenue to study the mass diffusivity and precise diffusion kinetics of the system. However, such a study is currently outside the scope of the research due to the inability to measure the pressure inside the Linkam stage while performing TDTR measurements.

Additionally, previous MD work by Babaei, McGaughey, and Wilmer pointed out that while adsorbed gas density increases with time, it actually decreases as the MOF thickness increases.[268] Therefore, an overall increased adsorbed gas density in the thicker sample is an unlikely culprit for its reduced thermal conductivity in comparison to the 400 nm thin film. The difference is more likely linked to variance in morphology and the presence of defects (indicated by BET measurements) in the thicker samples due to different fabrication techniques.

In the experimental geometry, TDTR is primarily sensitive to the thermal effusivity ($\sqrt{\kappa C_v}$) of the sample (except for the thinnest 200-250 nm SURMOF HKUST-1 sample, where TDTR is sensitive to both thermal conductivity and heat capacity simultaneously, as discussed in Section 3.1.3), where the thermal conductivity ($\kappa$) is the fitting parameter and the volumetric heat capacity ($C_v$) is taken as a known parameter (either measured, calculated from LD, or obtained from the literature[226]). Effective medium theory would predict that an increase in the density of the material (upon loading) would result in an increase in the thermal conductivity due to an increase in the density of the porous composite (Figure 5.13 (d) inset). I measure a decrease in the thermal effusivity ($\alpha_{eff}$) upon loading with all of the guests, except water, indicating that the drastic drop in thermal conductivity cannot be explained by the increase in the density or volumetric heat capacity (Figure 5.12 (a)).

The inset in Figure 5.12 (a) plots Eqn. 5.1 as a function of volumetric heat capacity in addition to the thermal conductivities for the pristine and infiltrated HKUST-1 samples. While the infiltrated HKUST-1 thermal conductivities follow the trend captured by Eqn. 5.1, the fact that they do not sit directly on the line implies a more complex heat transfer picture where the adsorbate acts to introduce compositional disorder into the system. In fact, previous molecular dynamics studies on gas loaded MOF systems have reported similar thermal trends, concluding that the

reduction in $\kappa$ upon infiltration is due to higher vibrational scattering rates introduced by the collisions between gas molecules and the MOF lattice sites. [283]

All of the adsorbates studied resulted in reduced thermal conductivities ranging from 40% to 80% depending on the guest molecule. In addition to this, I find that the thermal diffusivity $(\kappa/C_v)$ is even more greatly impacted than the thermal conductivity, by the presence of the adsorbates (Figure 5.12 (b)). In the case of adsorbed water, for example, a threefold thermal conductivity reduction, coupled with a sixfold increase in volumetric heat capacity, leads to an 18-fold reduction in thermal diffusivity. Since the relevant timescale associated with heat dissipation in rapid adsorption applications is inversely proportional to thermal diffusivity, these results highlight the importance in choosing MOFs with appropriate thermal properties for such applications.

A characteristic decrease in the thermal conductivity of HKUST-1 SURMOF films and thick samples upon infiltration with all guest species is experimentally observed. Figure 5.4 provides direct evidence for the coordination between the solid guests with the HKUST-1 framework, however, as previously discussed, the interaction between the liquid and gaseous adsorbates within the pore is known to a lesser extent. Prestipino *et al.* showed that $H_2O$ (g) present in the pores of HKUST-1 chemically bind to the Cu(II) sites, resulting in significant modifications to the first coordination sphere.[254] This structures a hypothesis of the fundamental chemical nature of the infiltrated species-MOF interaction that can reduce the thermal conductivity of guest@MOFs. Specifically, hydration results in the distortion of the intrinsic Cu-O bonds in the Cu(II) dimer and lengthening of the Cu-Cu distance resulting in an overall increase in cell volume. Perhaps the polar liquid adsorbates (methanol, ethanol) may create similarly complex guest-host interactions. Therefore, one might posit that the fundamental chemical interactions between the

guest molecules and HKUST-1 pore are responsible for driving down the thermal conductivity in the materials studied in his work.

To investigate this further, we turn to MD and SED to resolve the effects of bonding morphology (orientation and number) on this observed reduction in thermal conductivity and vibrational scattering. Allendorf *et al.* proposed that each TCNQ within a pore likely forms two covalent bonds once infiltrated, occurring between two *cis* terminating nitrile groups and the Cu(II) dimers within the open metal sites (OMS) (Figure 5.10).[227] Others have identified other possible phases of TCNQ within HKUST-1 including a neutral and dimeric species that do not coordinate to the open $Cu^{2+}$ sites.[271] Additionally, the spatial distribution of TCNQ within single crystal HKUST-1 has found that the diffusive properties of TCNQ occur heterogeneously within the MOF, where it concentrates at the crystal edges.[236] The pore diffusion of $F_4$/$H_4$-TCNQ has not been as thoroughly investigated. These previous works help to inform the likely morphology of the solid guest infiltrated films, yet there still remains uncertainty in how different variations in the concentration and bonded orientation of guest molecules within pores will affect the thermal conductivity of the guest@MOF system.

MD simulations were performed with liquid (methanol, ethanol, and water) adsorbates in a free unbound state within the pores, and a solid (TCNQ) guest, where the bonding morphology was varied by changing the number of bonds and concentration of guest molecules in the pore. Figure 5.13 (a)-(c) illustrates the different bonding nature of the systems studied via MD. Here, the simulations consider TCNQ infiltrated in three different states within the MOF pore: formation of two covalent bonds in a *cis* configuration (Figure 5.13 (a)), four covalent bonds forming a full bridge across the pore (Figure 5.13 (b)), and an unbonded “free state” (Figure 5.13 (c)), which is similar to the interaction modeled for the liquid adsorbates. The concentration of

molecules within the large 9 x 9 Å pore ($n_p$) in HKUST-1 was also varied from one to ten for the TCNQ. Since the unit cell of HKUST-1 contains one large pore and many interconnected channels and small pores which are all accessible to the smaller liquid adsorbates, MD simulations for methanol, ethanol, and water were performed where the adsorbates had access to any areas of void within the HKUST-1 unit cell, and are denoted according to the number of molecules per unit cell ($n_{uc}$). The methanol, ethanol, and water adsorbate densities were set to 168.75, 98, and 369 molecules respectively, which were considered to saturate the unit cell. I use the nomenclature '$\text{guest}_{n_{p/uc}=x,\ b=y}$@HKUST-1' to indicate the adsorbed bonding conditions, where $n_p$ is the number of molecules per pore, $n_{uc}$ is the number of molecules per unit cell, and $b$ is the number of covalent bonds formed with the host ($b$=0 indicates an unbound free state). I estimate that the experimental results for the gas adsorbate resembles the '$n_{uc}$=x, $b$=0' case, the liquid guests resemble a combination of the '$n_{uc}$=x, $b$=0' and '$n_{uc}$=x, $b$=1' cases and the solid guests resemble the '$n_p$=1, $b$=2' MD case, however additional phases resembling the '$n_p$=1, $b$=0' and '$n_p$=2, $b$=0' structures have also been reported to exist within the TCNQ@HKUST-1 system.[271]

The room temperature MD and experimental results plotted in Figure 5.13 (d) for the morphological study of guest-host interactions show a reduced thermal conductivity upon all loading cases. In the MD, the greatest reduction occurs for the highest adsorbate loading density in an unbound state (for TCNQ, methanol, and ethanol), and the smallest reduction occurs for a single TCNQ molecule bonded on all sides by all four terminating nitrile groups. In the former case, non-bonded TCNQ or liquid molecules are free to collide with the framework and scatter vibrational modes, resulting in the highest reduction in thermal conductivity. A larger number of guest molecules results in an increased reduction, as there is a higher frequency of adsorbate-framework collisions. This is what would be expected in the case of liquid adsorbates or gas

adsorbates that are saturated within the MOF pore. In the latter case, the TCNQ is more sterically hindered and oriented within the pore, forming a 'thermal bridge', which results in new heat transfer pathways that compete with the vibrational scattering introduced by the guest, resulting in the smallest overall reduction in thermal conductivity. The intermediate cases involve the TCNQ bonded on one side to the pore (*b=2*), where the TCNQ can still rattle, but has less freedom to collide with the adsorbate framework.

Additionally, the MD and experimental results for the water@HKUST-1 stand out compared to the other infiltrated systems investigated. The MD results predict that adsorption with water produces a smaller reduction in thermal conductivity than the other liquid adsorbates modeled in an unbound state. In fact, the MD predicted reduction by the water adsorbate is closer to the fully bonded TCNQ ($n_p=1, b=4$). This is likely a result of the thermal conductivity of water, which is ~3x higher than methanol and ethanol, which may compete with the adsorbate-framework collisions responsible for the reduction in thermal conductivity upon adsorption. In comparison, the measured thermal conductivity of water@HKUST-1 ($0.25 \pm 0.09$ $Wm^{-1}K^{-1}$) is less than both the pristine HKUST-1 ($0.63 \pm 0.13$ $Wm^{-1}K^{-1}$) and also what would be expected for bulk liquid water occupying the same contiguous void space ($0.61$ $Wm^{-1}K^{-1}$ x 68% void fraction = $0.41$ $Wm^{-1}K^{-1}$). This experimental result shows that while the adsorbate reduces the thermal conductivity of the HKUST-1, confinement in the MOF pore geometry also acts to reduce the intrinsic thermal conductivity of the liquid adsorbate. This is an important conclusion, because it highlights the shortcomings of effective medium theory for properly predicting the thermal transport in this MOF-adsorbate system (Figure 5.13 (d) inset).

Without any direct evidence for the bonding experienced by the polar liquid and gaseous guest molecules within the HKUST-1 pores, I also compare the mass effects of the guests

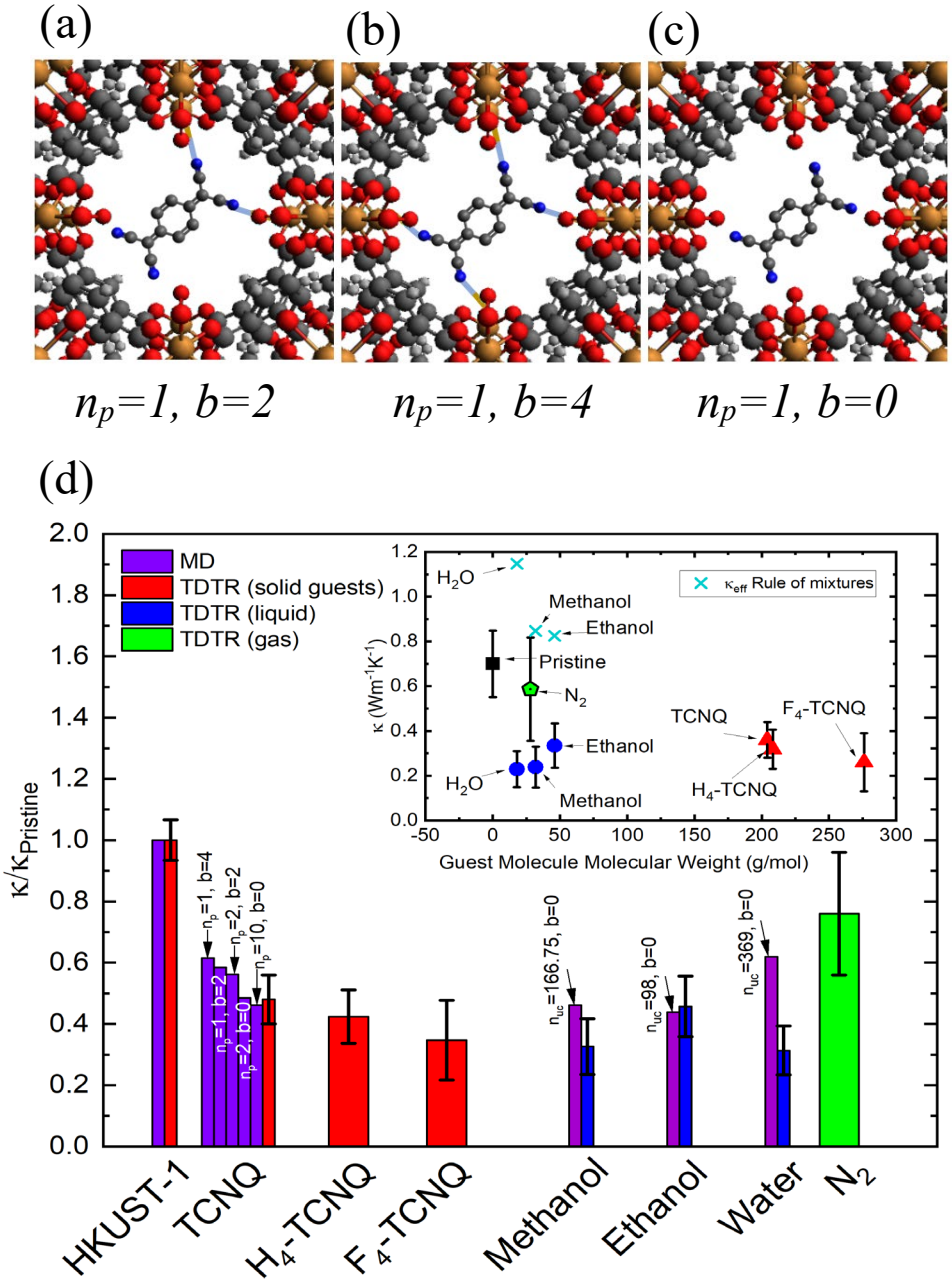


Figure 5.13: (a)-(c) Illustrations for the MD simulations where the nomenclature '$n$=x, $b$=y' indicates the adsorbed bonding conditions, here $n_p$ is the number of adsorbate molecules per pore, $n_{uc}$ is the number of adsorbates per unit cell, and $b$ is the number of covalent bonds formed between the guest and host ($b$=0 indicates unbound, free state). (a) Shows the formation of two covalent bonds forming on one side (*cis* to each other) of a single TCNQ molecule ($n_p$=1, $b$=2), (b) illustrates the case where a single TCNQ creates four covalent bonds with the host ($n_p$=1, $b$=4), and (c) illustrates an unbonded "free state' where a single TCNQ molecule resides in each pore ($n_p$=1, $b$=0). The concentration of molecules for the solid TCNQ adsorbates within the pore was varied from one to ten. Since the HKUST-1 unit cells contain one large pore and a network of channels and small pores that can be filled by the smaller liquid adsorbates, the MD for the liquid adsorbates was performed at a density of adsorbates per unit cell ($n_{uc}$) instead of per pore with

*b=0*, where $n_{uc}$ is considered fully saturated. (d) Normalized room temperature thermal conductivity comparing the MD (purple) to the TDTR measured results for the HKUST-1 and solid (red), liquid (blue), and gaseous (green) guest@HKUST-1. All thermal conductivities have been normalized to the thermal conductivity of the pristine HKUST-1 ($\kappa_{Pristine}$). I note the experimental data for the 400 nm thin films are shown for TCNQ, $F_4$-TCNQ, and $N_2$. The $H_4$-TCNQ results are from the 5.5 μm thick samples, and the methanol, ethanol, and water are from the 200 nm samples. The inset shows the experimentally measured thermal conductivity for the guest molecules as a function of molecular weight, and includes the effective medium theory predicted results for the liquid adsorbates.

to the total thermal conductivity of the infiltrated MOF system by plotting the experimentally obtained thermal conductivity to the molecular weight of the guest molecule (Figure 5.13 (d) inset). The heaviest guest ($F_4$-TCNQ) is over an order of magnitude more massive than the lightest guest ($H_2O$). I note that the liquid guests fill the pores of HKUST-1 with a liquid void fraction between 82%-100% (98-369 molecules per unit cell), and the TCNQ guests average one molecule per pore.[238,260] $N_2$ gas adsorption occurred at ambient pressures, which likely resulted in a low concentration of $N_2$ guest molecules in the pore (<1 mmol/g), according to nitrogen adsorption isotherms for HKUST-1.[259] The experimental results for the solid guest molecules compared against the liquid polar guest (methanol, ethanol, water) and $N_2$ gas, do not show the emergence of an obvious guest dependent thermal trend; however it is possible that the effects of bonding morphology revealed from the MD may fall within the uncertainty of my experimental measurements. The MD and experimental results show a decrease in thermal conductivity upon infiltration, and neither the mass nor the bonding morphology of the guest suitably predicts the magnitude of the reduction.

MD-derived SED calculations were performed in the [100] crystallographic plane before and after adsorption with liquid and solid guests, to further elucidate the adsorbate-induced thermal conductivity reduction via the extrinsic scattering of low frequency vibrational modes introduced by the guests.[284,285] SED demonstrates that the effect of the adsorbate in each case

(water, methanol, ethanol, and TCNQ) was to reduce vibrational mode lifetimes. Figure 5.14 provides the SED results for water, methanol, and TCNQ. The effects of the liquid adsorbates, in a free unbound state (*b=0*) are so drastic that the peaks disappear (i.e., no vibrational modes exist) for modes less than 2.5 THz, therefore a scattering rate could not be calculated. The effect of increased vibrational mode scattering from the liquid adsorbates is most pronounced for lower frequency phonons (< 2.5 THz). In the pristine HKUST-1, these low frequency modes are thought to be responsible for carrying the majority of the heat, since they have the longest lifetimes (> 500 ps), compared to the higher frequency phonons which intrinsically have very short lifetimes (1.16 and 0.64 ps for the modes occurring at 56.6 and 91.6 THz, respectively). In this picture, the role of the liquid adsorbate is to scatter the long lifetime, low frequency vibrational modes of the HKUST-1, diminishing the thermal conductivity of the liquid infiltrated system. It is likely that gaseous adsorbates would produce a similar result, where the vibrational mode scattering rate may be reduced as a function of the number of gas molecules in the pore. The SED for the infiltrated TCNQ coordinated to the OMS of the MOF shows a different picture from the liquids, where the scattering rate is not as drastic for low frequency modes, and occur over a broader range of frequencies. Since spectral peaks can be resolved and identified at low frequencies, the mode resolved scattering rates can be calculated, and are shown in the inset of Figure 5.14. In the case of TCNQ@HKUST-1, vibrational mode lifetimes are reduced over a broad range, from approximately 0 – 15.3 THz, upon infiltration. Vibrational mode lifetimes could not be accurately derived above ~3 THz and below ~15.3 THz for the TCNQ@HKUST-1 due to the lack of clearly defined peaks in this regime. Figure 5.14 also shows that the high-frequency modes (>15.3 THz) are relatively unaffected by adsorption, however the lifetimes for the low-frequency modes (0.5-15 THz), are greatly affected by the presence of TCNQ. As mentioned previously, these modes

carry the majority of heat at room temperature and are responsible for the large reduction in thermal conductivity upon guest adsorption measured experimentally. Vibrational mode lifetimes $\lesssim$ 15.3 THz of the TCNQ in a bonded orientation results in shorter lifetimes than in the pristine MOF. In total, the MD and SED suggests that extrinsic adsorbate-MOF collisions increase scattering rates of extended vibrational modes to drive down the thermal conductivity, where an unbound adsorbate is more effective than a bonded adsorbate in diminishing these vibrational mode lifetimes. Figure 5.13 (d) shows that the experimentally measured thermal conductivity of the TCNQ and TCNQ analogue infiltrated MOFs more closely resemble the unbonded, '*b*=0' MD cases, although their true bonding morphology is expected to resemble the bonded '*b=2'*.[286] This suggests that while extrinsic adsorbate/MOF collisions likely play a significant role in diminishing

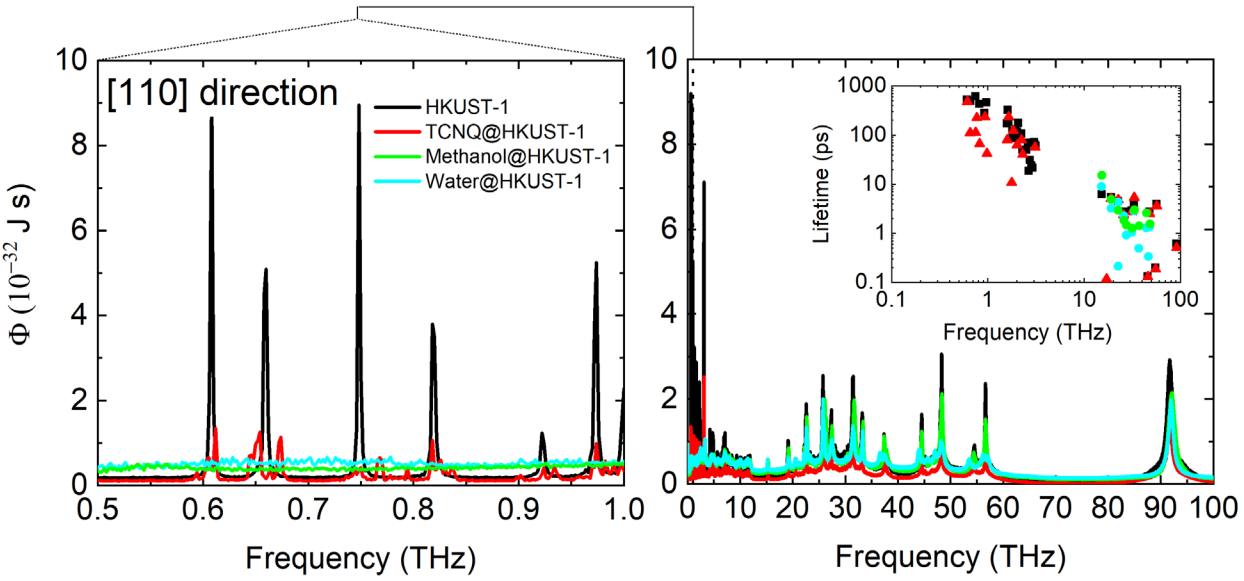


Figure 5.14: Spectral energy density (SED) results of pristine HKUST-1 (black) and infiltrated with TCNQ (red) coordinated though two *cis* terminating nitrile, and water (cyan) and methanol (green) infiltrated to saturation in an unbound state. The MD-derived SED calculations were performed for the {100} crystallographic plane only. Φ is a representation of the extended vibrational mode (i.e. propagon) energy in the frequency domain. The right panel shows the full spectrum of modes, and the left panel shows a zoom in from 0.5-1 THz. The inset shows the corresponding vibrational mode lifetimes. In the pristine case, many sharp peaks are observed at lower frequencies that indicate modes with long lifetimes.

the thermal conductivity, the role of the bond between the adsorbate/MOF may not produce a competing 'thermal bridge' effect as suggested by the MD. Instead, it may further aid in reducing the thermal conductivity though changing the vibrational structure via intrinsic mechanisms (i.e., hybridizations).

The MD and MD -derived SED results allow for the interpretation of the experimental data for the MOFs from the perspective that guest molecules collide with the framework, which is an extrinsic effect that assumes that the vibrational structure is unchanged. This argument has been previously put forth in the literature, and there is sound evidence that this phenomena is significant when adsorbates experience weak interactions when infiltrated into the MOF pore.[231,283] However, in the case where adsorbates coordinate to the OMS, intrinsic mechanisms may also contribute to the reduction in the thermal conductivity of the system in the form of an adsorbate induced change in the vibrational structure.

To investigate the role of the adsorbate bond on the vibrational structure of HKUST-1, I turn to harmonic lattice dynamics (LD) which captures the effects of bond strength of the guest/host interaction. LD simulations were performed only on HKUST-1 infiltrated with solid adsorbates (TCNQ and $F_4$-TCNQ), which capture the effects of bond strength of the guest/host interaction. The infiltrated cases modeled here are similar to the '$n$=1, $b$=2' case modeled in the MD. I reiterate that the infiltrated MOFs are crystalline systems that contain intrinsic disorder stemming both from the introduction of guest molecules, and from their large unit cells. In particular, a large number of atoms in the unit cell can result in low lying optical modes that are close to the acoustic modes which produces an increased phase space for scattering events that promotes reduced vibrational mode lifetimes.[66,129] Indeed, the LD derived dispersions show

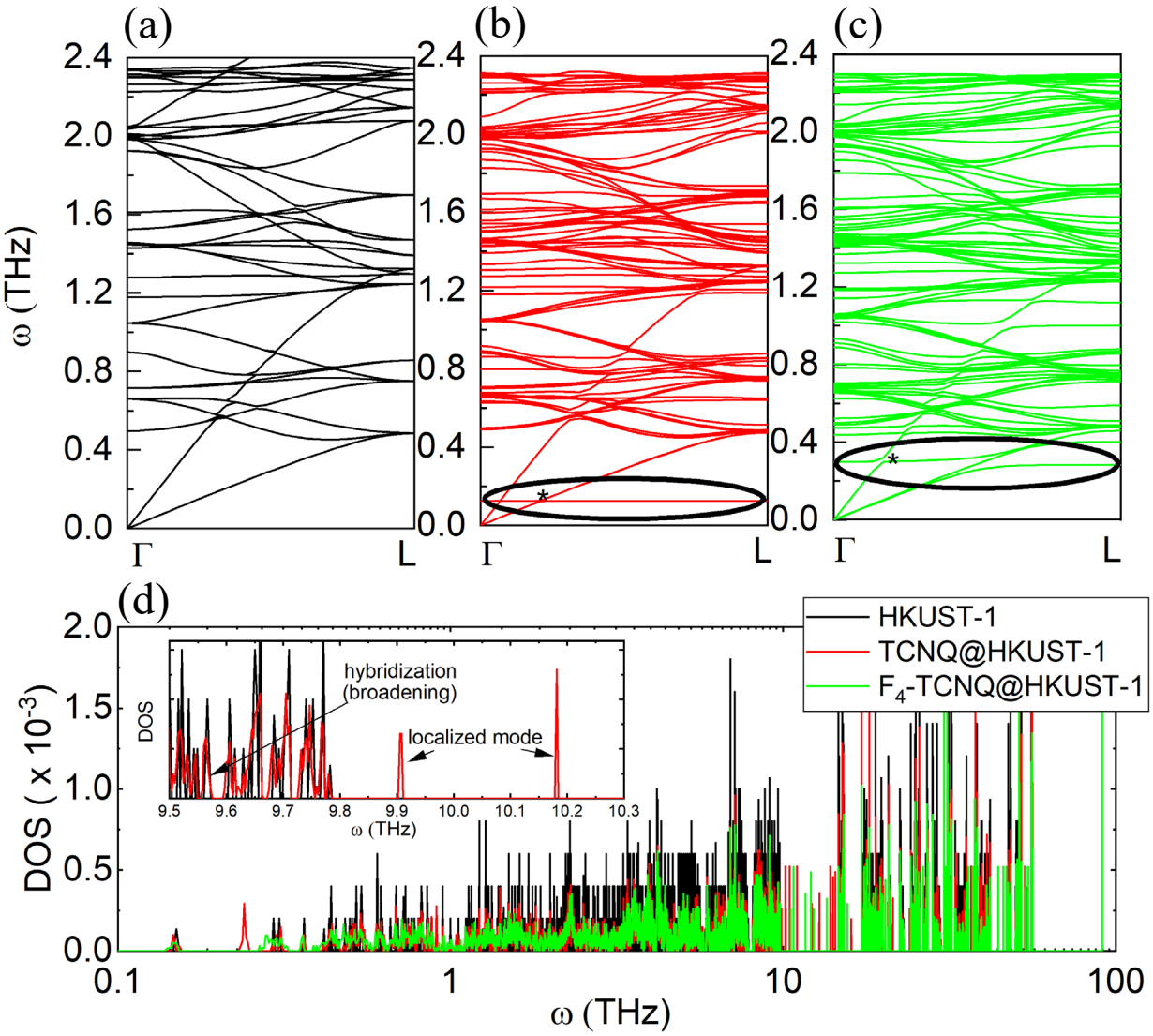


Figure 5.15: LD derived dispersions for (a) pristine HKUST-1, (b) TCNQ@HKUST-1, and (c) $F_4$-TCNQ@HKUST-1. The circled areas in the dispersion indicate the emergence of flat modes upon adsorption. The asterisks indicate possible phonon hybridization such as anti-crossings occurring within the dispersions upon guest adsorption. (d) The vibrational density of states is plotted on a log scale for the TCNQ($F_4$-TCNQ)@HKUST-1 systems. The emergence of new modes upon infiltration is apparent in both the TCNQ and $F_4$-TCNQ DOS from 10-20 THz. The inset is a zoom in of the DOS from 9.5-10.3 THz and highlights the hybridization occurring upon TCNQ adsorption.

evidence of low lying optical propagons and avoided crossings occurring in the infiltrated HKUST-1 systems studied here (Figure 5.15 (a)-(c)). Additionally, the trend in lifetimes captured by SED (Figure 5.14 (inset)) shows that the thermal transport in pristine HKUST-1 can be

described by a propagon-diffuson picture, and the addition of a guest adds disorder which breaks the crystal periodicity. Therefore, I offer an interpretation of the heat transport in these partially disordered material by calculating the inverse participation ratio (IPR), which provides insight into how vibrational modes with different frequency and localization characteristics contribute to thermal conductivity.[287] Additionally, the Allen-Feldman (A-F) method for calculating thermal conductivity also provides insight in the limit where vibrational modes are defined as diffusons.[74]

Figure 5.16 (a) replots the vibrational density of states (DOS) for the pristine and TCNQ infiltrated HKUST-1 compared to a single, isolated TCNQ molecule. From this, it is evident that the emergence of a new population of localized modes within the TCNQ@HKUST-1 system corresponds with molecular modes intrinsic to the single TCNQ molecule.[45–47] The IPR offers a methodology to comprehend the effect of this new population of modes, conceptualizing the contribution of delocalized extended modes (propagons and diffusons) and localized (locons) modes given by:

$$IPR = \frac{\sum_i^N (\sum_{\alpha=1}^3 u_{i\alpha}^2)^2}{(\sum_{i=1}^N (\sum_{\alpha=1}^3 u_{i\alpha}^2))^2}, \tag{5.2}$$

where $N$ is the number of atoms in the unit cell (624) and $u_{i\alpha}$ is the eigenvector component for atom $i$ in the direction $\alpha$.[83] Here, I define locons whose eigenvectors spread across 20% or less of the atoms in the unit cell (corresponding to 125 atoms, IPR=1/N ≥0.008), which has been shown by others to be a reasonable delineation.[83,288] Figure 5.16 (b) shows the IPR results calculated for the vibrational modes at the Γ point of the Brillouin zone. The non-propagating modes become increasingly localized in the infiltrated cases, where modes outside of the blue shaded region (IPR ≥0.008) are localized. To quantify these results, I plot the accumulation of the total number of locons at the Γ point as a function of frequency in Figure 5.16 (d). In total, the HKUST-1 infiltrated

TCNQ and $F_4$-TCNQ show that 40% and 38% of the modes become localized respectively, compared to only 2% in the pristine HKUST-1, at the Γ point. In particular, a high concentration of localized modes appears between 13-32 THz. Together, Figure 5.16 (c) and (d) show that the more weakly bonded $F_4$-TCNQ results in slightly less localized modes than the stronger bonded TCNQ, and that low frequency non-propagating modes (< 4.65 THz) contribute considerably to the total thermal conductivity of the infiltrated material.

The IPR results (Figure 5.16 (b),(d)) show that the bonded adsorbate contributes to a substantial population of localized modes that span a broad range of frequencies. In particular, these modes are concentrated from 13-32 THz, which corresponds to a high degree of overlap with the single isolated TCNQ molecule vibrational spectrum. This shows that the coordinated guest molecules residing in the pores of the MOF contribute to the reduction of the thermal conductivity of the MOF through two intrinsic mechanisms resulting in a change of the vibrational structure of the MOF. First, hybridization (i.e., avoided crossings) with propagons will tend to broaden peaks in the vibrational density of states,[130] and such behavior has been shown to significantly reduce the thermal conductivity (though the mechanism is still heavily debated).[66,73] I see evidence of hybridization occurring in the infiltrated systems captured as low lying optical and acoustic coupling in the dispersions and broadening of peaks in the DOS shown in Figure 5.15. Second, the adsorbates add disorder into the system resulting in a substantial increase of localized incoherent vibrational modes over a broad frequency range, which increases the phase space for scattering events to occur, thus driving down extended vibrational mode lifetimes (Figure 5.16(b)(d)). The

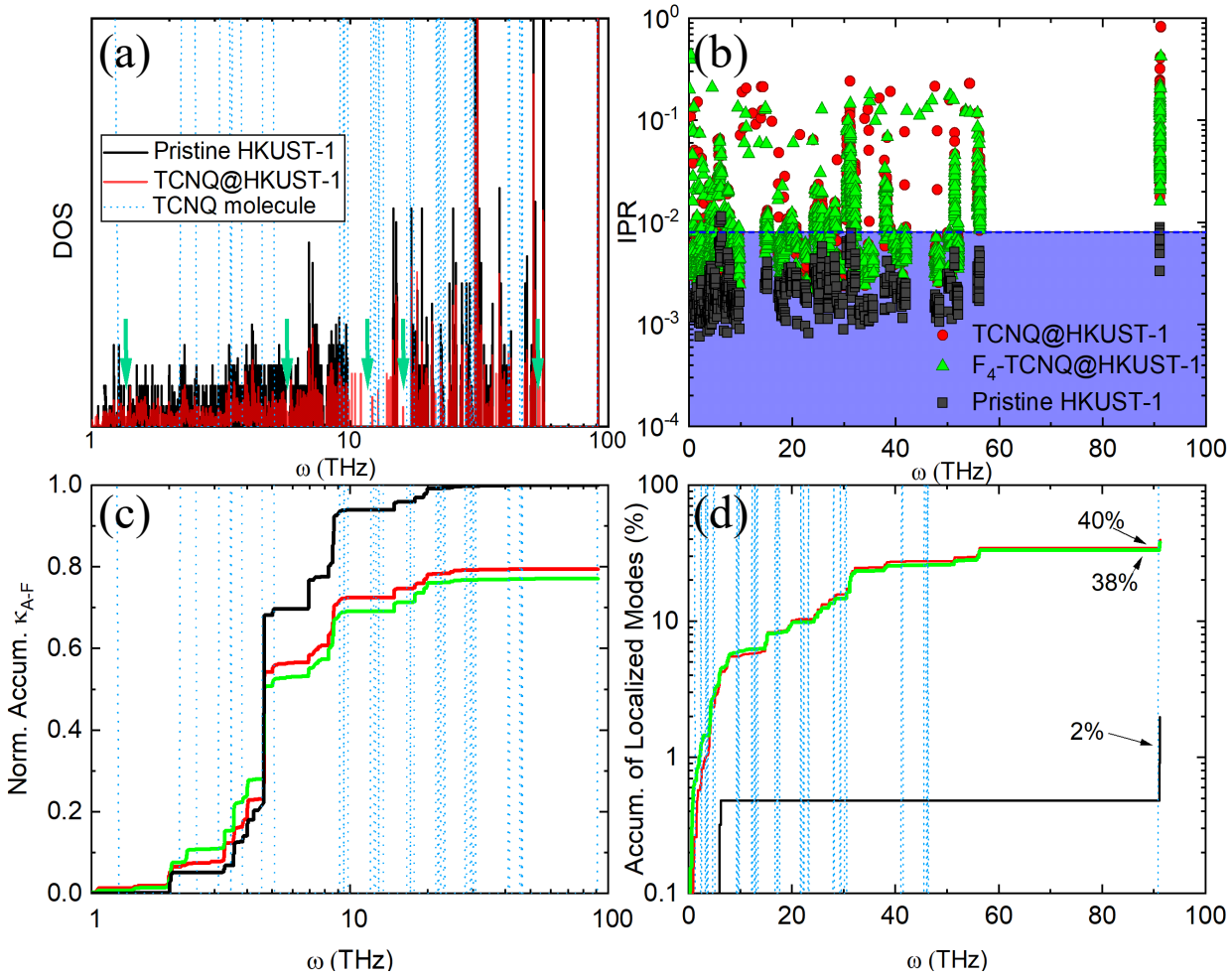


Figure 5.16: (a) Vibrational density of states (DOS) for the HKUST-1 (black) and, TCNQ@HKUST-1 (red) compared to the vibrational spectrum of a single isolated TCNQ molecule (blue dotted lines). The DOS for, $F_4$-TCNQ@HKUST-1 (green) systems has been left off for clarity. There is an emergence of new modes over a broad range of frequencies upon infiltration that overlap with the TCNQ molecular modes (pointed out by the green arrows). (b) Mode resolved inverse participation ratio (IPR) calculated at the Γ wave vector only. The blue shaded region corresponds to the delocalized modes, where the transition from delocalized to localized modes occurs at an IPR ≥ 0.008, corresponding to where the eigenvectors that are is spread across 20% or less of the atoms in the supercell (125 atoms). (c) Thermal conductivity accumulation from non-propagating modes (diffusons and locons) calculated from Allen-Feldman theory at 300 K normalized to the $\kappa_{A\text{-}F}$ for pristine HKUST-1 and (d) the accumulation of IPR calculated localized modes at the Γ wave vector with the molecular spectrum of TCNQ superimposed (blue dotted lines).

localized modes in the DOS appear as delta functions,[130] and are clearly seen from 9.7 – 16.2 THz in Figure 5.16 (a), though IPR results indicate they occur over many frequencies. The effect of

hybridization and localized modes over a broad frequency is evidence that the coordinated nature of the adsorbate introduces intrinsic effects, which further contributes to the reduction in thermal conductivity of the adsorbate-MOF system.

The effects of non-propagating modes (diffusons) are captured by calculating the normalized thermal conductivity accumulation function from the A-F method.[74] Figure 5.16 (c) shows the A-F thermal conductivity accumulation normalized to the pristine HKUST-1 thermal conductivity. The results show that low frequency non-propagating modes (0-4.65 THz) contribute to a higher degree to the thermal conductivity for the infiltrated HKUST-1, however short wavelength modes > 4.65 THz participate to a larger degree in the pristine case. This indicates anincrease in the contribution to thermal conductivity of non-propagating modes at frequencies below 4.65 THz when infiltrated, however there is a reduction in diffuson contribution at higher frequencies which is consistent with the majority of the molecular vibrational modes from the isolated TCNQ molecule. Note that the contribution of propagons is not included in the A-F thermal conductivity approach. In total, the A-F derived thermal conductivities show a reduction in thermal conductivity for both the TCNQ and $F_4$-TCNQ infiltrated systems (21% and 24% respectively), where varying the bond strength of the guests to the host lattice by ~8%, and the mass of the guest atom by 35% leads to only a ~3% difference in the thermal conductivity between the lighter stronger bonded TCNQ and the heavier weaker bonded $F_4$-TCNQ guest molecules. This indicates that the guest/host bond strength does not greatly affect the thermal conductivity reduction.

In summary, the thermal conductivity of thin film and thick polycrystalline HKUST-1 infiltrated with gas, liquid, and solid adsorbates were experimentally measured with TDTR, and the thermal transport processes were investigated by MD, SED, and LD. These adsorbates allow

for the investigation of a variety of weak and strong guest-host interactions on the thermal conductivity of HKUST-1. I find that the thermal and mechanical properties of the thin and thick samples are quite consistent despite very different fabrication techniques and locations. Upon infiltration, the thermal conductivity of HKUST-1 decreases by 40 – 80% depending on the adsorbate, that cannot be explained by effective medium approximations. Adsorbates that weakly interact with the pore promote high adsorbate-MOF collisions that result in the reduction in thermal conductivity through enhanced vibrational scattering rates of low frequency modes, where liquid adsorbates significantly reduce the lifetimes of low frequency vibrational modes. Coordination between the adsorbate and MOF also results in reduced lifetimes of low frequency modes through extrinsic adsorbate-MOF collisions, but to a lesser extent. In addition, coordinated adsorbates also change the vibrational structure of the HKUST-1 through hybridizations with acoustic vibrational modes that are concomitant with an increased population of localized modes occurring over a broad range of frequencies. Together, the experimental and LD results show that the degree of orbital overlap experienced by the solid guests does not greatly affect the degree of thermal conductivity reduction experienced upon guest adsorption.

This work experimentally and theoretically investigates the role of coordination (by choosing solid guest adsorbates that produce varying degrees of orbital overlap with the MOF) and composition of guests introduced to the HKUST-1 pore. The MD revealed that the bonding morphology (i.e., bond concentration and orientation) may play the largest role in predicting the magnitude of reduction in thermal conductivity, where an unbonded guest molecule that can collide with the pore wall may produce the largest reduction, and bonds formed between the guest/host can serve to compete with scattering processes by acting as ‘thermal bridges’. However, the experimental and LD results indicate that adsorbate-MOF bonding serves to enhance, rather

than hinder vibrational scattering rates through promoting changes to the vibrational structure of the MOF via hybridization.

## 5.4 Results: The Effects of Pore Morphology (ZIF-8 vs. HKUST-1)

The high structural tunability of MOFs allows for this class of material to come in many shapes and sizes. In particular, the physical and chemical structure of the pores can be deliberately tuned to achieve specific topologies and structures comprising of well-defined pore geometries including: squared, rectangular, triangular, and window-connected cages.[244] The pore chemistries can also contain (or lack) open metal sites (OMS) within the pore, which are a feature of the coordination chemistry responsible during the MOF fabrication process. In particular, MOFs that contain OMS contain metal nodes that are not fully coordinated by ligands, so that a lone electron pair is available on each metal site to interact with any nearby adsorbates, and often leads to an increased interaction with sorbate molecules compared to MOFs where the metal sites are fully coordinated (non-OMS MOFs).[289] In this section, I investigate the roles of pore composition and morphology on the effect of adsorbates on the thermal conductivity of MOFs by comparing and contrasting the thermal conductivity of pristine and infiltrated ZIF-8 with HKUST-1.

The chemical and mechanical stability, combined with the wealth of information on the adsorption and diffusion properties of ZIF-8 and HKUST-1 make these two MOFs great candidates for studying the roles of pore composition and morphology on thermal transport.[247,259,260,290] They both contain cubic unit cells, however exhibit very different pore morphologies due to the nature of their metal nodes and organic linkers ($Zn^{2+}$ cations that result in tetrahedral coordination, vs. Cu dimer SBUs that result in octahedral coordination geometries). Specifically, HKUST-1exhibits 9 x 9 Å rigid square pores, whereas ZIF-8 contains flexible/floppy cage-like pores that are ~11.6 Å in diameter (see Table 5.1 for a side by side comparison of

composition and morphology characteristics).[245,259–262] Additionally, their pore compositions are also different. HKUST-1 contains OMS that promote increased interactions between the copper dimer SBU nodes and adsorbates, that make their way into the pores. The metal $Zn^{2+}$ nodes in ZIF-8 however, are fully coordinated to the ligands and therefore ZIF-8 is classified as a non-OMS MOF. It has been indicated that the adsorbate-framework interaction within the pores of non-OMS MOFs are much weaker (hydrogen bonding, Coulombic interactions, van der Waals bonding) with the pore compared to OMS type MOFs.[291] In this work, the thermal conductivities of thin ZIF-8 films were measured experimentally with TDTR in pristine activated form, and infiltrated with gas

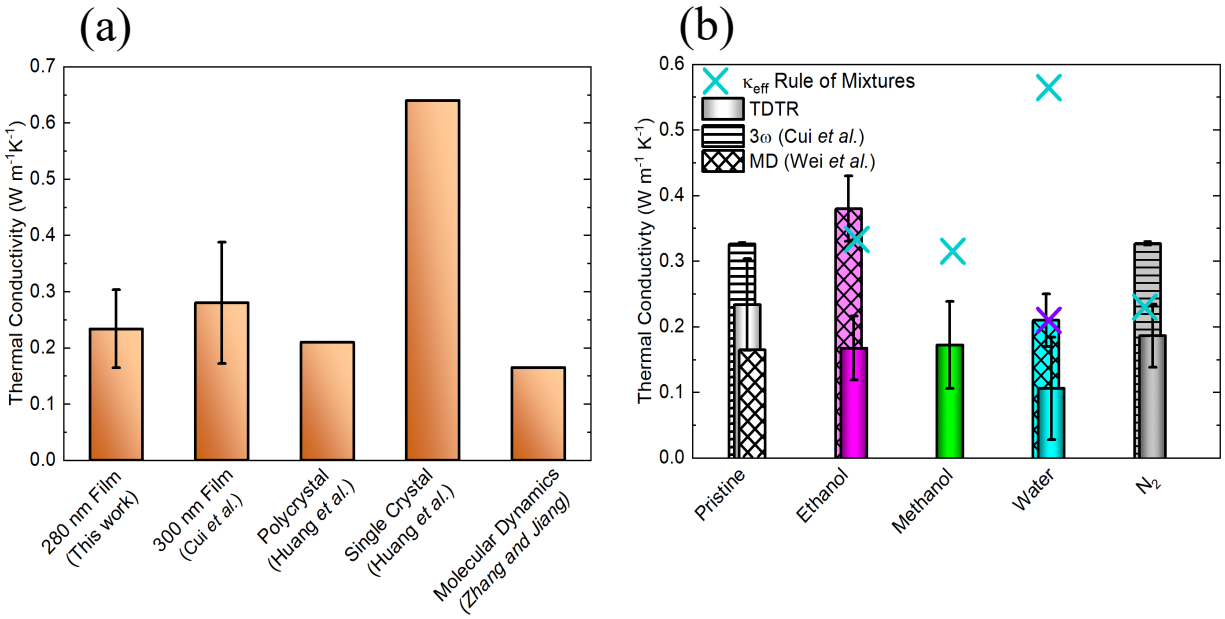


Figure 5.17: (a) Thermal conductivity of the pristine activated ZIF-8 thin film from this work compared to previously reported experimental measurements performed on 300 nm thin polycrystalline films (Cui *et al.*),[121] polycrystal and single-crystal particles (Huang *et al.*),[292] and an equilibrium molecular dynamics simulation study (Zhang and Jiang).[244] (b) The thermal conductivity of 280 nm thin ZIF-8 films measured with TDTR in pristine activated and infiltrated form. The adsorbates include liquid ethanol, methanol, and water and $N_2$ gas. The ethanol and water adsorbate results are compared to MD simulations carried out by Wei *et al.* when the adsorbates saturate the pores at 160 molecules per pore.[293] The $N_2$ adsorbate results are compared to experimental results from Cui *et al.* measured at a chamber pressure of 0.70 atm.[121] The expected thermal conductivity from effective medium theory when the pores are fully saturated (blue symbols) and when the pores are 29% filled (purple symbol) are also plotted.

($N_2$) and liquid (ethanol, methanol, and water) adsorbates. The pristine and infiltrated ZIF-8 results are compared to the pristine and infiltrated HKUST-1 to illuminate how pore composition and morphology affects the role of adsorbates on the thermal conductivity of MOFs.

The thermal conductivity of pristine and infiltrated polycrystalline ZIF-8 thin films were measured using TDTR. Figure 5.17 (a) compares the TDTR results of the 280 nm polycrystalline ZIF-8 thin film studied here, to previous experimental[119,121] and computational[244] reports. These previous experimental results were obtained on samples of differing morphologies, including 300 nm polycrystalline thin films (which most closely resemble the morphology of the film studied here) measured by 3$\omega$,[121] and polycrystal and single-crystal samples of ZIF-8 measured with Raman-resistance temperature detectors (Raman-RTD).[292] It should be noted that Cui *et al.* reports a thermal conductivity of 0.326 $Wm^{-1}K^{-1}$for their pristine ZIF-8 films, however a closer look at all of their data reveals that the average thermal conductivity that they measure on all of their samples is $0.28 \pm 0.11$ $Wm^{-1}K^{-1}$, which is what is plotted in Figure 5.17 (a) and is much more consistent with the value measured in this work ($0.23 \pm 0.07$ $Wm^{-1}K^{-1}$). Figure 5.17 (a) shows that the previously reported experimental and MD derived thermal conductivities are within the same order of magnitude. Differences in the experimental results may be attributed to different concentrations of grain boundaries and defects occurring in the polycrystalline films vs. the polycrystalline and single crystal particles.[292] Further, the higher thermal conductivity exhibited by single-crystal ZIF-8 can be attributed to the lack of inter-crystal thermal contact resistances, where interfacial resistance between adjacent crystals and grain boundaries within the polycrystalline particle and films serve to reduce their overall thermal conductivity.[28,292]

The pristine activated ZIF-8 thermal conductivity results are compared to liquid and gas infiltrated ZIF-8 in Figure 5.17 (b). These results are also assessed against previous reported

measurements of pristine and $N_2$ (g) infiltrated ZIF-8 films,[121] and MD[293] reported in the literature for ethanol and water infiltrated ZIF-8. Figure 5.17 (b) shows that the TDTR experimental measurements do not indicate a discernable change, within uncertainties, in the thermal conductivity of ZIF-8 in the presence of all adsorbates. These results are in contrast to the reported values from the MD simulations, which predicted between a 27%-130% increase in the thermal conductivity upon adsorption with water and ethanol respectively.[293] In fact, the previously published MD results are more in line with what would be expected from an effective medium theory (EMT) approach for calculating the thermal conductivity, assuming the pores were fully saturated with the adsorbate. Since water is not easy infiltrated into the hydrophobic ZIF-8, I also show the expected EMT results when water fills ~29% of the pore void fraction. Previous experimental reports of ZIF-8 infiltrated with $N_2$ (g) at a pressure of 0.7 atm indicate no discernable change in thermal conductivity in comparison to their pristine ZIF-8 film, which are consistent with what I observe with TDTR.[121] In total, the TDTR measurements show that adsorbates neither hinder nor enhance the thermal transport in infiltrated ZIF-8 films, and that EMT is not appropriate for predicting the thermal conductivity of these two-phase materials.

A major goal of this dissertation is to address the challenge in understanding the thermal transport in porous crystalline material by clarifying the role of adsorbates on the thermal properties of crystalline porous material. As a broad material class, the generality of adsorbate-induced thermal conductivity in MOFs is still to be determined. However, I offer insight into this by comparing and contrasting the experimentally measured thermal conductivity results of pristine and infiltrated ZIF-8 and HKUST-1 MOFs. The thermal conductivities of the activated pristine ZIF-8 and HKUST-1 measured here are $0.23 \pm 0.07$ and $0.64 \pm 0.14$ $Wm^{-1}K^{-1}$, respectively. The higher thermal conductivity exhibited by the HKUST-1 is expected, and can be attributed to both

the higher concentration of metal atoms in the unit cell (accomplished through the SBU), and also due to its rigid nature in comparison to ZIF-8. This stems from the principle that the modulus of a material is proportional to the thermal conductivity, where soft materials tend to be thermally insulative and stiff materials tend to be thermally conductive.[91] The elastic modulus of single crystal ZIF-8 has been reported as 2.97 ± 0.05 GPa,[261] while HKUST-1 is much higher at 9.3 GPa.[273] In the case of the MOFs studied here, composition outcompetes any differences in pore morphologies, where the larger pore size in the ZIF-8 is not necessarily attributable to the lower thermal conductivity of the two MOFs under investigation, which has been shown to be the case in simulations of idealized model structures.[231]

Further, Table 5.1 displays the MOF's composition and morphologies. Highlighting their similarities, they both have cubic unit cells with very similar densities (~0.95-0.96 g $cm^{-3}$), BET surface areas (~1450-1805 $m^2$ $g^{-1}$) and pore volumes (0.65-0.69 $cm^3g^{-1}$).[235,245,259–262] However they exhibit very different pore morphologies, and the compositional presence of OMS within HKUST-1 promotes strong interactions with any adsorbates in comparison to the non-OMS ZIF-8. The presence of adsorbates in ZIF-8 and HKUST-1 results in different trends in the thermal conductivity of the guest@MOF species. The normalized experimentally measured thermal conductivity of the ZIF-8 and HKUST-1 MOFs are plotted in Figure 47 (a), where each sample has been normalized to the pristine value of their respective MOF species. Adsorbates serve to significantly reduce the thermal conductivity of HKUST-1, while they neither enhance nor hinder the thermal conductivity of ZIF-8. While it is not possible to individually tease out the effect of pore morphology (shape) vs. composition (OMS vs. non-OMS) directly, I can turn to the MD/SED results presented previously to offer an evidence-based hypothesis for the different response in thermal conductivity upon infiltration for each MOF. Due to the presence of the OMS's within

HKUST-1, it is likely that adsorbates coordinate to the host structure, whereas in the ZIF-8 they likely experience weak interactions.[267] The MD and SED results in Figure 5.13 and Figure 5.14 demonstrated that adsorbates in an unbound state that are free to collide with the pore would promote the highest reduction in thermal conductivity, while coordination between the guest/host would dampen the effect by acting like a 'thermal bridge'. Therefore, if the only difference between the two MOFs was how the guests interacted with the pore, one would expect that the ZIF-8 would experience the largest reduction in thermal conductivity upon guest infiltration, however experimentally the opposite trend is observed. Interestingly, MD results from Hasan, McGaughey and Wilmer show that only MOFs with small pores would experience a reduction in thermal conductivity in the presence of adsorbates due to extrinsic vibrational scattering introduced by gas-crystal interactions, where they set the upper limit to pores with diameters of ~1.7 nm.[232] Above this threshold, thermal conductivity was not expected to change with increasing gas density due to less frequent gas-adsorbate collisions. ZIF-8 contains slightly larger pores (1.16 nm)[262] than HKUST-1 (0.9 nm), that begin to approach the upper limit established previously from MD. Therefore, the pores may be large enough where adsorbate induced phonon scattering is reduced due to less frequent gas-adsorbate collisions. Additionally, the intrinsic flexibility of ZIF-8 also likely plays a significant role in the lack of change in thermal conductivity upon infiltration. ZIF-8 pores are capable of large deformation at room temperature, where reversible rotation/reorientation of the mIm linker (while preserving the crystallinity) allows for the passage of molecules larger than the pore's intrinsic aperture size (~0.34 nm); this intrinsic structural quality of ZIF-8 increases the pore aperture without increasing the pore volume, resulting in additional adsorbates to be accommodated into the pores leading to a more efficient packing.[249] From a thermal perspective, increasing the density of the system by adding adsorbates into the

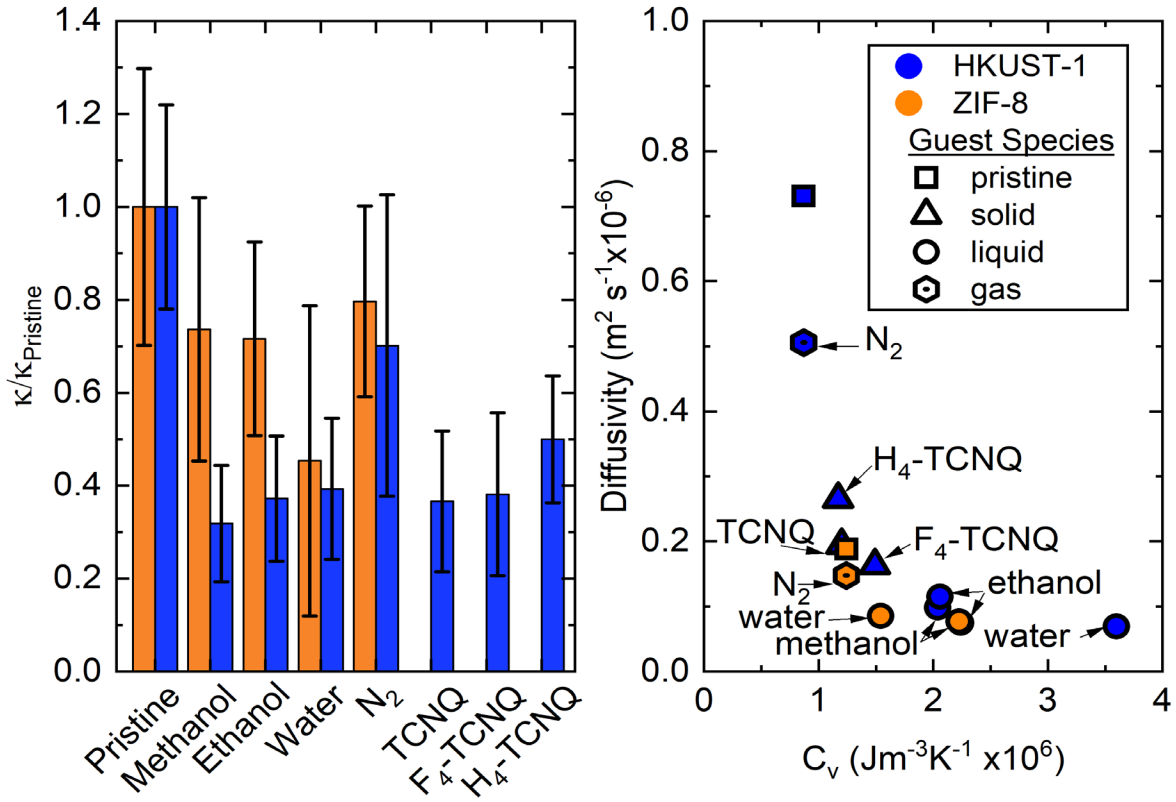


Figure 5.18: (Left) Normalized thermal conductivity of ZIF-8 and HKUST-1 infiltrated with various adsorbates. All samples have been normalized to the thermal conductivity of their respective pristine MOF. (Right) The thermal diffusivity vs. volumetric heat capacity for the pristine and infiltrated ZIF-8 and HKUST-1 MOFs.

pores would be expected to result in an increased degree of resistance toward deformation (increase in elastic constants). The unit cell deformation and mechanical stiffening followed by adsorption would be predicted to increase the thermal conductivity, and therefore may compete with the effect of phonon scattering introduced by collisions between the guest and pore, so that the thermal conductivity is neither enhanced or reduced.

Thermal diffusivities ($\kappa/\rho c$, where $\rho$ is density and $c$ is heat capacity) of ZIF-8 and HKUST-1 in Figure 5.18 (b) further contrast the thermal processes exhibited by these two MOFs. HKUST-1 shows a huge change in thermal diffusivity upon infiltration whereas ZIF-8 does not. For example, in the presence of water, HKUST-1 experiences an 18-fold reduction while ZIF-8 only experiences an approximately 3-fold reduction in thermal diffusivity. This result is critical,

because heat dissipation time scales in rapid adsorption applications are proportional to the thermal diffusivity, and therefore it is essential that the vastly different sensitivities in the thermal diffusivities of MOFs intended for gas adsorption applications should be considered. Figure 5.18 (b) indicates how two MOFs similarly designed for gas storage applications may produce very different efficiencies due to how their thermal properties change in the presence of adsorbates. HKUST-1 thermal diffusivity is drastically lowered by adsorbates, which would exacerbate the challenge of dissipating the heat produced during exothermic adsorption, while ZIF-8 changes minimally and may perform better under rapid loading conditions.

## 5.5 Conclusion

Metal organic frameworks offer a unique system to study the thermal properties of periodic porous crystals in pristine and adsorbed states. I showed that infiltrated HKUST-1 MOFs result in a reduction in thermal conductivity with all adsorbate species studied, and that the role of adsorbates in ZIF-8 neither enhances nor hinders the thermal transport. These results are crucial, because they show how the composition and pore morphology of MOFs dictate the role of adsorbates on the thermal transport properties within this material class. These results are also significant because they inform the limited current studies of the thermal transport of MOFs that draw conflicting conclusions on the role of adsorbates on thermal conductivity.[119–121,232,239,244,292,294,295] Specifically, simulations performed on adsorbed gas species have indicated that the adsorbate will reduce the thermal conductivity of MOFs due to enhanced scattering in the framework caused by gas-framework collisions,[232] while others have computationally shown an increase upon gas adsorption will occur since adsorbates act to increase the available heat transfer channels within the material.[120] Here, I show that as a general rule, effective medium theory is not an appropriate approximation for describing the thermal conductivity of guest infiltrated MOFs.

The role of adsorbates on the thermal conductivity of the guest@MOF system depends on the bonding morphology between the adsorbate-MOF, and also the physical/mechanical properties of the MOF. In the case where adsorbates experience weak interactions within the pore (hydrogen bonding, van der Waals forces, or unbound free state) the thermal conductivity is reduced through an extrinsic mechanism of enhanced vibrational scattering rates of the low frequency MOF vibrational modes through adsorbate-crystal collisions. However, when the adsorbate strongly interacts with the MOF pore through coordination, the extrinsic effects of the adsorbate are accompanied by intrinsic effects that modify the vibrational structure of the system promoting a reduction in thermal conductivity. Specifically, coordinated adsorbates change the vibrational structure of the MOF by producing hybridization with acoustic vibrational modes that are connected to an increased population of localized incoherent vibrational modes over a broad range of frequencies. The magnitude of these extrinsic and intrinsic effects in reducing the thermal conductivity of the MOF system is dependent on both the pore size and the mechanical properties. In the case of HKUST-1 which is comparably rigid with relatively small pore sizes, the effect of adsorbates drastically reduces the thermal conductivity from the pristine state by 40-80%, depending on the adsorbate. Alternatively, in ZIF-8, the larger, structurally flexible pores dampen the thermally inhibiting effects of the adsorbates so that the thermal conductivity is neither enhanced nor reduced upon infiltration.

# Chapter 6

## 6. Summary, Future Projects, and Impact

"The future will feature ideas that are barely glints in the engineers' eyes right now…How do I know? Because ingenuity is rampant as never before in this massively networked world, and the rate of innovation is accelerating, through serendipitous searching, not deliberate planning."

- Matt Ridley, The Rational Optimist

Progress in modern technologies require device miniaturization coupled with material optimization and high performance – do more with less! In order to engineer highly efficient nanomaterials, it is imperative to understand the roles of composition and morphology on the fundamental behavior of heat carriers. In this dissertation I considered two classes of nano-materials with relevance towards energy harvesting applications such as thermoelectric systems, and gas sorption technologies like gas separation and storage. I showed that the role of extrinsic defect scattering from compositional disorder in nano-composite chalcogenide crystalline material leads to a reduced thermal conductivity as opposed to intrinsic phonon-phonon processes that are responsible for the intrinsically low thermal conductivity of each parent material. Additionally, I also illuminated the role of guest molecules on the thermal transport in porous crystalline materials by studying how adsorbate composition effects the thermal processes in two metal organic frameworks, HKUST-1 and ZIF-8, with varying pore compositions and morphologies. Here I showed that the adsorbates add disorder into the material system resulting in both extrinsic (adsorbate-crystal collisions) and intrinsic (change to the vibrational structure including hybridization, and an increase in the population of localized modes) effects that serve to reduce the thermal conductivity of the guest infiltrated system. The extent of these diminishing effects on

the overall thermal transport is dependent on both the adsorbate-MOF bonding morphology, and the morphology of the MOF itself (pore size, modulus).

## 6.1 Summary

This section provides a brief summary of each chapter within this dissertation. Chapter 2 introduced core concepts of macroscopic heat transport, with special focus on Fourier's law of heat conduction. This set the stage for an overview of microscopic heat transport concepts that discuss kinetic theory to model the thermal conductivity of crystalline material in addition to the different mechanisms and origins of phonon scattering. Then I moved to an overview of modified analysis frameworks for describing the thermal transport in disordered material, to compare and contrast the differences between heat transport processes in ordered crystalline material and disordered amorphous material. This provided the reader with context in understanding that ambiguity exists in establishing an analytical framework to address the thermal transport in crystalline material containing high degrees of disorder, such as structured nano-composites presented in Chapter 4 and infiltrated MOFs presented in Chapter 5. Chapter 2 also discussed the relationship between the mechanical and thermal properties of material through the Leibfried and Schlomann relation, and provides a review of thermal measurements on porous material that summarizes the state of the field regarding thermal transport processes in this material class, which is further developed in Chapter 5.

Chapter 3 detailed the experimental techniques used in this dissertation to obtain the thermal measurements reported in Chapter 4 and 5, and also the group velocity and elastic modulus measurements reported in Chapter 5. This chapter contains an overview of the analytical procedure for both obtaining, and evaluating the data with respect to the thermal and acoustic wave response for a pulsed Gaussian surface heating source, heating a multilayer sample, and also quantifies the

uncertainties of each measurement technique. Here, I showed how a single pump-probe thermometry technique can be configured to measure both the thermal and mechanical properties of a sample via TDTR and pump-probe Brillouin scattering, respectively.

In Chapter 4 the thermal conductivities of ALD-grown thin film PbTe-PbSe nano-composite were reported to examine the effects of engineered disorder in the form of point defects, nano-precipitates, internal interfaces, and grain boundaries in chalcogenides. The compositional variation and resulting point and planar defects gave rise to additional phonon scattering events that reduced the thermal conductivity below that of the corresponding ALD-grown control PbTe and PbSe films. Temperature dependent thermal conductivity measurements further supported these findings that the phonon scattering and resulting thermal conductivities in these ALD-grown PbTe-PbSe thermoelectric materials are driven by extrinsic defect scattering processes as opposed to phonon-phonon scattering processes intrinsic to the PbTe or PbSe. The implication of this work is that polycrystalline, nanostructured ALD composites of thermoelectric PbTe-PbSe films are effective in reducing the phonon thermal conductivity, and hereby represent a pathway for further improvement of the figure of merit (ZT), enhancing their thermoelectric application potential.

In Chapter 5 the thermal conductivity of two metal organic frameworks (HKUST-1 and ZIF-8) were measured in pristine and infiltrated form, to study the effect of pore composition and morphology, and adsorbates, on the thermal processes of infiltrated crystalline material. Upon infiltration, the thermal conductivity of HKUST-1 decreases by 40 – 80% depending on the adsorbate. The experimental results for HKUST-1 were supported by MD, SED, and LD simulations that explored the mechanisms for the adsorbate initiated reduced thermal conductivity from both a disordered propagon/diffuson/locon framework. I showed that the bonding morphology (unbonded vs. coordinated) between the MOF and adsorbate results in slightly

different thermal transport phenomena within the guest@MOF material. Specifically, the MD shows that adsorbates in an unbound state produce many adsorbate-crystal collisions, which is an extrinsic effect that increases low frequency vibrational mode scattering rates that reduce the thermal conductivity of the MOF. When the adsorbate is coordinated to the MOF however, intrinsic effects such as changes to the vibrational structure of the HKUST-1 occur that serve to drive down the thermal conductivity. From a phonon picture, the LD shows the emergence of mode hybridization as indicated by anti-crossing and flat modes in the dispersions, features that have been attributed to diminished thermal transport. The inverse participation ratio indicated that infiltration with a guest significantly increases the population of locons over a broad frequency (not just high frequency), that contribute to the reduction of the thermal conductivity. Further, the influence of adsorbates on ZIF-8 was negligible, where the thermal conductivity was neither enhanced or diminished. While the extrinsic and intrinsic adsorbate effects were likely present, competing thermal effects from the larger pores (that reduce the frequency of adsorbate-crystal collisions) and the intrinsic pore flexibility (which leads to high loading densities resulting in an enhanced resistance to deformation) of the ZIF-8 MOF likely dampen the effects of the adsorbates. In total, I show that an effective medium approximation is not appropriate for describing infiltrated MOF material.

## 6.2 Future work

- **Temperature Dependent Measurements of MOF Thermal Conductivity**

In Chapter 5, I showed that the thermal transport mechanisms in MOFs can be interpreted from a disordered framework (propagons, diffusons, locons), since these crystalline materials contain significant disorder due to their large unit cells, and through the introduction of adsorbates which breaks the crystal periodicity. There still exists ambiguity in quantifying the

contributions of different characteristic vibrational modes in these MOF systems (i.e., differentiating propagons from diffusons). Temperature dependent thermal conductivity measurements provide more insight into the role of characteristic modes on the thermal properties of these complicated MOF material. Figure 6.1 shows preliminary results from experimental temperature dependent measurements obtained with TDTR on 400 nm thin films and 5.5 μm thick samples compared with the Leibfried and Schlomann (L-S) prediction for lattice thermal conductivity (Eqn. 2.14). The temperature dependent HKUST-1 trends are compared to the L-S prediction for thermal conductivity, instead of an effective medium prediction, because L-S provides a propagon perspective by including three-phonon scattering strength terms from the average Gruneisen parameter. Both pristine and infiltrated MOF's exhibit a typical $T^{-1}$ temperature dependent trend that is consistent with crystalline materials, where thermal conductivities above the Debye temperature of the solids are mainly driven by anharmonic phonon-phonon scattering processes.[52] The L-S prediction qualitatively captures the temperature dependence for the thin film better than the thick samples. This might be due to higher sample quality of the thin films as compared to the thick samples (supported by BET surface area calculations (Table 5.2)), where defect scattering from incomplete coordination to the BTC linker could potentially lead to the deviation from the characteristic $\kappa \propto T^{-1}$ behavior. These preliminary temperature dependent results are quite surprising, because they show that the dominating mechanism limiting thermal transport in both the pristine and infiltrated HKUST-1 maybe intrinsic (phonon-phonon scattering from increased anharmonicity at higher temperatures) rather than extrinsic defect scattering resulting from the large disorder of the material system.[280] It also indicates the need to differentiate between contributions from propagons and diffusons in these material. If this trend can be further validated on more pristine and infiltrated HKUST-1 samples, and in other MOFs (like ZIF-8), it

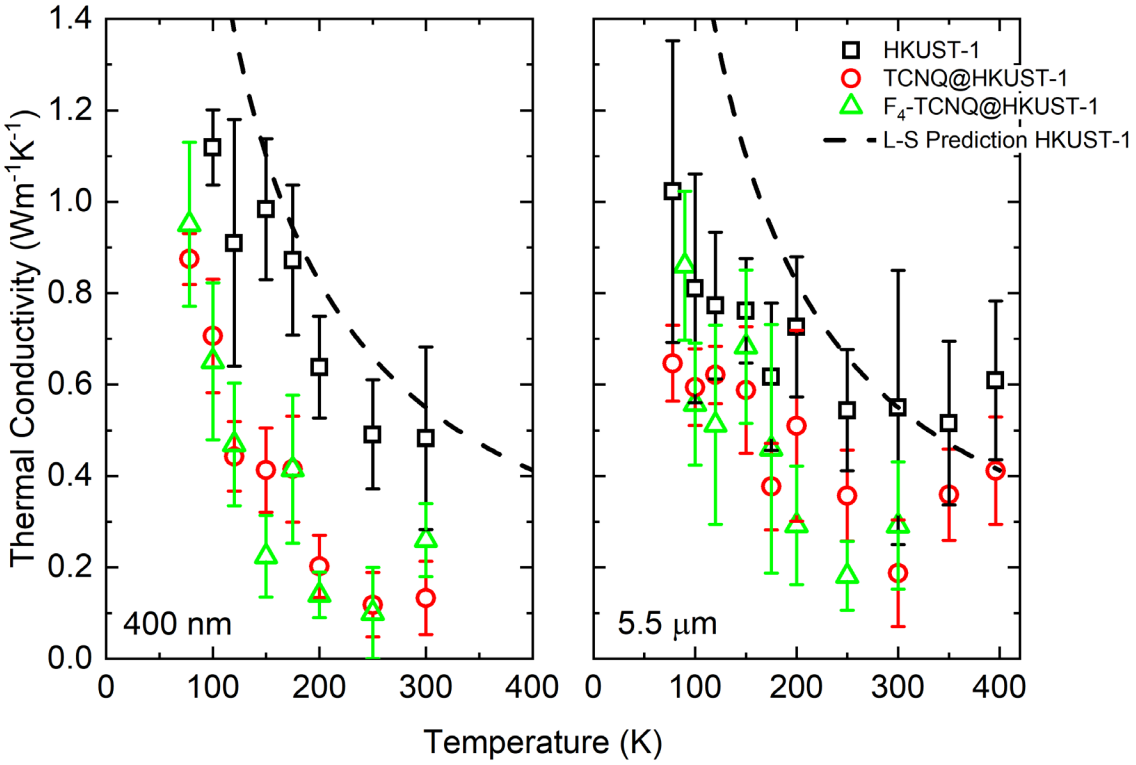


Figure 6.1: Preliminary experimentally measured temperature dependent thermal conductivity for pristine, TCNQ@HKUST-1 and $F_4$-TCNQ@HKUST-1 (left) 400 nm thin films and (right) 5.5 μm thick HKUST-1. The Leibfried and Schlomann (L-S) relation (Eqn. 2.14) is plotted as a dashed line.

might demonstrate that the plane-wave propagating character of vibrational modes dominates in these material systems. Similarly, a combination of anharmonic properties, and the interaction between guest and host phonon modes would also be responsible for the thermal trends in the infiltrated MOFs.

There has only been one paper, to my knowledge, that has reported similar experimental temperature dependent results occurring in pristine MOF-5. Huang *et al.* reported that the mean free path (MFP) in pristine MOF-5 is proportional to $T^{-2.16}$, owing to both inter-phonon scattering and lattice distortion.[119] While the pristine HKUST-1 thin films reported here follow a $T^{-1}$ trend quite well, the TCNQ and $F_4$-TCNQ infiltrated HKUST-1 trends approach $T^{-2}$,

echoing that lattice distortion may occur in the presence of adsorbates in HKUST-1. Huang *et al.* also showed that the minimum MFP of MOF-5 is on the order of the cage size (7.16 Å), which is much smaller than the lattice constant. They show with simulations that acoustic phonons are reflected at the connector between the cage and bridge.[233] It is still not known whether this assessment can be generalized to other MOFs with varying cage structures, and further investigation into this would serve to help generalize these concepts.

- **TDTR Sensitivity to Thermal Processes in the Pores:**

In its standard configuration, the ultrafast timescales and sensitivities of TDTR make it well equipped for measuring the thermal conductivity, and thermal boundary resistance of thin film material. Therefore, the TDTR measurements acquired on the MOFs in Chapter 5, represent the thermal conductivity of the solid component of the MOF porous scaffolding, not the effective medium (MOF/air) itself.[16] A useful avenue for continuing to develop the accessibility of TDTR to measure other thermal phenomena is exploring when TDTR may become sensitive to the thermal processes occurring within the pore. Specifically, what experimental configurations should be considered to gain or lose sensitivity to convection? As shown previously (Eqn. 3.7) the timescale ($\tau_i$) for free convection is long (on the order of 1 ms). Standard TDTR is likely not sensitive to the long timescales of convective processes within the pores when typical modulation frequencies of 1-10 MHz are used, due to the short time scale of the measurement (ps-ns). Measurements taken at lower modulation frequencies ($<10^4$ Hz), or in a steady state regime, may become more sensitive to convective processes due to an increase in the measurement time scale determined by the pump modulation frequency ($f$) (Eqn. 3.11).

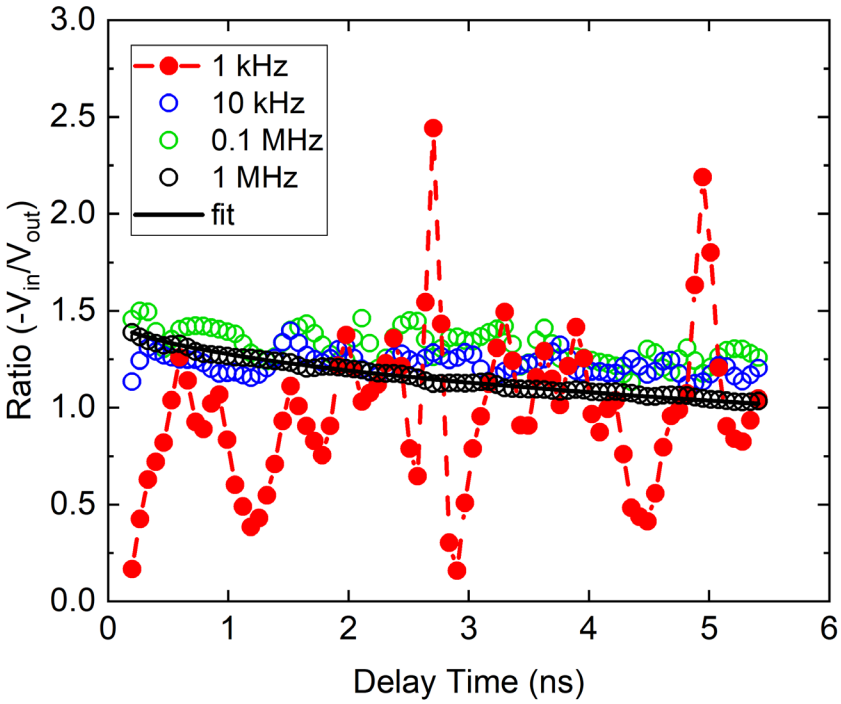


Figure 6.2: Raw TDTR data taken on a 400 nm HKUST-1 sample as it was exposed to a saturated $N_2$ (g) environment at ambient pressure with pump modulation frequencies ranging from $1x10^3$-$1x10^6$ Hz.

Figure 6.2 shows preliminary TDTR data acquired on a 400 nm thick HKUST-1 as it was exposed to a saturated nitrogen environment within the Linkam stage for one hour. The data were taken over a pump modulation frequency range of 1 kHz to 1 MHz. The figure shows the low SNR that results at low modulation frequencies, where the thermal model can only be fit to the data collected a 1 MHz with high fidelity. Future work in improving the SNR at these low modulation frequencies through clever mathematical representation of the TDTR signal, or enhancement of components, may open avenues for TDTR to become sensitive to thermal processes within pores.

## 6.3 Impact

The research detailed in this dissertation has led to two publications and one mature manuscript that is pending submission. I published the PbTe-PbSe nanocomposite work in

*Advanced Functional Materials* as a first author in September 2019 under the title: **Thermal Conductivity and Phonon Scattering Processes of ALD Grown PbTe-PbSe Thermoelectric Thin Films.** I also published the work detailing the thermal processes of HKUST-1 with liquid adsorbates as a joint first co-author in *Nature Communications* in August 11, 2020 under the title: **Observation of Reduced Thermal Conductivity in a Metal-Organic Framework Due to the Presence of Adsorbates**. In less than a year, this paper has been accessed over 4,025 times, and referenced nine times, according to the Web of Science. Metrics provided by *Nature Communications* state that this article is in the 96$^{th}$ percentile of the articles tracked of a similar age in all journals. In addition, a mature manuscript has been prepared detailing the effects of the bonding morphology of TCNQ and TCNQ derivative solid guest molecules on the thermal processes in HKUST-1. This paper will be submitted to *Adw. Chemie Int. Ed.* (which is a high impact (12.959) chemistry journal), under the title: **Hybridization from Guest-Host Interactions Reduce the Thermal Conductivity of Metal Organic Frameworks.** In addition to this, I have contributed to and published four other journal articles with colleagues throughout my time as a Ph.D. student at UVA. In total I have six published papers, and one paper currently undergoing the submission process, all related to the nanoscale heat transfer of low thermal conductivity functional materials.

7. M. E. DeCoster, H. Babaei, S. S. Jung, Z. Hassan, H. Baumgart, J. T. Gaskins, A. Giri, E. Tiernan, J. A. Tomko, P. M. Norris, A. J. H. McGaughey, C. Wilmer, E. Redel, G. Giri, and P. E. Hopkins. Hybridization from Guest-Host Interactions Reduce the Thermal Conductivity of Metal Organic Frameworks (MOFs). **submitted,** *PNAS* (April 2021)

6. H. Babaei, M. E. DeCoster, M. Jeong, Z. M. Hassan, T. Islamoglu, H. Baumgart, A. J. H. McGaughey, E. Redel, O. K. Farha, P. E. Hopkins, J. A. Malen, C. E. Wilmer. Observation

of Reduced Thermal Conductivity in a Metal-Organic Framework due to the Presence of Adsorbates. *Nature Communications*, 11, 4010 (2020).

5. H. Li, M. E. DeCoster, C. Ming, M Wang, Y. Chen, P. E. Hopkins, L. Chen and H. Katz. Enhanced Molecular Doping for High Conductivity in Polymers with Volume Freed for Dopants. *Macromolecules.* 52, 24, 9804-9812 (2019).

4. M. E. DeCoster, X. Chen, K. Zhang, C. M. Rost, E. R. Hoglund, J. M. Howe, T. E. Beechem, H. Baumgart, and P. E. Hopkins. Thermal Conductivity and Phonon Scattering Processes of ALD Grown PbTe–PbSe Thermoelectric Thin Films. *Adv. Fun. Mater.* 201, 904073 (2019)

3. M. E. DeCoster, K. E. Meyer, B. D. Piercy, J. T. Gaskins, B. F. Donovan, A. Giri, N. A. Strnad, D. M. Potrepka, A. A. Wilson, M. D. Losego, P. E. Hopkins. Density and Size Effects on the Thermal Conductivity of Atomic Layer Deposited TiO2 and Al2O3 Thin Films. *Thin Solid Films*, 650, 71-77 (2018)

2. X. Zhao, D. Madan, Y. Chen, J. Zhou, H. Li, S. M. Thon, A. E. Bragg, M. E. DeCoster, P. E. Hopkins, and H. E. Katz, High Conductivity and Electron-Transfer Validation in an n-Type Fluoride-Anion-Doped Polymer for Thermoelectrics in Air. *Adv. Mater.* 29, 1606928 (2017).

1. H. Li, M. E. DeCoster, R. M. Ireland, J. Song, P. E. Hopkins, and H. E. Katz, Modification of the Poly(bisdodecylquaterthiophene) Structure for High and Predominantly Nonionic Conductivity with Matched Dopants. *J. Am. Chem. Soc.* 139, 11149–11157 (2017).

# 7. References


1. McCray, W. P. MBE deserves a place in the history books. *Nat. Nanotechnol.* **2**, 259 (2007).
2. Minnich, A. J., Dresselhaus, M. S., Ren, Z. F. & Chen, G. Bulk nanostructured thermoelectric materials: current research and future prospects. *Energy Environ. Sci.* **2**, 466–479 (2009).
3. Zebarjadi, M., Esfarjani, K., S. Dresselhaus, M., F. Ren, Z. & Chen, G. Perspectives on thermoelectrics: from fundamentals to device applications. *Energy Environ. Sci.* **5**, 5147–5162 (2012).
4. Wiedemann, G. & Franz, R. Ueber die Warme-Leitungsfahigkeit der matalle. *Ann. Phys.* **165**, 497–531 (1853).
5. Venkatasubramanian, R. Lattice thermal conductivity reduction and phonon localizationlike behavior in superlattice structures. *Phys. Rev. B* **61**, 3091–3097 (2000).
6. Bies, W. E., Radtke, R. J. & Ehrenreich., H. Phonon dispersion effects and the thermal conductivity reduction in GaAs/AlAs superlattices. *J. Appl. Phys.* **88**, 1498–1503 (2000).
7. Borca-Tasciuc, T. *et al.* Thermal conductivity of symmetrically strained Si/Ge superlattices. *Superlattices Microstruct.* **28**, 199–206 (2000).
8. Cheaito, R. The Role of Size Effects on the Thermal Conductivity of Thin Film Alloys and Superlattices. (University of Virginia, 2015).
9. Song, D. & Chen, G. Thermal conductivity of periodic microporous silicon films. *Appl. Phys. Lett.* **84**, 687–689 (2004).
10. Hopkins, P. E., Norris, P. M., Phinney, L. M., Policastro, S. A. & Kelly, R. G. Thermal conductivity in nanoporous gold films during electron-phonon nonequilibrium. *J. Nanomater.* **2008**, 418050–418050 (2008).

11. Siemens, M. E. *et al.* Quasi-ballistic thermal transport from nanoscale interfaces observed using ultrafast coherent soft X-ray beams. *Nat. Mater.* **9**, 26–30 (2010).

12. Luckyanova, M. N. *et al.* Coherent Phonon Heat Conduction in Superlattices. *Science* **338**, 936–939 (2012).

13. Ravichandran, J. *et al.* Crossover from incoherent to coherent phonon scattering in epitaxial oxide superlattices. *Nat. Mater.* **13**, 168–172 (2014).

14. Cheaito, R. *et al.* Interplay between total thickness and period thickness in the phonon thermal conductivity of superlattices from the nanoscale to the microscale: Coherent versus incoherent phonon transport. *Phys Rev B* **97**, 085306–085306 (2018).

15. Kaviany, M. *Principles of Heat Transfer in Porous Media*. (Springer-Verlag, 1991).

16. Hopkins, P. E., Kaehr, B., Piekos, E. S., Dunphy, D. & Brinker, C. J. Minimum thermal conductivity considerations in aerogel thin films. *J. Appl. Phys.* **111**, 113532–113532 (2012).

17. Hummer, E., Lu, X., Rettelbach, Th. & Fricke, J. Heat transfer in opacified aerogel powders. *J. Non-Cryst. Solids* **145**, 211–216 (1992).

18. Spagnol, S., Lartigue, B. & Trombe, A. Experimental investigations on the thermal conductivity of silica aerogels by a guarded thin-film-heater method. *J. Heat Transf.* **131**, 074501–074501 (2009).

19. Nolas, G. S., Weakley, T. J. R., Cohn, J. L. & Sharma, R. Structural properties and thermal conductivity of crystalline Ge clathrates. *Phys. Rev. B* **61**, 3845–3850 (2000).

20. Beekman, M. & Cahill, D. G. Inorganic Crystals with Glass-Like and Ultralow Thermal Conductivities†. *Cryst. Res. Technol.* **52**, 1700114 (2017).

21. DeCoster, M. E. *et al.* Density and size effects on the thermal conductivity of atomic layer deposited TiO2 and Al2O3 thin films. *Thin Solid Films* **650**, 71–77 (2018).

22. Zhao, X. *et al.* High Conductivity and Electron-Transfer Validation in an n-Type Fluoride-Anion-Doped Polymer for Thermoelectrics in Air. *Adv. Mater.* **29**, 1606928 (2017).

23. Li, H. *et al.* Modification of the Poly(bisdodecylquaterthiophene) Structure for High and Predominantly Nonionic Conductivity with Matched Dopants. *J. Am. Chem. Soc.* **139**, 11149–11157 (2017).

24. Li, L. *et al.* Enhanced Molecular Doping for High Conductivity in Polymers with Volume Freed for Dopants. *Macromolecules* **52**, 9804-9812 (2019).

25. Historical Development of the Word 'Energy' | Energy Fundamentals. https://home.uni-leipzig.de/energy/energy-fundamentals/01.htm.

26. Rovelli, C. *The Order of Time*. (Riverhead Books, 2018).

27. Kapitza, P. L. The study of heat transfer in Helium II. *Zhurnal Eksp. Teor. Fiz.* **11**, 1–31 (1941).

28. Swartz, E. T. & Pohl, R. O. Thermal boundary resistance. *Rev. Mod. Phys.* **61**, 605–668 (1989).

29. Capinski, W. S. *et al.* Thermal-conductivity measurements of GaAs/AlAs superlattices using a picosecond optical pump-and-probe technique. *Phys. Rev. B* **59**, 8105–8113 (1999).

30. Capinski, W. S. & Maris, H. J. Improved apparatus for picosecond pump-and-probe optical measurements. *Rev. Sci. Instrum.* **67**, 2720–2726 (1996).

31. Latour, B., Volz, S. & Chalopin, Y. Microscopic description of thermal-phonon coherence: From coherent transport to diffuse interface scattering in superlattices. *Phys. Rev. B* **90**, 014307–014307 (2014).

32. Wolf, E. New theory of partial coherence in the space–frequency domain. Part I: spectra and cross spectra of steady-state sources. *JOSA* **72**, 343–351 (1982).

33. Joulain, K., Mulet, J.-P., Marquier, F., Carminati, R. & Greffet, J.-J. Surface electromagnetic waves thermally excited: Radiative heat transfer, coherence properties and Casimir forces revisited in the near field. *Surf. Sci. Rep.* **57**, 59–112 (2005).

34. Singer, A. *et al.* Transverse-Coherence Properties of the Free-Electron-Laser FLASH at DESY. *Phys. Rev. Lett.* **101**, 254801 (2008).

35. Pickering, T., Hamm, J. M., Page, A. F., Wuestner, S. & Hess, O. Cavity-free plasmonic nanolasing enabled by dispersionless stopped light. *Nat. Commun.* **5**, 4972 (2014).

36. Chen, G., Borca-Tasciuc, D. & Yang, R. G. Nanoscale heat transfer. *Encycl. Nanosci Nanotechnol* **7**, 429–459 (2004).

37. Yao, T. Thermal Properties of AlAs/GaAs superlattices. *Appl. Phys. Lett.* **51**, 1798–1798 (1987).

38. Tamura, S., Hurley, D. C. & Wolfe, J. P. Acoustic-phonon propagation in superlattices. *Phys. Rev. B* **38**, 1427–1449 (1988).

39. Hicks, L. D., Harman, T. C. & Dresselhaus, M. S. Use of quantum-well superlattices to obtain a high figure of merit from nonconventional thermoelectric materials. *Appl. Phys. Lett.* **63**, 3230–3232 (1993).

40. Majumdar, A. Microscale heat conduction in dielectric thin films. *J. Heat Transf.* **115**, 7–16 (1993).

41. Chen, G. Thermal conductivity and ballistic-phonon transport in the cross-plane direction of superlattices. *Phys. Rev. B* **57**, 14958–14973 (1998).

42. Chen, G. *Nanoscale Energy Transport and Conversion: A Parallel Treatment of Electrons, Molecules, Phonons, and Photons*. (Oxford University Press, 2005).

43. Ziman, J. M. *Electrons and Phonons*. (Clarendon Press, 1960).

44. Xiao, Y. & Zhao, L.-D. Charge and phonon transport in PbTe-based thermoelectric materials. *Npj Quantum Mater.* **3**, (2018).

45. Stoner, R. J. & Maris, H. J. Kapitza conductance and heat flow between solids at temperatures from 50 to 300 K. *Phys. Rev. B* **48**, 16373–16387 (1993).

46. Klemens, P. G. The thermal conductivity of dielectric solids at low temperatures. *Proc. Phys. Soc. Lond. Sect. A* **208**, 108–133 (1951).

47. Ziman, J. M. The general variational principle of transport theory. *Can. J. Phys.* **34**, 1256–1273 (1956).

48. Callaway, J. Model for lattice thermal conductivity at low temperatures. *Phys. Rev.* **113**, 1046–1051 (1959).

49. Klemens, P. G. Thermal Resistance due to Point Defects at High Temperatures. *Phys. Rev.* **119**, 507–509 (1960).

50. Seyf, H. R. *et al.* Rethinking phonons: The issue of disorder. *Npj Comput. Mater.* **3**, 49 (2017).

51. Maznev, A. A. & Wright, O. B. Demystifying umklapp vs normal scattering in lattice thermal conductivity. *Am. J. Phys.* **82**, 1062–1066 (2014).

52. Klemens, P. G. The scattering of low-frequency lattice waves by static imperfections. *Proc. Phys. Soc. Lond. Sect. A* **68**, 1113–1128 (1955).

53. Touloukian, Y. S., Powell, R. W., Ho, C. Y. & Klemens, P. G. *Thermophysical Properties of Matter - Thermal Conductivity: Nonmetallic Solids*. vol. 2 (U.S. Department of Energy, 1971).

54. Cahill, D. G., Watson, S. K. & Pohl, R. O. Lower limit to the thermal conductivity of disordered crystals. *Phys. Rev. B* **46**, 6131–6140 (1992).

55. Liu, W. & Asheghi, M. Thermal Conductivity Measurements of Ultra-Thin Single Crystal Silicon Layers. *J. Heat Transf.* **128**, 75–83 (2006).

56. Lee, S. M., Cahill, D. G. & Venkatasubramanian, R. Thermal conductivity of Si-Ge superlattices. *Appl. Phys. Lett.* **70**, 2957–2959 (1997).

57. Cahill, D. G., Watanabe, F., Rockett, A. & Vining, C. B. Thermal conductivity of epitaxial layers of dilute SiGe alloys. *Phys. Rev. B* **71**, 235202 (2005).

58. Devyatkova, E. D. & Smirnov, I. A. Thermal Conductivity of PbTe. *Sov. Phys. Solid State* **4**, 2507 (1962).

59. Devyatkova, E. D. & Smirnov, I. A. Thermal Conductivity of PbSe. *Sov. Phys. Solid State* **2**, 1984 (1960).

60. DeCoster, M. E. *et al.* Thermal Conductivity and Phonon Scattering Processes of ALD Grown PbTe–PbSe Thermoelectric Thin Films. *Adv. Funct. Mater.* **0**, 1904073.

61. Sales, B. C., Mandrus, D. & Williams, R. K. Filled Skutterudite Antimonides: A New Class of Thermoelectric Materials. *Science* **272**, 1325–1328 (1996).

62. Ross, R. G., Andersson, P. & Bäckström, G. Unusual PT dependence of thermal conductivity for a clathrate hydrate. *Nature* **290**, 322–323 (1981).

63. Yu, R. C., Tea, N., Salamon, M. B., Lorents, D. & Malhotra, R. Thermal conductivity of single crystal ${\mathrm{C}}_{60}$. *Phys. Rev. Lett.* **68**, 2050–2053 (1992).

64. Cen, C., Warusawithana, M. P. & Levy, J. Coherent phonon generation and detection in ultrathin SrTiO_3 grown directly on silicon. *Ann. Phys.* **524**, 429–433 (2012).

65. Tadano, T., Gohda, Y. & Tsuneyuki, S. Impact of Rattlers on Thermal Conductivity of a Thermoelectric Clathrate: A First-Principles Study. *Phys. Rev. Lett.* **114**, 095501 (2015).

66. Li, W., Carrete, J., Madsen, G. K. H. & Mingo, N. Influence of the optical-acoustic phonon hybridization on phonon scattering and thermal conductivity. *Phys. Rev. B* **93**, 205203 (2016).

67. L.D. Landau & E.M. Lifshitz. *Quantum Mechanics*.

68. Giri, A. & Hopkins, P. E. Giant reduction and tunability of the thermal conductivity of carbon nanotubes through low-frequency resonant modes. *Phys. Rev. B* **98**, 045421 (2018).

69. Wybourne, M. N., Kiff, B. J. & Batchelder, D. N. Anomalous Thermal Conduction in Polydiacetylene Single Crystals. *Phys. Rev. Lett.* **53**, 580–583 (1984).

70. H. Lee, C., Hase, I., Sugawara, H., Yoshizawa, H. & Sato, H. Low-Lying Optical Phonon Modes in the Filled Skutterudite CeRu $_4$ Sb $_{12}$. *J. Phys. Soc. Jpn.* **75**, 123602 (2006).

71. Slack, G. A. & Tsoukala, V. G. Some properties of semiconducting IrSb $_3$$. *J. Appl. Phys.* **76**, 1665–1671 (1994).

72. Cohn, J. L., Nolas, G. S., Fessatidis, V., Metcalf, T. H. & Slack, G. A. Glasslike Heat Conduction in High-Mobility Crystalline Semiconductors. *Phys. Rev. Lett.* **82**, 779–782 (1999).

73. Christensen, M. *et al.* Avoided crossing of rattler modes in thermoelectric materials. *Nat. Mater.* **7**, 811–815 (2008).

74. Allen, P. B. & Feldman, J. L. Thermal conductivity of disordered harmonic solids. *Phys. Rev. B* **48**, 12582–12588 (1993).

75. Larkin, J. M. & McGaughey, A. J. H. Thermal conductivity accumulation in amorphous silica and amorphous silicon. *Phys. Rev. B* **89**, 144303–144303 (2014).

76. Braun, J., L. *et al.* Size effects on the thermal conductivity of amorphous silicon thin films. *Phys. Rev. B* **93**, (2016).

77. Einstein, A. Elementary observations on thermal molecular motion in solids. *Ann. Phys.* **35**, 679–694 (1911).

78. Cahill, D. G. & Pohl, R. O. Heat flow and lattice vibrations in glasses. *Solid State Commun.* **70**, 927–930 (1989).

79. Slack, G. A. The thermal conductivity of nonmetallic crystals. in *Solid State Physics: Advances in Research and Applications* (eds. Ehrenreich, H., Seitz, F. & Turnbull, D.) vol. 34 1–73 (Academic Press, 1979).

80. Cahill, D. G. & Pohl, R. O. Lattice vibrations and heat transport in crystals and glasses. *Annu. Rev. Phys. Chem.* **39**, 93–121 (1988).

81. Majumdar, A. Lower limit of thermal conductivity: Diffusion versus localization. *Microscale Thermophys. Eng.* **2**, 5–9 (1998).

82. Allen, P. B., Feldman, J. L., Fabian, J. & Wooten, F. Diffusons, locons and propagons: character of atomic vibrations in amorphous Si. *Philos. Mag. B* **79**, 1715–1731 (1999).

83. Lv, W. & Henry, A. Direct calculation of modal contributions to thermal conductivity via Green–Kubo modal analysis. *New J. Phys.* **18**, 013028 (2016).

84. Feldman, J. L., Kluge, M. D., Allen, P. B. & Wooten, F. Thermal conductivity and localization in glasses: Numerical study of a model of amorphous silicon. *Phys. Rev. B* **48**, 12589–12602 (1993).

85. Moon, J., Latour, B. & Minnich, A. J. Propagating elastic vibrations dominate thermal conduction in amorphous silicon. *Phys. Rev. B* **97**, 024201 (2018).

86. Lv, W. & Henry, A. Non-negligible Contributions to Thermal Conductivity From Localized Modes in Amorphous Silicon Dioxide. *Sci. Rep.* **6**, 35720 (2016).

87. Attfield, J. P. Mechanisms and Materials for NTE. *Front. Chem.* **6**, (2018).

88. Braun, J. L. *et al.* Charge-Induced Disorder Controls the Thermal Conductivity of Entropy-Stabilized Oxides. *Adv. Mater.* **30**, 1805004 (2018).

89. Debye, P. *Vorträge Über Die Kinetische Theorie Der Materie and Elektrizität,*. (Terubner, 1914).

90. Stan, G. *et al.* Thermal conductivity of entropy stabilized oxides: approaching the minimum limit in single crystal solid solutions through charge induced atomic-scale disorder. (2018).

91. Leibfried, G. & Schlomann, E. Nach. Akad. Wiss. Gottingen. *Math Phyz Kl.* **4**, (1954).

92. Poirier, J. P. *Introduction to the Physics of the Earth's Interior*. (Cambridge University Press, 2000).

93. Roufosse, M. & Klemens, P. G. Thermal conductivity of complex dieletric crystals. *Phys. Rev. B* **7**, 5379–5386 (1973).

94. Slack, G. A. Nonmetallic crystals with high thermal conductivity. *J. Phys. Chem. Solids* **34**, 321–335 (1973).

95. Van De Walle, W. & Janssen, H. Impact of pore scale parameters on the thermal conductivity of porous building blocks. *MATEC Web Conf.* **282**, 02012 (2019).

96. Maxwell, J. C. *A treatise on electricity and magnetism*. (Oxford : Clarendon Press, 1873).

97. Ge, Z., Cahill, D. G. & Braun, P. V. Thermal Conductance of Hydrophilic and Hydrophobic Interfaces. *Phys. Rev. Lett.* **96**, 186101 (2006).

98. Pernot, G. *et al.* Precise control of thermal conductivity at the nanoscale through individual phonon-scattering barriers. *Nat. Mater.* **9**, 491–495 (2010).

99. Jelle, B. P. Traditional, state-of-the-art and future thermal building insulation materials and solutions – Properties, requirements and possibilities. *Energy Build.* **43**, 2549–2563 (2011).

100. Chatterjee, A. *et al.* Heat conduction model based on percolation theory for thermal conductivity of composites with high volume fraction of filler in base matrix. *Int. J. Therm. Sci.* **136**, 389–395 (2019).

101. Nan, C. W., Birringer, R., Clarke, D. R. & Gleiter, H. Effective thermal conductivity of particulate composites with interfacial thermal resistance. *J. Appl. Phys.* **81**, 6692–6699 (1997).

102. R.S, L. R. S. LVI. On the influence of obstacles arranged in rectangular order upon the properties of a medium. *Lond. Edinb. Dublin Philos. Mag. J. Sci.* **34**, 481–502 (1892).

103. Minnich, A. & Chen, G. Modified effective medium formulation for the thermal conductivity of nanocomposites. *Appl. Phys. Lett.* **91**, 073105–073105 (2007).

104. Bruggeman, D. A. G. Computation of different physical constants of heterogeneous substances. I. Dielectric constants and conductivenesses of the mixing bodies from isotropic substances (Berechnung verschiedener physikalischer Konstanten von heterogenen Substanzen. I. Dielektrizitätskonstanten und Leitfähigkeiten der Mischkörper aus isotropen Substanzen). *Ann. Phys. Ann. Phys.* **416**, 636–664 (1935).

105. Nait-Ali, B., Haberko, K., Vesteghem, H., Absi, J. & Smith, D. S. Preparation and thermal conductivity characterisation of highly porous ceramics: Comparison between experimental results, analytical calculations and numerical simulations. *J. Eur. Ceram. Soc.* **27**, 1345–1350 (2007).

106. Wicklein, B. *et al.* Thermally insulating and fire-retardant lightweight anisotropic foams based on nanocellulose and graphene oxide. *Nat. Nanotechnol.* **10**, 277–283 (2015).

107. Double-negative-index ceramic aerogels for thermal superinsulation | Science. https://science.sciencemag.org/content/363/6428/723.

108. Notario, B. *et al.* Experimental validation of the Knudsen effect in nanocellular polymeric foams. *Polymer* **56**, 57–67 (2015).

109. Song, D. & Chen, G. Thermal conductivity of periodic microporous silicon films. *Appl. Phys. Lett.* **84**, 687–689 (2004).

110. Benedetto, G., Boarino, L. & Spangnolo, R. Evaluation of thermal conductivity of porous silicon layers by a photoacoustic method. *Appl. Phys. A* **64**, 155–159 (1997).

111. Romano, G. & Grossman, J. C. Phonon bottleneck identification in disordered nanoporous materials. *Phys. Rev. B* **96**, 115425 (2017).

112. Wolf, S., Neophytou, N. & Kosina, H. Thermal conductivity of silicon nanomeshes: Effects of porosity and roughness. *J. Appl. Phys.* **115**, 204306 (2014).

113. Hopkins, P. E. *et al.* Reduction in the thermal conductivity of single crystalline silicon by phononic crystal patterning. *Nano Lett.* **11**, 107–112 (2011).

114. Wei, T. Y., Lu, S. Y. & Chang, Y. C. A new class of opacified monolithic aerogels of ultralow high-temperature thermal conductivities. *J. Phys. Chem. C* **113**, 7424–7428 (2009).

115. Archie, G. E. The Electrical Resistivity Log as an Aid in Determining Some Reservoir Characteristics. *Trans. AIME* **146**, 54–62 (1942).

116. Hopkins, P. E. *et al.* Measuring the thermal conductivity of porous, transparent SiO_2 films with time domain thermoreflectance. *J. Heat Transf.* **133**, 061601–061601 (2011).

117. Hashin, Z. & Shtrikman, S. A Variational Approach to the Theory of the Effective Magnetic Permeability of Multiphase Materials. *J. Appl. Phys.* **33**, 3125–3131 (1962).

118. Landauer, R. The Electrical Resistance of Binary Metallic Mixtures. *J. Appl. Phys.* **23**, 779–784 (1952).

119. Huang, B. L. *et al.* Thermal conductivity of a metal-organic framework (MOF-5): Part II. Measurement. *Int. J. Heat Mass Transf.* **50**, 405–411 (2007).

120. Han, L., Budge, M. & Alex Greaney, P. Relationship between thermal conductivity and framework architecture in MOF-5. *Comput. Mater. Sci.* **94**, 292–297 (2014).

121. Cui, B. *et al.* Thermal Conductivity of ZIF-8 Thin-Film under Ambient Gas Pressure. *ACS Appl. Mater. Interfaces* **9**, 28139–28143 (2017).

122. Erickson, K. J. *et al.* Thin Film Thermoelectric Metal–Organic Framework with High Seebeck Coefficient and Low Thermal Conductivity. *Adv. Mater.* **27**, 3453–3459 (2015).

123. Freitas, S. K. S., Borges, R. S., Merlini, C., Barra, G. M. O. & Esteves, P. M. Thermal Conductivity of Covalent Organic Frameworks as a Function of Their Pore Size. *J. Phys. Chem. C* **121**, 27247–27252 (2017).

124. Qiu, P. F. *et al.* High-temperature electrical and thermal transport properties of fully filled skutterudites RFe4Sb12 (R = Ca, Sr, Ba, La, Ce, Pr, Nd, Eu, and Yb). *J. Appl. Phys.* **109**, 063713 (2011).

125. Takabatake, T., Suekuni, K., Nakayama, T. & Kaneshita, E. Phonon-glass electron-crystal thermoelectric clathrates: Experiments and theory. *Rev. Mod. Phys.* **86**, 669–716 (2014).

126. de Boor, J. *et al.* Temperature and structure size dependence of the thermal conductivity of porous silicon. *EPL Europhys. Lett.* **96**, 16001 (2011).

127. Schoedel, A. & Yaghi, O. M. Porosity in Metal-Organic Compounds. in *Macrocyclic and Supramolecular Chemistry* (ed. Izatt, R. M.) 200–219 (John Wiley & Sons, Ltd, 2016). doi:10.1002/9781119053859.ch9.

128. Muraoka, K., Sada, Y., Miyazaki, D., Chaikittisilp, W. & Okubo, T. Linking synthesis and structure descriptors from a large collection of synthetic records of zeolite materials. *Nat. Commun.* **10**, 4459 (2019).

129. Li, W. & Mingo, N. Ultralow lattice thermal conductivity of the fully filled skutterudite ${\text{YbFe}}_{4}{\text{Sb}}_{12}$ due to the flat avoided-crossing filler modes. *Phys. Rev. B* **91**, 144304 (2015).

130. Keppens, V. *et al.* Localized vibrational modes in metallic solids. *Nature* **395**, 876–878 (1998).

131. Gunatilleke, W. D. C. B. *et al.* Thermal conductivity of a perovskite-type metal–organic framework crystal. *Dalton Trans.* **46**, 13342–13344 (2017).

132. Sales, B. C., Mandrus, D., Chakoumakos, B. C., Keppens, V. & Thompson, J. R. Filled skutterudite antimonides: Electron crystals and phonon glasses. *Phys. Rev. B* **56**, 15081–15089 (1997).

133. Greenstein, A., Hudiono, Y., Graham, S. & Nair, S. Effects of nonframework metal cations and phonon scattering mechanisms on the thermal transport properties of polycrystalline zeolite LTA films. *J. Appl. Phys.* **107**, 063518 (2010).

134. Inzoli, I., Simon, J. M., Bedeaux, D. & Kjelstrup, S. Thermal Diffusion and Partial Molar Enthalpy Variations of n-Butane in Silicalite-1. *J. Phys. Chem. B* **112**, 14937–14951 (2008).

135. Fang, J., Huang, Y., Lew, C. M., Yan, Y. & Pilon, L. Temperature dependent thermal conductivity of pure silica MEL and MFI zeolite thin films. *J. Appl. Phys.* **111**, 054910 (2012).

136. Handa, Y. Paul. & Cook, J. G. Thermal conductivity of xenon hydrate. *J. Phys. Chem.* **91**, 6327–6328 (1987).

137. Krivchikov, A. I. *et al.* Thermal conductivity of Xe clathrate hydrate at low temperatures. *Phys. Rev. B* **73**, 064203 (2006).

138. Cook, J. G. & Leaist, D. G. An exploratory study of the thermal conductivity of methane hydrate. *Geophys. Res. Lett.* **10**, 397–399 (1983).

139. Talin, A. A. *et al.* Tunable Electrical Conductivity in Metal-Organic Framework Thin-Film Devices. *Science* **343**, 66–69 (2014).

140. Chakoumakos, B. C., Sales, B. C., Mandrus, D. & Keppens, V. Disparate atomic displacements in skutterudite-type LaFe3CoSb12, a model for thermoelectric behavior. *Acta Crystallogr. Sect. B* **B55**, 341–347 (1999).

141. Paddock, C. A. & Eesley, G. L. Transient thermoreflectance from thin metal films. *J. Appl. Phys.* **60**, 285–290 (1986).

142. Takahata, K., Iguchi, Y., Tanaka, D., Itoh, T. & Terasaki, I. Low thermal conductivity of the layered oxide (Na,Ca)Co_2O_4: Another example of a phonon glass and an electron crystal. *Phys. Rev. B* **61**, 12551–12555 (2000).

143. Giri, A. *et al.* Mechanisms of nonequilibrium electron-phonon coupling and thermal conductance at interfaces. *J. Appl. Phys.* **117**, 105105–105105 (2015).

144. Norris, P. M. *et al.* Femtosecond pump-probe nondestructive examination of materials. *Rev. Sci. Instrum.* **74**, 400–406 (2003).

145. Eesley, G. L. Generation of nonequlibrium electron and lattice temperatures in copper by picosecond laser pulses. *Phys. Rev. B* **33**, 2144–2151 (1986).

146. DeCoster, M. E. *et al.* Thermal Conductivity and Phonon Scattering Processes of ALD Grown PbTe–PbSe Thermoelectric Thin Films. *Adv. Funct. Mater.* **0**, 1904073.

147. Donovan, B. F. *et al.* Thermal boundary conductance across metal-gallium nitride interfaces from 80 - 450 K. *Appl. Phys. Lett.* **105**, 203502–203502 (2014).

148. Cheaito, R. *et al.* Thermal boundary conductance accumulation and interfacial phonon transmission: Measurements and theory. *Phys. Rev. B* **91**, 035432–035432 (2015).

149. Schmidt, A. J., Chen, X. & Chen, G. Pulse accumulation, radial heat conduction, and anisotropic thermal conductivity in pump-probe transient thermoreflectance. *Rev. Sci. Instrum.* **79**, 114902–114902 (2008).

150. Cahill, D. G. *et al.* Nanoscale thermal transport. II. 2003-2012. *Appl. Phys. Rev.* **1**, 011305–011305 (2014).

151. Rost, C. M. *et al.* Hafnium nitride films for thermoreflectance transducers at high temperatures: Potential based on heating from laser absorption. *Appl. Phys. Lett.* **111**, 151902 (2017).

152. Braun, J. L., Szwejkowski, C. J., Giri, A. & Hopkins, P. E. On the Steady-State Temperature Rise During Laser Heating of Multilayer Thin Films in Optical Pump–Probe Techniques. *J. Heat Transf.* **140**, 052801-052801–10 (2018).

153. Cahill, D. G. Analysis of heat flow in layered structures for time-domain thermoreflectance. *Rev. Sci. Instrum.* **75**, 5119–5122 (2004).

154. Wilson, R. B., Apgar, B. A., Martin, L. W. & Cahill, D. G. Thermoreflectance of metal transducers for optical pump-probe studies of thermal properties. *Opt. Express* **20**, 28829 (2012).

155. Wang, Y., Park, J. Y., Koh, Y. K. & Cahill, D. G. Thermoreflectance of metal transducers for time-domain thermoreflectance. *J. Appl. Phys.* **108**, 043507 (2010).

156. Hopkins, P. E. & Duda, J. C. Heat Transfer - Mathematical Modelling, Numerical Methods and Information Technology. 305–330 (2011).

157. Schmidt, A. J. Pump-probe thermoreflectance. *Annu. Rev. Heat Transf.* **16**, 159–181 (2013).

158. Kang, K., Koh, Y. K., Chiritescu, C., Zheng, X. & Cahill, D. G. Two-tint pump-probe measurements using a femtosecond laser oscillator and sharp-edged optical filters. *Rev. Sci. Instrum.* **79**, 114901–114901 (2008).

159. Gengler, J. J., Roy, S., Jones, J. G. & Gord, J. R. Two-color time-domain thermoreflectance of various metal transducers with an optical parametric oscillator. *Meas. Sci. Technol.* **23**, 055205–055205 (2012).

160. Hopkins, P. E. Contributions of inter- and intraband excitations to electron heat capacity and electron-phonon coupling in noble metals. *J. Heat Transf.* **132**, 014504–014504 (2010).

161. Giri, A., Gaskins, J. T., Foley, B. M., Cheaito, R. & Hopkins, P. E. Experimental evidence of excited electron number density and temperature effects on electron-phonon coupling in gold films. *J. Appl. Phys.* **117**, 044305–044305 (2015).

162. Wang, W. & Cahill, D. G. Limits to Thermal Transport in Nanoscale Metal Bilayers due to Weak Electron-Phonon Coupling in Au and Cu. *Phys. Rev. Lett.* **109**, 175503–175503 (2012).

163. Hopkins, P. E. & Norris, P. M. Substrate influence in electron-phonon coupling measurements in thin Au films. *Appl. Surf. Sci.* **253**, 6289–6294 (2007).

164. Dai, J., Mukundhan, P., Kim, C. & Maris, H. J. Analysis of a picosecond ultrasonic method for measurement of stress in a substrate. *J. Appl. Phys.* **119**, 105705 (2016).

165. Thomsen, C., Maris, H. J. & Tauc, J. Picosecond acoustics as a non-destructive tool for the characterization of very thin films. *Thin Solid Films* **154**, 217–223 (1987).

166. Antonelli, G. A., Perrin, B., Daly, B. C. & Cahill, D. G. Characterization of mechanical and thermal properties using ultrafast optical metrology. *MRS Bull.* **31**, 607–613 (2006).

167. Braun, J. L. & Hopkins, P. E. Upper limit to the thermal penetration depth during modulated heating of multilayer thin films with pulsed and continuous wave lasers: A numerical study. *J. Appl. Phys.* **121**, 175107 (2017).

168. Schmidt, A., Chiesa, M., Chen, X. & Chen, G. An optical pump-probe technique for measuring the thermal conductivity of liquids. *Rev. Sci. Instrum.* **79**, 064902–064902 (2008).

169. Axelevitch, A., Gorenstein, B. & Golan, G. Investigation of Optical Transmission in Thin Metal Films. *Phys. Procedia* **32**, 1–13 (2012).

170. Liu, J. *et al.* Simultaneous measurement of thermal conductivity and heat capacity of bulk and thin film materials using frequency-dependent transient thermoreflectance method. *Rev. Sci. Instrum.* **84**, 034902–034902 (2013).

171. Hopkins, P. E. *et al.* Criteria for cross-plane dominated thermal transport in multilayer thin film systems during modulated laser heating. *J. Heat Transf.* **132**, 081302–081302 (2010).

172. Koh, Y. K., Cahill, D. G. & Sun, B. Nonlocal theory for heat transport at high frequencies. *Phys. Rev. B* **90**, 205412–205412 (2014).

173. Carslaw, H. S. & Jaeger, J. C. *Conduction of Heat in Solids*. (Oxford University Press, 1959).

174. Feldman, A. Algorithm for solutions of the thermal diffusion equation in a stratified medium with a modulated heating source. *High Temp.-High Press.* **31**, 293–298 (1999).

175. Schmidt, A. J., Cheaito, R. & Chiesa, M. A frequency-domain thermoreflectance method for the characterization of thermal properties. *Rev. Sci. Instrum.* **80**, 094901–094901 (2009).

176. Koh, Y. K. & Cahill, D. G. Frequency dependence of the thermal conductivity of semiconductor alloys. *Phys. Rev. B* **76**, 075207–075207 (2007).

177. Costescu, R. M., Wall, M. A. & Cahill, D. G. Thermal conductance of epitaxial interfaces. *Phys. Rev. B* **67**, 054302–054302 (2003).

178. Hopkins, P. E. *et al.* Criteria for Cross-Plane Dominated Thermal Transport in Multilayer Thin Film Systems During Modulated Laser Heating. *J. Heat Transf.* **132**, 081302-081302–10 (2010).

179. Cen, C., Warusawithana, M. P. & Levy, J. Coherent phonon generation and detection in ultrathin SrTiO_3 grown directly on silicon. *Ann. Phys.* **524**, 429–433 (2012).

180. Costescu, R. M., Wall, M. A. & Cahill, D. G. Thermal conductance of epitaxial interfaces. *Phys. Rev. B* **67**, 054302–054302 (2003).

181. Cheaito, R. The Role of Size Effects on the Thermal Conductivity of Thin Film Alloys and Superlattices. (University of Virginia, 2015).

182. Tas, G. & Maris, H. J. Picosecond ultrasonic study of phonon reflection from solid-liquid interfaces. *Phys. Rev. B* **55**, 1852–1857 (1997).

183. Pine, A. S. *Light scattering in solids*. (Springer-Verlag, 1975).

184. Cardona, M. Light scattering in solids II. in *Light Scattering in solids II* 69 (Springer-Verlag, 1975).

185. Sandercock, J. R. Brillouin-Scattering Measurements on Silicon and Germanium. *Phys. Rev. Lett.* **28**, 237–240 (1972).

186. Vacher, R. & Pelous, J. Behavior of thermal phonons in amorphous media from 4 to 300 K. *Phys. Rev. B* **14**, 823–828 (1976).

187. Raetz, S. *et al.* Evaluation of the Structural Phase Transition in Multiferroic (Bi1−x Prx)(Fe0.95 Mn0.05)O3 Thin Films by A Multi-Technique Approach Including Picosecond Laser Ultrasonics. *Appl. Sci.* **9**, 736 (2019).

188. Thomsen, C., Grahn, H. T., Maris, H. J. & Tauc, J. Picosecond interferometric technique for the study of phonons in the Brillouin frequency range. *Opt Comm* **60**, 55–58 (1986).

189. Wen, H. *et al.* Electronic Origin of Ultrafast Photoinduced Strain in BiFeO_3. *Phys. Rev. Lett.* **110**, 037601–037601 (2013).

190. Taylor, J. R. *An Introduction to Error Analysis: The Study of Uncertainties In Physical Measurements.* (University Science Books, 1997).

191. Snyder, G. J. & Toberer, E. S. Complex thermoelectric materials. *Nat. Mater.* **7**, 105–114 (2008).

192. Chen, X. *et al.* Seebeck Coefficient Enhancement of ALD PbTe/PbSe Nanolaminate Structures Deposited Inside Porous Silicon Templates. *ECS J. Solid State Sci. Technol.* (2016) doi:10.1149/2.0151609jss.

193. El-Sharkawy, A. A., Abou El-Azm, A. M. & Kenawy, M. I. thermophysical properties of polycrystalline PbS, PbSe, and PbTe in the temperature range 300 - 700 K. *Int. J. Thermophys.* **4**, 261–269 (1983).

194. Harman, T. C., Taylor, P. J., Spears, D. L. & Walsh, M. P. Thermoelectric quantum-dot superlattices with high ZT. *J. Electron. Mater.* **29**, L1–L2 (2000).

195. Koh, Y. K., Vineis, C. J., Calawa, S. D., Walsh, M. P. & Cahill, D. G. Lattice thermal conductivity of nanostructured thermoelectric materials based on PbTe. *Appl. Phys. Lett.* **94**, 153101–153101 (2009).

196. Skelton, J. M., Parker, S. C., Togo, A., Tanaka, I. & Walsh, A. Thermal physics of the lead chalcogenides PbS, PbSe, and PbTe from first principles. *Phys. Rev. B* **89**, 205203 (2014).

197. Chen, X. *et al.* Seebeck Coefficient Enhancement of ALD PbTe/PbSe Nanolaminate Structures Deposited Inside Porous Silicon Templates. *ECS J. Solid State Sci. Technol.* (2016) doi:10.1149/2.0151609jss.

198. Tian, Z. *et al.* Phonon conduction in PbSe, PbTe, and PbTe_1-xSe_x from first-principles calculations. *Phys. Rev. B* **85**, (2012).

199. Zebarjadi, M., Esfarjani, K., Dresselhaus, M. S., Ren, Z. F. & Chen, G. Perspectives on thermoelectrics: from fundamentals to device applications. *Energy Environ. Sci.* **5**, 5147–5162 (2012).

200. Harman, T. C., Taylor, P. J., Spears, D. L. & Walsh, M. P. Thermoelectric quantum-dot superlattices with high ZT. *J. Electron. Mater.* **29**, L1–L2 (2000).

201. Cheaito, R. *et al.* Interplay between total thickness and period thickness in the phonon thermal conductivity of superlattices from the nanoscale to the microscale: Coherent versus incoherent phonon transport. *Phys. Rev. B* **97**, 085306 (2018).

202. Cheaito, R. *et al.* Experimental Investigation of Size Effects on the Thermal Conductivity of Silicon-Germanium Alloy Thin Films. *Phys. Rev. Lett.* **109**, 195901–195901 (2012).

203. Poudel, B. *et al.* High-thermoelectric performance of nanostructured bismuth antimony telluride bulk alloys. *Science* **320**, 634–638 (2008).

204. Donovan, B. F. *et al.* Elastic mismatch induced reduction of the thermal conductivity of silicon with aluminum nano-inclusions. *Appl. Phys. Lett.* **112**, 213103 (2018).

205. Chen, L., Braun, J. L., Donovan, B. F., Hopkins, P. E. & Poon, S. J. Ballistic transport of long wavelength phonons and thermal conductivity accumulation in nanograined silicon-germanium alloys. *Appl. Phys. Lett.* **111**, 131902 (2017).

206. Esfarjani, K., Chen, G. & Stokes, H. T. Heat transport in silicon from first-principles calculations. *Phys. Rev. B* **84**, 085204–085204 (2011).

207. Minnich, A. J. *et al.* Thermal Conductivity Spectroscopy Technique to Measure Phonon Mean Free Paths. *Phys. Rev. Lett.* **107**, 095901–095901 (2011).

208. Johnson, J. A. *et al.* Direct Measurement of Room-Temperature Nondiffusive Thermal Transport Over Micron Distances in a Silicon Membrane. *Phys. Rev. Lett.* **110**, 025901–025901 (2013).

209. Chen, G. *Nanoscale Energy Transport and Conversion: A Parallel Treatment of Electrons, Molecules, Phonons, and Photons*. (Oxford University Press, 2005).

210. Marconet, A. M., Asheghi, M. & Goodson, K. E. From the Casimir Limit to Phononic Crystals: Twenty Years of Phonon Transport Studies using Silicon-on-Insulator Technology. *J. Heat Transf.* **135**, 061601–061601 (2013).

211. Beechem, T. E. *et al.* Size dictated thermal conductivity of GaN. *J. Appl. Phys.* **120**, 095104 (2016).

212. Hopkins, P. E., Serrano, J. R., Phinney, L. M., Li, H. & Misra, A. Boundary scattering effects during electron thermalization in nanoporous gold. *J. Appl. Phys.* **109**, 013524–013524 (2011).

213. Simkin, M. V. & Mahan, G. D. Minimum thermal conductivity of superlattices. *Phys. Rev. Lett.* **84**, 927–930 (2000).

214. Ravichandran, J. *et al.* Crossover from incoherent to coherent phonon scattering in epitaxial oxide superlattices. *Nat. Mater.* **13**, 168–172 (2014).

215. Luckyanova, M. N. *et al.* Coherent Phonon Heat Conduction in Superlattices. *Science* **338**, 936–939 (2012).

216. Lee, S. M. & Cahill, D. G. Heat transport in thin dielectric films. *J. Appl. Phys.* **81**, 2590–2595 (1997).

217. Chen, P. *et al.* Role of Surface-Segregation-Driven Intermixing on the Thermal Transport through Planar Si/Ge Superlattices. *Phys. Rev. Lett.* **111**, 115901–115901 (2013).

218. Uchinokura, K., Sekine, T. & Matsuura, E. Critical-point analysis of the two-phonon Raman spectrum of silicon. *J. Phys. Chem. Solids* **35**, 171–180 (1974).

219. Ovsyannikov, S. V., Ponosov, Y. S., Shchennikov, V. V. & Mogilenskikh, V. E. Raman spectra of lead chalcogenide single crystals. *Phys. Status Solidi C* **1**, 3110–3113 (2004).

220. Koh, Y. K., Vineis, C. J., Calawa, S. D., Walsh, M. P. & Cahill, D. G. Lattice thermal conductivity of nanostructured thermoelectric materials based on PbTe. *Appl. Phys. Lett.* **94**, 153101–153101 (2009).

221. Shulumba, N., Hellman, O. & Minnich, A. J. Intrinsic localized mode and low thermal conductivity of PbSe. *Phys. Rev. B* **95**, 014302 (2017).

222. Latour, B., Volz, S. & Chalopin, Y. Microscopic description of thermal-phonon coherence: From coherent transport to diffuse interface scattering in superlattices. *Phys. Rev. B* **90**, 014307–014307 (2014).

223. Devyatkova, E. D. & Smirnov, I. A. *A. Sov. Phys. Solid State USSR* **2**, 1984 (1960).

224. Devyatkova, E. D. & Smirnov, I. A. *A. Sov. Phys. Solid State USSR* **4**, 2507 (1962).

225. Xie, L. S., Skorupskii, G. & Dincă, M. Electrically Conductive Metal–Organic Frameworks. *Chem. Rev.* acs.chemrev.9b00766 (2020) doi:10.1021/acs.chemrev.9b00766.

226. Erickson, K. J. *et al.* Thin Film Thermoelectric Metal–Organic Framework with High Seebeck Coefficient and Low Thermal Conductivity. *Adv. Mater.* **27**, 3453–3459 (2015).

227. Allendorf, M. D. *et al.* Guest-Induced Emergent Properties in Metal–Organic Frameworks. *J. Phys. Chem. Lett.* **6**, 1182–1195 (2015).

228. Lee, J. *et al.* Metal–organic framework materials as catalysts. *Chem. Soc. Rev.* **38**, 1450–1459 (2009).

229. Liu, J. *et al.* CO2/H2O Adsorption Equilibrium and Rates on Metal−Organic Frameworks: HKUST-1 and Ni/DOBDC. *Langmuir* **26**, 14301–14307 (2010).

230. Abrahams, B. F., Hoskins, B. F., Michail, D. M. & Robson, R. Assembly of porphyrin building blocks into network structures with large channels. *Nature* **369**, 727–729 (1994).

231. Babaei, H., McGaughey, A. J. H. & Wilmer, C. E. Effect of pore size and shape on the thermal conductivity of metal-organic frameworks. *Chem. Sci.* **8**, 583–589 (2016).

232. Babaei, H. & Wilmer, C. E. Mechanisms of Heat Transfer in Porous Crystals Containing Adsorbed Gases: Applications to Metal-Organic Frameworks. *Phys. Rev. Lett.* **116**, 025902 (2016).

233. Huang, B. L., McGaughey, A. J. H. & Kaviany, M. Thermal conductivity of metal-organic framework 5 (MOF-5): Part I. Molecular dynamics simulations. *Int. J. Heat Mass Transf.* **50**, 393–404 (2007).

234. Zhang, K. *et al.* Alcohol and water adsorption in zeolitic imidazolate frameworks. *Chem. Commun.* **49**, 3245–3247 (2013).

235. Babaei, H. *et al.* Observation of reduced thermal conductivity in a metal-organic framework due to the presence of adsorbates. *Nat. Commun.* **11**, 4010 (2020).

236. Rivera-Torrente, M. *et al.* Micro-spectroscopy of HKUST-1 metal–organic framework crystals loaded with tetracyanoquinodimethane: effects of water on host–guest chemistry and electrical conductivity. *Phys. Chem. Chem. Phys.* **21**, 25678–25689 (2019).

237. Neumann, T. *et al.* Superexchange Charge Transport in Loaded Metal Organic Frameworks. *ACS Nano* **10**, 7085–7093 (2016).

238. Talin, A. A. *et al.* Tunable Electrical Conductivity in Metal-Organic Framework Thin-Film Devices. *Science* **343**, 66–69 (2014).

239. Sun, L. *et al.* A Microporous and Naturally Nanostructured Thermoelectric Metal-Organic Framework with Ultralow Thermal Conductivity. *Joule* **1**, 168–177 (2017).

240. Hopkins, P. E., Kaehr, B., Piekos, E. S., Dunphy, D. & Brinker, C. J. Minimum thermal conductivity considerations in aerogel thin films. *J. Appl. Phys.* **111**, 113532–113532 (2012).

241. Cheaito, R. *et al.* Experimental Investigation of Size Effects on the Thermal Conductivity of Silicon-Germanium Alloy Thin Films. *Phys. Rev. Lett.* **109**, 195901–195901 (2012).

242. Toberer, E. S., Zevalkink, A. & Snyder, G. J. Phonon engineering through crystal chemistry. *J. Mater. Chem.* **21**, 15843–15852 (2011).

243. Suppression of thermal conductivity by rattling modes in thermoelectric sodium cobaltate | Nature Materials. https://www.nature.com/articles/nmat3739.

244. Zhang, X. & Jiang, J. Thermal Conductivity of Zeolitic Imidazolate Framework-8: A Molecular Simulation Study. *J. Phys. Chem. C* **117**, 18441–18447 (2013).

245. Chui, S. S.-Y., Lo, S. M.-F., Charmant, J. P. H., Orpen, A. G. & Williams, I. D. A Chemically Functionalizable Nanoporous Material [Cu3(TMA)2(H2O)3]n. *Science* **283**, 1148–1150 (1999).

246. Lin, K.-S., Adhikari, A. K., Ku, C.-N., Chiang, C.-L. & Kuo, H. Synthesis and characterization of porous HKUST-1 metal organic frameworks for hydrogen storage. *Int. J. Hydrog. Energy* **37**, 13865–13871 (2012).

247. Tanaka, S. *et al.* Adsorption and Diffusion Phenomena in Crystal Size Engineered ZIF-8 MOF. *J. Phys. Chem. C* **119**, 28430–28439 (2015).

248. Lee, J. H., Jeoung, S., Chung, Y. G. & Moon, H. R. Elucidation of flexible metal-organic frameworks: Research progresses and recent developments. *Coord. Chem. Rev.* **389**, 161–188 (2019).

249. Fairen-Jimenez, D. *et al.* Opening the Gate: Framework Flexibility in ZIF-8 Explored by Experiments and Simulations. *J. Am. Chem. Soc.* **133**, 8900–8902 (2011).

250. The Effect of Pressure on ZIF-8: Increasing Pore Size with Pressure and the Formation of a High-Pressure Phase at 1.47 GPa - Moggach - 2009 - Angewandte Chemie International Edition - Wiley Online Library. https://onlinelibrary.wiley.com/doi/full/10.1002/anie.200902643.

251. Hendon, C. H. & Walsh, A. Chemical principles underpinning the performance of the metal–organic framework HKUST-1. *Chem. Sci.* **6**, 3674–3683 (2015).

252. Lee, J.-C., Kim, J.-O., Lee, H.-J., Shin, B. & Park, S. Meniscus-Guided Control of Supersaturation for the Crystallization of High Quality Metal Organic Framework Thin Films. *Chem. Mater.* **31**, 7377–7385 (2019).

253. Ghorbanpour, A., Huelsenbeck, L. D., Smilgies, D.-M. & Giri, G. Oriented UiO-66 thin films through solution shearing. *CrystEngComm* **20**, 294–300 (2018).

254. Prestipino, C. *et al.* Local Structure of Framework Cu(II) in HKUST-1 Metallorganic Framework: Spectroscopic Characterization upon Activation and Interaction with Adsorbates. *Chem. Mater.* **18**, 1337–1346 (2006).

255. Janiak, C. Demonstration of permanent porosity in flexible and guest-responsive organic zeolite analogs (now called MOFs). *Chem. Commun.* **49**, 6933–6937 (2013).

256. Tian, T. *et al.* A sol–gel monolithic metal–organic framework with enhanced methane uptake. *Nat. Mater.* **17**, 174–179 (2018).

257. Pan, Y., Liu, W., Zhao, Y., Wang, C. & Lai, Z. Improved ZIF-8 membrane: Effect of activation procedure and determination of diffusivities of light hydrocarbons. *J. Membr. Sci.* **493**, 88–96 (2015).

258. Qiu, W. *et al.* Effect of Activation Temperature on Catalytic Performance of CuBTC for CO Oxidation. *Chin. J. Catal.* **33**, 986–992 (2012).

259. Moellmer, J., Moeller, A., Dreisbach, F., Glaeser, R. & Staudt, R. High pressure adsorption of hydrogen, nitrogen, carbon dioxide and methane on the metal–organic framework HKUST-1. *Microporous Mesoporous Mater.* **138**, 140–148 (2011).

260. Van Assche, T. R. C. *et al.* High Adsorption Capacities and Two-Step Adsorption of Polar Adsorbates on Copper–Benzene-1,3,5-tricarboxylate Metal–Organic Framework. *J. Phys. Chem. C* **117**, 18100–18111 (2013).

261. Tan, J. C., Bennett, T. D. & Cheetham, A. K. Chemical structure, network topology, and porosity effects on the mechanical properties of Zeolitic Imidazolate Frameworks. *Proc. Natl. Acad. Sci. U. S. A.* **107**, 9938–9943 (2010).

262. Park, K. S. *et al.* Exceptional chemical and thermal stability of zeolitic imidazolate frameworks. *Proc. Natl. Acad. Sci.* **103**, 10186–10191 (2006).

263. Arslan, H. K. *et al.* High-throughput fabrication of uniform and homogenous MOF coatings. *Adv. Funct. Mater.* **21**, 4228–4231 (2011).

264. Jung, S., Huelsenbeck, L., Hu, Q., Robinson, S. & Giri, G. Conductive, Large-Area, and Continuous 7,7,8,8-Tetracyanoquinodimethane@HKUST-1 Thin Films Fabricated Using Solution Shearing. *ACS Appl. Mater. Interfaces* (2021) doi:10.1021/acsami.1c00640.

265. Stassen, I. *et al.* Chemical vapour deposition of zeolitic imidazolate framework thin films. *Nat. Mater.* **15**, 304–310 (2016).

266. Bentley, J. *et al.* Effects of Open Metal Site Availability on Adsorption Capacity and Olefin/Paraffin Selectivity in the Metal–Organic Framework Cu3(BTC)2. *Ind. Eng. Chem. Res.* **55**, 5043–5053 (2016).

267. Kökçam-Demir, Ü. *et al.* Coordinatively unsaturated metal sites (open metal sites) in metal–organic frameworks: design and applications. *Chem. Soc. Rev.* **49**, 2751–2798 (2020).

268. Babaei, H., McGaughey, A. J. H. & Wilmer, C. E. Transient Mass and Thermal Transport during Methane Adsorption into the Metal–Organic Framework HKUST-1. *ACS Appl. Mater. Interfaces* **10**, 2400–2406 (2018).

269. Bordiga, S. *et al.* Adsorption properties of HKUST-1 toward hydrogen and other small molecules monitored by IR. *Phys. Chem. Chem. Phys.* **9**, 2676–2685 (2007).

270. Kozłowski, H., Kowalik-Jankowska, T. & Jeżowska-Bojczuk, M. Chemical and biological aspects of Cu2+ interactions with peptides and aminoglycosides. *Coord. Chem. Rev.* **249**, 2323–2334 (2005).

271. Usov, P. M. *et al.* Guest–Host Complexes of TCNQ and TCNE with Cu3(1,3,5-benzenetricarboxylate)2. *J. Phys. Chem. C* **121**, 26330–26339 (2017).

272. Heintz, R. A. *et al.* New Insight into the Nature of Cu(TCNQ): Solution Routes to Two Distinct Polymorphs and Their Relationship to Crystalline Films That Display Bistable Switching Behavior. *Inorg. Chem.* **38**, 144–156 (1999).

273. Bundschuh, S. *et al.* Mechanical properties of metal-organic frameworks: An indentation study on epitaxial thin films. *Appl. Phys. Lett.* **101**, 101910 (2012).

274. Erickson, K. J. *et al.* Thin Film Thermoelectric Metal–Organic Framework with High Seebeck Coefficient and Low Thermal Conductivity. *Adv. Mater.* **27**, 3453–3459 (2015).

275. Yu, K., Kiesling, K. & Schmidt, J. R. Trace Flue Gas Contaminants Poison Coordinatively Unsaturated Metal–Organic Frameworks: Implications for CO2 Adsorption and Separation. *J. Phys. Chem. C* **116**, 20480–20488 (2012).

276. Kapelewski, M. T. *et al.* M2(m-dobdc) (M = Mg, Mn, Fe, Co, Ni) Metal–Organic Frameworks Exhibiting Increased Charge Density and Enhanced H2 Binding at the Open Metal Sites. *J. Am. Chem. Soc.* **136**, 12119–12129 (2014).

277. Xu, Y., Goto, M., Kato, R., Tanaka, Y. & Kagawa, Y. Thermal conductivity of ZnO thin film produced by reactive sputtering. *J. Appl. Phys.* **111**, 084320–084320 (2012).

278. Banerjee, R. *et al.* High-throughput synthesis of zeolitic imidazolate frameworks and application to CO2 capture. *Science* **319**, 939–943 (2008).

279. Lv, W. & Henry, A. Examining the Validity of the Phonon Gas Model in Amorphous Materials. *Sci. Rep.* **6**, 37675 (2016).

280. Huang, B. L., McGaughey, A. J. H. & Kaviany, M. Thermal conductivity of metal-organic framework 5 (MOF-5): Part I: Molecular dynamics simulations. *Int. J. Heat Mass Transf.* **50**, 393–404 (2007).

281. Sing, K. S. W. *et al. Pure Appl. Chem.* **57**, 603–919 (1985).

282. Thommes, M. *et al.* Physisorption of gases, with special reference to the evaluation of surface area and pore size distribution (IUPAC Technical Report). *Pure Appl. Chem.* **87**, 1051–1069 (2015).

283. Babaei, H. & Wilmer, C. E. Mechanisms of Heat Transfer in Porous Crystals Containing Adsorbed Gases: Applications to Metal-Organic Frameworks. *Phys. Rev. Lett.* **116**, 025902 (2016).

284. Batyrev, I. G., Norman, A. G., Zhang, S. B. & Wei, S. H. Growth model for atomic ordering: The case for quadruple-period ordering in GaAsSb alloys. *Phys. Rev. Lett.* **90**, (2003).

285. Thomas, J. A., Turney, J. E., Iutzi, R. M., Amon, C. H. & McGaughey, A. J. H. Predicting phonon dispersion relations and lifetimes from the spectral energy density. *Phys. Rev. B* **81**, 081411 (2010).

286. Allendorf, M. D. *et al.* Guest-Induced Emergent Properties in Metal–Organic Frameworks. *J. Phys. Chem. Lett.* **6**, 1182–1195 (2015).

287. Larkin, J. M. & McGaughey, A. J. H. Predicting alloy vibrational mode properties using lattice dynamics calculations, molecular dynamics simulations, and the virtual crystal approximation. *J. Appl. Phys.* **114**, 023507–023507 (2013).

288. Lundgren, N. W., Barbalinardo, G. & Donadio, D. Mode Localization and Suppressed Heat Transport in Amorphous Alloys. *ArXiv201108318 Cond-Mat* (2020).

289. Yoon, J. W. *et al.* Selective nitrogen capture by porous hybrid materials containing accessible transition metal ion sites. *Nat. Mater.* **16**, 526–531 (2017).

290. Gee, J. A., Chung, J., Nair, S. & Sholl, D. S. Adsorption and Diffusion of Small Alcohols in Zeolitic Imidazolate Frameworks ZIF-8 and ZIF-90. *J. Phys. Chem. C* **117**, 3169–3176 (2013).

291. Xiang, S., Zhou, W., Gallegos, J. M., Liu, Y. & Chen, B. Exceptionally High Acetylene Uptake in a Microporous Metal−Organic Framework with Open Metal Sites. *J. Am. Chem. Soc.* **131**, 12415–12419 (2009).

292. Huang, J., Fan, A., Xia, X., Li, S. & Zhang, X. In Situ Thermal Conductivity Measurement of Single-Crystal Zeolitic Imidazolate Framework-8 by Raman-Resistance Temperature Detectors Method. *ACS Nano* **14**, 14100–14107 (2020).

293. Wei, W., Huang, J., Li, W., Peng, H. & Li, S. Impacts of Ethanol and Water Adsorptions on Thermal Conductivity of ZIF-8. *J. Phys. Chem. C* **123**, 27369–27374 (2019).

294. Liu, D. *et al.* MOF-5 composites exhibiting improved thermal conductivity. *Int. J. Hydrog. Energy* **37**, 6109–6117 (2012).

295. Chae, J. *et al.* Nanophotonic Atomic Force Microscope Transducers Enable Chemical Composition and Thermal Conductivity Measurements at the Nanoscale. *Nano Lett.* **17**, 5587-5594 (2017).

# 8. Appendix A

Table A 1: Full list and details of the individual MOF samples that were measured in Chapter 5.

| # | Sample | MOF Thickness (nm) | Transducer | Adsorbate | Transducer thickness (nm) | Thermal Conductivity ($Wm^{-1}K^{-1}$) | $G_{Au/SiO2}$ ($Wm^{-2}K^{-1}$) |
|---|---|---|---|---|---|---|---|
| 1 | HKUST-1 | 200 | Al | Pristine | 82 | 0.66 ± 0.04 | - |
| 2 | | | | Methanol | | 0.25 ± 0.09 | |
| 3 | | | | Ethanol | | 0.35 ± 0.10 | |
| 4 | HKUST-1 | 200 | Au | Pristine | 75 | 0.47 ± 0.10 | 4.7-e7 |
| 5 | | | | Water | | 0.24 ± 0.09 | |
| 6 | HKUST-1 | 250 | Al | Pristine | 83 | 0.78 ± 0.20 | - |
| 7 | HKUST-1 | 250 | Au | Pristine | 80 | 0.70 ± 0.15 | 6.94E+07 |
| 8 | | | | TCNQ | | 0.19 ± 0.09 | |
| 9 | HKUST-1 | 300 | Au | Pristine | 82 | 0.73 ± 0.14 | 6.94E+07 |
| 10 | | | | Water | 78 | 0.13 ± 0.11 | 4.70E+07 |
| 11 | | | | TCNQ | 80 | 0.21 ± 0.08 | 6.94E+07 |
| 12 | HKUST-1 | 350 | Al | Pristine | 82 | 0.45 ± 0.21 | - |
| 13 | | | | Methanol | | 0.14 ± 0.07 | |
| 14 | | | | Ethanol | | 0.18 ± 0.08 | |
| 15 | HKUST-1 | 400 | Au | Pristine | 80 | 0.77 ± 0.07 | 7.25E+07 |
| 16 | | | | Pristine | | 0.64 ± 0.10 | |
| 17 | | | | Pristine | | 0.88 ± 0.15 | |
| 18 | | | | TCNQ | | 0.38 ± 0.10 | |
| 19 | | | | TCNQ | | 0.46 ± 0.11 | |
| 20 | | | | $F_4$-TCNQ | 65 | 0.26 ± 0.13 | 3.80E+07 |
| 21 | HKUST-1 | 5500 | Au | Pristine | 80 | 0.86 ± 0.10 | 6.24E+07 |
| 22 | | | | Pristine | | 0.55 ± 0.20 | |
| 23 | | | | $N_2$ | | 0.31 ± 0.18 | |
| 24 | | | | Methanol | | 0.22 ± 0.08 | |
| 25 | | | | Ethanol | | 0.18 ± 0.09 | |
| 26 | | | | Water | | 0.38 ± 0.09 | |
| 27 | | | | TCNQ | 65 | 0.14 ± 0.06 | 9.81E+07 |
| 28 | | | | TCNQ | | 0.19 ± 0.12 | |
| 29 | | | | TCNQ | | 0.18 ± 0.06 | |
| 30 | | | | $F_4$-TCNQ | 80 | 0.23 ± 0.09 | 6.24E+07 |
| 31 | | | | $H_4$-TCNQ | | 0.32 ± 0.08 | |
| 32 | ZIF-8 | 280 | Au | Pristine | 80 | 0.23 ± 0.07 | 7.35E+07 |
| 33 | | | | $N_2$ | | 0.19 ± 0.05 | |
| 34 | | | | Methanol | | 0.17 ± 0.07 | |
| 35 | | | | Ethanol | | 0.17 ± 0.06 | |
| 36 | | | | Water | | 0.11 ± 0.08 | |